Available online at www.sciencedirect.com
ScienceDirect
Annals of Physics 322 (2007) 1790–1924
ANNALS of PHYSICS
www.elsevier.com/locate/aop

BEC–BCS crossover, phase transitions and phase separation in polarized resonantly-paired superfluids

Daniel E. Sheehy *, Leo Radzihovsky

Department of Physics, University of Colorado, Boulder, CO 80309, USA

Received 2 August 2006; accepted 6 September 2006
Available online 21 November 2006

Abstract

We study resonantly-paired s-wave superfluidity in a degenerate gas of two species (hyperfine states labeled by $\uparrow,\downarrow$) of fermionic atoms when the numbers $N_\uparrow$ and $N_\downarrow$ of the two species are *unequal*, i.e., the system is "polarized." We find that the continuous crossover from the Bose–Einstein condensate (BEC) limit of tightly-bound diatomic molecules to the Bardeen–Cooper–Schrieffer (BCS) limit of weakly correlated Cooper pairs, studied extensively at equal populations, is interrupted by a variety of distinct phenomena under an imposed population difference $\Delta N \equiv N_\uparrow - N_\downarrow$. Our findings are summarized by a "polarization" (ΔN) versus Feshbach-resonance detuning (δ) zero-temperature phase diagram, which exhibits regions of phase separation, a periodic FFLO superfluid, a polarized normal Fermi gas and a polarized molecular superfluid consisting of a molecular condensate and a fully polarized Fermi gas. We describe numerous experimental signatures of such phases and the transitions between them, in particular focusing on their spatial structure in the inhomogeneous environment of an atomic trap.

Keywords: Feshbach resonance; Polarized superfluids; BEC–BCS crossover; Fermionic superfluidity

* Corresponding author.
E-mail address: sheehyde@iastate.edu (D.E. Sheehy).

0003-4916/$ - see front matter
doi:10.1016/j.aop.2006.09.009

1. Introduction

1.1. Background and motivation

One of the most exciting recent developments in the study of degenerate atomic gases has been the observation [1–9] of singlet paired superfluidity of fermionic atoms interacting via an s-wave Feshbach resonance [10–18].

A crucial and novel feature of such experiments is the *tunability* of the position (detuning, δ) of the Feshbach resonance, set by the energy of the diatomic molecular (''closed-channel'') bound state relative to the open-channel atomic continuum, which allows a degree of control over the fermion interactions that is unprecedented in other (e.g., solid-state) contexts. As a function of the magnetic-field controlled detuning, δ, fermionic pairing is observed to undergo the Bose–Einstein condensate to Bardeen–Cooper–Schrieffer (BEC–BCS) crossover [19–29] between the Fermi-surface momentum-pairing BCS regime of strongly overlapping Cooper pairs (for large positive detuning) to the coordinate-space pairing BEC regime of dilute Bose-condensed diatomic molecules (for negative detuning).

Except for recent experiments [30–35] that followed our original work [36], and a wave of recent theoretical [37–83] activity, most work has focused on the case of an *equal* mixture of two hyperfine states (forming a pseudo-spin 1/2 system), observed to exhibit pseudo-spin singlet superfluidity near an s-wave Feshbach resonance. Here, we present an extensive study of such systems for an *unequal* number of atoms in the two pairing hyperfine states, considerably extending results and calculational details beyond those reported in our recent Letter [36]. Associating the two pairing hyperfine states with up ($\uparrow$) and down ($\downarrow$) projections of the pseudo-spin 1/2, the density difference $\delta n = n_\uparrow - n_\downarrow$ between the two states is isomorphic to an imposed ''magnetization'' $m \equiv \delta n$ (an easily controllable experimental ''knob''), with the chemical potential difference $\delta\mu = \mu_\uparrow - \mu_\downarrow$ corresponding to a purely Zeeman field $h \equiv \delta\mu/2$.

This isomorphism makes a connection to a large body of work in a related condensed-matter system, namely BCS superconductors under an applied Zeeman magnetic field, providing further motivation for our study. In contrast to a normal Fermi liquid that exhibits Pauli paramagnetism, a conventional homogeneous BCS state [84,85] at zero temperature remains unmagnetized until, at a critical Zeeman field H_c^Z, it is destroyed in a first-order transition to the unpaired magnetized normal state. A natural question is whether there can be a ''compromise'' state that exhibits both pairing *and* nonzero magnetization. One proposal for such a state dates back to work of Fulde and Ferrell (FF) [86] and Larkin and Ovchinnikov (LO) [87], and has been the subject of strong interest for many years [88–94], finding putative realizations in a variety of systems ranging from heavy-fermion superconductors [95] to dense quark matter [92,94]. These so-called FFLO states, theoretically predicted to be the ground state for a narrow range of applied Zeeman field near the above-mentioned transition, are quite unusual in that, while exhibiting off-diagonal long-range order (i.e., superfluidity), they spontaneously break rotational and translational symmetry, forming a crystal of pairing order (i.e., a supersolid [96–99]) with lattice vectors $Q \approx k_{F\uparrow} - k_{F\downarrow}$, where $k_{F\sigma}$ is the spin-σ Fermi wavevector.

The observation of such magnetized superfluidity in condensed-matter systems has been elusive for a variety of reasons, primarily because an applied *physical* magnetic field H couples not only to spin polarization (i.e., the Zeeman effect) but also to the orbital motion

of *charged* electrons. The latter coupling leads to the Meissner effect, in which a charged superconductor expels an externally applied magnetic field. For type I superconductors, for sufficiently large $H > H_c$, the energy cost of expelling the field exceeds the condensation energy of the superconducting state and the system is driven normal via a first-order transition. Because this thermodynamic critical field $H_c = \Delta\sqrt{4\pi N(\epsilon_F)}$ is much smaller than [100] the critical (Clogston limit [84]) Zeeman field $H_c^Z = \Delta\sqrt{N(\epsilon_F)/\chi_P}$ (where χ_P is the Pauli magnetic susceptibility), i.e., $H_c/H_c^Z = \sqrt{4\pi\chi_P} \ll 1$, in condensed-matter systems the effects of a purely Zeeman field are expected to be obscured by the orbital effects of the physical applied magnetic field [101]. The effects of impurities [88,91], that are always present in condensed-matter systems, can further complicate the realization of FFLO and other magnetized superfluid states (see, however, recent work [95]).

In contrast, trapped atomic systems are natural settings where paired superfluidity at a finite imposed magnetic moment, $\Delta N = N_\uparrow - N_\downarrow$, can be experimentally studied by preparing mixtures with different numbers $N_\uparrow$, $N_\downarrow$ of two hyperfine-state species, with the (Legendre-conjugate) chemical potential difference $\delta\mu = \mu_\uparrow - \mu_\downarrow$ a realization of the corresponding effective (purely) Zeeman field.

Beyond the aforementioned isomorphism in the weakly-paired BCS regime, atomic gases interacting via a Feshbach resonance allow studies of magnetized paired superfluidity as a function of Feshbach resonance detuning across the resonance and deep into the strongly-paired molecular BEC regime, inaccessible in condensed-matter systems.

1.2. Theoretical framework and its validity

The goal of our present work is to extend the study of s-wave paired resonant superfluidity to the case of an unequal number of the two hyperfine-state species, $\Delta N/N = (N_\uparrow - N_\downarrow)/N \neq 0$, namely, to calculate the phase diagram as a function of detuning, δ, and polarization, $\Delta N/N$ (or, equivalently, the chemical potential difference $\delta\mu$).

An appropriate microscopic model of such a Feshbach-resonantly interacting fermion system is the so-called two-channel model [10,24–26,29] that captures the dynamics of atoms in the open channel, diatomic molecules in the closed channel and the coupling between them, which corresponds to the decay of closed-channel diatomic molecules into two atoms in the open channel.

As we will show, the model is characterized by a key dimensionless parameter

$$\gamma = \frac{\sqrt{8}}{\pi}\sqrt{\frac{\Gamma_0}{\epsilon_F}}, \tag{1}$$

determined by the ratio of the Feshbach resonance width $\Gamma_0 \approx 4m\mu_B^2 a_{bg}^2 B_w^2/\hbar^2$ (where μ_B is the Bohr magneton), to the Fermi energy ϵ_F, and describes the strength of the atom-molecule coupling that can be extracted from the two-body scattering length observed [13,17] to behave as

$$a_s = a_{bg}\left(1 - \frac{B_w}{B - B_0}\right), \tag{2}$$

as a function of the magnetic field B near the resonance position B_0. Equivalently, γ is the ratio of the inter-atomic spacing $n^{-1/3}$ (where n is the atom density) to the effective range r_0 characterizing the energy dependence of two-body scattering amplitude in the open

channel. As was first emphasized by Andreev, Gurarie and Radzihovsky [26,29] in the context of pairing in an unpolarized (symmetric) Fermi gas, in the limit of a vanishingly narrow resonance, $\gamma \to 0$, the two-channel model is exactly solvable by a mean-field solution. Consequently, for a finite but narrow resonance $\gamma \ll 1$, the system admits a detailed *quantitative* analytical description for an arbitrary value of detuning (*throughout* the BEC–BCS crossover), with its accuracy controlled by a systematic perturbative expansion in γ.

This important observation also holds for asymmetric mixtures with an arbitrary magnetization. Hence in the narrow Feshbach resonance limit we can accurately study this system by a perturbative expansion in γ about a variational mean-field solution. To implement this we compute the energy in a generalized BCS-like variational state, and minimize the energy over the variational parameters. Explicitly, the variational state is parametrized by the bosonic condensate order parameter $b_{\mathbf{Q}}$, where $\mathbf{Q}$ is a center of mass wavevector that allows for a periodically modulated condensate. Our choice of the variational ground state is sufficiently rich as to include the normal state, the gapped singlet BCS state as well as its molecular BEC cousin, a magnetized paired superfluid state with gapless atomic excitations, a FFLO state [102,103], and inhomogeneous ground states that are a phase-separated coexistence of any two of the above pure states. Our variational ansatz is *not*, however, general enough to allow for the very interesting possibility of a uniform but anisotropic paired superfluid ground state, e.g., a nematic superfluid [45,49], nor of more exotic multi-$\mathbf{Q}$ FFLO superfluids [102,103].

Most of our work focuses on the narrow resonance ($\gamma \ll 1$) limit, studied within the two-channel model. Although experiments do not lie in this regime, the analysis provides valuable and *quantitatively* trustworthy predictions for the behavior of the system (throughout the phase diagram), at least in this one nontrivial limit. However, typical present-day experiments [1–9] fall in a broad Feshbach resonance, $\gamma \simeq 10^1 - 10^4 \gg 1$, regime [104] (see Appendix A). To make contact with these experiments we also extend our results to the broad resonance limit, complementing our two-channel analysis with an effective single-channel model. For a broad resonance, we can ignore the dispersion of the closed-channel molecular mode and integrate it out, thereby reducing the two channel model to an effective single (open) channel model with a tunable four-Fermi coupling related to the atomic s-wave scattering length. Although in this broad resonance regime our mean-field variational theory is not guaranteed to be *quantitatively* accurate, we expect that it remains qualitatively valid. Indeed, we find a reassuring qualitative consistency between these two approaches.

Furthermore, to make detailed predictions for cold-atom experiments we extend our bulk analysis to include a trap, $V_{\mathrm{T}}(r)$. We do this within the local density approximation (LDA). Much like the WKB approximation, this corresponds to using expressions for the bulk system, but with an effective local chemical potential $\mu(r) = \mu - V_{\mathrm{T}}(r)$ in place of μ. The validity of the LDA approximation relies on the smoothness of the trap potential, namely that $V_{\mathrm{T}}(r)$ varies slowly on the scale of the *longest* physical length λ (the Fermi wavelength, scattering length, effective range, etc.) in the problem, i.e., $(\lambda/V_{\mathrm{T}}(r))\, \mathrm{d}V_{\mathcal{T}}(r)/\mathrm{d}r \ll 1$. Its accuracy can be equivalently controlled by a small parameter that is the ratio of the single particle trap level spacing δE to the smallest characteristic energy E_c of the studied phenomenon (e.g, the chemical potential, condensation energy, etc.), by requiring $\delta E/E_c \ll 1$.

1.3. Outline

The rest of the paper is organized as follows. In Section 2, we summarize our main results. In Section 3, we review the standard two-channel and one-channel models of fermions interacting via an s-wave Feshbach resonance. Focusing on a narrow resonance described by the two-channel model, we compute the system's ground state energy in Section 4. By minimizing it we map out the detuning-polarization phase diagram. Focusing first on uniformly-paired states (i.e., ignoring the FFLO state), we do this for the case of positive detuning (the BCS and crossover regimes) in Section 5, and for negative detuning (the BEC regime) in Section 6, finding a variety of phases and the transitions between them. In Section 7, we revisit the positive-detuning regime to study the periodically-paired FFLO state. In Section 8, we complement our analysis of the two-channel model with a study of the one-channel model, finding an expected qualitative agreement. To make predictions that are relevant to cold-atom experiments, in Section 9 we extend our bulk (uniform-system) analysis to that of a trap. We conclude in Section 10 with a discussion of our work in the context of recent and future experiments and relate it to other theoretical studies that have recently appeared in the literature. We relegate many technical details to a number of Appendices.

2. Summary of principal results

Having motivated our study and discussed its theoretical framework and validity, below we present a summary of the main predictions of our work, thereby allowing a reader not interested in derivations easy access to our results. As discussed above, the quantitative validity of our calculations is guaranteed in the narrow resonance $\gamma \ll 1$ limit, with all expressions given to leading order in γ. Our results (summarized by Figs. 1–6) are naturally organized into a detuning-polarization phase diagram (see Figs. 3 and 4) and our presentation logically splits into predictions for a bulk system and for a trapped system.

2.1. Bulk system

In this somewhat theoretically-minded presentation of our results, we focus on the two-channel description, outlining the system's phenomenology as a function of detuning, $\delta \simeq 2\mu_B(B - B_0)$ (with B_0 the magnetic field at which the Feshbach resonance is tuned to zero energy), and chemical potential difference h, or imposed polarization $\Delta N/N$.

2.1.1. BCS regime: $\delta \gg 2\epsilon_F$

For large positive detuning, the closed-channel molecules are energetically costly, and the atom density is dominated by open-channel atoms, exhibiting a weak attraction mediated by virtual closed-channel molecules. Consequently, for a weak chemical potential difference (or Zeeman field) h we find a standard s-wave singlet (non-polarized) BCS superfluid ground state, that, as a function of detuning, undergoes a BCS–BEC crossover that is identical to the well-studied crossover at vanishing h. Deep in the BCS regime, for fixed chemical potential μ, this singlet paired state becomes unstable when the Zeeman field h overwhelms the superconducting gap $\Delta_{BCS}(\mu)$. For simplicity, for now ignoring the FFLO

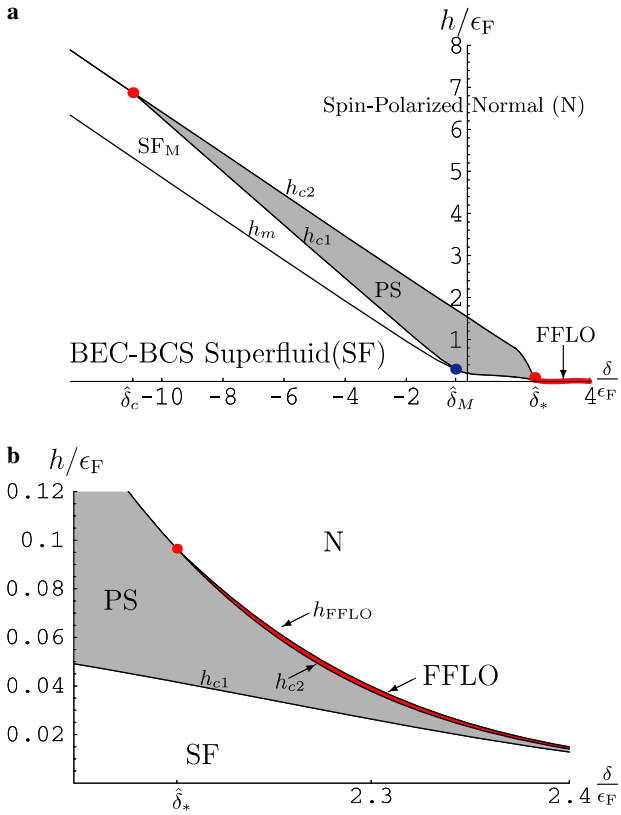

Fig. 1. (a) Global phase diagram as a function of Feshbach resonance detuning at fixed total atom number N and chemical potential difference h within the two-channel model, showing homogeneous superfluid (SF), magnetized superfluid (SF_M), FFLO and spin-polarized normal (N) phases as well as a regime of phase separation (PS, shaded). (b) Zoom-in of the positive-detuning BCS regime, showing the regime of phase separation (gray) and FFLO state (red online). See Fig. 41 for a similar phase diagram within the one-channel model. $\hat{\delta}_* \equiv \delta_*/\epsilon_F$, $\hat{\delta}_M \equiv \delta_M/\epsilon_F$ and the tricritical point $\hat{\delta}_c \equiv \delta_c/\epsilon_F$ indicate limiting detuning values for FFLO, SF_M and phase separated states, respectively. (For interpretation of the references to color in this figure legend, the reader is referred to the web version of this paper.)

state, the BCS superfluid then undergoes a first-order transition to the partially-polarized normal Fermi gas state at

$$h_c(\mu,\delta) = \frac{\Delta_{BCS}(\mu)}{\sqrt{2}}, \tag{3a}$$

$$= 4\sqrt{2}e^{-2}\mu e^{-\frac{\delta-2\mu}{\gamma\sqrt{\epsilon_F\mu}}}, \tag{3b}$$

consistent with established results first found by Clogston [84] and Sarma [85]. As is generically the case for first-order transitions, thermodynamic quantities exhibit jump discontinuities as h crosses h_c. In particular, we find the discontinuities in the atomic, molecular and total densities are, respectively,

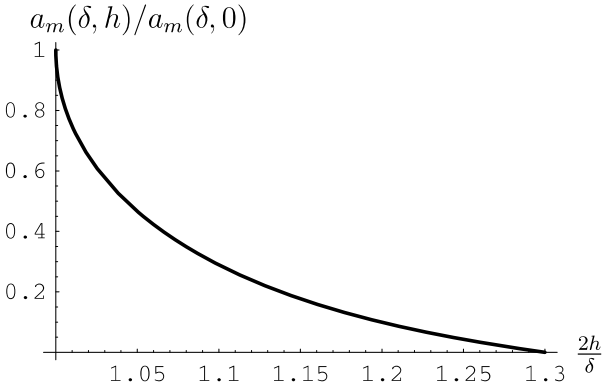

Fig. 2. Plot of molecular scattering length $a_m(\delta,h)$ Eq. (16), normalized to its value at $h = 0$, as a function of $2h/|\delta|$.

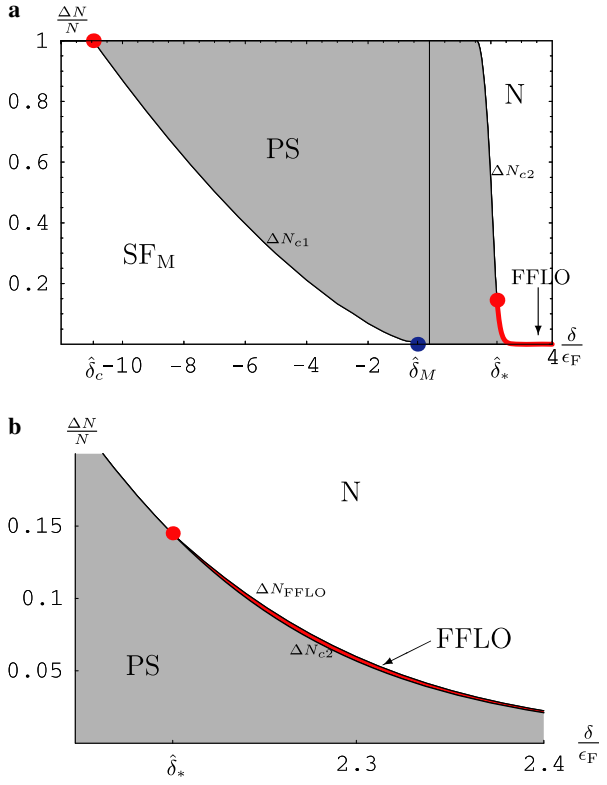

Fig. 3. Global phase diagram (a) as a function of Feshbach resonance detuning at fixed population difference $\frac{\Delta N}{N} = \frac{N_\uparrow - N_\downarrow}{N_\uparrow + N_\downarrow}$. The regime of phase separation (PS) is gray, and the FFLO regime (too thin to see on this scale) intervenes along a thin line at positive detuning, indicated with a thick dark (red online) line. (b) Zoom in of the BCS regime at positive detuning showing the regime of phase separation and the FFLO regime.

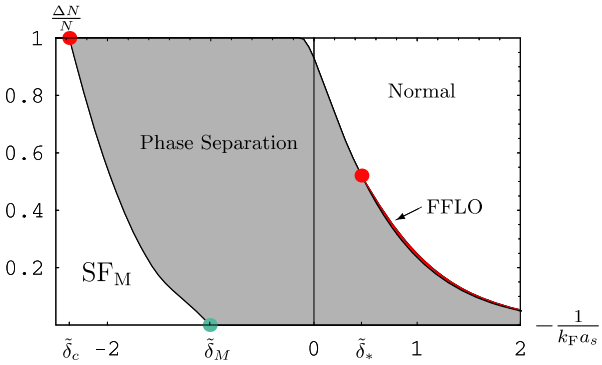

Fig. 4. Polarization $\Delta N/N$ vs. detuning $\propto -\frac{1}{k_F a_s}$ phase diagram of the one-channel model (appropriate for resonance width $\gamma \to \infty$) within mean-field theory showing regimes of FFLO, superfluid (SF), magnetized superfluid (SF_M), and phase separation (PS). Note that here (in contrast to a narrow Feshbach resonance $\gamma \ll 1$, Fig. 3) at unitarity, $(k_F a_s)^{-1} = 0$, the boundary between N and PS is at $\Delta N/N < 1$, consistent with experiments [30].

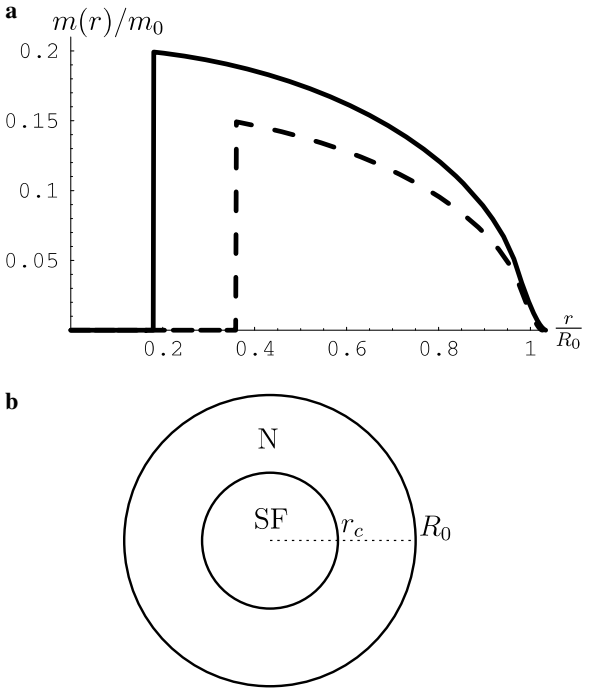

Fig. 5. (a) Local magnetization $m(r)$ radial profile confined to the normal outer shell of the cloud, $r > r_c$, for coupling $(k_F|a_s|)^{-1} = 1.5$ and $\frac{\Delta N}{N} = 0.15$ (dashed) and $\frac{\Delta N}{N} = 0.20$. (b) Sequence of shells, with increasing radius, implied by the magnetization profiles in (a).

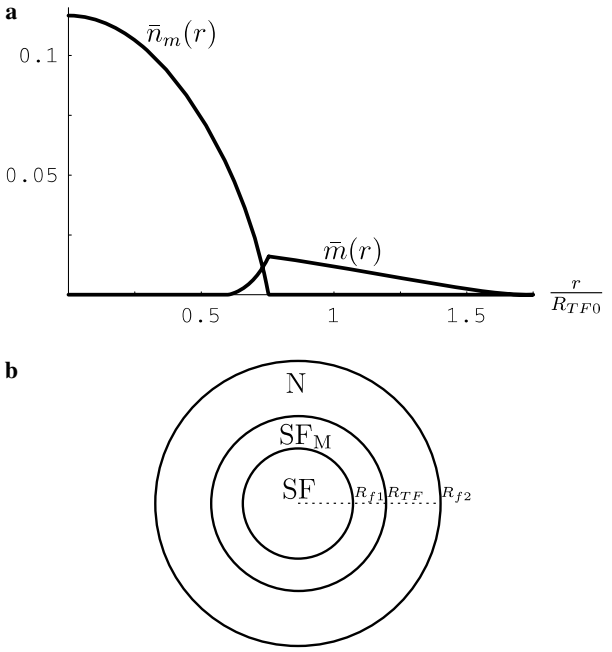

Fig. 6. (a) Normalized molecular density $\bar{n}_m(r)$ and normalized magnetization $\bar{m}(r)$ of a trapped fermion gas as a function of radius r (normalized to the radius of the unpolarized cloud, with parameters given in Section 9.2). (b) Schematic of the sequence of shells, with increasing radius, implied by the curves in (a).

$$\Delta n_a \equiv n^a_{\rm SF} - n^a_{\rm N} \simeq \frac{c\Delta^2_{\rm BCS}}{\sqrt{\mu}}\left(1 - \frac{1}{2}\ln\frac{\Delta_{\rm BCS}}{8e^{-2}\mu}\right) > 0, \tag{4a}$$

$$\Delta n_m \equiv n^m_{\rm SF} - n^m_{\rm N} \simeq \frac{\Delta^2_{\rm BCS}}{g^2} > 0, \tag{4b}$$

$$\Delta n \equiv n_{\rm SF} - n_{\rm N}, \quad \simeq \frac{2\Delta^2_{\rm BCS}}{g^2} + \frac{c\Delta^2_{\rm BCS}}{\sqrt{\mu}}\left(1 - \frac{1}{2}\ln\frac{\Delta_{\rm BCS}}{8e^{-2}\mu}\right) > 0, \tag{4c}$$

where $n^a_{\rm SF}$ and $n^a_{\rm N}$ are the free atomic densities in the superfluid and normal states, respectively, $n^m_{\rm SF}$ and $n^m_{\rm N}$ are their molecular analogs and n is the total (whether free or paired) atom density. Here, $c \equiv m^{3/2}/\sqrt{2}\pi^2\hbar^3$ is defined by the three-dimensional density of states $N(\epsilon) = c\sqrt{\epsilon}$. The species imbalance (magnetization) $m = (N_\uparrow - N_\downarrow)/V$ also exhibits a jump discontinuity

$$\Delta m \equiv m_{\rm SF} - m_{\rm N} \simeq -2ch_c\sqrt{\mu} < 0, \tag{5}$$

across h_c.

In the more experimentally-relevant (to cold atoms) fixed total atom number N ensemble, the density difference between the normal and superfluid states makes it impossible for the normal state to satisfy the imposed number constraint immediately above $h_{c1}(N,\delta) \equiv h_c(\mu_{\rm SF}({\rm N}),\delta)$. [Here, $\mu_{\rm SF,N}$ are the superfluid (SF) and normal (N) state chemical

potentials corresponding to the imposed N.] Consequently, we find that in the fixed number ensemble the transition at h_c opens up into a coexistence region $h_{c1}(\delta) < h < h_{c2}(\delta)$ in which the gas is an inhomogeneous mixture of phase-separated superfluid and normal states, with respective volume fractions $x(h,\delta)$ and $1 - x(h,\delta)$ varying according to

$$x(h,\delta) = \frac{n - n_{\rm N}[h,\mu_c(h)]}{n_{\rm SF}[\delta,\mu_c(h)] - n_{\rm N}[h,\mu_c(h)]}, \tag{6}$$

to satisfy the imposed total atom number constraint $n = N/V = x n_{\rm SF} + (1-x) n_{\rm N}$. Here, $\mu_c(h)$ is the critical chemical potential as a function of h, implicitly given by Eq. (3b), specifying the SF–N first-order phase boundary. The coexistence region is bounded by $h_{c2}(\delta)$ from above, corresponding to a Zeeman field below which a pure partially-polarized normal Fermi gas phase cannot satisfy the imposed number constraint while remaining the ground state.

A more careful analysis, that includes a periodically-paired FFLO state in the variational ansatz, shows that, in fact, deep in the BCS regime, for detuning $\delta > \delta_* \approx 2\epsilon_{\rm F}$, the first-order transition is actually (from the singlet BCS state) into a magnetized superfluid FFLO state. As illustrated in Fig. 1b and consistent with many deep-BCS studies [86,87,89], we find that this fragile state only survives over a narrow sliver of Zeeman fields (or imposed polarization) [103] undergoing a continuous [105–108] transition at $h_{\rm FFLO}(\delta)$ to a partially-polarized normal Fermi gas ground state. Our work is an extension of these earlier BCS studies to a varying detuning (controlling the strength of the attractive interactions), with our main result in this regime the location of the critical detuning

$$\delta_* \approx \epsilon_{\rm F}\left[2 - \frac{\gamma}{2}\ln(0.159\gamma)\right], \tag{7}$$

accurately predicted for a narrow resonance ($\gamma \ll 1$), below which the FFLO state is unstable for any h or ΔN. As seen in Fig. 1b, above δ_*, deep in the BCS regime, the boundaries h_{c1}, h_{c2}, and $h_{\rm FFLO}$ display exponential behavior [defining $\Delta_{\rm F} \equiv \Delta_{\rm BCS}(\epsilon_{\rm F})$]:

$$h_{c1}(\delta) \approx \frac{1}{\sqrt{2}}\Delta_{\rm F}\exp\left[-\frac{\delta^2\Delta_{\rm F}^2}{8\gamma^2\epsilon_{\rm F}^4}\right], \quad \delta \gg 2\epsilon_{\rm F}, \tag{8a}$$

$$h_{c2}(\delta) \approx \frac{1}{\sqrt{2}}\Delta_{\rm F}\exp\left[-\frac{\delta\Delta_{\rm F}^2}{16\gamma\epsilon_{\rm F}^3}\right], \quad \delta \gg 2\epsilon_{\rm F}, \tag{8b}$$

$$h_{\rm FFLO}(\delta) \approx \eta\Delta_{\rm F}\exp\left[-\frac{\eta^2\delta\Delta_{\rm F}^2}{8\gamma\epsilon_{\rm F}^3}\right], \quad \delta \gg 2\epsilon_{\rm F} \tag{8c}$$

never crossing with increasing detuning, the latter two boundaries asymptoting to a ratio $h_{\rm FFLO}/h_{c2} = \eta\sqrt{2} \approx 1.066$ previously found by Fulde and Ferrell [86].

2.1.2. Crossover regime: $0 < \delta < 2\epsilon_F$

As the detuning is lowered below approximately $2\epsilon_{\rm F}$, it becomes favorable (for low chemical potential difference h) to convert a finite fraction of the Fermi sea (between $\mu \approx \delta/2$ and $\epsilon_{\rm F}$) into Bose-condensed molecules. Since in this crossover regime the pairing strength (proportional to the growing molecular density) is no longer driven by Fermi surface pairing and is therefore no longer exponentially weak, the response to the chemical potential difference, h, (or the imposed polarization, ΔN) changes qualitatively from the weakly-paired BCS regime discussed above.

Consequently, the FFLO state, driven by mismatched Fermi-surface pairing, is no longer stable for $\delta < \delta_*$ [given by Eq. (7)], leading to a direct first-order transition between a paired superfluid and a partially polarized normal Fermi gas (see Fig. 1).

As above, for imposed atom number the phase boundary splits into a superfluid-normal coexistence region bounded by $h_{c1}(\delta)$ and $h_{c2}(\delta)$. The lower boundary, $h_{c1}(\delta)$, is still determined by the value of the gap, Δ. However, because the gap is in turn set by the molecular condensate $\Delta = g\sqrt{n_m(\delta)}$, that in this regime is no longer exponentially small but grows as a power-law with detuning reduced below $2\epsilon_F$, $h_{c1}(\delta)$ is also a power-law in $2\epsilon_F - \delta$. We note, however, that while $h_{c1}(\delta)$ is significantly larger than its exponentially small value in the BCS regime, it nevertheless remains small compared to μ for a narrow resonance, justifying a linear response (in h) approximation for the normal-state energy near h_{c1}.

The upper boundary, $h_{c2}(\delta)$, (no longer in the linear Pauli-paramagnetic regime, i.e., $h_{c2} \ll \mu$) is increased even more dramatically beyond that of Eq. (8b), due to the superfluid-normal density difference enhanced by a large molecular density n_m that here is a finite fraction of the total atom density. This considerably spreads the coexistence region for δ below $2\epsilon_F$, with $h_{c1}(\delta)$ given by

$$h_{c1}(\delta) \simeq \epsilon_F \sqrt{\frac{\gamma}{3}} \sqrt{1 - \left(\frac{\delta}{2\epsilon_F}\right)^{3/2}}, \quad \delta_M < \delta < 2\epsilon_F, \tag{9}$$

and the critical detuning δ_M given by

$$\delta_M \approx -1.24\epsilon_F\sqrt{\gamma}. \tag{10}$$

Here, $h_{c2}(\delta)$ is implicitly given by

$$\epsilon_F^{3/2} \simeq \frac{1}{2}\left[\left(\frac{\delta}{2} + h_{c2}(\delta)\right)^{3/2} - \left(\frac{\delta}{2} - h_{c2}(\delta)\right)^{3/2} \Theta\left(\frac{\delta}{2} - h_{c2}(\delta)\right)\right], \quad \delta < 2\epsilon_F, \tag{11}$$

which is well-approximated by

$$h_{c2}(\delta) \simeq 2^{2/3}\epsilon_F - \frac{\delta}{2}, \quad \delta < 2^{2/3}\epsilon_F, \tag{12}$$

over most of the range of interest.

2.1.3. BEC regime: $\delta < 0$

In the BEC regime, a new *uniform magnetized* superfluid (SF_M) phase appears, for detunings below δ_M, when the population imbalance $\Delta N = N_\uparrow - N_\downarrow$ is imposed. The SF_M ground state consists of closed-channel singlet molecules, with the remaining unpaired atoms forming a fully-polarized Fermi sea that carries the imposed magnetization.

As illustrated in the phase diagram, Fig. 1, for $\delta < \delta_M$ a spin-singlet (unpolarized) molecular (BEC) superfluid undergoes a second-order quantum phase transition at

$$h_m(\delta) \approx |\delta|/2, \quad \delta < \delta_M, \tag{13}$$

to the magnetized SF_M superfluid. The transition turns into a (sharp at low T) crossover at any finite temperature, since then the magnetization is finite for arbitrarily small h, even below h_m. In the narrow-resonance limit, the phase boundary $h_m(\delta)$ is determined by the vanishing of the majority-species chemical potential $\mu_\uparrow = h - |\delta|/2$. Physically, this

corresponds to the condition that the gain in the Zeeman energy $-h\Delta N$ compensates the loss of the molecular binding energy $|\delta|/2$ per atom.

For intermediate negative detuning $\delta_c < \delta < \delta_M$, upon increasing the Zeeman field h the magnetized superfluid, SF_M, undergoes a first-order transition at $h_c(\delta)$ [given by the implicit Eq. (221b) in the main text]. In the more experimentally-relevant fixed atom number N ensemble this transition at $h_c(\delta)$ opens up (as is standard for a first-order transition) into a phase-separated region of coexistence between the SF_M and a fully-polarized normal atomic gas. This phase-separated regime is bounded by

$$h_{c1}(\delta) \approx 0.65|\delta|, \quad \delta_c < \delta < 0, \tag{14}$$

$$h_{c2}(\delta) \approx 2^{2/3}\epsilon_F + \frac{|\delta|}{2}, \quad \delta < 0, \tag{15}$$

that are continuations of the boundaries [Eqs. (8a), (8b), (9) and (12)] found in the BCS and crossover regimes above. We find that the SF_M-phase separation instability, initiated at h_{c1}, is signaled by an enhanced compressibility and a corresponding suppression (with increasing h) of the molecular scattering length

$$a_m \simeq \frac{\pi^2\epsilon_F\gamma^2}{16\sqrt{m}|\delta|^{3/2}} F_4\left(\frac{2h}{|\delta|}\right), \tag{16}$$

plotted in Fig. 2. The function $F_4(x)$ is defined in Eq. (195) of the main text. In the narrow resonance limit, $\gamma \ll 1$, indeed h_{c1} is determined by the vanishing of a_m, as given in Eq. (14) above.

As illustrated in Fig. 1a, for sufficiently large negative detuning, $\delta < \delta_c$, the $h_{c1}(\delta)$ and $h_{c2}(\delta)$ boundaries cross and the first-order SF_M–N transition and the corresponding phase-coexistence region are eliminated. The SF_M then undergoes a direct continuous transition at $h_{c2}(\delta)$ into a fully-polarized normal state.

It is now straightforward to convert the phase diagram and our other predictions to the more experimentally-relevant ensemble of fixed total atom number N and imposed atomic species difference (polarization) $\Delta N = N_\uparrow - N_\downarrow$. As can be seen in Fig. 3, in this ensemble for positive detuning (BCS and crossover regimes), the singlet BCS superfluid is confined to the detuning axis, and is unstable to phase separation and coexistence with a normal atomic gas for any imposed population imbalance. The upper boundary of the coexistence region and the phase boundary of the FFLO phase are then, respectively, given by

$$\frac{\Delta N_{c2}}{N} \approx \frac{3\Delta_F}{2\sqrt{2}\epsilon_F} \exp\left[-\frac{\delta\Delta_F^2}{16\gamma\epsilon_F^3}\right], \tag{17}$$

$$\frac{\Delta N_{FFLO}}{N} \approx \frac{3\eta\Delta_F}{2\epsilon_F} \exp\left[-\frac{\eta^2\delta\Delta_F^2}{8\gamma\epsilon_F^3}\right]. \tag{18}$$

As seen from the phase diagram these two boundaries cross at δ_*, thereby eliminating the FFLO state for lower detuning. For a narrow Feshbach resonance ($\gamma \ll 1$) at even lower detuning (see Fig. 3(a))

$$\delta_p \simeq 2^{2/3}\epsilon_F, \tag{19}$$

the normalized critical polarization $\Delta N_{c2}/N$ reaches unity according to

$$\frac{\Delta N_{c2}}{N} \approx 1 - \epsilon_{\mathrm{F}}^{-\frac{3}{2}}(\delta - \delta_p)^{3/2}\Theta(\delta - \delta_p). \tag{20}$$

This implies that for these lower detunings, $\delta < \delta_p$, only a fully polarized normal Fermi gas can appear. In contrast, as illustrated in Fig. 4, for a broad resonance (large γ) $\Delta N_{c2}/N < 1$, consistent with experiments [30] that find $\Delta N_{c2}/N \approx 0.7$ near unitarity.

For sufficiently negative detuning, $\delta < \delta_M$, the uniform magnetic superfluid state, $\mathrm{SF_M}$, appears at low population imbalance. For $\delta_c < \delta < \delta_M$ it becomes unstable to phase separation and coexistence with the fully-polarized atomic Fermi gas for $\Delta N > \Delta N_{c1}$, with

$$\frac{\Delta N_{c1}}{N} \approx 0.029\left(\frac{\delta}{\epsilon_{\mathrm{F}}}\right)^{3/2}. \tag{21}$$

As this population imbalance is approached, the molecular scattering length $a_m(\delta,\Delta N)$ drops precipitously and the corresponding molecular condensate Bogoliubov sound velocity

$$u(\delta,\Delta N) \simeq u_0(\delta)\sqrt{1-\frac{\Delta N}{N}}\sqrt{F_4\left(1+\frac{2^{5/3}}{|\hat{\delta}|}\left(\frac{\Delta N}{N}\right)^{2/3}\right)}, \tag{22}$$

(where $\hat{\delta} \equiv \delta/\epsilon_{\mathrm{F}}$) vanishes according to

$$u \sim 0.38u_0\left(1-\frac{\Delta N_{c1}}{N}\right)^{1/2}\left(1-\frac{\Delta N}{\Delta N_{c1}}\right)^{1/2}, \quad \Delta N \to \Delta N_{c1}. \tag{23}$$

Finally, for $\delta < \delta_c$, the $\mathrm{SF_M}$ state is stable for any population imbalance up to the fully polarized limit of $\Delta N = N$, where it is identical to the fully polarized (single species) Fermi gas.

2.2. Trapped system

To make a more direct connection with atomic-gas experiments we summarize the extension of the above bulk results to the case of a trapped gas. This is particularly simple to do in the case of a trap potential that varies smoothly on the scale of the Fermi wavelength, i.e., when the Fermi energy is much larger than the trap level spacing, the regime of most atomic gas experiments. In this regime, the trap potential can be easily taken into account via the local density approximation (LDA). Namely, we treat the trapped system as a locally uniform one (thereby taking advantage of our bulk results), but with a local chemical potential given by $\mu(\mathbf{r}) = \mu - V_T(\mathbf{r})$. The true chemical potential μ and chemical potential difference h still appear and are determined by constraints of the total atom number N and species imbalance ΔN. For simplicity we consider an isotropic trap with $V_T(\mathbf{r}) = \frac{1}{2}m\Omega_T^2 r^2$, but our results can be easily generalized to an arbitrary anisotropic trap.

The phase transitions and coexistence discussed above are strikingly accentuated by the trap. To see this, note that (within the LDA approximation) the local phenomenology of a trapped cloud is that of the bulk one at an effective chemical potential $\mu(r)$. Hence, a radial slice through a trapped cloud is an effective chemical potential "scan" through the bulk-system phase diagram at fixed μ and h (the latter displayed in the main text, Fig. 32). Consequently, as we first predicted in our earlier publication [36], a trapped cloud consists of a combination of shells of the various superfluid and normal phases, with the exact structure

determined by the value of detuning and population imbalance (or, equivalently, the Zeeman field h). A critical value of the chemical potential μ_c separating two phases in the bulk system translates, within LDA, into a critical radius r_c, given by $\mu(r_c) = \mu_c$ (more generally a hypersurface), that is the boundary between two corresponding phase shells in a trapped gas.

More concretely, on the BCS side of the resonance (ignoring for simplicity the narrow sliver of the FFLO state), the normal and (singlet BCS-) SF phases translate into two shells of a trapped cloud. Because the bulk $h_c(\mu)$ [see Eq. (3b)] is an increasing function of μ and $\mu(r)$ is a decreasing function of r, the SF phase (that in the bulk appears at high chemical potential and low h) forms the cloud's inner core of radius $r_c(\delta,h,N)$ set by $h_c(\mu(r_c)) = h$. The normal phase forms the outer shell with inner radius $r_c(\delta,h,N)$ and outer shell radius $R_0(\delta,h,N)$ determined by the vanishing of the normal phase chemical potential, $\mu_N(R_0,\delta,h,N) = 0$. The resulting magnetization density profile $m(r)$, confined to (and thereby vividly imaging) the outer normal shell, is illustrated in Fig. 5a. Following our original prediction [36], this shell structure has recently been experimentally observed in Refs. [30,31], and subsequently calculated theoretically by a number of groups [53,55,59,58].

On the BEC side of the resonance, the appearance of an additional phase, the $\mathrm{SF_M}$, allows for the possibility of a triple-shell cloud structure $\mathrm{SF} \to \mathrm{SF_M} \to \mathrm{N}$ with increasing radius at low population imbalance (small h). The inner (R_{f1}) and outer (R_{TF}) boundaries of the $\mathrm{SF_M}$ shell occur where the population imbalance $m(r)$ becomes nonzero at the SF–$\mathrm{SF_M}$ boundary and where the molecular density $n_m(r)$ vanishes at the $\mathrm{SF_M}$–N boundary, respectively. The radii of the shells are given by the bulk critical fields $h_m(\mu(R_{f1})) = h$ and $h_c(\mu(R_{\mathrm{TF}})) = h$. The cloud's radial profile for $n_m(r)$ and $m(r)$ for this case is illustrated in Fig. 6. For larger population imbalance R_{f1} is driven to zero, resulting in a double-shell $\mathrm{SF_M} \to \mathrm{N}$ structure. At even higher ΔN, R_{TF} vanishes leading to a fully polarized, normal cloud of radius R_{f2}.

Another interesting prediction of our work [36] is the possibility to realize in resonantly-interacting degenerate Fermi gases the enigmatic FFLO state [86,87]. In an idealized box-like trap the molecular occupation distribution $n_{\mathbf{q}} = \langle b^\dagger_{\mathbf{q}} b_{\mathbf{q}} \rangle$ of this inhomogeneous superfluid exhibits finite momentum pairing peaks set by Fermi surface mismatch $Q(\delta) \sim k_{\mathrm{F}\uparrow} - k_{\mathrm{F}\downarrow}$

$$Q(\delta) \approx \frac{\sqrt{2}\lambda \Delta_{\mathrm{BCS}}(\epsilon_{\mathrm{F}})}{\hbar v_{\mathrm{F}}}, \tag{24}$$

(here $\lambda \simeq 1.200$) corresponding to reciprocal lattice vectors of this supersolid [102]. This will translate into *spontaneous* Bragg peaks (observable by projecting onto a molecular condensate [1]) appearing at $\hbar Q t/m$ in the cloud's shadow images after expansion time t, akin to that exhibited by a superfluid released from a lattice potential [109], where, in contrast to the FFLO state, Bragg peaks are explicitly induced by the periodicity of the optical potential.

However, realistic magnetic and optical traps produce a harmonic (more generally, power-law, rather than box-like) confining potential, that leads to a large density variation in the gas. Consequently, following the above arguments, within LDA in a realistic trap the gas can only exhibit a thin shell of FFLO phase, whose width δr (among other parameters, N, ΔN, and δ) is set by the inverse trap curvature and proportional to the difference in critical chemical potentials for the transition into the FFLO and

normal phases. Clearly, to resolve the abovementioned Bragg peaks, the Bragg peak width $\hbar/\delta r$ must be much smaller than Q, or, equivalently, the FFLO shell width δr must be larger than the FFLO period $2\pi/Q$. Since FFLO state is confined to a narrow sliver of the phase diagram and to be meaningful (i.e., LDA reliable) the shell width must be much larger than the period $2\pi/Q$, its direct observation in density profiles may be difficult for present-day experiments. Similar conclusions about the effect of the trap on the FFLO phase have been found in recent work by Kinnunen et al. [53] that does not rely on the LDA approximation.

On the other hand, the identification of the FFLO state through less direct probes maybe possible. For example, its spontaneous breaking of orientational symmetry for an isotropic trap should be detectable in noise experiments [110–112] sensitive to angle-dependence of pairing correlations across a Fermi surface.

Furthermore, gapless atomic excitations available in the FFLO and SF_M states should be observable through Bragg spectroscopy and reflected in thermodynamics such as power-law (rather than nearly activated paired-superfluid) heat capacity. The latter should also exhibit a latent heat peak across the first-order $SF_M \to N$, $SF \to FFLO$, $FFLO \to N$ [105], and $SF \to N$ phase transitions, and a nearly mean-field singularity across the continuous $SF \to SF_M$ transition.

Finally, we note that our above results (that are quantitatively accurate at least in the narrow resonance limit) show no evidence of a homogeneous but magnetized superfluid near the unitary limit $a_s \to \infty$, nor in the BCS and crossover regimes defined by positive detuning. We find unambiguously that this magnetized superfluid phase only appears on the BEC side for sufficiently negative detuning, $\delta < \delta_M$, embodied in the SF_M ground state. We do, however, find that the corresponding inverse scattering length $(k_F a_{sM})^{-1} = -2\hat{\delta}_M/\pi\gamma$ shifts toward the unitary limit with increased resonance width (saturating at $(k_F a_{sM})^{-1} \simeq 1$ within mean-field theory) and upon increasing temperature. Whether this is sufficient or not to explain the putative existence of such a phase, as claimed in the Rice experiments [31] (that were based on an apparent observation, in the unitary limit, of a critical population imbalance for the transition to phase separation), remains an open question.

3. Two-channel model of s-wave Feshbach resonance

The two-channel model of fermions interacting via an s-wave Feshbach resonance, briefly discussed in Section 1.2, describes open-channel fermions ($\hat{c}_{\mathbf{k}\sigma}$) and closed-channel molecular bosons ($\hat{b}_{\mathbf{q}}$) coupled by molecule-atom interconversion [10,24–26,113]. It is characterized by the following model Hamiltonian:

$$\mathcal{H} = \sum_{\mathbf{k},\sigma} \epsilon_k \hat{c}^\dagger_{\mathbf{k}\sigma} \hat{c}_{\mathbf{k}\sigma} + \sum_{\mathbf{q}} \left(\frac{\epsilon_q}{2} + \delta_0\right) \hat{b}^\dagger_{\mathbf{q}} \hat{b}_{\mathbf{q}} + \frac{g}{\sqrt{V}} \sum_{\mathbf{k},\mathbf{q}} \left(\hat{b}^\dagger_{\mathbf{q}} \hat{c}_{\mathbf{k}+\frac{\mathbf{q}}{2}\downarrow} \hat{c}_{-\mathbf{k}+\frac{\mathbf{q}}{2}\uparrow} + \hat{c}^\dagger_{-\mathbf{k}+\frac{\mathbf{q}}{2}\uparrow} \hat{c}^\dagger_{\mathbf{k}+\frac{\mathbf{q}}{2}\downarrow} \hat{b}_{\mathbf{q}}\right), \tag{25}$$

where V is the system volume (that we shall generally set to unity) $\epsilon_k \equiv k^2/2m$, m is the atom mass and the "bare" detuning δ_0 is related to the position of the Feshbach resonance δ in a way that we determine below. The molecule-atom interconversion term is characterized by a coupling g that measures the amplitude for the decay of a closed-channel s-wave singlet diatomic molecule into a pair of open-channel fermions.

Although within some approximation the model $\mathcal{H}$, Eq. (25), can be derived from a more microscopic starting point of purely fermionic atoms interacting via a van der Waals potential and including exchange and hyperfine interactions (see e.g., Ref. [23]), the model's ultimate justification is that, as we will show below, it reproduces the Feshbach resonance phenomenology. Namely, for positive detuning $\delta > 0$ the model exhibits a resonance at rest-energy δ, whose width is controlled by g, and exhibits a true molecular bound state at negative detuning $\delta < 0$. Associated with the resonance the open-channel s-wave scattering length $a_s(\delta)$ diverges and changes sign as $-1/\delta$, when the resonance at δ is tuned through zero energy.

3.1. Scattering theory in the vacuum

The above properties follow directly from the scattering amplitude $f_0(E)$, that can be easily computed exactly for two atom scattering in the vacuum [26,29]. The latter follows from the T-matrix $f_0(E) = -(m/2\pi\hbar^2)T(E)$ that, in a many-body language, is given by the diagram in Fig. 7a, with the molecular propagator *exactly* given by the RPA-like geometric series of fermion polarization bubbles illustrated in Fig. 7b. With the details of the calculations relegated to Appendix A (see also Refs. [26,29]), we find at low E

$$f_0(E) = -\frac{\hbar}{\sqrt{m}} \frac{\sqrt{\Gamma_0}}{E - \delta + i\sqrt{\Gamma_0}\sqrt{E}}, \tag{26}$$

where δ is the renormalized (physical) detuning and Γ_0 is a parameter characterizing the width of the resonance, respectively given by

$$\delta = \delta_0 - g^2 \int \frac{d^3p}{(2\pi\hbar)^3} \frac{m}{p^2}, \tag{27}$$

$$\Gamma_0 \equiv \frac{g^4 m^3}{16\pi^2\hbar^6}. \tag{28}$$

The integral in Eq. (27) is cut off by the ultraviolet scale $\Lambda \simeq 2\pi/d$, set by the inverse size d of the closed-channel (molecular) bound state, so that

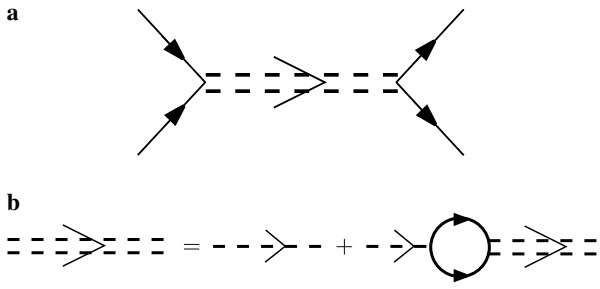

Fig. 7. (a) Feynman diagram corresponding to the atom scattering amplitude, with solid lines indicating atoms and the single (double) dashed lines indicating the bare (full) molecular propagator. (b) A self-consistent equation for the molecular propagator.

$$\delta = \delta_0 - \frac{g^2 m \Lambda}{2\pi^2 \hbar^2}, \tag{29}$$

giving the relation between the bare and physical detuning.

The s-wave scattering length [114] $a_s = -f_0(0)$ is then given by

$$a_s(\delta) = -\hbar\sqrt{\frac{\Gamma_0}{m}}\frac{1}{\delta}. \tag{30}$$

Thus, to reproduce the experimentally observed dependence of the scattering length on the magnetic field B, Eq. (2), we take [10] $\delta \approx 2\mu_B(B - B_0)$, representing the Zeeman energy splitting (at large two-atom separation) between the open and closed channels. The relevant magnetic moment is naturally dominated by the two-atom *electronic* spin state (hence the proportionality constant of the Bohr magneton μ_B above), that is approximately a singlet for the closed channel and a triplet for the open channel. Detailed multi-channel calculations (see, e.g., Ref. [18]) allow a more accurate determination of parameters when necessary. Equating a_s in Eq. (30) with $a_s^{\rm exp}$, Eq. (2), allows us to determine the Feshbach resonance energy width Γ_0 (or equivalently the parameter g) arising in the model in terms of the experimentally measured "width" B_w defined by the dependence of the scattering length on B in Eq. (2):

$$\Gamma_0 \approx \frac{4m\mu_B^2 a_{bg}^2 B_w^2}{\hbar^2}. \tag{31}$$

The bound states of the model are determined by the real negative-energy poles of $f_0(E)$, that can be shown to appear only at negative detuning [115], $\delta < 0$. For small negative detuning, $|\delta| \ll \Gamma_0$, the pole is at low energy, $E \ll \Gamma_0$, so that E in the denominator of $f_0(E)$ can be neglected relative to $\sqrt{\Gamma_0 E}$. At more negative detuning, $|\delta| \gg \Gamma_0$, one can instead ignore the $\sqrt{\Gamma_0 E}$ and the pole is simply given by the detuning δ. Together these limits give:

$$E_p(\delta) \approx \begin{cases} -\frac{\delta^2}{\Gamma_0} = -\frac{\hbar^2}{2ma_s^2} & \text{for } |\delta| \ll \Gamma_0, \\ \delta & \text{for } |\delta| \gg \Gamma_0, \end{cases} \tag{32}$$

a standard result [114] consistent with the observed phenomenology of Feshbach resonances [13,17]. The complete $E_p(\delta)$ interpolating between these limiting expressions is given by

$$E_p(\delta) = -\frac{\Gamma_0}{2}\left[1 + \frac{2|\delta|}{\Gamma_0} - \sqrt{1 + \frac{4|\delta|}{\Gamma_0}}\right], \tag{33a}$$

$$= -\frac{2\hbar^2}{m r_0^2}\left[1 + \frac{|r_0|}{a_s} - \sqrt{1 + \frac{2|r_0|}{a_s}}\right], \tag{33b}$$

obtained by solving the quadratic equation $1/f_0(E_p) = 0$. In Eq. (33b) we expressed E_p in terms of the scattering length a_s and the effective range parameter $r_0 = -2\hbar/\sqrt{m\Gamma_0}$. We note in passing that, unlike the case of a non-resonant short-range potential where $r_0 > 0$ and measures the range of the potential (hence the name), here, for a resonant interaction, $r_0 < 0$ is negative, with its magnitude characterizing the closed-channel molecular

lifetime $\tau \sim \hbar/\sqrt{\Gamma_0 \delta}$ at positive detuning [26,29]. In terms of a_s and r_0 the scattering amplitude takes the standard form [114]

$$f_0(k) = \frac{1}{-a_s^{-1} + r_0 k^2/2 - \mathrm{i}k}, \tag{34}$$

where $k = \sqrt{2m_r E/\hbar^2}$ and $m_r = m/2$ is the two-atom reduced mass.

As can be seen by analyzing Eq. (26), the physical bound state disappears [115] for positive δ. However, as illustrated in Fig. 8, a positive energy resonance does not appear until δ reaches the threshold value of $\delta_* = \Gamma_0/2$, corresponding to $|a_s(\delta_*)| = |r_0|$. This absence of a resonance for a range of positive detuning $0 < \delta < \delta_*$ is a property unique (due to the absence of a centrifugal barrier) to an s-wave resonance, contrasting with finite angular momentum resonances [116,29].

For larger positive detuning, $\delta > \Gamma_0/2$ ($|a_s| < |r_0|$), a finite-width resonance appears at a complex $E_p(\delta)$ given by

$$E_p(\delta) = E_r(\delta) - \mathrm{i}\Gamma(\delta), \tag{35}$$

with

$$E_r(\delta) = \delta - \frac{1}{2}\Gamma_0 = \frac{2\hbar^2}{m r_0^2}\left(\frac{|r_0|}{|a_s|} - 1\right), \tag{36a}$$

$$\Gamma(\delta) = \frac{\Gamma_0}{2}\sqrt{\frac{4\delta}{\Gamma_0} - 1} = \frac{2\hbar^2}{m r_0^2}\sqrt{2|r_0|/|a_s| - 1}, \tag{36b}$$

where the imaginary part Γ measures the resonance width (i.e., molecular decay rate is $\Gamma/\hbar$).

3.2. Scattering at finite density: Small parameter

As already discussed in the Introduction, at finite density $n = k_F^3/3\pi^2$ the two-channel model admits a dimensionless parameter $\gamma \propto 1/(k_F|r_0|)$ that is the ratio of the average atom spacing $n^{-1/3}$ to the effective range. The parameter γ controls a perturbative expansion

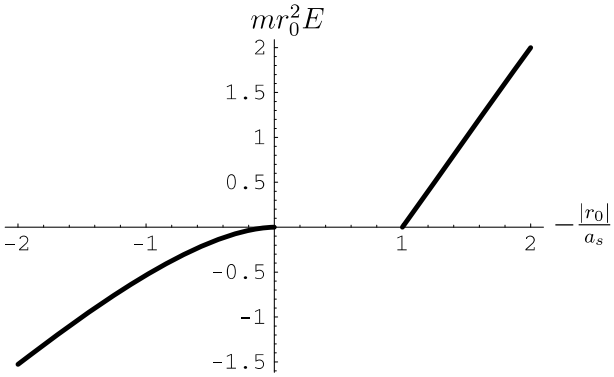

Fig. 8. Plot of the negative-energy bound-state [$E < 0$, Eq. (33b)] and positive-energy resonance [$E > 0$, Eq. (36a)] positions as a function of $-|r_0|/a_s$.

(about an exactly solvable non-interacting $g = 0$ limit) of any physical quantity and is given by

$$\gamma \equiv \frac{g^2 N(\epsilon_F)}{\epsilon_F} = \frac{\sqrt{8}}{\pi}\sqrt{\frac{\Gamma_0}{\epsilon_F}} = \frac{g^2 c}{\sqrt{\epsilon_F}} = \frac{8}{\pi}\frac{1}{k_F|r_0|}, \tag{37}$$

related to the ratio of the Feshbach resonance width (controlled by the atom-molecule coupling g) to the Fermi energy. The key observation is that γ is independent of the scattering length a_s and detuning δ, and as such, once set small, remains small throughout the crossover, even for a Feshbach resonance tuned through zero. Hence, two-channel model predictions for a *narrow* Feshbach resonance, (defined by $\gamma \ll 1$, i.e., width of the resonance much smaller than the Fermi energy) are quantitatively accurate throughout the BEC–BCS crossover.

This contrasts qualitatively with a one-channel model characterized by a dimensionless gas parameter na_s^3 that diverges for a Feshbach resonance tuned to zero (i.e., "on resonance") and therefore does not exhibit a small expansion parameter throughout the crossover.

The dimensionless parameter γ naturally emerges in a perturbative expansion in atom-molecule coupling. More physically, it can also be deduced by estimating the ratio of the energy associated with the atom-molecule Feshbach-resonance interaction to the kinetic energy, i.e, the non-interacting part of the Hamiltonian Eq. (25). To see this note that the atom-molecule coupling energy E_{FR} per atom scales like

$$E_{FR} \sim g n^{1/2}, \tag{38}$$

where we estimated the value of $\hat{b}(\mathbf{r})$ by $\hat{b} \sim \sqrt{n}$. This interaction energy is to be compared to the non-interacting part of the Hamiltonian, i.e., the kinetic energy per atom

$$E_0 \sim \epsilon_F, \tag{39}$$

with the square of the ratio

$$\gamma \sim (E_{FR}/E_0)^2, \tag{40}$$

$$\sim g^2 n/\epsilon_F^2, \tag{41}$$

giving the scale of the dimensionless parameter γ in Eq. (37).

Another instructive way to estimate the interaction strength and to derive the dimensionless coupling that controls perturbation theory is to integrate out (in a coherent-state path-integral sense) the closed-channel molecular field $b(\mathbf{r})$ from the action. As $b(\mathbf{r})$ couples to atoms only linearly this can be done exactly by a simple Gaussian integration. The resulting action only involves fermionic atoms that interact via an effective four-Fermi *dispersive* vertex. After incorporating fermion-bubble self-energy corrections of the T-matrix the latter is given by $T_k = (4\pi\hbar^2/m) f_\mu(k) \approx (4\pi\hbar^2/m) f_0(k_F)$, with a key factor that is the finite-density analog of the scattering amplitude, $f_0(k)$, Eq. (34). To gauge the strength of the molecule-mediated interaction energy we compare the interaction per atom $(4\pi\hbar^2/m) f_0(k) n$ to the kinetic energy per atom ϵ_F. Hence, the dimensionless coupling that is a measure of the atomic interaction is

$$\hat{\lambda}_k \equiv (4\pi\hbar^2/m)|f_0(k_F)|n/\epsilon_F, \tag{42}$$

$$\sim k_F |f_0(k_F)|, \tag{43}$$

dropping numerical prefactors. At large detuning (i.e., deep in the BCS regime) $\hat{\lambda}_k \sim k_F|a_s| \ll 1$ and the theory is perturbative in $\hat{\lambda}_k$. However, as detuning is reduced $|a_s(\delta)|$ and $\hat{\lambda}_k(\delta)$ grow, and close to the resonance a_s^{-1} may be neglected in the denominator of Eq. (34). In this regime, the coupling saturates at $\hat{\lambda}_k^\infty$:

$$\hat{\lambda}_k^\infty \sim \frac{k_F}{|r_0 k_F^2/2 - ik_F|}, \tag{44}$$

whose magnitude crucially depends on the dimensionless ratio $\gamma \propto 1/(k_F|r_0|)$, with

$$\hat{\lambda}_k^\infty \sim \begin{cases} \frac{1}{r_0 k_F} & \text{for } |r_0|k_F \gg 1, \\ 1 & \text{for } |r_0|k_F \ll 1. \end{cases} \tag{45}$$

Hence, in contrast to two-particle vacuum scattering, in which the cross section diverges when the Feshbach resonance is tuned to zero energy, at finite density, for sufficiently large a_s, the effective coupling $\hat{\lambda}_k$ ceases to grow and saturates at $\hat{\lambda}_k^\infty$, with the saturation value depending on whether this growth is cut off by the atom spacing $1/k_F$ or the effective range r_0. The former case corresponds to a narrow resonance [$\gamma \propto (|r_0|k_F)^{-1} \ll 1$], with the interaction remaining weak (and therefore perturbative) throughout the BCS–BEC crossover, right through the strong-scattering $\frac{1}{k_F|a_s|} = 0$ point. In contrast, in the latter wide-resonance case [$\gamma \propto (|r_0|k_F)^{-1} \gg 1$], sufficiently close to the unitary point $1/a_s = 0$ the effective coupling $\hat{\lambda}_k^\infty$, Eq. (45), grows to $\mathcal{O}(1)$ precluding a perturbative expansion in atom interaction near the unitary point.

3.3. Relation to single-channel model

In this latter broad-resonance limit, of relevance to most experimentally-realized Feshbach resonances to date, the r_0k^2 contribution to the dispersion (arising from the molecular kinetic energy) of the effective coupling $\hat{\lambda}_k$ can be neglected and one obtains an effective single (open-) channel description.

The reduction to a single-channel model in the broad resonance limit can be executed in an operator formalism, with the derivation becoming exact in the infinite Feshbach resonance width ($\gamma \to \infty$) limit [28]. The expression for the scattering length

$$\frac{1}{a_s} = -\frac{4\pi\hbar^2}{mg^2}\left(\delta_0 - \frac{g^2 m\Lambda}{2\pi^2\hbar^2}\right), \tag{46}$$

obtained from Eqs. (28)–(30) dictates that a proper transition to the broad resonance limit corresponds to $g \to \infty$ while adjusting the bare detuning according to

$$\delta_0 = -\frac{g^2}{\lambda}, \tag{47}$$

such that the physical scattering length a_s remains fixed. This allows us to trade the bare detuning δ_0 and coupling g for a new coupling λ that physically corresponds to a non-resonant attractive interaction depth [29] that can be used to tune the scattering length. Inserting Eq. (47) into $\mathcal{H}$, Eq. (25), we obtain ($V = 1$):

$$\mathcal{H} = \sum_{\mathbf{k},\sigma} \epsilon_k \hat{c}^\dagger_{\mathbf{k}\sigma}\hat{c}_{\mathbf{k}\sigma} + \sum_{\mathbf{q}} \left(\frac{\epsilon_q}{2} - \frac{g^2}{\lambda}\right)\hat{b}^\dagger_{\mathbf{q}}\hat{b}_{\mathbf{q}} + g\sum_{\mathbf{k},\mathbf{q}} \left(\hat{b}^\dagger_{\mathbf{q}}\hat{c}_{\mathbf{k}+\frac{\mathbf{q}}{2}\downarrow}\hat{c}_{-\mathbf{k}+\frac{\mathbf{q}}{2}\uparrow} + \hat{c}^\dagger_{-\mathbf{k}+\frac{\mathbf{q}}{2}\uparrow}\hat{c}^\dagger_{\mathbf{k}+\frac{\mathbf{q}}{2}\downarrow}\hat{b}_{\mathbf{q}}\right), \tag{48}$$

The corresponding Heisenberg equation of motion governing the molecular field $\hat{b}_{\mathbf{q}}$ dynamics is given by

$$\dot{\hat{b}}_{\mathbf{q}} = -\frac{\mathrm{i}}{\hbar}\left[\hat{b}_{\mathbf{q}}, \mathcal{H}\right], \tag{49a}$$

$$= -\frac{\mathrm{i}}{\hbar}\left[\left(\frac{\epsilon_q}{2} - \frac{g^2}{\lambda}\right)\hat{b}_{\mathbf{q}} + g\sum_{\mathbf{k}} \hat{c}_{\mathbf{k}+\frac{\mathbf{q}}{2}\downarrow}\hat{c}_{-\mathbf{k}+\frac{\mathbf{q}}{2}\uparrow}\right]. \tag{49b}$$

Now, in the large $g \to \infty$ limit (keeping λ fixed) the molecular kinetic energy term $\propto \epsilon_q/2$ on the right and the $\dot{\hat{b}}_{\mathbf{q}}$ term on the left are clearly subdominant, reducing the Heisenberg equation to a simple constraint relation

$$\hat{b}_{\mathbf{q}} = \frac{\lambda}{g}\sum_{k} \hat{c}_{\mathbf{k}+\frac{\mathbf{q}}{2}\downarrow}\hat{c}_{-\mathbf{k}+\frac{\mathbf{q}}{2}\uparrow}. \tag{50}$$

Hence, we see that in the extreme broad-resonance limit the molecular field's dynamics is "slaved" to that of pairs of atoms according to Eq. (50). Substituting this constraint into the Hamiltonian, Eq. (48), allows us to eliminate the closed-channel molecular field in favor of a purely open-channel atomic model with the Hamiltonian

$$\mathcal{H} = \sum_{\mathbf{k},\sigma} \epsilon_k \hat{c}^{\dagger}_{\mathbf{k}\sigma}\hat{c}_{\mathbf{k}\sigma} + \lambda\sum_{\mathbf{kqp}} \hat{c}^{\dagger}_{\mathbf{k}\uparrow}\hat{c}^{\dagger}_{\mathbf{p}\downarrow}\hat{c}_{\mathbf{k}+\mathbf{q}\downarrow}\hat{c}_{\mathbf{p}-\mathbf{q}\uparrow}, \tag{51}$$

where we redefined the momenta in the interaction term to simplify the final expression.

For future reference, we note that the scattering length in the one-channel model, when expressed in terms of the coupling λ [by combining Eqs. (27) and (30)], is

$$\frac{m}{4\pi a_s \hbar^2} = \frac{1}{\lambda} + \int \frac{\mathrm{d}^3 k}{(2\pi\hbar)^3}\frac{1}{2\epsilon_k}, \tag{52}$$

a well-known formula that can also be derived from the Hamiltonian Eq. (51) directly. Evaluating the momentum integral (cut off at Λ) gives the scattering length in the one-channel model

$$a_s(\lambda) = \frac{\pi}{2\Lambda}\frac{\lambda}{\lambda + 2\pi^2\hbar^2/m\Lambda}, \tag{53}$$

whose behavior is controlled by the new coupling λ, with $a_s(\lambda)$ diverging at $\lambda_0 = -2\pi^2\hbar^2/m\Lambda$.

A clear advantage of the one-channel model is that, as shown above, it naturally emerges as the correct Hamiltonian in the experimentally-relevant case of a wide resonance, $\gamma \gg 1$. However, a notable disadvantage is that, in the most interesting regime of a Feshbach resonance tuned to zero energy, its dimensionless gas parameter $k_{\mathrm{F}}|a_s| \to \infty$, precluding a controlled perturbative calculation throughout the crossover. Thus, in this manuscript we shall first compute using the two-channel model that is under more stringent theoretical control, obtaining results that are *quantitatively* accurate for a narrow resonance and qualitatively accurate for a wide resonance. Then, with these well-controlled results as a guide, we shall re-derive the properties of the system within (an uncontrolled) mean-field theory on the single-channel model, obtaining qualitative agreement with the results of the two-channel model.

4. Two-channel model at finite atom density: Ground state energy

Having introduced the two-channel model of fermionic atoms interacting via an s-wave Feshbach resonance, we now study its ground state at finite atom density. We work in the grand-canonical ensemble by introducing two chemical potentials

$$\mu_\uparrow = \mu + h, \tag{54a}$$

$$\mu_\downarrow = \mu - h, \tag{54b}$$

that tune the densities n_σ of atoms in hyperfine spin states $\sigma = \uparrow,\downarrow$. Comprised of two opposite-spin fermions, the molecular density is controlled by the sum $2\mu = \mu_\uparrow + \mu_\downarrow$ of the two chemical potentials. The appropriate grand-canonical Hamiltonian is then given by

$$H = \mathcal{H} - \sum_{\mathbf{k},\sigma} \mu_\sigma \hat{c}^\dagger_{\mathbf{k}\sigma}\hat{c}_{\mathbf{k}\sigma} - 2\mu \sum_{\mathbf{q}} \hat{b}^\dagger_{\mathbf{q}}\hat{b}_{\mathbf{q}}. \tag{55}$$

Equivalently, it can be written in terms of the total chemical potential μ, that tunes the total (open and closed channel) atom number N and the chemical potential difference, $\delta\mu = \mu_\uparrow - \mu_\downarrow$, or equivalently Zeeman field $h = \delta\mu/2$, that tunes the polarization (difference in the two atom species) $\Delta N = N_\uparrow - N_\downarrow$:

$$H = \mathcal{H} - \mu\hat{N} - h(\Delta\hat{N}), \tag{56}$$

$$\hat{N} \equiv \sum_{\mathbf{k},\sigma} \hat{c}^\dagger_{\mathbf{k}\sigma}\hat{c}_{\mathbf{k}\sigma} + 2\sum_{\mathbf{q}} \hat{b}^\dagger_{\mathbf{q}}\hat{b}_{\mathbf{q}}, \tag{57}$$

$$\Delta\hat{N} \equiv \sum_{\mathbf{k}} \left(\hat{c}^\dagger_{\mathbf{k}\uparrow}\hat{c}_{\mathbf{k}\uparrow} - \hat{c}^\dagger_{\mathbf{k}\downarrow}\hat{c}_{\mathbf{k}\downarrow}\right), \tag{58}$$

with $\hat{N}$ the total atom number operator and $\Delta\hat{N} \equiv \hat{N}_\uparrow - \hat{N}_\downarrow$ the species asymmetry operator; their expectation values are the imposed total atom number N and polarization (magnetic moment) ΔN. We shall also find it useful to define the magnetization via

$$m = (N_\uparrow - N_\downarrow)/V, \tag{59}$$

with V the system volume. For future reference, we note that the polarization is related to m by

$$\frac{\Delta N}{N} = \frac{m}{n}, \tag{60}$$

with $n = (N_\uparrow + N_\downarrow)/V$ the total atom density.

Combining Eq. (55) with Eq. (25) then yields the two-channel model in the grand-canonical ensemble:

$$\begin{aligned} H = &\sum_{\mathbf{k},\sigma} (\epsilon_k - \mu_\sigma)\hat{c}^\dagger_{k\sigma}\hat{c}_{k\sigma} + \sum_{\mathbf{q}} \left(\frac{\epsilon_q}{2} + \delta_0 - 2\mu\right)\hat{b}^\dagger_{\mathbf{q}}\hat{b}_{\mathbf{q}} \\ &+ \frac{g}{\sqrt{V}} \sum_{\mathbf{k},\mathbf{q}} \left(\hat{b}^\dagger_{\mathbf{q}}\hat{c}_{\mathbf{k}+\frac{\mathbf{q}}{2}\downarrow}\hat{c}_{-\mathbf{k}+\frac{\mathbf{q}}{2}\uparrow} + \hat{c}^\dagger_{-\mathbf{k}+\frac{\mathbf{q}}{2}\uparrow}\hat{c}^\dagger_{\mathbf{k}+\frac{\mathbf{q}}{2}\downarrow}\hat{b}_{\mathbf{q}}\right), \end{aligned} \tag{61}$$

where henceforth we shall generally set $V = 1$. We analyze this model, Eq. (61), via a variational mean-field treatment that, as discussed at length above, is quantitatively accurate for a narrow Feshbach resonance with corrections controlled by powers of $\gamma \ll 1$. We

parametrize the variational state by the value of a single complex field $B_{\mathbf{Q}}$, that dominates the expectation value of the molecular operator $\hat{b}_q$ according to $B_{\mathbf{Q}} = \langle \hat{b}_{\mathbf{Q}} \rangle$. Such a variational state captures a number of possible pure ground states depending on $B_{\mathbf{Q}}$, such as: (i) a normal Fermi gas, with $B_{\mathbf{Q}} = 0$, (ii) a uniform (BEC–BCS) singlet superfluid, with $B_{Q=0} \neq 0$, (iii) a periodically modulated FFLO superfluid, a supersolid, with $B_{\mathbf{Q}\neq 0} \neq 0$, that in real space is characterized by a condensate [102] $B(r) = B_{\mathbf{Q}} e^{i\mathbf{Q}\cdot\mathbf{r}}$. In addition, we will admit the important possibility of an inhomogeneous coexistence of a pair of these ground states, that, as we will see, arises over a large portion of the detuning-polarization phase diagram (Fig. 3).

The grand-canonical Hamiltonian corresponding to this class of variational states is given by

$$H = \sum_{\mathbf{k},\sigma} (\epsilon_k - \mu_\sigma) \hat{c}^\dagger_{\mathbf{k}\sigma} \hat{c}_{\mathbf{k}\sigma} + \left(\frac{\epsilon_Q}{2} + \delta_0 - 2\mu \right) |B_{\mathbf{Q}}|^2 + g \sum_{\mathbf{k}} \left(B^*_{\mathbf{Q}} \hat{c}_{\mathbf{k}+\frac{\mathbf{Q}}{2}\downarrow} \hat{c}_{-\mathbf{k}+\frac{\mathbf{Q}}{2}\uparrow} + \hat{c}^\dagger_{-\mathbf{k}+\frac{\mathbf{Q}}{2}\uparrow} \hat{c}^\dagger_{\mathbf{k}+\frac{\mathbf{Q}}{2}\downarrow} B_{\mathbf{Q}} \right). \tag{62}$$

Its quadratic form in atomic operators, $\hat{c}_{\mathbf{k}\sigma}$, $\hat{c}^\dagger_{\mathbf{k}\sigma}$, allows for an exact treatment, leading to a ground state energy $E_G[B_{\mathbf{Q}}]$, that we compute below using two complementary approaches, via Green functions and via a canonical transformation method. The subsequent minimization of $E_G[B_{\mathbf{Q}}]$ then unambiguously determines the phase behavior (i.e. Figs. 1 and 3) as a function of detuning and Zeeman field, or equivalently, the polarization.

4.1. Green-function approach

In this subsection, we compute the ground state energy of H, Eq. (62), by simply calculating the average

$$E_G = \langle B_{\mathbf{Q}} | H | B_{\mathbf{Q}} \rangle, \tag{63a}$$

$$= \left(\frac{\epsilon_Q}{2} + \delta_0 - 2\mu \right) |B_{\mathbf{Q}}|^2 + \langle B_{\mathbf{Q}} | H_f | B_{\mathbf{Q}} \rangle, \tag{63b}$$

in the variational state $|B_{\mathbf{Q}}\rangle$ labeled by $B_{\mathbf{Q}}$, where $H_f = H_K + H_F$ is the fermion part of the Hamiltonian with its kinetic and Feshbach resonance parts given by

$$H_K = \sum_{\mathbf{k},\sigma} (\epsilon_k - \mu_\sigma) \hat{c}^\dagger_{\mathbf{k}\sigma} \hat{c}_{\mathbf{k}\sigma}, \tag{64a}$$

$$H_F = \sum_{\mathbf{k}} \left(\Delta^*_{\mathbf{Q}} \hat{c}_{\mathbf{k}+\frac{\mathbf{Q}}{2}\downarrow} \hat{c}_{-\mathbf{k}+\frac{\mathbf{Q}}{2}\uparrow} + \hat{c}^\dagger_{-\mathbf{k}+\frac{\mathbf{Q}}{2}\uparrow} \hat{c}^\dagger_{\mathbf{k}+\frac{\mathbf{Q}}{2}\downarrow} \Delta_{\mathbf{Q}} \right), \tag{64b}$$

with the pair field $\Delta_{\mathbf{Q}} \equiv g B_{\mathbf{Q}}$.

These averages can be computed from the fermion Green function, which can be easily obtained from the coherent-state action, S_f. The latter is constructed from H_f in a standard way [117], using the fermion anticommutation rules

$$\{ \hat{c}_{\mathbf{k}\sigma}, \hat{c}^\dagger_{\mathbf{k}'\sigma'} \} = \delta_{\sigma,\sigma'} \delta_{\mathbf{k},\mathbf{k}'}, \tag{65}$$

by first writing H_f in the Bogoliubov–de Gennes form

$$H_{\rm f} = \sum_{\mathbf{k}} \hat{\Psi}^\dagger(\mathbf{k}) \begin{pmatrix} \xi_{-\mathbf{k}+\frac{\mathbf{Q}}{2}\uparrow} & \Delta_{\mathbf{Q}} \\ \Delta^*_{\mathbf{Q}} & -\xi_{\mathbf{k}+\frac{\mathbf{Q}}{2}\downarrow} \end{pmatrix} \hat{\Psi}(\mathbf{k}) + \sum_{\mathbf{k}} \xi_{\mathbf{k}+\frac{\mathbf{Q}}{2}\downarrow}, \tag{66}$$

where $\xi_{k\sigma} \equiv \epsilon_k - \mu_\sigma$ and the Nambu spinor

$$\hat{\Psi}(\mathbf{k}) \equiv \begin{pmatrix} \hat{c}_{-\mathbf{k}+\frac{\mathbf{Q}}{2}\uparrow} \\ \hat{c}^\dagger_{\mathbf{k}+\frac{\mathbf{Q}}{2}\downarrow} \end{pmatrix}. \tag{67}$$

Note that, to get Eq. (66) in this desirable matrix form, the components of the Nambu spinor are defined with momentum-shifted arguments. From Eq. (66) we construct a coherent-state path integral for the partition function $Z = \int D\Psi D\Psi^\dagger \exp[-S_f]$, with effective action [with $\omega_n = \pi T(2n+1)$ the fermionic Matsubara frequency; here $\hbar = 1$]

$$S_f = -\sum_{\omega_n} \sum_{\mathbf{k}} \Psi^\dagger_\alpha(\mathbf{k},\omega_n) G^{-1}_{\alpha\beta}(\mathbf{k},\omega_n) \Psi_\beta(\mathbf{k},\omega_n), \tag{68}$$

where

$$\Psi(\mathbf{k},\omega_n) \equiv \frac{1}{\sqrt{\beta}} \int_0^\beta {\rm d}\tau e^{{\rm i}\omega_n\tau} \Psi(\mathbf{k},\tau), \tag{69}$$

is an anticommuting Grassman field and

$$G^{-1}_{\alpha\beta}(\mathbf{k},\omega_n) = -\begin{pmatrix} -{\rm i}\omega_n + \xi_{-\mathbf{k}+\frac{\mathbf{Q}}{2}\uparrow} & \Delta_{\mathbf{Q}} \\ \Delta^*_{\mathbf{Q}} & -{\rm i}\omega_n - \xi_{\mathbf{k}+\frac{\mathbf{Q}}{2}\downarrow} \end{pmatrix}. \tag{70}$$

From Eqs. (68) and (70) the Green function $G_{\alpha\beta}(\mathbf{k},\omega_n)$ [obtained by inverting Eq. (70)]

$$G_{\alpha\beta}(\mathbf{k},\omega_n) = \frac{1}{({\rm i}\omega_n - \xi_{\mathbf{k}-\frac{\mathbf{Q}}{2}\uparrow})({\rm i}\omega_n + \xi_{\mathbf{k}+\frac{\mathbf{Q}}{2}\downarrow}) - |\Delta_{\mathbf{Q}}|^2} \times \begin{pmatrix} {\rm i}\omega_n + \xi_{\mathbf{k}+\frac{\mathbf{Q}}{2}\downarrow} & \Delta_{\mathbf{Q}} \\ \Delta^*_{\mathbf{Q}} & {\rm i}\omega_n - \xi_{\mathbf{k}-\frac{\mathbf{Q}}{2}\uparrow} \end{pmatrix}, \tag{71}$$

is easily related to averages of the fermion fields through a Gaussian integration, giving

$$-G_{\alpha\beta}(\mathbf{k},\omega_n) = \langle \Psi_\alpha(\mathbf{k},\omega_n) \Psi^\dagger_\beta(\mathbf{k},\omega_n) \rangle, = \begin{pmatrix} \langle \hat{c}_{-\mathbf{k}+\frac{\mathbf{Q}}{2},-\omega_n\uparrow} \hat{c}^\dagger_{-\mathbf{k}+\frac{\mathbf{Q}}{2},-\omega_n\uparrow} \rangle & \langle \hat{c}_{-\mathbf{k}+\frac{\mathbf{Q}}{2},-\omega_n\uparrow} \hat{c}_{\mathbf{k}+\frac{\mathbf{Q}}{2},\omega_n\downarrow} \rangle \\ \langle \hat{c}^\dagger_{\mathbf{k}+\frac{\mathbf{Q}}{2},\omega_n\downarrow} \hat{c}^\dagger_{-\mathbf{k}+\frac{\mathbf{Q}}{2},-\omega_n\uparrow} \rangle & \langle \hat{c}^\dagger_{\mathbf{k}+\frac{\mathbf{Q}}{2},\omega_n\downarrow} \hat{c}_{\mathbf{k}+\frac{\mathbf{Q}}{2},\omega_n\downarrow} \rangle \end{pmatrix}. \tag{72}$$

Armed with expressions Eqs. (72) and (71), the averages in $\langle B_{\mathbf{Q}}|H_{\rm F}|B_{\mathbf{Q}}\rangle$ can be easily computed. Specializing to the zero temperature limit (continuous ω_n, with Matsubara sums replaced by integrals), with details relegated to Appendix B, we find:

$$\begin{aligned} \langle H_{\rm K} \rangle &= \sum_{\mathbf{k}} \varepsilon_k + \sum_{\mathbf{k}} \frac{\varepsilon_k^2}{E_k} [\Theta(-E_{\mathbf{k}\uparrow}) - \Theta(E_{\mathbf{k}\downarrow})] \\ &\quad + \sum_{\mathbf{k}} \left(\frac{\mathbf{k}\cdot\mathbf{Q}}{2m} + h \right) [1 - \Theta(-E_{\mathbf{k}\uparrow}) - \Theta(E_{\mathbf{k}\downarrow})], \end{aligned} \tag{73a}$$

$$\langle H_{\rm F} \rangle = \sum_k \frac{|\Delta_{\mathbf{Q}}|^2}{E_k} [\Theta(-E_{\mathbf{k}\uparrow}) - \Theta(E_{\mathbf{k}\downarrow})], \tag{73b}$$

where $\Theta(x)$ is the Heaviside step function and $E_{\mathbf{k}\sigma}$ is the excitation energy for hyperfine state σ with (taking $\Delta_{\mathbf{Q}}$ real)

$$\varepsilon_k \equiv \frac{k^2}{2m} - \mu + \frac{Q^2}{8m}, \tag{74a}$$

$$E_k \equiv (\varepsilon_k^2 + \Delta_{\mathbf{Q}}^2)^{1/2}, \tag{74b}$$

$$E_{\mathbf{k}\uparrow} \equiv E_k - h - \frac{\mathbf{k}\cdot\mathbf{Q}}{2m}, \tag{74c}$$

$$E_{\mathbf{k}\downarrow} \equiv E_k + h + \frac{\mathbf{k}\cdot\mathbf{Q}}{2m}. \tag{74d}$$

Combining Eqs. (73a) and (73b) with Eq. (63b), we thus have the following expression for the mean-field ground-state energy $E_G(\Delta_{\mathbf{Q}},\mathbf{Q})$:

$$\begin{aligned} E_{\mathrm{G}}(\Delta_{\mathbf{Q}},\mathbf{Q}) = &\left(\frac{\epsilon_Q}{2} + \delta_0 - 2\mu\right)\frac{\Delta_{\mathbf{Q}}^2}{g^2} - \sum_k (E_k - \varepsilon_k) + \sum_{\mathbf{k}} E_k(1 + \Theta(-E_{\mathbf{k}\uparrow}) - \Theta(E_{\mathbf{k}\downarrow})) \\ &+ \sum_{\mathbf{k}} \left(\frac{\mathbf{k}\cdot\mathbf{Q}}{2m} + h\right)(1 - \Theta(-E_{\mathbf{k}\uparrow}) - \Theta(E_{\mathbf{k}\downarrow})), \end{aligned} \tag{75}$$

which can be put in the simpler form

$$\begin{aligned} E_{\mathrm{G}}(\Delta_{\mathbf{Q}},\mathbf{Q}) = &\left(\frac{\epsilon_Q}{2} + \delta_0 - 2\mu\right)\frac{\Delta_{\mathbf{Q}}^2}{g^2} - \sum_k (E_k - \varepsilon_k) \\ &+ \sum_{\mathbf{k}} [E_{\mathbf{k}\uparrow}\Theta(-E_{\mathbf{k}\uparrow}) + E_{\mathbf{k}\downarrow}\Theta(-E_{\mathbf{k}\downarrow})]. \end{aligned} \tag{76}$$

Using the Green function Eq. (71), together with Eq. (72), the expectation values of the total atom number $\langle\hat{N}\rangle$ and the number difference (magnetic moment) $\langle\Delta\hat{N}\rangle$, can also be computed:

$$N = \frac{2\Delta_{\mathbf{Q}}^2}{g^2} + \sum_k \left(\langle\hat{c}_{\mathbf{k}\uparrow}^\dagger\hat{c}_{\mathbf{k}\uparrow}\rangle + \langle\hat{c}_{\mathbf{k}\downarrow}^\dagger\hat{c}_{\mathbf{k}\downarrow}\rangle\right), \tag{77}$$

$$= \frac{2\Delta_{\mathbf{Q}}^2}{g^2} + \sum_k \left(1 - \frac{\varepsilon_k}{E_k}[\Theta(E_{\mathbf{k}\uparrow}) - \Theta(-E_{\mathbf{k}\downarrow})]\right), \tag{78}$$

$$\Delta N = \sum_{\mathbf{k}} \left(\langle\hat{c}_{\mathbf{k}\uparrow}^\dagger\hat{c}_{\mathbf{k}\uparrow}\rangle - \langle\hat{c}_{\mathbf{k}\downarrow}^\dagger\hat{c}_{\mathbf{k}\downarrow}\rangle\right), \tag{79}$$

$$= \sum_{\mathbf{k}} (\Theta(-E_{\mathbf{k}\uparrow}) - \Theta(-E_{\mathbf{k}\downarrow})). \tag{80}$$

These expressions will be important for eliminating the chemical potentials appearing in E_{G} in favor of the experimentally-controlled atom number N and polarization $\Delta N/N$.

Eq. (76) is quite general, encompassing (as noted above) both uniform and periodic FFLO-type paired states as well as an unpaired normal state. In various limits, however, it simplifies considerably. In Appendix C we review the most well-studied such limit, namely the conventional equal-population BEC–BCS crossover at $h = 0$ and $\mathbf{Q} = 0$.

With our primary result Eq. (76) in hand, the remainder of the paper is conceptually straightforward, simply amounting to minimizing $E_{\rm G}(B_{\mathbf{Q}})$ over $B_{\mathbf{Q}}$ and $\mathbf{Q}$ to find their optimum values as a function of detuning δ, polarization ΔN (or h) and total atom number N (or μ). Although this can be done numerically, considerable insight is obtained by approximate analytic analysis, possible for a narrow Feshbach resonance, $\gamma \ll 1$. Before turning to this, in the next subsection we present another derivation of $E_{\rm G}(B_{\mathbf{Q}})$, Eq. (76).

4.2. Canonical transformation approach

In this subsection, we present an alternate derivation of Eq. (76) for $E_{\rm G}$, using only the canonical commutation relations of the fermion operators $\hat{c}_{\mathbf{k}\sigma}$. As in the preceding subsection, we focus on the fermion portion $H_{\rm f}$ of the total Hamiltonian, with the starting point Eq. (66):

$$H_{\rm f} = \sum_{\mathbf{k}} \hat{\Psi}^{\dagger}(\mathbf{k}) \hat{H}_f \hat{\Psi}(\mathbf{k}) + \sum_{\mathbf{k}} \xi_{\mathbf{k}+\frac{\mathbf{Q}}{2}\downarrow}, \tag{81}$$

$$\hat{H}_{\rm f} \equiv \begin{pmatrix} \xi_{-\mathbf{k}+\frac{\mathbf{Q}}{2}\uparrow} & \Delta^{*}_{\mathbf{Q}} \\ \Delta_{\mathbf{Q}} & -\xi_{\mathbf{k}+\frac{\mathbf{Q}}{2}\downarrow} \end{pmatrix}, \tag{82}$$

where without loss of generality we have taken $\Delta_{\mathbf{Q}}$ real. The matrix $\hat{H}_f$ can be diagonalized using the unitary matrix $\hat{U}$

$$\hat{U} = \begin{pmatrix} u_k & v_k \\ v_k & -u_k \end{pmatrix}. \tag{83}$$

Here, the coherence factors

$$u_k = \frac{1}{\sqrt{2}} \sqrt{1 + \frac{\varepsilon_k}{E_k}}, \tag{84a}$$

$$v_k = \frac{1}{\sqrt{2}} \sqrt{1 - \frac{\varepsilon_k}{E_k}}, \tag{84b}$$

are analogues of those appearing in BCS theory [118–120], whose form is constrained to preserve the canonical commutation relations, Eq. (65), that require $u_k^2 + v_k^2 = 1$. Since, by construction, the left and right columns of $\hat{U}$ are the eigenvectors of $\hat{H}_f$ (with eigenvalues $E_{\mathbf{k}\uparrow}$ and $-E_{\mathbf{k}\downarrow}$, respectively), this accomplishes a diagonalization of H_f in Eq. (81). We find:

$$H_f = \sum_{\mathbf{k}} \begin{pmatrix} \hat{\alpha}^{\dagger}_{\mathbf{k}\uparrow} & \hat{\alpha}_{\mathbf{k}\downarrow} \end{pmatrix} \begin{pmatrix} E_{\mathbf{k}\uparrow} & 0 \\ 0 & -E_{\mathbf{k}\downarrow} \end{pmatrix} \begin{pmatrix} \hat{\alpha}_{\mathbf{k}\uparrow} \\ \hat{\alpha}^{\dagger}_{\mathbf{k}\downarrow} \end{pmatrix} + \sum_{\mathbf{k}} \xi_{\mathbf{k}+\frac{\mathbf{Q}}{2}\downarrow}, \tag{85}$$

with the Bogoliubov (normal mode) operators $\hat{\alpha}_{\mathbf{k}\sigma}$ following from the operation of $\hat{U}$ on the Nambu spinor Eq. (67):

$$\hat{\alpha}_{\mathbf{k}\uparrow} = u_k \hat{c}_{-\mathbf{k}+\frac{\mathbf{Q}}{2}\uparrow} + v_k \hat{c}^{\dagger}_{\mathbf{k}+\frac{\mathbf{Q}}{2}\downarrow}, \tag{86a}$$

$$\hat{\alpha}^{\dagger}_{\mathbf{k}\downarrow} = v_k \hat{c}_{-\mathbf{k}+\frac{\mathbf{Q}}{2}\uparrow} - u_k \hat{c}^{\dagger}_{\mathbf{k}+\frac{\mathbf{Q}}{2}\downarrow}. \tag{86b}$$

Thus, using $\{\hat{\alpha}_{\mathbf{k}\downarrow}, \hat{\alpha}^{\dagger}_{\mathbf{k}\downarrow}\} = 1$, we have

$$H_{\rm f} = \sum_{\mathbf{k}} \left(E_{\mathbf{k}\uparrow} \hat{\alpha}^{\dagger}_{\mathbf{k}\uparrow} \hat{\alpha}_{\mathbf{k}\uparrow} + E_{\mathbf{k}\downarrow} \hat{\alpha}^{\dagger}_{\mathbf{k}\downarrow} \hat{\alpha}_{\mathbf{k}\downarrow} \right) + \sum_{\mathbf{k}} \left(\xi_{\mathbf{k}+\frac{\mathbf{Q}}{2}\downarrow} - E_{\mathbf{k}\downarrow} \right). \tag{87}$$

Recall that our aim is to compute the ground-state energy. If it were true that $E_{\mathbf{k}\uparrow}$ and $E_{\mathbf{k}\downarrow}$ were both positive, the first two terms in Eq. (87) would simply count the excitation energy associated with the excitation quanta $\hat{\alpha}_{\mathbf{k}\sigma}$ (Bogoliubov quasiparticles) above the ground state defined as the vacuum of $\hat{\alpha}_{\mathbf{k}\sigma}$ particles, i.e., $\hat{\alpha}_{\mathbf{k}\sigma}|B_{\mathbf{Q}}\rangle = 0$. This would also allow an immediate identification of the constant part of H_f [the second line of Eq. (87)] with the fermion contribution $E_{\rm Gf} = \langle H_{\rm K}\rangle + \langle H_{\rm F}\rangle$ to the ground-state energy.

However, because the energies $E_{\mathbf{k}\sigma}$ are *not* positive definite, the second line of Eq. (87) is *not* the ground state energy when either of $E_{\mathbf{k}\sigma} < 0$. It is nonetheless possible to write $H_{\rm f}$ as a sum of the excitation and ground-state energies. To this end, we use step functions to separate the sum over momenta into regions that have $E_{\mathbf{k}\sigma} > 0$ and $E_{\mathbf{k}\sigma} < 0$:

$$\sum_{\mathbf{k}} E_{\mathbf{k}\sigma} \hat{\alpha}^{\dagger}_{\mathbf{k}\sigma} \hat{\alpha}_{\mathbf{k}\sigma} = \sum_{\mathbf{k}} \left[E_{\mathbf{k}\sigma} \Theta(E_{\mathbf{k}\sigma}) \hat{\alpha}^{\dagger}_{\mathbf{k}\sigma} \hat{\alpha}_{\mathbf{k}\sigma} + E_{\mathbf{k}\sigma} \Theta(-E_{\mathbf{k}\sigma})(1 - \hat{\alpha}_{\mathbf{k}\sigma} \hat{\alpha}^{\dagger}_{\mathbf{k}\sigma}) \right], \tag{88}$$

where, for the momenta satisfying $E_{\mathbf{k}\sigma} < 0$, we used the anti-commutation relation $\{\hat{\alpha}_{\mathbf{k}\sigma}, \hat{\alpha}^{\dagger}_{\mathbf{k}\sigma}\} = 1$. Using Eq. (88), we can write H_f as

$$H_{\rm f} = \sum_{\mathbf{k}\sigma} \left(E_{\mathbf{k}\sigma} \Theta(E_{\mathbf{k}\sigma}) \hat{\alpha}^{\dagger}_{\mathbf{k}\sigma} \hat{\alpha}_{\mathbf{k}\sigma} - E_{\mathbf{k}\sigma} \Theta(-E_{\mathbf{k}\sigma}) \hat{\alpha}_{\mathbf{k}\sigma} \hat{\alpha}^{\dagger}_{\mathbf{k}\sigma} \right) + E_{\rm Gf}, \tag{89}$$

with

$$E_{\rm Gf} \equiv \sum_{\mathbf{k}} \left(E_{\mathbf{k}\uparrow} \Theta(-E_{\mathbf{k}\uparrow}) + E_{\mathbf{k}\downarrow} \Theta(-E_{\mathbf{k}\downarrow}) + \xi_{\mathbf{k}+\frac{\mathbf{Q}}{2}\downarrow} - E_{\mathbf{k}\downarrow} \right). \tag{90}$$

With these manipulations, each pair of operators in the sum in the first line of Eq. (89) by construction multiplies a *positive* excitation energy that is $|E_{\mathbf{k}\sigma}|$. Thus, they represent excitations above the ground state with the fermion part of the ground state energy given by $\langle H_{\rm f}\rangle = E_{\rm Gf}$. Using the definitions of $E_{\mathbf{k}\sigma}$ (and $\sum_{\mathbf{k}} \mathbf{k} \cdot \mathbf{Q} = 0$), it is straightforward to see that $E_{\rm Gf}$ agrees with the result from the preceding subsection, i.e., $\langle H_{\rm K}\rangle + \langle H_{\rm F}\rangle$:

$$E_{\rm Gf} = \sum_{k} (\varepsilon_k - E_k) + \sum_{\mathbf{k}} \left(E_{\mathbf{k}\uparrow} \Theta(-E_{\mathbf{k}\uparrow}) + E_{\mathbf{k}\downarrow} \Theta(-E_{\mathbf{k}\downarrow}) \right), \tag{91}$$

which is our result for the fermion contribution to the ground-state energy $E_{\rm G}(B_{\mathbf{Q}})$, Eq. (76).

This method for computing the ground-state energy has the additional benefits that (i) it provides a physical interpretation to the step functions appearing in $E_{\rm G}(B_{\mathbf{Q}})$ and (ii) it allows a straightforward computation of the fermion ground-state wavefunction $|B_{\mathbf{Q}}\rangle$ that we now derive. Clearly, $|B_{\mathbf{Q}}\rangle$ must be annihilated by the excitation part $H^e_{\rm f}$ of the Hamiltonian $H_{\rm f}$:

$$H^e_{\rm f} \equiv \sum_{\mathbf{k}\sigma} \left(E_{\mathbf{k}\sigma} \Theta(E_{\mathbf{k}\sigma}) \hat{\alpha}^{\dagger}_{\mathbf{k}\sigma} \hat{\alpha}_{\mathbf{k}\sigma} - E_{\mathbf{k}\sigma} \Theta(-E_{\mathbf{k}\sigma}) \hat{\alpha}_{\mathbf{k}\sigma} \hat{\alpha}^{\dagger}_{\mathbf{k}\sigma} \right). \tag{92}$$

The step functions divide the momentum sum into three regions: (1) $\mathbf{k}$ such that $E_{\mathbf{k}\uparrow} > 0$ and $E_{\mathbf{k}\downarrow} > 0$, (2) $\mathbf{k}$ such that $E_{\mathbf{k}\uparrow} < 0$ and (3) $\mathbf{k}$ such that $E_{\mathbf{k}\downarrow} < 0$. From the explicit expressions Eqs. (74c) and (74d) it is easy to see that the $E_{\mathbf{k}\sigma}$ cannot both be negative; thus, these are the only three possibilities.

Consider momenta such that condition (1) is satisfied, which we denote $\mathbf{k}_1$. For such momenta, the summand in Eq. (92) is $E_{\mathbf{k}_1\uparrow} \hat{\alpha}^{\dagger}_{\mathbf{k}_1\uparrow} \hat{\alpha}_{\mathbf{k}_1\uparrow} + E_{\mathbf{k}_1\downarrow} \hat{\alpha}^{\dagger}_{\mathbf{k}_1\downarrow} \hat{\alpha}_{\mathbf{k}_1\downarrow}$, which annihilates factors

of the form $(u_{\mathbf{k}_1} + v_{\mathbf{k}_1}\hat{c}^\dagger_{\mathbf{k}_1+\frac{\mathbf{Q}}{2}\downarrow}\hat{c}^\dagger_{-\mathbf{k}_1+\frac{\mathbf{Q}}{2}\uparrow})$. Of course, if we set $\mathbf{Q} = 0$, this is the usual factor in the BCS ground-state wavefunction [118–120] that encodes pairing correlations; thus, the states $\mathbf{k}_1$ are *paired* at nonzero center of mass momentum $\mathbf{Q}$. This can also be seen from the form of the ground-state energy Eq. (91): Since the Θ functions in the second term of this equation *vanish* for states satisfying condition (1) they have the standard BCS contribution to the ground-state energy from the first term of Eq. (91).

Now consider states in region (2). For them, the excitation energy is $-E_{\mathbf{k}_2\uparrow}\hat{\alpha}_{\mathbf{k}_2\uparrow}\hat{\alpha}^\dagger_{\mathbf{k}_2\uparrow} + E_{\mathbf{k}_2\downarrow}\hat{\alpha}^\dagger_{\mathbf{k}_2\downarrow}\hat{\alpha}_{\mathbf{k}_2\downarrow}$. By examining the form of Eq. (86a), it is clear that an operator annihilated by this summand is simply $\hat{c}^\dagger_{-\mathbf{k}_2+\frac{\mathbf{Q}}{2}\uparrow}$. Thus, states $\mathbf{k}_2$ are simply filled by unpaired spin-$\uparrow$ fermions, i.e., they are unpaired. States in region 3 are similarly unpaired, but with spin-$\downarrow$. Expressing $|B_{\mathbf{Q}}\rangle$ as a product over these three regions of momenta yields our variational fermion ground state wavefunction:

$$|B_{\mathbf{Q}}\rangle = \prod_{\mathbf{k}\in\mathbf{k}_3}\hat{c}^\dagger_{\mathbf{k}+\frac{\mathbf{Q}}{2}\downarrow}\prod_{\mathbf{k}\in\mathbf{k}_2}\hat{c}^\dagger_{-\mathbf{k}+\frac{\mathbf{Q}}{2}\uparrow}\prod_{\mathbf{k}\in\mathbf{k}_1}(u_{\mathbf{k}} + v_{\mathbf{k}}\hat{c}^\dagger_{\mathbf{k}+\frac{\mathbf{Q}}{2}\downarrow}\hat{c}^\dagger_{-\mathbf{k}+\frac{\mathbf{Q}}{2}\uparrow})|0\rangle, \tag{93}$$

with $|0\rangle$ the fermionic atom vacuum.

We now describe our general strategy. The ground state energy Eq. (76) is a function of $\Delta_{\mathbf{Q}}$ (or equivalently $B_{\mathbf{Q}}$) and $\mathbf{Q}$. By minimizing it over $\Delta_{\mathbf{Q}}$ and $\mathbf{Q}$, we find possible ground states of the two-channel model at particular values of μ, h and detuning. Ground states at fixed imposed atom number (relevant for atomic physics experiments) are stationary with respect to $\Delta_{\mathbf{Q}}$ and $\mathbf{Q}$, and satisfy the total number and polarization constraints:

$$0 = \frac{\partial E_G}{\partial \Delta_{\mathbf{Q}}}, \tag{94a}$$

$$0 = \frac{\partial E_G}{\partial \mathbf{Q}}, \tag{94b}$$

$$N = -\frac{\partial E_G}{\partial \mu}, \tag{94c}$$

$$\Delta N = -\frac{\partial E_G}{\partial h}, \tag{94d}$$

the latter two being equivalent to Eqs. (78) and (80). We shall refer to Eqs. (94a)–(94d) as the gap, momentum, number and polarization equations, respectively. It is crucial to emphasize that E_G has numerous stationary points and we must be sure to ascertain that the particular stationary point we are studying is indeed a *minimum* [121,122] of E_G. Thus, while often in studies of the BEC–BCS crossover at $h = 0$ authors simply simultaneously solve the number and gap equation, at $h \neq 0$ this can (and has in a number of works in the literature [47,67,45,121–123]) lead to incorrect results, especially at negative detunings where E_G is particularly complicated. Moreover, frequently we shall find that the ground-state at a particular δ, N, and ΔN (or even at fixed δ, N, and h) is a *phase-separated mixture* of two of these phases, with fractions x and $1 - x$ that must be determined. With these caveats in mind, we now turn to the analysis of Eqs. (76) and (94a)–(94d).

5. Positive-detuning regime of two-channel model at finite population difference

In this section, we consider our system at $\delta > 0$ with a finite population imbalance (polarization) between the species undergoing pairing, encompassing the BCS $\delta \gg 2\epsilon_F$

and crossover $0 < \delta < 2\epsilon_F$ regimes. As discussed in Section 4, it is convenient to first study the equivalent problem of pairing with a finite *chemical potential* difference $\delta\mu = 2h$ between the species. What phases do we expect in this regime? For equal chemical potentials ($\mu_\uparrow = \mu_\downarrow = \mu$), the favored ground state is the paired superfluid (SF) state that (since $\mu > 0$ in this regime) is associated with pairing near the common Fermi surface at momentum $k_F = \sqrt{2m\mu}$. This paired SF state is of course described by the BCS ground state. For very large chemical potential difference h, we expect pairing to be destroyed ($\Delta_{\mathbf{Q}} = 0$) and the ground-state to be a normal (N) Pauli-paramagnetic Fermi gas with $N_\uparrow > N_\downarrow$. The remaining logical possibility is that, for intermediate values of h, we may have a phase exhibiting nonzero pairing and a nonzero population difference ($\Delta N \neq 0$); it remains to be seen whether such a ground state is stable anywhere in the $\delta - \Delta N$ phase diagram.

One set of possible ground states that accomplish this is the so-called FFLO class of states, [86,87] already well-studied for a BCS-type superconductor. The fact that our Feshbach resonance model is closely related to the BCS model of interacting fermions ensures that we will indeed find that FFLO-like states are stable over portions of the phase diagram at large positive detuning.

As we will show, within our restricted ground-state ansatz, these three states (FFLO, SF and N) are the *only homogeneous ground states* that are stable at positive detuning, with the phase diagram dominated by phase separated mixtures of SF and N or SF and FFLO. Furthermore, the FFLO state is only stable for a very narrow window of h (or ΔN) values that vanishes below $\delta_* \simeq 2\epsilon_F$. The reason that FFLO states can only exist for a restricted narrow window of parameters is simply that, in order to accommodate both pairing *and* a nonzero polarization ΔN, the system must pair at a *finite wavevector* $Q \sim k_{F\uparrow} - k_{F\downarrow}$. This corresponds to a moving superfluid that, at sufficiently high superfluid velocity (corresponding to a critical $Q \sim k_{F\uparrow} - k_{F\downarrow} \propto h$) is unstable (via the Landau criterion) to quasiparticle proliferation, as seen from the form of $E_{\mathbf{k}\sigma}$ [Eqs. (74c) and (74d)].

From a pedagogical point of view, it is easiest to proceed by first neglecting the FFLO state entirely, setting $\mathbf{Q} = 0$ at the outset in our expression for E_G (which simplifies it considerably), before determining the phase diagram (Figs. 9 and 10). Afterwards, in Section 7 we will return to the FFLO state, finding the regime of the phase diagram in which it is stable.

5.1. Ground-state energy at $\boldsymbol{Q} = 0$

In this subsection, we focus on the $\mathbf{Q} = 0$ case, which greatly simplifies the ground-state energy E_G. Although this is in preparation for studying possible uniform ground-states at $\delta > 0$, the results of the present section will also apply to the negative-detuning BEC regime, to be studied in Section 6, where, as we will show, the FFLO state is unstable and $\mathbf{Q} = 0$ is the only possibility. With this in mind, in this subsection we shall make no approximations that rely on $\delta > 0$.

We start with the general expression Eq. (75) at $\mathbf{Q} = 0$, for simplicity of notation dropping the zero subscript on Δ (i.e. $\Delta_0 \to \Delta$):

$$E_G = (\delta - 2\mu)\frac{\Delta^2}{g^2} + \sum_k \left(\xi_k - E_k + \frac{\Delta^2}{2\epsilon_k}\right) + \sum_k E_k(1 + \Theta(-E_{k\uparrow}) - \Theta(E_{k\downarrow})) + h\sum_k (1 - \Theta(-E_{k\uparrow}) - \Theta(E_{k\downarrow})), \tag{95}$$

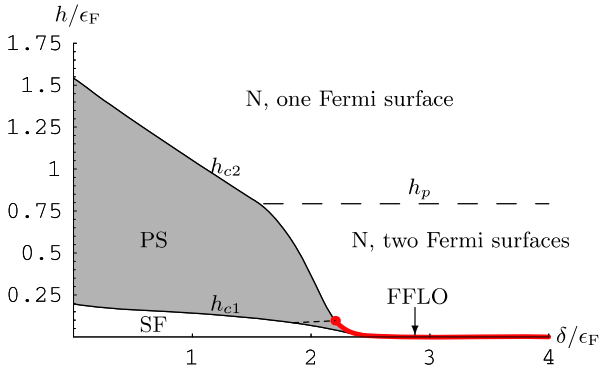

Fig. 9. Positive detuning (δ)-chemical potential difference (h) phase diagram of the two-channel model for the case $\gamma = 0.1$ showing the superfluid phase (SF), normal phase (N), FFLO phase (along red curve, too thin to see) and the regime of phase separation (PS). Above the horizontal dashed line the N phase is fully spin-polarized ($N_\uparrow = N$, $N_\downarrow = 0$), consisting of a single Fermi surface, while below the dashed line the N phase has two Fermi surfaces. The dashed line in the shaded PS regime separates SF–N coexistence from SF–FFLO coexistence and is derived in Section 7.2.

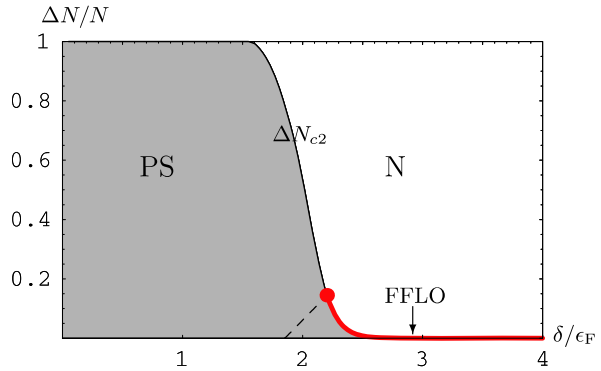

Fig. 10. Positive detuning (δ)-population difference (ΔN) phase diagram of the two-channel model for the case $\gamma = 0.1$ showing the regime of phase separation (PS), the normal phase (N) and the FFLO phase (along red curve). The SF phase is confined to the $\Delta N = 0$ axis. As in Fig. 9, the dashed line in the shaded PS regime separates SF-N coexistence from SF–FFLO coexistence (the latter sharing a boundary with the FFLO phase). (For interpretation of the references to color in this figure legend, the reader is referred to the web version of this paper.)

where now $\xi_k = \epsilon_k - \mu$, the excitation energies are simply

$$E_{k\uparrow} = E_k - h, \tag{96a}$$

$$E_{k\downarrow} = E_k + h, \tag{96b}$$

plotted for $\mu > 0$ in Fig. 11, and we have used Eq. (29) to exchange the bare detuning δ_0 for the physical detuning δ.

Without loss of generality we take $h > 0$, so that $\Theta(E_{k\downarrow}) = 1$ and Eq. (95) can be written in the simpler form

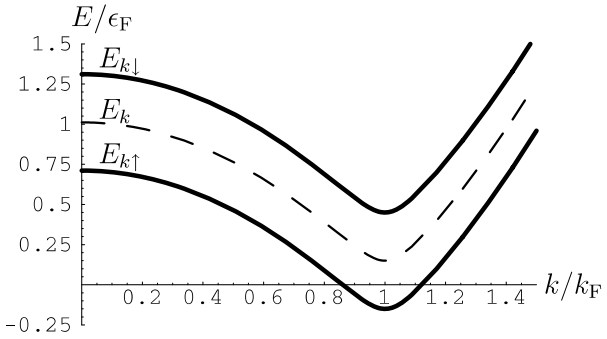

Fig. 11. (Dashed line) Plot of quasiparticle excitation energy $E_k = \sqrt{\xi_k^2 + \Delta^2}$ for a BCS superconductor, normalized to ϵ_F for the case $\mu = \epsilon_F$ and $\Delta = 0.15\epsilon_F$. Solid lines: Spin-up and spin-down quasiparticle excitation energies for the case $h = 0.3\epsilon_F$.

$$E_G = (\delta - 2\mu)\frac{\Delta^2}{g^2} + \sum_k \left(\xi_k - E_k + \frac{\Delta^2}{2\epsilon_k}\right) + \sum_k (E_k - h)\Theta(h - E_k). \tag{97}$$

The last h-dependent term is only nonzero when $h > E_k$ for some k. For $\mu > 0$, this means E_G is identically *h-independent* until the spin-up band crosses zero energy (depicted in Fig. 11) at $h > \Delta$.

Eq. (97) may be further simplified by rewriting the h-dependent momentum sums in terms of the magnetization $m(h)$. The simplest way to do this is to recall Eq. (94d) for the population difference

$$N_\uparrow - N_\downarrow = -\frac{\partial E_G}{\partial h}, \tag{98}$$

which can be written in terms of the magnetization $m(h)$ as [using Eqs. (59); note we have taken the system volume V to be unity]:

$$m(h) = \int \frac{d^3k}{(2\pi)^3}\Theta(h - E_k), \tag{99a}$$

$$= \frac{2c}{3}\Big[(\mu + \sqrt{h^2 - \Delta^2})^{3/2}\Theta(\mu + \sqrt{h^2 - \Delta^2}) - (\mu - \sqrt{h^2 - \Delta^2})^{3/2}\Theta(\mu - \sqrt{h^2 - \Delta^2})\Big], \tag{99b}$$

where in the last equality we evaluated the integral over momenta by first converting to an energy integral using the usual prescription $\int \frac{d^3k}{(2\pi)^3}\cdots = \int N(\epsilon)d\epsilon\cdots$ with the three-dimensional density of states per spin

$$N(\epsilon) = c\sqrt{\epsilon}, \tag{100}$$

$$c \equiv \frac{m^{3/2}}{\sqrt{2}\pi^2}. \tag{101}$$

Thus [using the condition that the magnetic contribution of Eq. (97) vanishes at $h = 0$], we have the following general expression for the $\mathbf{Q} = 0$ ground-state energy (also converting the first momentum sum to an integral):

$$E_{\rm G} = (\delta - 2\mu)\frac{\Delta^2}{g^2} + \int \frac{d^3k}{(2\pi)^3}\left(\xi_k - E_k + \frac{\Delta^2}{2\epsilon_k}\right) - \int_0^h m(h')\mathrm{d}h'. \tag{102}$$

The steps connecting the last term of Eq. (97) to the last term of Eq. (102) can also be derived in a more straightforward approach by manipulating the h-dependent momentum sums in Eq. (97), as shown in Appendix D.

Possible $\mathbf{Q} = 0$ ground-states correspond to minima of Eq. (102) [which thus satisfy the gap equation, Eq. (94a)] having magnetization m given by Eq. (99b) and density n given by

$$n = -\frac{1}{V}\frac{\partial E_{\rm G}}{\partial \mu}. \tag{103}$$

Quite frequently, we shall be interested in systems at fixed *imposed* total atom (as free atoms and molecules) density n. This introduces another natural scale, $\epsilon_{\rm F}$, that is the Fermi energy at asymptotically large detuning for $g \to 0$:

$$n = \frac{4}{3}c\epsilon_{\rm F}^{3/2}. \tag{104}$$

We use $\epsilon_{\rm F}$ as a convenient energy scale to normalize quantities with dimensions of energy. Thus, we define

$$\hat{\mu} \equiv \frac{\mu}{\epsilon_{\rm F}}, \tag{105a}$$

$$\hat{\Delta} \equiv \frac{\Delta}{\epsilon_{\rm F}}, \tag{105b}$$

$$\hat{\delta} \equiv \frac{\delta}{\epsilon_{\rm F}}, \tag{105c}$$

$$\hat{h} \equiv \frac{h}{\epsilon_{\rm F}}, \tag{105d}$$

$$e_{\rm G} \equiv \frac{E_{\rm G}}{c\epsilon_{\rm F}^{5/2}}, \tag{105e}$$

with the last definition providing a convenient normalization for the ground-state energy. We shall typically determine quantities (such as critical chemical potential differences and polarizations) as a function of the normalized detuning $\hat{\delta}$. To make contact with experiments that typically plot physical observables as a function of the inverse scattering length through the dimensionless parameter $-(k_{\rm F}a_s)^{-1}$, we note that our normalized detuning $\hat{\delta}$ is proportional to this parameter and given by [combining Eq. (30) with Eqs. (37) and (105c)]

$$\hat{\delta} = -\frac{\pi}{2}\gamma\frac{1}{k_{\rm F}a_s}. \tag{106}$$

Converting the momentum integral in Eq. (102) to an energy integral, we have for $e_{\rm G}$:

$$e_{\rm G} = \gamma^{-1}\hat{\Delta}^2(\hat{\delta} - 2\hat{\mu}) - \int_0^{\hat{h}} \hat{m}(\hat{h}')\,\mathrm{d}\hat{h}' + \int_0^{\infty} \mathrm{d}x\sqrt{x}\left(x - \hat{\mu} - \sqrt{(x-\hat{\mu})^2 + \hat{\Delta}^2} + \frac{\hat{\Delta}^2}{2x}\right), \tag{107}$$

where $\hat{m}(\hat{h})$ is the dimensionless form of Eq. (99b):

$$\hat{m}(\hat{h}) \equiv \frac{2}{3}\left[(\hat{\mu}+\sqrt{\hat{h}^2-\hat{\Delta}^2})^{3/2}\Theta(\hat{\mu}+\sqrt{\hat{h}^2-\hat{\Delta}^2}) - (\hat{\mu}-\sqrt{\hat{h}^2-\hat{\Delta}^2})^{3/2}\Theta(\hat{\mu}-\sqrt{\hat{h}^2-\hat{\Delta}^2})\right]. \tag{108}$$

For future reference, we note that the relations between $m(h)$, ΔN and $\hat{m}(\hat{h})$ can be summarized by

$$\frac{m(h)}{n} = \frac{\Delta N}{N} = \frac{3}{4}\hat{m}(\hat{h}). \tag{109}$$

With these definitions of dimensionless variables, the gap, number and polarization equations [i.e., Eqs. (94a), (94c), and (94d), respectively] become

$$0 = \frac{\partial e_{\mathrm{G}}}{\partial \hat{\Delta}}, \tag{110a}$$

$$\frac{4}{3} = -\frac{\partial e_{\mathrm{G}}}{\partial \hat{\mu}}, \tag{110b}$$

$$\frac{4}{3}\frac{\Delta N}{N} = -\frac{\partial e_G}{\partial \hat{h}}. \tag{110c}$$

As we have already mentioned, the equations in the present section apply to the $\mathbf{Q}=0$ ground-state energy in the BCS regime (that we now proceed to study) and also in the BEC regime that we shall study in Section 6.

5.2. $\boldsymbol{Q}$ = 0 phases of the ground state energy in the BCS regime

In the present section, we study the phases of Eq. (107) for $\hat{h} \neq 0$ in the BCS limit of large positive detuning. In this regime, $\hat{\mu} \gg \hat{\Delta}$ and the integral in Eq. (107) is well-approximated by (see Appendix C):

$$\int_0^\infty \mathrm{d}x\sqrt{x}\left(x-\hat{\mu}-\sqrt{(x-\hat{\mu})^2+\hat{\Delta}^2}+\frac{\hat{\Delta}^2}{2x}\right) \simeq -\frac{8}{15}\hat{\mu}^{5/2} - \sqrt{\hat{\mu}}\hat{\Delta}^2\left(\frac{1}{2}-\ln\frac{\hat{\Delta}}{8\mathrm{e}^{-2}\hat{\mu}}\right). \tag{111}$$

This yields:

$$e_{\mathrm{G}} \simeq -\frac{\sqrt{\hat{\mu}}}{2}\hat{\Delta}^2 + \hat{\Delta}^2(\hat{\delta}-2\hat{\mu})\gamma^{-1} + \sqrt{\hat{\mu}}\hat{\Delta}^2\ln\frac{\hat{\Delta}}{8\mathrm{e}^{-2}\hat{\mu}} - \int_0^{\hat{h}}\mathrm{d}\hat{h}'\hat{m}(\hat{h}') - \frac{8}{15}\hat{\mu}^{5/2}, \tag{112}$$

as the BCS-regime normalized ground-state energy that we shall analyze in the remainder of this section.

5.2.1. Normal phase

Zero-temperature phases are stationary points of e_{G}, satisfying the gap equation Eq. (110a). Since e_{G} is a function only of $\hat{\Delta}^2$, it is obvious that $\hat{\Delta}=0$ is always such a stationary point. This solution represents the normal (N) state consisting of spin-up and spin-down Fermi surfaces characterized by chemical potentials $\mu_\uparrow$ and $\mu_\downarrow$. The corresponding

ground-state energy simply counts the energetic contributions from these two Fermi seas [see Eq. (B.19)]:

$$E_{\mathrm{G,N}} = \sum_{\mathbf{k}} [(\xi_k - h)\Theta(h - \xi_k) + (\xi_k + h)\Theta(-h - \xi_k)], \tag{113a}$$

$$= -\frac{4c}{15}\left[(\mu + h)^{5/2}\Theta(\mu + h) + (\mu - h)^{5/2}\Theta(\mu - h)\right]. \tag{113b}$$

We note that in the normal state Eq. (113b) is valid for an arbitrary relation between h and μ and therefore (in contrast to small $h \ll \mu$ approximations, valid in the superfluid regime, used below) allows us to access the high-polarization regime of the normal state.

In terms of our dimensionless variables, the normalized ground-state energy $e_{\mathrm{G,N}}$ is thus

$$e_{\mathrm{G,N}} = -\frac{4}{15}\left[(\hat{\mu} + \hat{h})^{\frac{5}{2}}\Theta(\hat{\mu} + \hat{h}) + (\hat{\mu} - \hat{h})^{\frac{5}{2}}\Theta(\hat{\mu} - \hat{h})\right], \tag{114a}$$

$$\simeq -\frac{8}{15}\hat{\mu}^{5/2} - \sqrt{\hat{\mu}}\hat{h}^2, \quad \hat{h} \ll \hat{\mu}. \tag{114b}$$

Eq. (114b) applies in the linear regime $\hat{h} \ll \hat{\mu}$, with $\sqrt{\hat{\mu}}\hat{h}^2$ the harmonic Pauli-paramagnetic contribution, and will frequently be sufficient in the low-polarization normal phase.

The normal-state atom density n_{N} and polarization m_{N} at fixed h and μ [following from Eqs. (94c) and (94d)] are also particularly simple:

$$n_{\mathrm{N}} = \frac{2c}{3}\left[(\mu + h)^{3/2}\Theta(\mu + h) + (\mu - h)^{3/2}\Theta(\mu - h)\right], \tag{115a}$$

$$m_{\mathrm{N}} = \frac{2c}{3}\left[(\mu + h)^{3/2}\Theta(\mu + h) - (\mu - h)^{3/2}\Theta(\mu - h)\right]. \tag{115b}$$

If we impose a total atom density $n = \frac{4}{3}c\epsilon_{\mathrm{F}}^{3/2}$ and population imbalance ΔN, Eqs. (115a), (115b) can be written in the dimensionless form

$$1 = \frac{1}{2}\left[(\hat{\mu} + \hat{h})^{\frac{3}{2}}\Theta(\hat{\mu} + \hat{h}) + (\hat{\mu} - \hat{h})^{\frac{3}{2}}\Theta(\hat{\mu} - \hat{h})\right], \tag{116a}$$

$$\frac{\Delta N}{N} = \frac{1}{2}\left[(\hat{\mu} + \hat{h})^{\frac{3}{2}}\Theta(\hat{\mu} + \hat{h}) - (\hat{\mu} - \hat{h})^{\frac{3}{2}}\Theta(\hat{\mu} - \hat{h})\right]. \tag{116b}$$

Note that the normal state undergoes a transition with increasing h from a system with two Fermi surfaces with energies $\mu \pm h$ to a system that is fully polarized, with only one Fermi surface. Clearly, this happens at $\hat{h} = \hat{\mu}$, namely $\mu_\downarrow = 0$ in terms of the dimensionful variables. According to Eq. (116a), this implies the transition occurs at $\hat{h}_p = 2^{-1/3}$, which, when inserted into Eq. (116b) indeed yields $\Delta N = N$, i.e., a fully polarized state. This critical $\hat{h}_p$ is displayed in Fig. 9 as a horizontal dashed line inside the N phase.

5.2.2. BCS superfluid phase and the superfluid to normal transition

At large positive detuning, fermionic attraction is weak and any pairing leads to Δ that is exponentially small in $(\hat{\delta} - 2\hat{\mu})/\gamma$. We have already partially taken this into account, using the approximation Eq. (111) to obtain Eq. (112). Next, we proceed by using the conditions $\hat{\Delta} \ll \hat{\mu}$ and $h \ll \hat{\mu}$ to simplify $\hat{m}(\hat{h})$ in Eq. (108) and in the remaining integral in Eq. (112). This yields

$$\hat{m}(\hat{h}) \simeq 2\sqrt{\hat{\mu}}\sqrt{\hat{h}^2 - \hat{\Delta}^2}\Theta(\hat{h} - \hat{\Delta}), \tag{117}$$

and

$$e_{\rm G} \simeq -\frac{\sqrt{\hat{\mu}}}{2}\hat{\Delta}^2 + \hat{\Delta}^2(\hat{\delta}-2\hat{\mu})\gamma^{-1} + \sqrt{\hat{\mu}}\hat{\Delta}^2\ln\frac{\hat{\Delta}}{8e^{-2}\hat{\mu}} - \sqrt{\hat{\mu}}\left[\hat{h}\sqrt{\hat{h}^2-\hat{\Delta}^2} - \hat{\Delta}^2\cosh^{-1}(\hat{h}/\hat{\Delta})\right]\Theta(\hat{h}-\hat{\Delta}) - \frac{8}{15}\hat{\mu}^{5/2}, \tag{118}$$

that we have plotted as a function of $\hat{\Delta}$ for various $\hat{h}$'s in Fig. 12. To determine the stable ground state, we study minima of $e_{\rm G}$, given by the gap equation, $\partial e_{\rm G}/\partial\hat{\Delta} = 0$ Eq. (110a):

$$0 \simeq \gamma^{-1}\hat{\Delta}(\hat{\delta}-2\hat{\mu}) + \hat{\Delta}\sqrt{\hat{\mu}}\ln\frac{\hat{\Delta}}{8e^{-2}\hat{\mu}} + \hat{\Delta}\sqrt{\hat{\mu}}\cosh^{-1}(\hat{h}/\hat{\Delta})\Theta(\hat{h}-\hat{\Delta}). \tag{119}$$

The nature of possible solutions depends on the value of $\hat{h}$, as is clear from the evolution of $e_{\rm G}(\hat{\Delta},\hat{h})$ with a set of increasing $\hat{h}$ values at fixed chemical potential $\hat{\mu}$, illustrated in Fig. 12. For $\hat{h}$ sufficiently small, $0 < \hat{h} < \hat{\Delta}_{\rm BCS}/2$, the BCS logarithm [see Eq. (118)] dominates, leading to a single BCS minimum at $\hat{\Delta} \simeq \hat{\Delta}_{\rm BCS}$, with

$$\hat{\Delta}_{\rm BCS}(\hat{\delta},\hat{\mu}) \equiv 8e^{-2}\hat{\mu}e^{-\gamma^{-1}(\hat{\delta}-2\hat{\mu})/\sqrt{\hat{\mu}}}, \tag{120}$$

with the normal state characterized by an unstable maximum at $\hat{\Delta} = 0$, discussed in Section 5.2.1. The corresponding BCS ground state energy is given by [inserting Eq. (120) into Eq. (118)]

$$e_{\rm G,SF} \simeq -\frac{8}{15}\hat{\mu}^{5/2} - \frac{\sqrt{\hat{\mu}}}{2}\hat{\Delta}_{\rm BCS}^2, \tag{121}$$

with the terms multiplying $\Theta(\hat{h}-\hat{\Delta})$ dropping out and therefore not influencing the location and depth of the BCS minimum for $\hat{h} < \hat{\Delta}_{\rm BCS}$. This behavior persists until $\hat{h} = \hat{h}_{*1} = \hat{\Delta}_{\rm BCS}/2$ at which point the normal state extremum at $\hat{\Delta} = 0$ develops into a metastable *local* minimum, separated from the stable SF minimum at $\hat{\Delta}_{\rm BCS}$ by a maximum at [85]

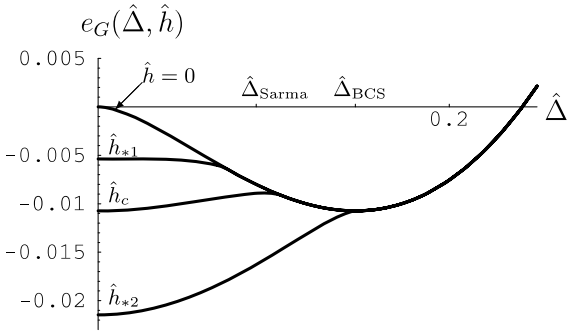

Fig. 12. Plot of $e_{\rm G}$ [Eq. (118), dropping the final $\hat{\Delta}$-independent constant] at $\hat{\mu} = 1$ as a function of $\hat{\Delta}$ for four values of $\hat{h}$ (labeled by $\hat{h}$): For $\hat{h} = 0$, no applied chemical potential difference, $e_G(\hat{\Delta})$ has a minimum at $\hat{\Delta} = \hat{\Delta}_{\rm BCS} \approx 0.15$, representing the fully paired BCS state. With increasing $\hat{h}$, for $\hat{h} = \hat{h}_{*1}$ a local minimum develops at $\hat{\Delta} = 0$ that becomes degenerate with the minimum at $\hat{\Delta}_{\rm BCS}$ for $\hat{h} = \hat{h}_c$. A local maximum is at $\hat{\Delta} = \hat{\Delta}_{\rm Sarma}$. For $\hat{h} > \hat{h}_{*2}$, the minimum at $\hat{\Delta}_{\rm BCS}$ disappears.

$$\hat{\Delta}_{\rm Sarma} \simeq \hat{\Delta}_{\rm BCS}\sqrt{\frac{2\hat{h}}{\hat{\Delta}_{\rm BCS}} - 1}, \quad \hat{h}_{*1} < \hat{h} < \hat{h}_{*2}, \tag{122}$$

where $\hat{h}_{*2} = \hat{\Delta}_{\rm BCS}$. Eq. (122) follows from Eq. (119) upon using $\cosh^{-1}x = \ln\sqrt{x^2-1} + x$ and Eq. (120). With a further increase in $\hat{h}$ the maximum at $\hat{\Delta}_{\rm Sarma}$ moves out towards the $\hat{h}$-independent BCS minimum, joining it at $\hat{h} = \hat{h}_{*2}$ as can be seen from Eq. (122), so that for $\hat{h} > \hat{h}_{*2}$ the only stationary point of $e_{\rm G}$ is at $\hat{\Delta} = 0$.

In contrast to a number of erroneous conclusions in the literature [47,67,45,121–123] (that identified $\Delta_{\rm Sarma}$ with a magnetized superfluid ground state by studying the gap equation without checking the corresponding energy), this maximum at $\Delta_{\rm Sarma}$, as first shown by Sarma [85], clearly does not correspond to any physical (stable) phase of an attractive Fermi gas.

The BCS ground state remains a global minimum for $0 < \hat{h} < \hat{h}_c(\hat{\mu})$. For $\hat{h} > \hat{h}_c(\hat{\mu})$, the energy $e_{\rm G,N}$ of the normal state $\hat{\Delta} = 0$ minimum drops below $e_{\rm G}(\hat{\Delta}_{\rm BCS})$. The fermion gas then undergoes a first-order transition to the normal ground state at the critical chemical potential difference $\hat{h}_c(\hat{\mu})$ given by equating the normal ground-state energy $e_{\rm G,N}$ Eq. (114a) with the exact [124] superfluid-state energy $e_{\rm G,SF}$,

$$e_{\rm G,SF} = \gamma^{-1}\hat{\Delta}^2(\hat{\delta} - 2\hat{\mu}) + \int_0^\infty {\rm d}x\sqrt{x}\left(x - \hat{\mu} - \sqrt{(x-\hat{\mu})^2 + \hat{\Delta}^2} + \frac{\hat{\Delta}^2}{2x}\right), \tag{123}$$

[obtained from Eq. (107) by setting $\hat{m} = 0$]. This yields

$$-\frac{4}{15}\left[(\hat{\mu}+\hat{h}_c)^{5/2}\Theta(\hat{\mu}+\hat{h}_c) + (\hat{\mu}-\hat{h}_c)^{5/2}\Theta(\hat{\mu}-\hat{h}_c)\right] \tag{124}$$

$$= \gamma^{-1}\hat{\Delta}_0^2(\hat{\delta} - 2\hat{\mu}) + \int_0^\infty {\rm d}x\sqrt{x}\left(x - \hat{\mu} - \sqrt{(x-\hat{\mu})^2 + \hat{\Delta}_0^2} + \frac{\hat{\Delta}_0^2}{2x}\right), \tag{125}$$

with the right-hand side evaluated at its minimum $\hat{\Delta} = \hat{\Delta}_0$ satisfying

$$0 = \left.\frac{\partial e_{\rm G,SF}}{\partial\hat{\Delta}}\right|_{\hat{\Delta}=\hat{\Delta}_0}, \tag{126}$$

$$= \frac{2}{\gamma}(\hat{\delta} - 2\hat{\mu}) + \int_0^\infty {\rm d}x\sqrt{x}\left(\frac{1}{x} - \frac{1}{\sqrt{(x-\hat{\mu})^2 + \hat{\Delta}_0^2}}\right), \tag{127}$$

where in the second line we canceled the $\hat{\Delta} = 0$ solution. Eqs. (124) and (127) then implicitly give $\hat{h}_c(\hat{\mu})$ [or, equivalently, $\hat{\mu}_c(\hat{h})$] that we will use shortly. In the limit of $\hat{\Delta}_0 \ll \hat{\mu}$ the right-hand side of Eq. (124) reduces to Eq. (121) with $\hat{\Delta}_0$ given by $\hat{\Delta}_{\rm BCS}$, yielding

$$\frac{4}{15}[(\hat{\mu}+\hat{h}_c)^{5/2} + (\hat{\mu}-\hat{h}_c)^{5/2}\Theta(\hat{\mu}-\hat{h}_c) - 2\hat{\mu}^{5/2}] \simeq \frac{1}{2}\sqrt{\hat{\mu}}\hat{\Delta}_{\rm BCS}^2$$
$$= 32{\rm e}^{-4}\hat{\mu}^{5/2}{\rm e}^{-2\gamma^{-1}(\hat{\delta}-2\hat{\mu})/\sqrt{\hat{\mu}}}. \tag{128}$$

Deep in the BCS regime ($\delta \gg 2\epsilon_{\rm F}$) the molecular condensate and the corresponding gap $\hat{\Delta}_{\rm BCS}$, given by Eq. (120) above, are exponentially small. We expect (and self-consistently find) that the critical Zeeman-field boundary $\hat{h}_c(\delta)$ tracks the gap $\hat{\Delta}_{\rm BCS}(\hat{\delta},\hat{\mu})$ and therefore must also be exponentially small in $(\hat{\delta} - 2\hat{\mu})/\gamma$.

As we will see below (when we consider the more experimentally-relevant ensemble of fixed atom number), the crossover regime $\delta < 2\epsilon_F$ corresponds to μ locking to a value slightly below $\delta/2$, with $\hat{\delta}/2 - \hat{\mu} \approx \mathcal{O}(\gamma \ln \gamma) \ll 1$. This is still sufficient to ensure that, in the crossover regime, the BCS estimate of $\hat{\Delta}_{BCS}(\hat{\mu}, \hat{\delta})$ and $e_{G,SF}$ remain valid [since $\hat{\Delta}_{BCS} \ll \hat{\mu}$ allowing the integral in Eq. (123) to be approximated by Eq. (111)], but with $\hat{\Delta}_{BCS}(\mu, \delta)/\hat{\mu} \approx \mathcal{O}(\gamma^{1/2})$ (rather than exponentially small in $1/\gamma$).

Consequently, in the BCS ($\hat{\delta} \gg 2\hat{\mu}$) and crossover [$\hat{\delta} - 2\hat{\mu} \approx \mathcal{O}(\gamma \ln \gamma)$] regimes the condition $\hat{h}_c \ll \hat{\mu}$ is well-satisfied. This allows an accurate approximation of the normal state energy $e_{G,N}$, Eq. (114a), and correspondingly the left-hand side of Eq. (128) by its lowest order Taylor expansion in $\hat{h}_c/\hat{\mu}$. This *linear* Pauli paramagnetic approximation then gives an accurate prediction for the critical Zeeman field

$$\hat{h}_c(\hat{\mu}) \simeq \hat{\Delta}_{BCS}/\sqrt{2}, \text{ for } \hat{h}_c \ll \hat{\mu}, \tag{129a}$$

$$\simeq 4\sqrt{2}e^{-2}\hat{\mu}e^{-\gamma^{-1}(\hat{\delta}-2\hat{\mu})/\sqrt{\hat{\mu}}}, \tag{129b}$$

that in the BCS regime self-consistently satisfies the condition $\hat{h}_c \ll \hat{\mu}$ used to obtain it.

For $\hat{\mu}$ close to $\hat{\delta}/2$, Eq. (124) is approximately [to $\mathcal{O}(\gamma)$] satisfied for *any* $\hat{h}$ since we can neglect the left-hand side and the second term on the right-hand side. This behavior is also reflected in the approximate formula (taken beyond its strict regime of validity) Eq. (129b) that exhibits rapid variation for $\hat{\mu}$ near $\hat{\delta}/2$. Thus, in this regime at the transition the critical $\hat{\mu}$ is approximately given by

$$\hat{\mu}_c(\hat{h}, \hat{\delta}) \approx \hat{\delta}/2. \tag{130}$$

Hence, below we will use Eq. (130) as an accurate (in $\gamma \ll 1$, narrow resonance limit) form for the high Zeeman field regime $\hat{h}_c(\hat{\mu}, \hat{\delta})$, where the BCS condition $\hat{\Delta} \ll \hat{\mu}$ is violated. This will be essential to determine the upper boundary $\hat{h}_{c2}(\hat{\delta})$ of the coexistence region in the crossover regime.

It is important to note that, because of the step functions in the ground-state energy Eq. (97), the curve of $e_G(\hat{\Delta}, \hat{h})$ is identically $\hat{h}$-independent for $\hat{\Delta} > \hat{h}$. Consequently the BCS minimum at $\hat{\Delta}_{BCS}$ (stable for $0 < \hat{h} < \hat{h}_c$) and the corresponding energy $e_G(\hat{\Delta}_{BCS})$ are strictly $\hat{h}$-independent, ensuring that the BCS state is indeed characterized by a vanishing magnetization,

$$m_{SF} = -\frac{\partial E_G}{\partial h} = 0, \tag{131}$$

and density given by

$$n_{SF} \simeq \frac{2\Delta^2}{g^2} + \frac{4c}{3}\mu^{3/2} + \frac{c\Delta^2}{\sqrt{\mu}}\left(\frac{5}{4} - \frac{1}{2}\ln\frac{\Delta}{8e^{-2}\mu}\right). \tag{132}$$

Since $\hat{h}$ only enters through a term multiplied by a step function, $\Theta(\hat{h} - \hat{\Delta})$, $\hat{h}$-independence of the stable minimum at $\hat{\Delta}_{BCS}$ persists until $\hat{h} = \hat{\Delta}_{BCS}$, beyond which the energy at this minimum *would* have become $\hat{h}$-dependent (resulting in a magnetized paired superfluid) had the minimum survived. However, as we saw above, the BCS minimum becomes unstable to the normal state for $\hat{h} \geqslant \hat{h}_c \simeq \hat{\Delta}_{BCS}/\sqrt{2}$, *before* the point of this magnetized-superfluid condition of $\hat{h} = \hat{\Delta}_{BCS}$ is reached.

As expected at a first-order transition with a tuned chemical potential (rather than tuned density), our system exhibits jumps in the density at $\hat{h}_c$. This occurs because the

densities of the superfluid and normal states at the transition $\hat{h}_c(\hat{\mu})$ [using Eq. (129a) and converting to dimensionful quantities]

$$n_{\rm SF} \simeq \frac{2\Delta_{\rm BCS}^2}{g^2} + \frac{4c}{3}\mu^{3/2} + \frac{c\Delta_{\rm BCS}^2}{\sqrt{\mu}}\left(\frac{5}{4} - \frac{1}{2}\ln\frac{\Delta_{\rm BCS}}{8e^{-2}\mu}\right), \tag{133}$$

$$n_{\rm N} \simeq \frac{4c}{3}\mu^{3/2} + \frac{c\Delta_{\rm BCS}^2}{4\sqrt{\mu}}, \tag{134}$$

are different. Thus, upon increasing $\hat{h}$ past $\hat{h}_c(\hat{\mu},\hat{\delta})$ there is a density discontinuity equal to

$$n_{\rm SF} - n_{\rm N} \simeq \frac{2\Delta_{\rm BCS}^2}{g^2} + \frac{c\Delta_{\rm BCS}^2}{\sqrt{\mu}}\left(1 - \frac{1}{2}\ln\frac{\Delta_{\rm BCS}}{8e^{-2}\mu}\right). \tag{135}$$

Similarly, since the BCS paired superfluid is characterized by a vanishing magnetization and the normal state by $m_{\rm N}$ given by Eq. (115b) there is a jump discontinuity in m equal to $m_{\rm N}$ evaluated at h_c.

5.3. First-order SF–N transition at fixed density: phase separation and coexistence

Because we are primarily interested in applications of the theory to degenerate trapped atomic-gas experiments, where it is the atom number N (rather than chemical potential μ) that is fixed (also it is $\Delta N = N_\uparrow - N_\downarrow$ rather than h that is imposed, but for pedagogical purposes we delay the analysis of this fixed ΔN ensemble until Section 5.5), in this section we study the above transition in the fixed *average* density $n = N/V$ and imposed h ensemble [125].

However, there is no guarantee that the system's true ground state corresponds to one of our assumed spatially homogeneous ground states. In fact, it is clear from the discussion at the end of the last subsection that the existence of the density discontinuity Eq. (135) at $h_c(\delta)$ implies that, at $h = h_c(\delta)$, a homogeneous atomic gas with density n anywhere in the range between $n_{\rm N}$ and $n_{\rm SF}$ is in fact unstable to phase separation. As we will see below, for densities in this range the ground state is an inhomogeneous coexistence of normal and superfluid phases at the critical chemical potential $\mu_c(h,\delta)$, with corresponding densities $n_{\rm N}(\mu_c(h,\delta),\delta)$, $n_{\rm SF}(\mu_c(h,\delta),\delta)$, appearing in fractions $1 - x(h,\delta,n)$ and $x(h,\delta,n)$, determined by the constraint that the *average* density is the imposed one (or equivalently the total number of atoms is N).

Thus, as illustrated in Fig. 13 (and the full phase diagram, Fig. 1), at fixed average density n, the critical Zeeman field $h_c(\delta)$ splits into lower- and upper-critical fields, $h_{c1}(\delta)$ and $h_{c2}(\delta)$, bounding the coexistence region from below and above, respectively. To understand how these emerge in detail, we imagine increasing the Zeeman field h (at fixed n and detuning δ within the BCS or crossover regimes) from low values starting from the singlet superfluid state as the global minimum. As h is increased, the chemical potential $\mu_{\rm SF}(n,\delta)$ (which, because the BCS superfluid is a singlet, is in fact h independent), determined by the superfluid equation of state (written in terms of dimensionless variables), satisfies

$$\frac{4}{3} = \frac{5\hat{\Delta}^2}{4\sqrt{\hat{\mu}_{\rm SF}}} + \frac{4}{3}\hat{\mu}_{\rm SF}^{3/2} + \frac{2\hat{\Delta}^2}{\gamma} - \frac{\hat{\Delta}^2}{2\sqrt{\hat{\mu}_{\rm SF}}}\ln\frac{\hat{\Delta}}{8e^{-2}\hat{\mu}_{\rm SF}}, \tag{136a}$$

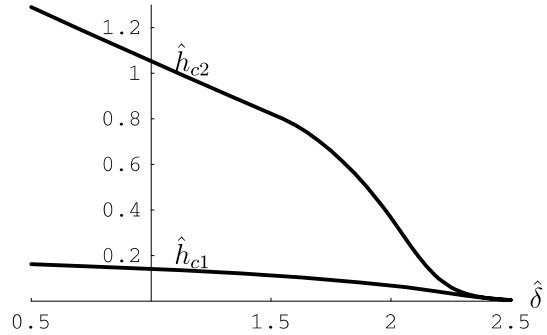

Fig. 13. Upper curve is $\hat{h}_{c2}$ [Eqs. (138a), (138b)] and lower curve is $\hat{h}_{c1}$ Eq. (136a), solved numerically, that bound the coexistence region in the BCS and crossover regimes.

to keep the density fixed at n. In this process, as $\hat{h}$ is increased, the ground-state energy function $e_{\rm G}(\hat{h},\hat{\mu},\hat{\delta})$ changes according to Eq. (107) with the relative level of the normal and superfluid minima changing (see Fig. 12). At a sufficiently large Zeeman field $\hat{h}_{c1}(\hat{\delta},n)$, given by

$$\hat{h}_{c1}=\hat{h}_c(\hat{\mu}_{\rm SF}), \tag{136b}$$

the two minima become degenerate. This would then naively imply that the system should jump to the normal ground state at these values of $\hat{\mu}=\hat{\mu}_{\rm SF}(n,\hat{\delta})$, h, and δ. However, as seen from Eqs. (133) and (134), since the normal ground state has a density that (at the same chemical potential μ) is distinct from that of the superfluid state, this discontinuous transition to the normal state would not keep the density fixed at the imposed value n.

The only solution to this dilemma (which is generic to first-order transitions) is for the system to get pinned at the coexistence curve $\hat{\mu}_c(\hat{h},\hat{\delta})$, Eq. (124), defined by equality of the normal-state and superfluid-state minima. A subsequent increase in $\hat{h}>\hat{h}_{c1}$ changes μ along the critical curve $\mu_c(h,\delta)$, keeping the normal and superfluid ground states degenerate. This, however, leads to a chemical potential $\hat{\mu}_c(\hat{h},\hat{\delta})$, illustrated in Fig. 14, that no longer allows the density of either of the pure ground states, N and SF to be equal to n. However, the total imposed atom number can still be satisfied by a mixture of coexisting SF and N states [39] in respective proportions $x(\hat{h},\hat{\delta})$ and $1-x(\hat{h},\hat{\delta})$, defined by

$$\frac{N}{V}=x(\hat{h},\hat{\delta})n_{\rm SF}(\hat{\mu}_c(\hat{h}),\hat{\delta}))+[1-x(\hat{h},\hat{\delta})]n_{\rm N}(\hat{h},\hat{\mu}_c(\hat{h})). \tag{137}$$

This evolution of the chemical potential according to $\hat{\mu}_c(\hat{h})$ continues until $\hat{h}$ has increased sufficiently, so that the number constraint equation can be satisfied by a pure normal state that minimizes $E_{\rm G}$. The corresponding value of the Zeeman field is precisely the upper-boundary of the coexistence region, with

$$\hat{h}_{c2}=\hat{h}_c(\hat{\mu}_{\rm N}), \tag{138a}$$

$$1=\frac{1}{2}\left[(\hat{\mu}_{\rm N}+\hat{h}_{c2})^{\frac{3}{2}}+(\hat{\mu}_{\rm N}-\hat{h}_{c2})^{\frac{3}{2}}\Theta(\hat{\mu}_{\rm N}-\hat{h}_{c2})\right], \tag{138b}$$

and $\hat{h}_c(\hat{\mu})$ given by Eq. (124) in the preceding subsection.

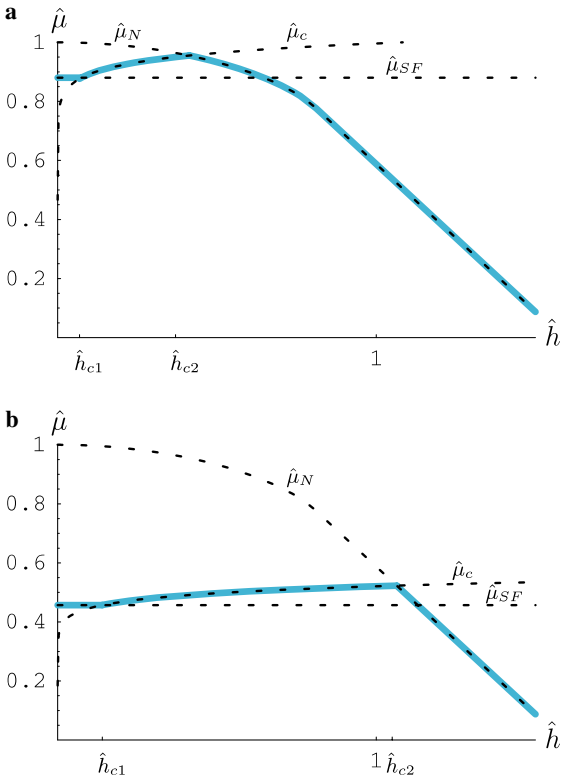

Fig. 14. Plots of the normalized chemical potential $\hat{\mu}(\hat{h},\hat{\delta})$ (solid blue line) as a function of the normalized chemical potential difference $\hat{h}$ at (a) high detuning $\hat{\delta}=2.0$ and (b) low detuning $\hat{\delta}=1.0$. For $\hat{h}<\hat{h}_{c1}$, the system is in the SF phase with $\hat{\mu}=\hat{\mu}_{\rm SF}$. For $\hat{h}_{c1}<\hat{h}<\hat{h}_{c2}$, the system is in the mixed phase, with $\hat{\mu}$ constrained to lie on the first-order critical boundary $\hat{\mu}=\hat{\mu}_c(\hat{h})$. For $\hat{h}_{c2}<\hat{h}$, the system is in the pure N phase, with $\hat{\mu}=\hat{\mu}_{\rm N}(\hat{h})$ [the solution to Eq. (116a)].

Hence, as is clear from the above discussion, the intersections of the $\hat{\mu}_c(\hat{h})$ curve with $\hat{\mu}_{\rm SF}(n,\hat{\delta})$ and $\hat{\mu}_{\rm N}(\hat{h},n)$ determine $\hat{h}_{c1}(n,\hat{\delta})$ and $\hat{h}_{c2}(n,\hat{\delta})$. The full evolution of the chemical potential with $\hat{h}$, from the SF state through the coexistence region and to the normal state for detuning in the BCS and crossover regimes, is illustrated in Fig. 14.

The two pairs of Eqs. (136a), (136b), (138a), (138b) for $\hat{h}_{c1}$ and $\hat{h}_{c2}$ can be straightforwardly solved numerically. We do this for the case of $\gamma=0.1$, with results illustrated in Fig. 13. In the next subsections, we obtain accurate analytic approximations for $\hat{h}_{c1}$ and $\hat{h}_{c2}$ in the BCS and crossover regimes.

5.3.1. h_{c1} and h_{c2} for the BCS limit $\delta \gg 2\epsilon_F$

As discussed in Section 5.2, at large $\hat{\delta}$ we will have $\hat{h}_{c1},\hat{h}_{c2}\ll\hat{\mu}$, allowing the use of Eqs. (129a), (129b) for $\hat{h}_c(\mu)$, valid in the linear-response (to $\hat{h}$) limit. Starting with $\hat{h}_{c1}$, for $\hat{\delta}\gg 2$ the normalized gap $\hat{\Delta}$ is exponentially small so that we may neglect the first term on the right side of Eq. (136a). The last term in Eq. (136a) may be simplified using the gap equation, yielding

$$\frac{4}{3} \approx \frac{4}{3}\hat{\mu}_{\rm SF}^{3/2} + \frac{2\hat{\Delta}^2}{\gamma} + \frac{\hat{\Delta}^2}{2\hat{\mu}_{\rm SF}\gamma}(\hat{\delta} - 2\hat{\mu}_{\rm SF}). \tag{139}$$

Solving Eq. (139) to leading order in small γ gives:

$$\hat{\mu}_{\rm SF} \approx 1 - \tfrac{1}{4}(\hat{\delta}+2)\hat{\Delta}^2\gamma^{-1}. \tag{140}$$

It is convenient to define the BCS gap Eq. (120) at $\hat{\mu}_{\rm SF} = 1$:

$$\hat{\Delta}_{\rm F}[\gamma,\hat{\delta}] \equiv 8e^{-2}e^{-\gamma^{-1}(\hat{\delta}-2)}. \tag{141}$$

With this definition, to leading order it is valid to replace $\hat{\Delta}^2$ on the right side of Eq. (140) with $\hat{\Delta}_{\rm F}^2$. Taking advantage of $\hat{\mu}_{\rm SF} \approx 1$, we Taylor expand $\hat{\Delta}$ in small $\hat{\mu}_{\rm SF} - 1$:

$$\hat{\Delta}[\gamma,\hat{\delta},\hat{\mu}_{\rm SF}] \simeq \hat{\Delta}_{\rm F}[\gamma,\hat{\delta}] + (\hat{\mu}_{\rm SF} - 1)\hat{\Delta}'[\gamma,\hat{\delta},1], \tag{142}$$

where

$$\hat{\Delta}'[\gamma,\hat{\delta},1] = 8e^{-2}e^{-\gamma^{-1}(\hat{\delta}-2)}\left(\frac{\hat{\delta}}{2\gamma} + \frac{1}{\gamma} + 1\right), \tag{143a}$$

$$\simeq 4e^{-2}\gamma^{-1}(\hat{\delta}+2)e^{-\gamma^{-1}(\hat{\delta}-2)}, \tag{143b}$$

$$\simeq \tfrac{1}{2}\gamma^{-1}(\hat{\delta}+2)\hat{\Delta}_{\rm F}[\gamma,\hat{\delta}], \tag{143c}$$

with the prime denoting differentiation with respect to $\hat{\mu}$. Using Eq. (142) along with Eq. (143c) and Eqs. (140), (136b) becomes

$$\hat{h}_{c1} \approx \frac{\hat{\Delta}[\gamma,\hat{\delta},\hat{\mu}_{\rm SF}]}{\sqrt{2}}, \tag{144a}$$

$$\approx \frac{1}{\sqrt{2}}\left[\hat{\Delta}_{\rm F} - \frac{\gamma^{-2}}{8}(\hat{\delta}+2)^2\hat{\Delta}_{\rm F}^3\right], \tag{144b}$$

$$\approx \frac{1}{\sqrt{2}}\hat{\Delta}_{\rm F}[\gamma,\hat{\delta}]\exp\left[-\frac{\hat{\delta}^2}{8\gamma^2}\hat{\Delta}_{\rm F}^2\right], \tag{144c}$$

where in the final result we have taken $\hat{\delta} \gg 2$ and re-exponentiated the second factor, valid since $\hat{\Delta}_{\rm F}$ is exponentially small for $\gamma \ll 1$. In the asymptotic large $\hat{\delta}$ limit, $\hat{h}_{c1}$ thus decays exponentially with $\hat{\delta}$, as seen in Fig. 13.

Similarly, $\hat{h}_{c2}$ can be obtained by solving Eqs. (138a), (138b) iteratively utilizing the fact that, in the large-$\hat{\delta}$ limit, $\hat{h}_{c2}$ is exponentially small while $\hat{\mu}_{\rm N} \approx 1$. Thus, in Eq. (138b) we can expand in $\hat{h}_{c2}/\hat{\mu}_{\rm N} \ll 1$, yielding

$$1 \approx \hat{\mu}_{\rm N}^{3/2} + \frac{3\hat{h}_{c2}^2}{8\sqrt{\hat{\mu}_{\rm N}}}, \tag{145}$$

which has the zeroth order solution $\hat{\mu}_{\rm N} \approx 1$; at this order Eq. (138a) yields $\hat{h}_{c2} \approx \hat{\Delta}_{\rm F}/\sqrt{2}$. Inserting the latter expression into Eq. (145) yields a leading-order correction to $\hat{\mu}_{\rm N}$:

$$\hat{\mu}_{\rm N} \approx 1 - \tfrac{1}{4}\hat{h}_{c2}^2 \approx 1 - \tfrac{1}{8}\hat{\Delta}_{\rm F}^2. \tag{146}$$

Using this inside Eq. (138a) together with the expansion Eq. (142) (but with $\hat{\mu}_N$ instead of $\hat{\mu}_{SF}$) our final leading-order result for $\hat{h}_{c2}$ is:

$$\hat{h}_{c2} \approx \frac{1}{\sqrt{2}}\left[\hat{\Delta}_F - \frac{1}{16\gamma}(\hat{\delta}+2)\hat{\Delta}_F^3\right], \tag{147a}$$

$$\approx \frac{1}{\sqrt{2}}\hat{\delta}_F[\gamma,\hat{\delta}]\exp\left[-\frac{\hat{\delta}}{16\gamma}\hat{\Delta}_F^2\right], \tag{147b}$$

that decays exponentially with increasing $\hat{\delta}$ as exhibited in Fig. 13. Note that, since $\hat{\delta}^2/8\gamma^2 \gg \hat{\delta}/16\gamma$ for large $\hat{\delta}$, $\hat{h}_{c2} > \hat{h}_{c1}$ in the large detuning limit, i.e., the curves in Fig. 13 never cross.

5.3.2. h_{c1} and h_{c2} for the crossover limit $0 < \delta < 2\epsilon_F$

We now compute $\hat{h}_{c1}(\hat{\delta})$ and $\hat{h}_{c2}(\hat{\delta})$ at small $\hat{\delta}$. To obtain $\hat{h}_{c1}$, we first note that at large detuning in the SF state at $\hat{h}=0$, the full gap and number equations are obtained from Eqs. (110a) and (110b) with Eq. (112) for e_G [see also Eqs. (C.12b) and (C.12d)]:

$$0 \simeq 2\hat{\Delta}(\hat{\delta}-2\hat{\mu})\gamma^{-1} + \sqrt{\hat{\mu}}\hat{\Delta}\ln\frac{\hat{\Delta}}{8e^{-2}\hat{\mu}}, \tag{148a}$$

$$\frac{4}{3} \simeq \frac{5}{4}\frac{\hat{\Delta}^2}{\sqrt{\hat{\mu}}} + \frac{4}{3}\hat{\mu}^{3/2} + \frac{2\hat{\Delta}^2}{\gamma} - \frac{\hat{\Delta}^2}{2\sqrt{\hat{\mu}}}\ln\frac{\hat{\Delta}}{8e^{-2}\hat{\mu}}. \tag{148b}$$

As $\hat{\delta}$ is reduced below *2*, the system undergoes a crossover from the BCS regime (where $\hat{\mu}$ is pinned near unity) to the BEC regime where $\hat{\Delta}$ is no longer exponentially small (although we still have $\hat{\Delta} \ll 1$) and $\hat{\mu}$ begins to track $\hat{\delta}/2$, as atoms pair up into Bose-condensed molecules (see Fig. C.1). How is this reflected in Eqs. (148a), (148b)? As $\hat{\delta}$ drops below *2*, $\hat{\Delta}$ grows such that $\hat{\Delta}/\hat{\mu}$ becomes $\mathcal{O}(\gamma^{1/2})$, so that we may neglect the final $\hat{\Delta}\ln\hat{\Delta}/\hat{\mu}$ term on the right side of Eqs. (148a), (148b). Taking $\gamma \ll 1$ in Eq. (148b) (so that the term $5\hat{\Delta}^2/4\sqrt{\hat{\mu}}$ may be neglected) thus yields the following approximate solutions to Eqs. (148a), (148b):

$$\hat{\mu} \approx \hat{\delta}/2, \tag{149a}$$

$$\hat{\Delta} \approx \sqrt{\frac{2\gamma}{3}}\sqrt{1-(\hat{\delta}/2)^{3/2}}. \tag{149b}$$

Note that the role of the equations has been reversed, with the gap equation fixing $\hat{\mu}$ to be close to $\hat{\delta}/2$ [to $\mathcal{O}(\gamma\ln\gamma)$], and the number equation fixing $\hat{\Delta}$; we shall also see such behavior in the asymptotic BEC regime at negative detuning. Using Eq. (149b) inside Eq. (129a) [still using the $\hat{h}_c \ll \hat{\mu}$ expression since, as we shall verify a posteriori, $\hat{h}_{c1}$ remains small in this regime], we find for $\hat{h}_{c1} = \hat{h}_c(\hat{\mu}_{SF})$:

$$\hat{h}_{c1} \approx \sqrt{\frac{\gamma}{3}}\sqrt{1-(\hat{\delta}/2)^{3/2}}. \tag{150}$$

Next, we compute $\hat{h}_{c2}$ in the crossover regime. As in the preceding subsection, $\hat{h}_{c2}$ is determined by combining the solution to the gap equation at low detunings ($\delta \simeq 2\mu$, which approximately solves the equation for $\hat{h}_c$ at low detunings, as discussed in Section 5.2.2) with the normal-state chemical potential $\hat{\mu}_N$, given by Eq. (138b). We shall denote the solution to this equation as $\hat{h}^{(N)}(\hat{\mu})$, defined by

$$1 = \frac{1}{2}\left([\hat{\mu} + \hat{h}^{(N)}(\hat{\mu})]^{3/2} + [\hat{\mu} - \hat{h}^{(N)}(\hat{\mu})]^{3/2}\Theta[\hat{\mu} - h^{(N)}(\hat{\mu})]\right). \tag{151}$$

Although Eq. (151) cannot be solved analytically for arbitrary $\hat{\mu}$, we *can* find solutions for $\hat{\mu} < \hat{h}$ [so that the second term on the right side of Eq. (151) vanishes] and in the limit $\hat{\mu} \gg \hat{h}$:

$$\hat{h}^{(N)}(\hat{\mu}) = 2^{2/3} - \hat{\mu} \quad \text{for } \hat{\mu} < 2^{-1/3}, \tag{152}$$

$$\approx \sqrt{\frac{8}{3}}\sqrt{1 - \hat{\mu}^{3/2}} \quad \text{for } \hat{\mu} \to 1. \tag{153}$$

Having defined $\hat{h}^{(N)}(\hat{\mu})$, it is straightforward to combine it with the approximate solution $\hat{\mu}_c \approx \hat{\delta}/2$ Eq. (130) to obtain $\hat{h}_{c2}(\hat{\delta})$:

$$\hat{h}_{c2} \approx \hat{h}^{(N)}(\hat{\delta}/2). \tag{154}$$

For low detunings ($\hat{\delta} < \hat{\delta}_p \approx 2^{2/3} \approx 1.59$), we can use Eq. (152) for $\hat{h}^{(N)}$, giving our final low-detuning result for $\hat{h}_{c2}$:

$$\hat{h}_{c2} \approx 2^{2/3} - \frac{\hat{\delta}}{2}, \tag{155}$$

a linear-in-$\hat{\delta}$ behavior that is clearly seen in the numerically-determined curve shown in Fig. 13.

5.4. Mixed state in the BCS regime

5.4.1. Phase fractions

We have argued in the preceding section that, for $\hat{h}_{c1}(\hat{\delta}) < \hat{h} < \hat{h}_{c2}(\hat{\delta})$ (the region between the two curves in Fig. 13), and neglecting the possibility of the FFLO state, our system is a mixed state in which the N and SF ground states coexist in $1 - x(\hat{\delta}, \hat{h})$ and $x(\hat{\delta}, \hat{h})$ fractions, respectively. To show this directly, here we study the properties of this phase-separated coexistence state by computing its energy and determining the optimum fractions of SF and N. [39] We note that our analysis from the start ignores the interfacial energy [73] between the two coexisting (N and SF) phases. For a macroscopic phase separation, this energy contribution is subdominant in the thermodynamic limit. However, ignoring it precludes us from determining the spatial SF–N profile in this regime. In the SF regions, $\hat{\Delta}$ is given by Eq. (120), with the chemical potential given by $\hat{\mu}_c(\hat{h}, \hat{\delta})$, Eq. (124) [inverting $\hat{h}_c(\hat{\mu}, \hat{\delta})$]. The energy of the mixed system in the canonical ensemble (appropriate for fixed density) is (normalized to $c\epsilon_F^{5/2}$)

$$e_{\mathrm{G,N+SF}} = -\left(\sqrt{\hat{\mu}}\frac{\hat{\Delta}^2}{2} + \frac{8}{15}\hat{\mu}^{5/2}\right)x - \left(\sqrt{\hat{\mu}}\hat{h}^2 + \frac{8}{15}\hat{\mu}^{5/2}\right)(1 - x) + \frac{4}{3}\hat{\mu}, \tag{156}$$

where in the second term we used Eq. (114b) for the normal-state contribution to the energy, valid since $\hat{\Delta} \ll 1$ on the BCS side. The final term comes from switching from the grand-canonical to the canonical ensemble (recall that in our notation the total *normalized* density is 4/3).

The total density of atoms is similarly constructed from contributions from the normal and paired regions

$$\frac{4}{3} = x\left(\frac{5}{4}\frac{\hat{\Delta}^2}{\sqrt{\hat{\mu}}} + \frac{4}{3}\hat{\mu}^{3/2} + 2\gamma^{-1}\hat{\Delta}^2\right) + (1-x)\left(\frac{4}{3}\hat{\mu}^{3/2} + \frac{\hat{h}^2}{2\sqrt{\hat{\mu}}}\right). \tag{157}$$

In the BCS regime, $\hat{\Delta} \ll \hat{\mu}$, so that we may neglect the term proportional to $\hat{\Delta}^2/\sqrt{\hat{\mu}}$ on the right side of Eq. (157). The remaining terms may be approximately solved for $\hat{\mu}$, yielding

$$\hat{\mu} \simeq 1 - \gamma^{-1}\hat{\Delta}^2 x - \frac{\hat{h}^2}{4}(1-x). \tag{158}$$

To determine the properties of the mixed state we look for $x(\hat{\delta}, \hat{h})$ that minimizes $e_{\mathrm{G,N+SF}}(x)$, Eq. (156), using the numerically-determined simultaneous solution to Eq. (158) and Eq. (120) for $\hat{\Delta}$ and $\hat{\mu}$. In the absence of a mixed state, the optimum x would jump discontinuously from $x = 1$ to $x = 0$ as $\hat{h}$ is increased. The existence of a solution where the optimum $0 < x(\hat{\delta}, \hat{h}) < 1$ therefore indicates a stable phase-separated state.

Defining them to be the endpoints of the region where x is greater than zero or less than unity (indicating a mixed state) yields an alternate procedure for finding $\hat{h}_{c1}(\hat{\delta})$ and $\hat{h}_{c2}(\hat{\delta})$ as given in Eqs. (136a) and (138a), (138b). The two methods of determining $\hat{h}_{c1}(\hat{\delta})$ and $\hat{h}_{c2}(\hat{\delta})$ are displayed in Fig. 15, showing excellent agreement.

5.4.2. Atom density

Another way to characterize the regime of phase separation is to study the total atom density n as a function of chemical potential and verify that, in the mixed regime $\hat{h}_{c1} < h < \hat{h}_{c2}$, it is impossible to adjust $\hat{\mu}$ to attain the imposed density by either of the *pure* SF or N phases. The normalized SF-state density $\hat{n} = n/c\epsilon_{\mathrm{F}}^{3/2}$ is given by [cf. Eq. (132)]

$$\hat{n}_{\mathrm{SF}}[\gamma, \hat{\delta}, \hat{\mu}, \hat{\Delta}] = \frac{5}{4}\frac{\hat{\Delta}^2}{\sqrt{\hat{\mu}}} + \frac{4}{3}\hat{\mu}^{3/2} + 2\gamma^{-1}\hat{\Delta}^2 - \frac{\hat{\Delta}^2}{2\sqrt{\hat{\mu}}}\ln\frac{\hat{\Delta}}{8\mathrm{e}^{-2}\hat{\mu}}, \tag{159}$$

with $\hat{\Delta}[\gamma, \hat{\delta}, \hat{\mu}]$ given by Eq. (120). In the N state, the normalized density is [cf. Eq. (115a)]

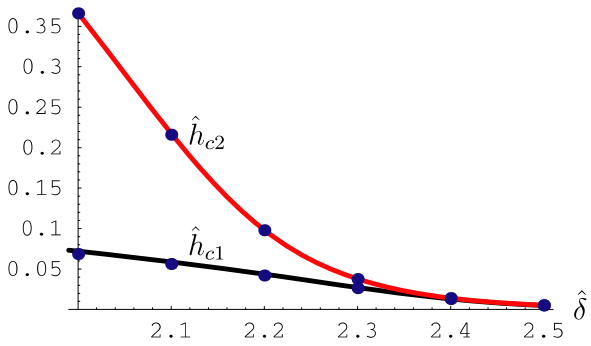

Fig. 15. Upper (red) curve is $\hat{h}_{c2}$ [Eqs. (138a), (138b)] and lower (black) curve is $\hat{h}_{c1}$ Eq. (136a). For comparison, the solid points on each curve are the same curves computed using the method described in Section 5.4.1. (For interpretation of the references to color in this figure legend, the reader is referred to the web version of this paper.)

$$\hat{n}_{\rm N}[\hat{h},\hat{\mu}] = \frac{2}{3}\left[(\hat{\mu}+\hat{h})^{3/2} + (\hat{\mu}-\hat{h})^{3/2}\Theta(\hat{\mu}-\hat{h})\right], \tag{160}$$

$$\simeq \frac{4}{3}\hat{\mu}^{3/2} + \frac{\hat{h}^2}{2\sqrt{\hat{\mu}}}. \tag{161}$$

Using these expressions we have

$$\hat{n}[\hat{h},\hat{\mu}] = \hat{n}_{\rm N}[\hat{h},\hat{\mu}]\Theta[\hat{\mu}_c(\hat{h})-\hat{\mu}] + \hat{n}_{\rm SF}[\gamma,\hat{\delta},\hat{\mu},\hat{\delta}]\Theta[\hat{\mu}-\hat{\mu}_c(\hat{h})], \tag{162}$$

where $\hat{\mu}_c(\hat{h})$ is implicitly defined as the solution of $\hat{h}_c(\hat{\mu}_c,\hat{\delta}) = \hat{h}$, with $\hat{h}_c(\hat{\mu})$ given by Eq. (124). In the simplest BCS regime $\hat{\mu}_c(\hat{h})$ satisfies

$$\hat{h} \simeq 4\sqrt{2}e^{-2}\hat{\mu}_c e^{-\gamma^{-1}(\hat{\delta}-2\hat{\mu}_c)/\sqrt{\hat{\mu}_c}}. \tag{163}$$

In Fig. 16, we plot $\hat{n}$ vs. $\hat{\mu}$ for $\hat{h} = .06$ with parameter values $\gamma = 0.1$ and $\hat{\delta} = 2.0$. At these values of the parameters, $\hat{h}_{c1} \approx 0.068$ at the physical density, thus, we expect the SF state to be stable. This is reflected in Fig. 16 in the fact that the $\hat{n}(\hat{\mu})$ curve intersects the physical density $\hat{n} = 4/3$ (horizontal dashed red line) for $\hat{\mu} > \hat{\mu}_c$.

With increasing $\hat{h}$, the discontinuity in $\hat{n}$ moves to higher values of $\hat{\mu}$. The regime of phase separation occurs when the physical density $\hat{n} = 4/3$ intersects this discontinuity, as shown in Fig. 17 for $\hat{h} = 0.13$, which satisfies $\hat{h}_{c1} < \hat{h} < \hat{h}_{c2} \approx 0.37$ (all other parameters being the same). Thus, we see that at this $\hat{h}$, no value of $\hat{\mu}$ yields $\hat{n} = 4/3$. At the critical $\hat{\mu}$ (where there is a discontinuity in $\hat{n}(\hat{\mu})$), $\hat{\mu}_c \approx 0.919$, there are two possible homogeneous values of $\hat{n}$, that can be read off Fig. 17 or determined from Eqs. (159) and (161) [using Eq. (120) for $\hat{\Delta}$]. These are $\hat{n}_{\rm N} \approx 1.18$ in the N state and $\hat{n}_{\rm SF} \approx 1.92$ in the SF state. Using these values allows us to determine the fractions x and $1-x$ of the system that are in the SF and N phases, respectively, using

$$\frac{4}{3} = x\hat{n}_{\rm SF} + (1-x)\hat{n}_{\rm N}, \tag{164}$$

which yields $x \approx 0.20$, i.e., most of the system is in the N phase.

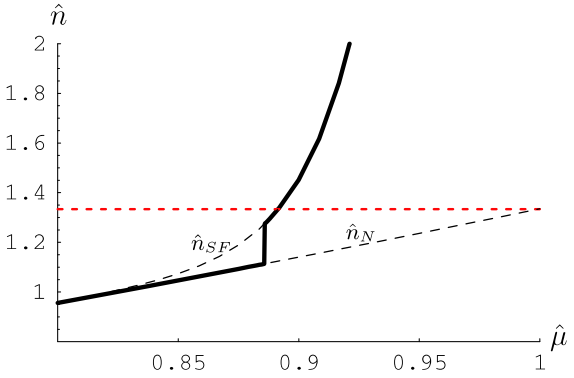

Fig. 16. Plot of the normalized density $\hat{n}$ [solid line, Eq. (162)] vs. $\hat{\mu}$ for $\hat{h} = .06$ with parameters $\hat{\delta} = 2$ and $\gamma = 0.1$. Thin dashed lines denote $\hat{n}_{\rm SF}$ and $\hat{n}_{\rm N}$. Since the imposed physical atom density ($\hat{n} = 4/3$, horizontal dashed red line) is intersected by the solid curve for $\hat{\mu}$ above the critical $\hat{\mu}$ (at which $\hat{n}$ is discontinuous), the system is in the SF state.

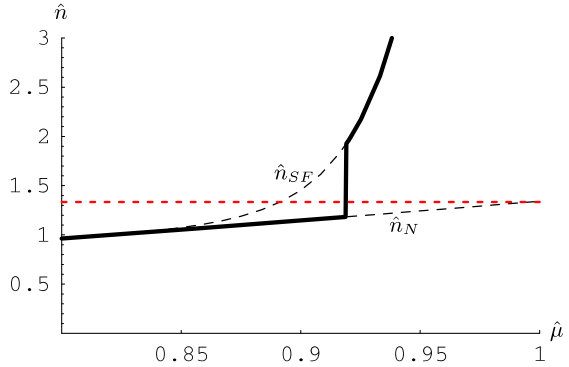

Fig. 17. Same as Fig. 16 but with $\hat{h} = 0.13$ raised into the regime of phase separation. At this $\hat{h}$, neither the SF nor the N yields the imposed density $\hat{n} = 4/3$, as illustrated by $\hat{n} = 4/3$ falling into the discontinuous region of coexistence.

With further increasing $\hat{h}$, the SF fraction decreases continuously until, above $\hat{h}_{c2}$ (when the vertical segment representing the mixed phase moves higher than $\hat{n} = 4/3$), the system enters the pure N phase. This is depicted in Fig. 18, which, for $\hat{h} = 0.40$, is slightly above $\hat{h}_{c2} \approx 0.37$. In Fig. 18 we did not display the entire vertical range of the discontinuity in $\hat{n}$, because at such large $\hat{h}$ for the system to be in the SF state requires a very large $\hat{\Delta}$, that, by virtue of the term $\hat{\Delta}^2/\gamma$ in Eq. (159), translates into a very large jump in $\hat{n}$ (for this case, to $\hat{n} \approx 8.2$) that is off the scale of Fig. 18.

5.5. Fixed population difference in the BCS and crossover regimes

Having characterized the regime of phase separation bounded by the critical curves $\hat{h}_{c1}(\hat{\delta})$ and $\hat{h}_{c2}(\hat{\delta})$ at fixed density, we next convert these boundaries to critical population differences $\Delta N_{c1}(\hat{\delta})$ and $\Delta N_{c2}(\hat{\delta})$, first focusing on the positive detuning (BCS and crossover) side of Fig. 3. In fact, since at $\hat{h}_{c1}(\hat{\delta})$ the system undergoes a first-order transition from the unmagnetized SF phase to the regime of phase separation, $\Delta N_{c1} = 0$ in the BCS regime.

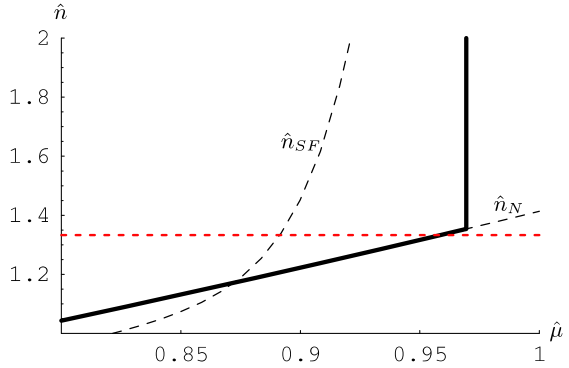

Fig. 18. Same as Figs. 16 and 17, but with $\hat{h} = 0.40 > \hat{h}_{c2}$, so that the normal state is stable.

Thus, the singlet BCS–BEC superfluid phase is confined to the $\Delta N/N = 0$ axis, and on the BCS side of the resonance an arbitrarily small population difference puts the system in the mixed state (although for a very small population imbalance the fraction of the system in the SF state will be close to unity). With increasing population difference, eventually the SF fraction disappears and the system enters the N phase at ΔN_{c2}. To compute ΔN_{c2} merely requires us to combine our result for $\hat{h}_{c2}(\hat{\delta})$ Eqs. (138a), and (138b) with the expression for $\Delta N(\hat{h})$ in the normal state, i.e., Eq. (116b), that gives

$$\frac{\Delta N_{c2}}{N} = \tfrac{1}{2}[(\hat{\mu}_{\rm N} + \hat{h}_{c2})^{3/2} - (\hat{\mu}_{\rm N} - \hat{h}_{c2})^{3/2}\Theta(\hat{\mu}_{\rm N} - \hat{h}_{c2})], \tag{165}$$

with $\hat{\mu}_{\rm N}$ given by Eq. (116a). Along with Eqs. (138a), (138b), (165) provides an accurate determination (see Fig. 19) of $\Delta N_{c2}(\hat{\delta})$ on the BCS side of the resonance [with accuracy only limited by the approximations used in computing Eq. (138a)]. We now determine explicit (but approximate) analytic expressions for $\Delta N_{c2}/N$ in the large and small $\hat{\delta}$ limits.

5.5.1. $\frac{\Delta N_{c2}(\hat{\delta})}{N}$ in the BCS regime of $\hat{\delta} \gg 2$

For large $\hat{\delta}$, $\hat{h}_{c2}(\hat{\delta})$ is exponentially small according to Eq. (147b) while $\hat{\mu}_{\rm N} \approx 1$ according to Eq. (146). Thus, in this limit we can expand Eq. (165) in small $\hat{h}_{c2}/\hat{\mu}_{\rm N}$, finding:

$$\frac{\Delta N_{c2}}{N} \approx \frac{3}{2}\sqrt{\hat{\mu}_{\rm N}}\hat{h}_{c2}, \tag{166}$$

with the linear dependence on $\hat{h}_{c2}$ simply reflecting the Pauli paramagnetism [117] of the N phase at small h. Inserting Eqs. (146) and (147a) into Eq. (166) (and taking $\hat{\delta} \gg 2$ in the latter), we find

$$\frac{\Delta N_{c2}}{N} \approx \frac{3\hat{\Delta}_{\rm F}}{2\sqrt{2}}\left(1 - \frac{1}{6}\hat{\Delta}_{\rm F}^2\right)\left(1 - \frac{\hat{\delta}}{16\gamma}\hat{\Delta}_{\rm F}^2\right), \tag{167a}$$

$$\approx \frac{3\hat{\Delta}_{\rm F}}{2\sqrt{2}}\exp\left[-\frac{\hat{\delta}}{16\gamma}\hat{\Delta}_{\rm F}^2\right], \tag{167b}$$

where in the final result we kept only leading-order terms in Eq. (167a) (i.e., we took $\hat{\delta}/\gamma \gg 1$) and re-exponentiated the last factor.

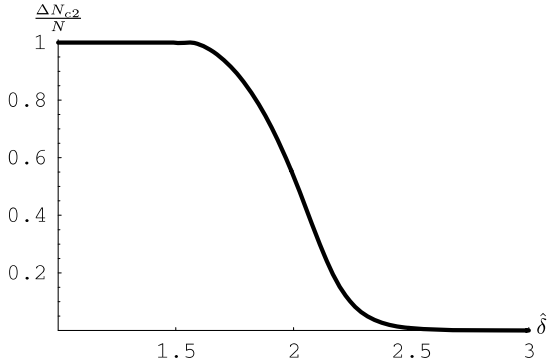

Fig. 19. Plot of the upper-critical polarization $\frac{\Delta N_{c2}}{N}$ as a function of detuning $\hat{\delta}$ for $\gamma = 0.1$, determined by Eq. (165) along with the numerical solution to Eqs. (138a), (138b).

5.5.2. $\frac{\Delta N_{c2}(\hat{\delta})}{N}$ in the crossover regime of $0 < \hat{\delta} < 2$

Next, we turn to intermediate detuning in the crossover regime. We recall from Section 5.3.1 that, at low $\hat{\delta}$, $\hat{h}_{c2}$ is approximately given by solving the number equation (138b) along with the approximate result $\hat{\mu}_N \approx \hat{\delta}/2$ valid in this regime. With $\hat{h}_{c2}(\hat{\delta})$ determined by the number equation

$$1 = \frac{1}{2}\left[\left(\frac{\hat{\delta}}{2} + \hat{h}_{c2}\right)^{\frac{3}{2}} + \left(\frac{\hat{\delta}}{2} - \hat{h}_{c2}\right)^{\frac{3}{2}} \Theta\left(\frac{\hat{\delta}}{2} - \hat{h}_{c2}\right)\right], \tag{168}$$

the upper-critical polarization is given by

$$\frac{\Delta N_{c2}}{N} = \frac{1}{2}\left[\left(\frac{\hat{\delta}}{2} + \hat{h}_{c2}\right)^{\frac{3}{2}} - \left(\frac{\hat{\delta}}{2} - \hat{h}_{c2}\right)^{\frac{3}{2}} \Theta\left(\frac{\hat{\delta}}{2} - \hat{h}_{c2}\right)\right]. \tag{169}$$

Physically, Eq. (168) encodes the instability of the polarized Fermi gas to a molecular superfluid as the point ($\hat{h}_{c2}$ and the corresponding ΔN_{c2}) at which the N and SF chemical potentials are equal to $\hat{\mu}_c \approx \hat{\delta}/2$, Eq. (130). This leads to Eqs. (168), and (169) translates $\hat{h}_{c2}$ to $\Delta N_{c2}/N$, determined by the polarizability of the N state.

We proceed by solving Eq. (168) for $\hat{h}_{c2}$ and using the result inside Eq. (169) to obtain the critical polarization. In the case where $\hat{h}_{c2} > \hat{\delta}/2$, this is particularly simple, as the second step function in Eq. (168) vanishes (as we found already in Section 5.3.1), giving Eq. (155) for $\hat{h}_{c2}$. Using this inside Eq. (169) yields

$$\frac{\Delta N_{c2}}{N} = 1, \quad \hat{\delta} < \hat{\delta}_p \simeq 2^{2/3}. \tag{170}$$

Thus, at such low detunings $\delta < \delta_p$, the normal state is only stable at full (100%) polarization. To understand this in more detail consider starting at large h in a fully-polarized (spin-$\uparrow$) normal state with $\Delta N = N$ ($m = n$) and $\mu_\downarrow = \mu - h < 0$. As h and ΔN are reduced one of two scenarios is possible depending on the value of the detuning δ: (1) For large $\delta > \delta_p$, upon lowering h, $\mu_\downarrow$ becomes positive first, converting spin-$\uparrow$ atoms to spin-$\downarrow$, partially depolarizing the Fermi sea. (2) For low $\delta < \delta_p$, case (1) is preempted by μ_N exceeding $\mu_c \simeq \delta/2$ causing the system to undergo a first-order transition to the SF state.

We have denoted by δ_p the critical detuning below which $\Delta N_{c2}(\delta) = N$. It is given by the solution of $\hat{h}_{c2}(\hat{\delta}_p) = \hat{h}_p = 2^{-1/3}$ [the intersection of the horizontal dashed line in Fig. 9 with $h_{c2}(\delta)$], giving

$$\hat{\delta}_p \simeq 2^{2/3}. \tag{171}$$

As $\hat{\delta}$ is increased above $\hat{\delta}_p$, $\Delta N_{c2}/N$ drops continuously below unity, before starting to decrease exponentially according to our large $\hat{\delta}$ prediction Eq. (167b). To calculate $\Delta N_{c2}(\hat{\delta})$ in the vicinity of $\hat{\delta}_p$, we take $\hat{h}_{c2}$ to be close to its value for $\hat{\delta} < 2^{2/3}$:

$$\hat{h}_{c2} = 2^{2/3} - \frac{\hat{\delta}}{2} - \epsilon. \tag{172}$$

with ϵ small. Inserting Eq. (172) into Eq. (168) and expanding to leading order in ϵ yields

$$1 \approx 1 - \frac{3}{2}\frac{\epsilon}{2^{2/3}} + \frac{1}{2}(\hat{\delta} - 2^{2/3})^{3/2}\left(1 + \frac{3}{2}\frac{\epsilon}{\hat{\delta} - 2^{2/3}}\right), \tag{173}$$

which can be easily solved for ϵ and inserted into Eq. (172) to find $\hat{h}_{c2}(\hat{\delta})$:

$$\hat{h}_{c2} \approx 2^{2/3} - \frac{\hat{\delta}}{2} - \frac{2^{2/3}}{3}(\hat{\delta} - 2^{2/3})^{3/2}, \quad \hat{\delta} > 2^{2/3} \tag{174}$$

Inserting Eq. (174) into Eq. (169) and again expanding in small deviation $\hat{\delta} - 2^{2/3}$, we find

$$\frac{\Delta N_{c2}}{N} \simeq 1 - (\hat{\delta} - 2^{2/3})^{3/2}\Theta(\hat{\delta} - 2^{2/3}), \tag{175}$$

$$\simeq 1 - (\hat{\delta} - \hat{\delta}_p)^{3/2}\Theta(\hat{\delta} - \hat{\delta}_p), \tag{176}$$

where we added a step function to emphasize that the second term is only nonzero for $\hat{\delta} > \hat{\delta}_p$. Our analysis in this section has neglected interactions, valid for a narrow resonance. The leading-order effects of finite γ will add corrections to the approximate relation $\hat{\mu} = \hat{\delta}/2$ and hence slightly adjust $\hat{\delta}_p$ (in the numerically generated curve of Fig. 19, $\hat{\delta}_p \approx 1.57 < 2^{2/3}$), but the qualitative picture remains the same.

5.6. Coexisting fractions $x(\Delta N)$ in the mixed state

As we have seen, at positive detuning for $0 < \Delta N < \Delta N_{c2}$, resonantly interacting fermions phase separate into an s-wave paired singlet SF and a spin-polarized N state with fractions $x(\delta,\Delta N)$ and $1 - x(\delta,\Delta N)$, respectively.

To calculate $x(\delta,\Delta N)$, we begin with Eq. (164) for the normalized density $\hat{n}$ expressed in terms of the densities $\hat{n}_{\rm SF}$ and $\hat{n}_{\rm N}$ in the SF and N regions Eqs. (159) and (160), respectively. Using the overall density constraint $\hat{n} = 4/3$, we solve Eq. (164) for x to obtain

$$x(\hat{\delta}, \hat{h}) = \frac{\frac{4}{3} - \hat{n}_{\rm N}[\hat{h}, \hat{\mu}_c(\hat{h})]}{\hat{n}_{\rm SF}[\hat{\delta}, \hat{\mu}_c(\hat{h}), \sqrt{2}\hat{h}] - \hat{n}_{\rm N}[\hat{h}, \hat{\mu}_c(\hat{h})]}, \tag{177}$$

with $\hat{\mu}_c(\hat{h})$ given by Eq. (163). Here, in the last argument of $\hat{n}_{\rm SF}[\hat{\delta}, \hat{\mu}_c(\hat{h}), \hat{\Delta}(\hat{\mu}_c)]$ we have substituted $\hat{\Delta}(\hat{\mu}_c) = \sqrt{2}\hat{h}$, valid everywhere in the mixed phase.

To compute $x(\hat{\delta}, \Delta N)$, we combine $x(\hat{\delta}, \hat{h})$ above with a computation of $\Delta N(\hat{\delta}, \hat{h})$ as a function of $\hat{h}$ in the mixed phase. Since any population difference can only occur in the N regions of fractional volume $1 - x$, we have

$$\frac{\Delta N(\gamma, \hat{\delta}, \hat{h})}{N} = \frac{1}{2}\Big[1 - x(\gamma, \hat{\delta}, \hat{h})\Big]\Big[(\hat{\mu}_c(\hat{h}) + \hat{h})^{3/2} - (\hat{\mu}_c(\hat{h}) - \hat{h})^{3/2}\Theta(\hat{\mu}_c(\hat{h}) - \hat{h})\Big]. \tag{178}$$

In Fig. 20, we present a numerical solution $x(\hat{\delta}, \Delta N)$ of Eqs. (177) and (178), for $\hat{\delta} = 1.5$ (solid line) and $\hat{\delta} = 2.0$ (dashed line), with $\gamma = 0.1$. The two curves are qualitatively similar, each describing a continuous depletion of $x(\hat{\delta}, \Delta N)$ from unity to zero. The main notable difference between the curves is that for $\hat{\delta} = 1.5$, $\frac{\Delta N_{c2}}{N} = 1$, while for $\hat{\delta} = 2.0$ the dashed curve reaches $x = 0$ at $\frac{\Delta N_{c2}}{N} \approx 0.535 < 1$, characterizing a transition to a non-fully-polarized N state. The rapid initial drop of x with $\frac{\Delta N}{N}$ reflects the fact that, when most of the system is paired at low polarization, the only way to polarize is to convert regions of the system from paired to unpaired (i.e. to decrease x), while for large polarization when much of the system is already in the normal phase, to attain higher polarization the system can further polarize already normal sections.

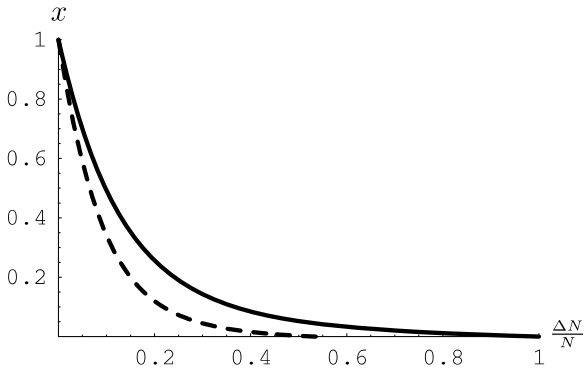

Fig. 20. Plot of the fraction $x(\delta,\Delta N)$ of mixed state that is in the SF phase as a function of polarization for detuning $\hat{\delta} = 1.5$ (solid line) and $\hat{\delta} = 2$ (dashed line).

6. Negative-detuning regime of two-channel model at finite population difference

In the present section we extend our analysis to the $\delta < 0$ BEC regime. As for $\delta > 0$, here too we minimize the ground-state energy Eq. (76) with respect to $\Delta_{\mathbf{Q}}$ and $\mathbf{Q}$, subject to the total atom number and imposed spin-polarization constraints. As we shall show in Section 7, the FFLO state is only stable above a critical detuning $\delta_* \approx 2\epsilon_F$ [given by Eq. (259) below], i.e., in the BCS regime. Physically this reflects the fragility of the FFLO state that is driven by atomic Fermi-surface mismatch, absent in the BEC regime where $\mu \approx \delta/2 < 0$. Therefore, in studying the BEC regime at the outset we shall focus on $\mathbf{Q} = 0$ pairing order as we did in Section 5. Thus, the ground state energy that we shall analyze is still given by Eq. (102), with its dimensionless form given by Eq. (107).

Before proceeding to our detailed analysis, we briefly summarize our main results, the negative-detuning phase diagrams at fixed chemical potential difference h and fixed spin imbalance ΔN, Figs. 21 and 22, respectively. The three critical h's (h_m, h_{c1} and h_{c2}) in

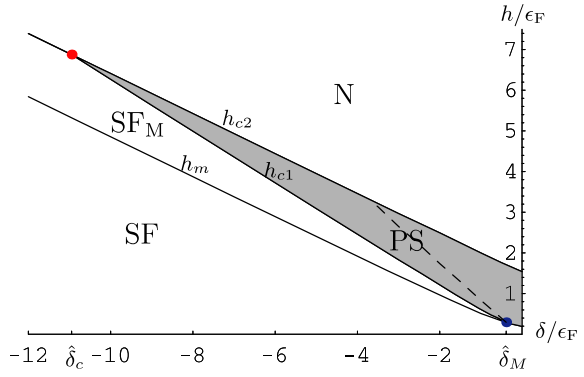

Fig. 21. Negative-detuning phase diagram of the two-channel model for the case $\gamma = 0.1$ at fixed chemical potential difference h showing regions of singlet superfluid (SF), magnetic superfluid (SF_M), phase separation (shaded, PS) and normal phase (N). To the right of the dashed line in the PS regime, SF and N states coexist, while to the left of the dashed line in the PS regime SF_M and N states coexist. δ_c is a tricritical point.

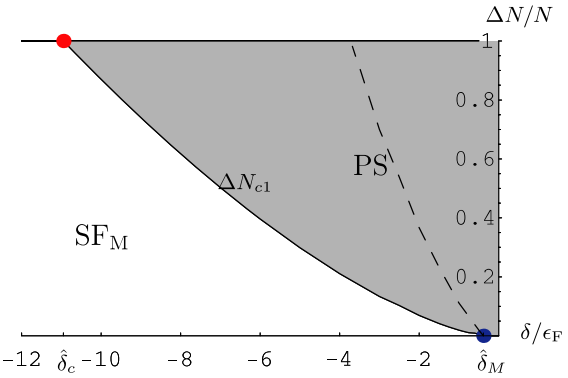

Fig. 22. Negative-detuning phase diagram of the two-channel model for the case $\gamma = 0.1$ at fixed spin population difference ΔN, showing regions of magnetic superfluid (SF_M) and phase separation (shaded, PS). The fully-polarized normal phase is confined to the upper boundary $\Delta N = N$, while the unpolarized SF state is confined to the $\Delta N = 0$ axis. To the right of the dashed line, the PS regime consists of coexisting SF and N states; to the left of the dashed line the PS regime consists of coexisting SF_M and N states.

Fig. 21 separating the singlet superfluid (SF), magnetic superfluid (SF_M), normal (N) states and phase-separation (PS) regime were computed by numerically solving the stationarity and number constraint conditions [i.e., Eqs. (110a) and (110b)], always ensuring that the solution is a minimum of the normalized ground-state energy e_G, Eq. (107). In the PS region, it is possible to solve the stationarity and number constraint equations, but the solution is *not* a minimum of e_G. [47,67,45,121] Then, to obtain Fig. 22, these critical h's were converted to critical population differences using Eq. (110c). The dashed lines in these figures separate different types of PS regime and are derived approximately in Section 6.4.3.

The main aim of this section is to present details of analytic calculations that complement this numerical analysis of the gap and number-constraint equations and lead to the phase diagrams in Figs. 21 and 22 in the narrow Feshbach resonance limit, $\gamma \ll 1$. These computations are aided by the fact that, for $\gamma \ll 1$, $\mu \simeq \delta/2$ and hence $\mu < 0$ for $\delta < 0$. Taking $\mu < 0$ yields an important simplification to the equation for the ground-state energy and consequently for the gap equation and the number and polarization constraints, since only one of the terms in Eq. (108) for the dimensionless magnetization contributes, yielding

$$\hat{m}(\hat{h}) = \frac{2}{3}\left(\sqrt{\hat{h}^2 - \hat{\Delta}^2} - |\hat{\mu}|\right)^{3/2} \Theta\left(\sqrt{\hat{h}^2 - \hat{\Delta}^2} - |\hat{\mu}|\right). \tag{179}$$

As in the preceding section, we proceed by inserting Eq. (179) into Eq. (107) for the normalized ground-state energy e_G. Stationary points of e_G satisfy the gap equation, Eq. (110a). In finding solutions to the gap equation we always verify that such stationary points are actually *minima* of e_G rather than saddle points or local maxima. Failure to do this in a number of recent theoretical works [47,67,121,45] has led to erroneous results. To impose constraints on the total atom number and spin population difference, we use Eqs. (110b) and (110c).

We will show that an accurate quantitative description of the BEC regime, for the case of a narrow resonance, can be found by expanding the normalized ground-state energy e_G

to leading order in γ. Although a full description requires keeping terms up to order $\mathcal{O}(\gamma^3)$ (as we show in Section 6.4 below), many essential features are correctly described in the leading-order $\gamma = 0$ limit.

6.1. Zero-coupling approximation

In the present section, we analyze the BEC regime in the zero-coupling limit $\gamma \to 0$ ($g \to 0$). As we shall show, many of the essential features of the phase diagram are captured in this extreme narrow resonance limit. Although the Feshbach resonance interconversion term that is proportional to g is required for pairing and equilibration between atoms and molecules, on the BEC side of the resonance the molecular density is determined by the number equation and therefore, in equilibrium, is finite even in the $g \to 0$ limit.

To treat this limit, we change variables from $\hat{\Delta}$ (which vanishes at $g \to 0$) to the normalized molecular condensate order parameter $\hat{B} = \hat{\Delta}/\sqrt{\gamma}$. The physical molecular boson density n_m is related to $\hat{B}$ via

$$n_m = |B|^2 = N(\epsilon_F)\epsilon_F|\hat{B}|^2 = c\epsilon_F^{3/2}\hat{B}^2, \tag{180}$$

where for simplicity we have taken $\hat{B}$ to be real. Inserting this variable change into Eq. (107), we find, expanding to leading order in small γ:

$$e_G = \hat{B}^2(\hat{\delta} - 2\hat{\mu}) - \int_0^{\hat{h}} \hat{m}(\hat{h}')\mathrm{d}\hat{h}', \tag{181}$$

where to the same order the magnetization Eq. (179) reduces to

$$\hat{m}(\hat{h}) = \frac{2}{3}(\hat{h} - |\hat{\mu}|)^{3/2}\Theta(\hat{h} - |\hat{\mu}|). \tag{182}$$

Performing the integral over $\hat{h}$ in Eq. (181), we find

$$e_G = \hat{B}^2(\hat{\delta} - 2\hat{\mu}) - \frac{4}{15}(\hat{h} - |\hat{\mu}|)^{5/2}\Theta(\hat{h} - |\hat{\mu}|). \tag{183}$$

The number and gap equations are then given by:

$$\frac{4}{3} = 2\hat{B}^2 + \frac{2}{3}(\hat{h} - |\hat{\mu}|)^{3/2}\Theta(\hat{h} - |\hat{\mu}|), \tag{184a}$$

$$0 = 2\hat{B}(\hat{\delta} - 2\hat{\mu}). \tag{184b}$$

In the normal (N) phase, $\hat{B} = 0$, Eq. (184b) is automatically satisfied, and the number equation reduces to

$$\hat{h} - |\hat{\mu}| = 2^{2/3}, \tag{185}$$

for the normal-state chemical potential. Returning to dimensionful quantities clarifies the meaning of Eq. (185):

$$(h + \mu)^{3/2} = 2\epsilon_F^{3/2}. \tag{186}$$

Since $h + \mu = \mu_\uparrow$, this simply states that the normal-phase spin-$\uparrow$ density $n_\uparrow = \frac{2}{3}c\mu_\uparrow^{3/2}$ is equal to the total fermion density, n.

In the superfluid phase, $\hat{B} \neq 0$, and Eqs. (184a), (184b) give

$$\hat{B}^2 = \frac{2}{3}\left[1 - \frac{1}{2}\left(\hat{h} - |\hat{\mu}|\right)^{3/2}\Theta(\hat{h} - |\hat{\mu}|)\right], \tag{187a}$$

$$\hat{\mu} = \frac{\hat{\delta}}{2}, \tag{187b}$$

which combine to yield

$$\hat{B}^2 = \frac{2}{3}\left[1 - \frac{1}{2}\left(\hat{h} - \frac{|\hat{\delta}|}{2}\right)^{3/2}\Theta\left(\hat{h} - \frac{|\hat{\delta}|}{2}\right)\right], \tag{188}$$

an expression that is only sensible when the right side is positive. What do the preceding expressions tell us about the BEC regime at $\hat{h} \neq 0$? For $\hat{h} < |\hat{\delta}|/2$, corresponding to Zeeman field less than the molecular binding energy, $\hat{B}^2 = 2/3$, which, in dimensionful units, gives the molecular density $n_m = n/2$. This is the usual singlet molecular superfluid (SF) phase in the BEC limit, in which all the atoms are bound into diatomic molecules [See Fig. 23(a)]. Although including nonzero interactions will deplete the molecular density somewhat, clearly this qualitative picture will still hold.

However, for $\hat{h} > |\hat{\delta}|/2$ the Zeeman field exceeds the molecular binding energy, and the molecular density continuously depletes with increasing $\hat{h}$ according to Eq. (188) as molecules break up into a fully-polarized Fermi sea with $\mu_\uparrow = h + \delta/2 > 0$ [see Fig. 23(b)]. Using Eqs. (187b) and (182), we find the corresponding magnetization

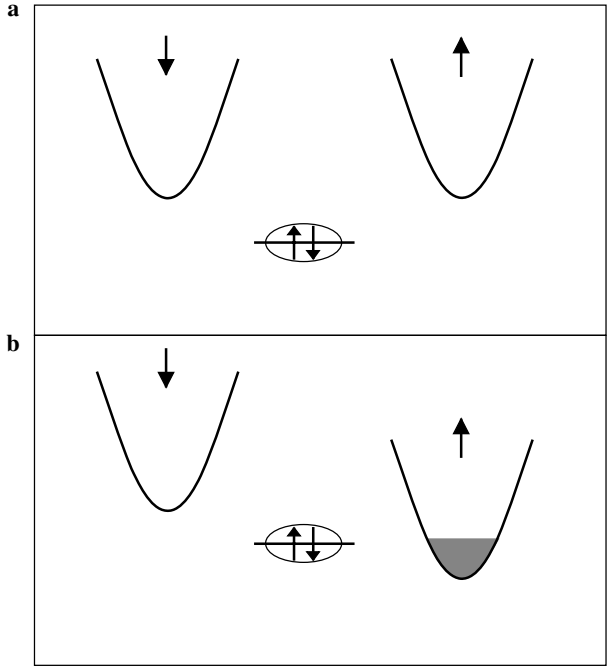

Fig. 23. A schematic of the population of atomic states (parabolas, labeled by spin) and the molecular level (line) in the BEC regime ($\delta < 0$) at (a) $h = 0$ and (b) $h > h_m$.

$$\hat{m}(\hat{h}) = \frac{2}{3}\left(\hat{h} - \frac{|\hat{\delta}|}{2}\right)^{3/2} \Theta\left(\hat{h} - \frac{|\hat{\delta}|}{2}\right), \tag{189}$$

continuously increasing from zero beyond $\hat{h} > |\hat{\delta}|/2$. We refer to this uniform state, consisting of both condensed molecules and spin-up polarized fermions, as the magnetic superfluid (SF_M) state.

At low energies, we expect the SF_M to be very similar to a uniform state of bosons and one species of fermion which has been previously explored in a different context [126]. In the present context, the SF_M state exists for $\hat{h}_m < \hat{h} < \hat{h}_{c2}$, with (in the $\gamma \to 0$ limit)

$$\hat{h}_m = |\hat{\delta}|/2, \tag{190a}$$

$$\hat{h}_{c2} = 2^{2/3} + |\hat{\delta}|/2, \tag{190b}$$

the latter defined by where $\hat{B}^2 = 0$ according to Eq. (188). The approximate linear dependences of $\hat{h}_m$ and $\hat{h}_{c2}$ on $\hat{\delta}$ are also clearly seen (away from the unitarity point $\delta = 0$) in the numerically-determined finite $\gamma = 0.1$ phase diagram (Fig. 21).

Expressing Eq. (188) for $\hat{B}(\hat{h})$ in terms of n_m, n and the physical magnetization, m:

$$n_m = \tfrac{1}{2}(n - m), \tag{191}$$

further clarifies its meaning. At $\hat{h}_m$, $\hat{m}(\hat{h}_m) = 0$ and all the atoms are confined into Bose-condensed molecules. Applying a sufficiently large $\hat{h} > \hat{h}_m$ such that $\mu_\uparrow = h + \delta/2 > 0$ populates the spin-up atomic band as illustrated in Fig. 23, depleting the number of molecular bosons according to Eq. (191). At $\hat{h} = \hat{h}_{c2}$, $m = n$ and the system is fully polarized. As we shall see in the next sections, this simple picture of molecular bosons depairing into free polarized atoms once the fermion band dips below the molecular level remains qualitatively correct for $\gamma > 0$.

6.2. Weak-coupling description of SF_M state

In the present section, we extend the above $\gamma \to 0$ analysis to higher order in γ. As we will show, the qualitative picture of the preceding subsection remains the same: A depletion of the condensate (and concomitant population of the spin-$\uparrow$ Fermi sea) with increasing $\hat{h}$ starting at $\hat{h}_m$, with a continuous depletion until $\hat{h}_{c2}$ beyond which the molecular density vanishes and all the atoms occupy the spin-$\uparrow$ band. The properties of the homogeneous magnetic superfluid SF_M, that consists of a molecular superfluid and a spin-$\uparrow$ Fermi sea, remain the same. The major *qualitative* modification from the preceding section is the continuation of the first-order phase transition curve $\hat{h}_{c1}(\hat{\delta})$, that we found in Section 5, into the BEC regime. Recall that, on the positive-detuning side of the resonance, $\hat{h}_{c1}(\hat{\delta})$ denotes the chemical potential difference above which the SF phase is unstable, via a first-order transition, to phase separation. At fixed polarization, this translates to $\Delta N_{c1} = 0$: For any $\Delta N \neq 0$ in the BCS regime the system phase separates.

As we shall see, in the BEC regime at moderate negative detunings, the SF_M state is similarly unstable to phase separation at $\hat{h}_{c1}$. However, since the SF_M state is *polarized*, the corresponding fixed-polarization boundary $\Delta N_{c1} \neq 0$. Remarkably, our naive formula for $\hat{h}_{c2}$, Eq. (190b), remains quantitatively correct, but, close to the resonance position, should be more generally interpreted as the chemical potential difference below which the spin-polarized N state is unstable to phase separation. At fixed atom density n, the

sequence of phases and regimes with increasing $\hat{h}$ is, then, SF $\to$ SF$_{\rm M}$ $\to$ PS $\to$ N. At large negative detuning, $\delta = \delta_c \simeq -10.6\epsilon_{\rm F}$, $\hat{h}_{c1}$ *intersects* $\hat{h}_{c2}$, so that the first-order behavior ends and, for $\delta < \delta_c$, we find the sequence of phases SF $\to$ SF$_{\rm M}$ $\to$ N separated by continuous transitions.

Before computing the $\hat{h}_{c1}(\hat{\delta})$ curve, we first analyze the SF$_{\rm M}$ phase in more detail by studying the $\mathcal{O}(\gamma^2)$ expression for $e_{\rm G}$, obtained by expanding the arguments of the integrals in Eq. (107) in small γ and evaluating the integrals term by term. We find:

$$e_{\rm G} = -\frac{4}{15}(\hat{h}-|\hat{\mu}|)^{5/2}\Theta(\hat{h}-|\hat{\mu}|) - \hat{V}_2\hat{B}^2 + \frac{1}{2}\hat{V}_4\hat{B}^4, \tag{192}$$

with

$$\hat{V}_2[\gamma,\hat{\delta},\hat{h},\hat{\mu}] \equiv 2\hat{\mu} - \hat{\delta} - \gamma\sqrt{|\hat{\mu}|}F_2(\hat{h}/|\hat{\mu}|), \tag{193a}$$

$$\hat{V}_4[\gamma,\hat{h},\hat{\mu}] \equiv \frac{\gamma^2\pi}{32|\hat{\mu}|^{3/2}}F_4(\hat{h}/|\hat{\mu}|), \tag{193b}$$

where we defined the functions $F_2(x)$ and $F_4(x)$:

$$F_2(x) \equiv \frac{\pi}{2} + \left[\sqrt{x-1} - \tan^{-1}\sqrt{x-1}\right]\Theta(x-1), \tag{194}$$

$$F_4(x) \equiv 1 - \frac{2}{\pi x^2}\left[\sqrt{x-1}(x+2) + x^2\tan^{-1}\sqrt{x-1}\right]\Theta(x-1). \tag{195}$$

To leading order in γ, the number Eq. (110b) and gap Eq. (110a) equations are:

$$\frac{4}{3} = 2\hat{B}^2 + \frac{\pi\gamma\hat{B}^2}{4\sqrt{|\hat{\mu}|}} + \frac{2}{3}(\hat{h}-|\hat{\mu}|)^{3/2}\Theta(\hat{h}-|\hat{\mu}|) - \frac{\gamma\hat{B}^2}{2\sqrt{|\hat{\mu}|}}\tan^{-1}\sqrt{\hat{h}/|\hat{\mu}|-1}\,\Theta(\hat{h}-|\hat{\mu}|), \tag{196a}$$

$$\hat{V}_2 = \hat{B}^2\hat{V}_4. \tag{196b}$$

On the BEC side of the resonance the saddle-point equations approximately switch roles, with the number equation Eq. (196a) approximately determining the boson density $\hat{B}^2$ and the gap equation Eq. (196b) approximately determining the chemical potential $\hat{\mu}$, as can be seen by solving these equations:

$$\hat{B}^2 = \frac{2}{3}\frac{1-\frac{1}{2}\left(\hat{h}-|\hat{\mu}|\right)^{3/2}}{1+\frac{\gamma}{8\sqrt{|\hat{\mu}|}}\left(\pi - 2\tan^{-1}\sqrt{\hat{h}/|\hat{\mu}|-1}\right)}, \tag{197a}$$

$$\hat{\mu} = \frac{\hat{\delta}}{2} + \frac{\gamma\sqrt{|\hat{\mu}|}}{2}\left[\frac{\pi}{2} + \sqrt{\hat{h}/|\hat{\mu}|-1} - \tan^{-1}\sqrt{\hat{h}/|\hat{\mu}|-1}\right], \tag{197b}$$

with the second equation determining $\hat{\mu}(\hat{\delta})$ through $\hat{V}_2 \approx 0$, correct to $\mathcal{O}(\gamma)$ since $\hat{V}_4$ is $\mathcal{O}(\gamma^2)$. At this level of approximation, Eq. (197b) is independent of Eq. (197a) allowing us to solve Eq. (197b) to determine $\hat{\mu}(\hat{\delta})$ which can then be used to compute $\hat{B}^2(\hat{\delta})$ through Eq. (197a). To order γ, $\hat{\mu}$ is determined by simply iterating Eq. (197b), which amounts to inserting the zeroth order result $\hat{\mu} \approx \hat{\delta}/2$ into the second term. This gives to $\mathcal{O}(\gamma)$

$$\hat{\mu} \simeq \hat{\mu}_1(\hat{\delta},\hat{h}) \equiv \frac{\hat{\delta}}{2} + \frac{\gamma\sqrt{|\hat{\delta}|}}{2\sqrt{2}}\left[\frac{\pi}{2} + \sqrt{2\hat{h}/|\hat{\delta}|-1} - \tan^{-1}\sqrt{2\hat{h}/|\hat{\delta}|-1}\right], \tag{198}$$

while to the same order $\hat{B}^2$ is given by

$$\hat{B}^2 = \frac{2}{3}\frac{1-\frac{1}{2}\left(\hat{h}-|\hat{\mu}_1(\hat{\delta},\hat{h})|\right)^{3/2}}{1+\frac{\gamma\sqrt{2}}{8\sqrt{|\hat{\delta}|}}(\pi-2\tan^{-1}\sqrt{2\hat{h}/|\hat{\delta}|-1})}, \tag{199}$$

describing the condensate depletion as a function of $\hat{h}$ and $\hat{\delta}$.

These expressions can be easily translated to the experimentally-relevant fixed-population ensemble. Expanding Eq. (179) to $\mathcal{O}(\gamma)$, we obtain

$$\hat{m} \simeq \frac{2}{3}(h-|\hat{\mu}|)^{3/2} - \frac{\gamma\hat{B}^2}{2\hat{h}}\sqrt{\hat{h}/|\hat{\mu}|-1}, \tag{200}$$

the lowest-order finite-γ correction to Eq. (182). This can be turned into an $\mathcal{O}(\gamma)$ expression for the quantity $(\hat{h}-|\hat{\mu}|)^{3/2}$ appearing in Eq. (197a):

$$\frac{2}{3}(\hat{h}-|\hat{\mu}|)^{3/2} \simeq \hat{m} + \frac{\gamma\hat{B}^2}{2\hat{h}}\left(\frac{3\hat{m}}{2}\right)^{1/3}, \tag{201}$$

$$\simeq \hat{m} + \frac{\gamma\hat{B}^2}{2|\hat{\mu}|}\left(\frac{3\hat{m}}{2}\right)^{1/3}, \tag{202}$$

where in the second line we took $\hat{h} \approx |\hat{\mu}|$, valid to leading order in small $\hat{m}$. Since, as we shall see, the $\mathrm{SF_M}$ state is generally only stable for $\hat{h} \approx |\hat{\mu}|$, this is approximately valid. Inserting Eq. (202) into Eq. (197a), and using $\hat{\mu} \approx \hat{\delta}/2$ [correct in this expression to $\mathcal{O}(\gamma)$] we find

$$\hat{B}^2 \simeq \frac{\frac{2}{3}-\frac{\hat{m}}{2}}{1+\frac{\gamma}{2|\hat{\delta}|}\left(\frac{3\hat{m}}{2}\right)^{\frac{1}{3}}+\frac{\sqrt{2}\gamma}{8\sqrt{|\hat{\delta}|}}\left(\pi-2\tan^{-1}\frac{(3\hat{m})^{1/3}2^{1/6}}{\sqrt{|\hat{\delta}|}}\right)}, \tag{203a}$$

$$\frac{n_m}{n} = \frac{\frac{1}{2}\left(1-\frac{\Delta N}{N}\right)}{1+\frac{\gamma}{2^{\frac{5}{3}}|\hat{\delta}|}\left(\frac{\Delta N}{N}\right)^{\frac{1}{3}}+\frac{\sqrt{2}\gamma}{8\sqrt{|\hat{\delta}|}}\left[\pi-2\tan^{-1}\frac{2^{5/6}}{\sqrt{|\hat{\delta}|}}\left(\frac{\Delta N}{N}\right)^{\frac{1}{3}}\right]}, \tag{203b}$$

where in Eq. (203b) we used Eqs. (104), (109), and (180) to express the final result for the physical molecular density $n_m(\Delta N)$. This corrects, to $\mathcal{O}(\gamma)$, Eq. (191) of the preceding section.

Finally, we consider the $\mathcal{O}(\gamma)$ corrections to Eqs. (190a), (190b) for $\hat{h}_m$ and $\hat{h}_{c2}$. The SF-$\mathrm{SF_M}$ transition at $\hat{h}_m$ occurs when the magnetization $\hat{m}(\hat{h})$ becomes nonzero. By examining Eq. (179) it is clear that $\hat{h}_m$ is exactly given by

$$\hat{h}_m = \sqrt{|\hat{\mu}|^2+\hat{\Delta}^2}, \tag{204a}$$

$$= \sqrt{|\hat{\mu}|^2+\gamma\hat{B}^2}, \tag{204b}$$

with $\hat{\mu}$ and $\hat{B}$ given by their values in the SF state (assuming $\hat{\delta} < \hat{\delta}_M$, so that this continuous transition is not preempted by a first-order SF–N transition). Expressions for $\hat{\mu}$ and $\hat{B}$ in the SF phase are derived in Appendix C, Eqs. (C.17) and (C.18). Inserting these expressions into Eq. (204b), we find, to leading order in γ (plotted in Fig. 24),

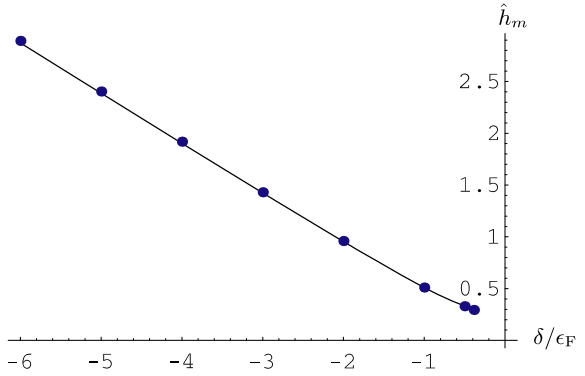

Fig. 24. Plot of $\hat{h}_m$, the normalized chemical potential difference above which the system enters the SF_M phase (i.e., $\Delta N \neq 0$) as a function of detuning δ. The analytical low-γ prediction of Eq. (205b) (solid line) shows excellent agreement with a numerical computation (points), here done for $\gamma = 0.1$.

$$\hat{h}_m \approx \sqrt{|\hat{\mu}|^2 + 2\gamma/3}, \tag{205a}$$

$$\approx \sqrt{\frac{\hat{\delta}^2}{4} + \gamma\left(\frac{2}{3} - \frac{\pi|\hat{\delta}|^{3/2}}{4\sqrt{2}}\right)}, \tag{205b}$$

where we displayed the intermediate result Eq. (205a) because it will be useful below.

To compute the upper-critical chemical potential difference $\hat{h}_{c2}$, below which the normal (N) state is unstable to pairing or phase separation, we note that stability of the N phase requires $\hat{V}_2 < 0$, so that e_G has positive upward curvature at $\hat{B} = 0$ [see Eq. (192)]. A second-order transition to the $\hat{B} \neq 0$ SF state occurs when $\hat{V}_2$ changes sign. We shall proceed to compute $\hat{h}_{c2}$ by finding the location of this assumed second-order N–SF_M transition. However, as we shall see, for $\hat{\delta} > \hat{\delta}_c$ this second-order transition is preempted by a first-order transition to the regime of phase separation. We study this first-order behavior in more detail in the next section. For now, we proceed with the second-order assumption that locates the boundary $\hat{h}_{c2}$ to a good accuracy, as will be seen in the following sections. The corresponding condition $\hat{V}_2 = 0$ is actually equivalent to our $\mathcal{O}(\gamma)$ expression Eq. (197b) for the gap equation. Combining this with Eq. (185) for the normal state chemical potential yields:

$$\hat{h}_{c2} = 2^{2/3} + \frac{|\hat{\delta}|}{2} - \frac{\gamma}{2}\sqrt{\hat{h}_{c2} - 2^{2/3}}\left(\frac{\pi}{2} + \frac{2^{1/3}}{\sqrt{\hat{h}_{c2} - 2^{2/3}}} - \tan^{-1}\frac{2^{1/3}}{\sqrt{\hat{h}_{c2} - 2^{2/3}}}\right), \tag{206a}$$

$$\approx 2^{2/3} + \frac{|\hat{\delta}|}{2} - \frac{\gamma|\hat{\delta}|^{1/2}}{\sqrt{8}}\left(\frac{\pi}{2} + \frac{2^{5/6}}{|\hat{\delta}|^{1/2}} - \tan^{-1}\frac{2^{5/6}}{|\hat{\delta}|^{1/2}}\right), \tag{206b}$$

with the second expression, obtained by approximating $\hat{h}_{c2} \approx 2^{2/3} + |\hat{\delta}|/2$ on the right side of Eq. (206a), correct to $\mathcal{O}(\gamma^1)$. As derived, Eq. (206b) denotes the chemical potential difference at which a putative second-order N to SF_M phase transition occurs. As noted above, this only occurs for sufficiently low detunings with a first-order transition occurring for higher detunings. Despite this, we shall see that the critical $\hat{h}$ for the first-order instability (which we also denote $\hat{h}_{c2}$) to good accuracy is given by Eq. (206b). We will demonstrate this assertion in Section 6.3.

6.3. Transition to the regime of phase separation

As mentioned above, the regime of phase separation we found on the BCS side of the resonance persists into the BEC regime, bounded by the $\hat{h}_{c1}(\hat{\delta})$ and $\hat{h}_{c2}(\hat{\delta})$ curves. A notable qualitative difference on the BEC side is the existence of a homogeneous magnetized superfluid (SF_M) state.

The condition for the instability of the SF_M to phase separation at $\hat{h}_{c1}(\hat{\delta})$ is of course precisely the same as we used on the BCS side: a first-order transition to the N phase in the grand-canonical ensemble at fixed $\hat{h}$ and $\hat{\mu}$. Although finding the location of this first-order transition is most accurately done by examining the precise structure of the ground-state energy as a function of applied chemical potential difference, to a good approximation it is signaled by a *vanishing* of the molecular scattering length a_m. To show this, we compute the molecular scattering length by using its relation $a_m = \frac{m}{2\pi} T_m$ to the molecular T-matrix T_m [114], the latter given to leading order (i.e. the Born approximation) by the diagram in Fig. 25. Direct calculation of this diagram (relegated to Appendix E) yields

$$a_m = \frac{cg^4 m}{64|\mu|^{3/2}} F_4(h/|\mu|), \tag{207}$$

$$= \frac{\sqrt{2}\pi^2 \epsilon_F \gamma^2}{64|\mu|^{3/2}\sqrt{m}} F_4(h/|\mu|), \tag{208}$$

involving the function $F_4(x)$ [defined in Eq. (195)] that we have already introduced in the definition of the quartic term $\hat{V}_4$ in the ground-state energy Eq. (192). This relation to $\hat{V}_4$ is expected as a_m measures the repulsion between molecular bosons.

Stability of a molecular Bose gas requires $a_m > 0$. [127] However, we find that while $a_m(h = 0) > 0$, it decreases monotonically with $h/|\mu|$ (as illustrated in Fig. 2), vanishing at $h/|\mu| \approx 1.30$. [128] Based on a detailed analysis of $e_G(\hat{B}, \hat{h})$ (see Section 6.4 below), we associate this vanishing of $a_m(\hat{h})$ with a first-order SF_M–N transition driven by the increased density of unpaired single-spin species atoms. Since (as discussed previously; see Section 5.3) at fixed atom number the system phase separates at such a first-order transition we identify this critical $\hat{h}$ with $\hat{h}_{c1}$. Combining the value $x \approx 1.30$ at which $F_4(x)$ vanishes with the relation $\hat{\mu} \approx \hat{\delta}/2$ that is valid in the SF_M state, we find

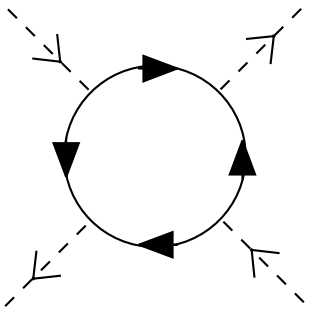

Fig. 25. Feynman diagram corresponding to the molecular scattering amplitude, with the solid lines indicating fermionic atom propagators and the dashed lines indicating scattering molecules.

$$\hat{h}_{c1} \approx 1.30|\hat{\mu}(n,\hat{\delta})|, \tag{209a}$$

$$\approx 0.65|\hat{\delta}|, \tag{209b}$$

At sufficiently negative $\hat{\delta}$, $\hat{h}_{c1}(\hat{\delta})$ *intersects* $\hat{h}_{c2}(\hat{\delta})$. Using the $\mathcal{O}(\gamma^0)$ result Eq. (190b) for $\hat{h}_{c2}$, we find the corresponding detuning

$$\hat{\delta}_c \approx -\frac{2^{2/3}}{0.15} \approx -10.6. \tag{210}$$

The implication of this is that, for $\hat{\delta} < \hat{\delta}_c$, the molecular bosons in the $\mathrm{SF_M}$ phase are repulsive for any $\hat{h}$ (and thus are stable). For $\hat{\delta} < \hat{\delta}_c$, the $\mathrm{SF_M}$ undergoes a *continuous* transition at $\hat{h}_{c2}$ to a fully-polarized atomic gas.

In the more experimentally-relevant ensemble of fixed atom numbers, we translate $\hat{h}_{c1}$ to the lower critical polarization ΔN_{c1} at which the $\mathrm{SF_M}$ state is unstable to phase separation. Using Eq. (209b) along with Eqs. (182) and (109) (as well as $\hat{\mu} \approx \hat{\delta}/2$) we find

$$\frac{\Delta N_{c1}}{N} \simeq \frac{1}{2}(0.15)^{3/2}|\hat{\delta}|^{3/2}, \tag{211a}$$

$$\simeq 0.029|\hat{\delta}|^{3/2}. \tag{211b}$$

We next turn to a more detailed demonstration of the preceding discussion by a careful analysis of the ground-state energy e_{G}.

6.4. Detailed analysis of the SF–SF_M and SF_M–N transitions

In the present section, we present a more precise determination of the first-order transition instability described in the preceding subsection. Doing so will provide more accurate (in γ) predictions for $\hat{h}_{c1}(\hat{\delta})$, $\Delta N_{c1}(\hat{\delta})$ and $\hat{h}_{c2}(\hat{\delta})$ (note that, as found for sufficiently low detuning on the BCS side, $\Delta N_{c2} = 1$ on the BEC side), as well as a more complete description of the first-order $\mathrm{SF_M}$–N transition. We start by expanding $e_{\mathrm{G}}(\hat{B})$ to higher order in $\hat{B}$:

$$e_{\mathrm{G}} \approx -\hat{V}_2\hat{B}^2 + \frac{\hat{V}_4}{2}\hat{B}^4 + \frac{\hat{V}_6}{3}\hat{B}^6 + \mathcal{O}(\hat{B}^8), \tag{212}$$

where for simplicity we have dropped a $\hat{B}$-independent term. Here, $\hat{V}_2$ and $\hat{V}_4$ are given in Eqs. (193a), (193b) and

$$\hat{V}_6[\hat{h},\hat{\mu}] = \frac{3\gamma^3}{32|\hat{\mu}|^{7/2}}F_6(\hat{h}/|\hat{\mu}|), \tag{213a}$$

$$F_6(x) \equiv -\frac{5\pi}{64} + \left[\frac{1}{3x^3\sqrt{x-1}} + \frac{5}{32}\tan^{-1}\sqrt{x-1} + \frac{\sqrt{x-1}}{96x^4}(-48+8x+10x^2+15x^3)\right]\Theta(x-1), \tag{213b}$$

is the the sixth-order coefficient.

6.4.1. SF–SF_M transition at $\hat{h}_m$

We first recall that, for low $\hat{h} < \hat{h}_m \approx |\hat{\mu}|$, it is sufficient to limit e_{G} to quartic order in $\hat{B}$. Standard minimization gives a nontrivial SF solution $\hat{B}^2 = \hat{V}_2/\hat{V}_4$ and energy $e_{\mathrm{G,SF}} = -\hat{V}_2^2/\hat{V}_4$ that [because of the step functions $\Theta(\hat{h}/|\hat{\mu}| - 1)$] are explicitly $\hat{h}$-independent. Hence, $\hat{m} = -\frac{\partial e_{\mathrm{G,SF}}}{\partial \hat{h}} = 0$ as expected in the singlet SF state.

For a more accurate description (and for later study of the SF_M–N transition; see below) we include the $\hat{V}_6\hat{B}^6$ term in the expansion of $e_G(\hat{B})$. Although $\hat{V}_6$ has a form similar to $\hat{V}_2$ and $\hat{V}_4$, namely a constant plus an $\hat{h}$-dependent correction that vanishes for $\hat{h} < \hat{h}_m$, examination of Eq. (213b) reveals the function $F_6(x)$ to be divergent at $x \to 1^+$. This divergence arises from the approximate way we evaluate the integral of $\hat{m}(x)$ (the Zeeman energy) appearing in Eq. (107):

$$-\int_{\hat{h}_m}^{\hat{h}} d\hat{h}'\hat{m}(\hat{h}') = -\frac{2}{3}\int_{\hat{h}_m}^{\hat{h}} d\hat{h}'\left(\sqrt{\hat{h}^2 - \gamma\hat{B}^2} - |\hat{\mu}|\right)^{3/2}, \tag{214}$$

perturbatively in $\gamma\hat{B}^2/(\hat{h}^2 - \hat{\mu}^2)$. Recall that $\hat{h}_m \equiv \sqrt{\hat{\mu}^2 + \gamma\hat{B}^2}$. Hence, strictly speaking we should only use these expressions in the regime where $\gamma\hat{B}^2/(\hat{h}^2 - \hat{\mu}^2) \ll 1$.

To elucidate the nature of the transition exhibited by $e_G(\hat{B}, \hat{h}, \hat{\delta})$, Eq. (212), we determine the location of its minima, given by

$$0 = -\hat{V}_2\hat{B} + \hat{V}_4\hat{B}^3 + \hat{V}_6\hat{B}^5, \tag{215}$$

which (in addition to the trivial stationary point at $\hat{B} = 0$ corresponding to the N state) has two nontrivial solutions

$$\hat{B}^2_{\pm} = \frac{\hat{V}_4}{2\hat{V}_6}\left[-1 \pm \sqrt{1 + 4\hat{V}_2\hat{V}_6/\hat{V}_4^2}\right], \tag{216}$$

that yield physical stationary points of e_G only when the right side of Eq. (216) is real and positive.

For sufficiently weak chemical potential difference, $\hat{h} < \hat{h}_m$, the Landau expansion coefficients are $\hat{V}_2 > 0$, $\hat{V}_4 > 0$ and $\hat{V}_6 < 0$. Hence as long as $4\hat{V}_2|\hat{V}_6| < \hat{V}_4^2$, the + and − solutions in Eq. (216) correspond to a minimum and a maximum, respectively with the complete shape illustrated in Fig. 26 (dashed line). By plotting the numerical solution of the non-Taylor expanded expression for e_G in Eq. (107) for this range of parameters ($\hat{\delta} < 0$, $\hat{h} < \hat{h}_m$) and comparing with the quartic and sixth order (in $\hat{B}$) approximation to e_G, it is clear that while the + solution minimum represents the physical, stable singlet-SF ground state, the − solution maximum is simply an artifact of truncation of e_G at sixth

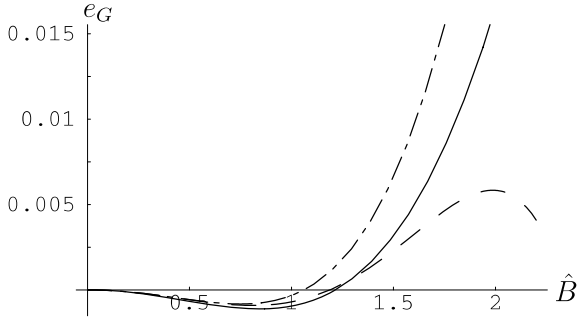

Fig. 26. Plot of e_G as a function of $\hat{B}$ for $\hat{h} < \hat{h}_m$, comparing fourth-order (dot-dashed), sixth-order (dashed) and exact numerical (solid) expressions. The sixth-order case approximates well the physical minimum at low $\hat{B}$ but has a maximum at larger $\hat{B}$ that is an artifact of the sixth-order truncation.

order. However, the + solution provides an accurate approximation to the true SF minimum, as shown in Fig. 26.

The SF–SF_M transition occurs at $\hat{h}_m \approx |\hat{\mu}|$. For $\hat{h} > \hat{h}_m$ two qualitative changes take place in the coefficients $\hat{V}_n(\hat{h},\hat{\delta})$. First, because of the positive argument of the step functions, the coefficients $\hat{V}_n(\hat{h},\hat{\delta})$ and therefore the minimum superfluid solution $\hat{B}_+$ and the corresponding energy $e_G(B_+)$ become nontrivial functions of the chemical potential difference $\hat{h}$. This then immediately gives a finite magnetization (population imbalance) $\hat{m} = -de_G/d\hat{h} \neq 0$, characteristic of the SF_M ground state. Second, for $\hat{h} > \hat{h}_m$ the coefficient $\hat{V}_6 > 0$. Hence the shape of the $e_G(\hat{B})$ function and the corresponding nature of the transition out of the SF_M state (SF_M - N transition) are determined by the signs of the $\hat{V}_2$ and $\hat{V}_4$ coefficients.

6.4.2. Second-order SF_M–N transition: $\hat{\delta} < \hat{\delta}_c$

Generically a transition is continuous if there is only a single minimum in the energy function that vanishes continuously as a parameter is tuned. As can be seen from Eq. (216), this is possible for $e_G(\hat{B})$ when $\hat{V}_4 > 0$ and $\hat{V}_6 > 0$, in which case

$$\hat{B}_+^2 = \hat{B}_{SF_M}^2 = \frac{\hat{V}_4}{2\hat{V}_6}\left[\sqrt{1 + 4\hat{V}_2\hat{V}_6/\hat{V}_4^2} - 1\right], \tag{217}$$

(which vanishes continuously as $\hat{V}_2 \to 0$) characterizes the SF_M state while $\hat{B}_-^2 < 0$ and therefore no longer corresponds to an extremum of e_G, as $\hat{B}_-$ is complex.

The evolution of $e_G(\hat{B})$ with $\hat{V}_2$ for such a continuous transition is illustrated in Fig. 27. The continuous SF_M–N transition is then determined by the vanishing of $\hat{V}_2(\hat{h},\hat{\delta})$ when the SF_M minimum at $\hat{B}_+$ vanishes into the normal state maximum at $\hat{B} = 0$, with this taking place at $\hat{h}_c$ satisfying

$$F_2(\hat{h}_c/|\hat{\mu}|) = \frac{2\hat{\mu} - \hat{\delta}}{\gamma\sqrt{|\hat{\mu}|}}. \tag{218}$$

At fixed imposed density, the condition of $\hat{V}_4(\hat{h}_c,\hat{\delta}) > 0$ for such a continuous transition is satisfied for $\hat{\delta} < \hat{\delta}_c$ with $\hat{\delta}_c$ approximately given by Eq. (210). When combined with the

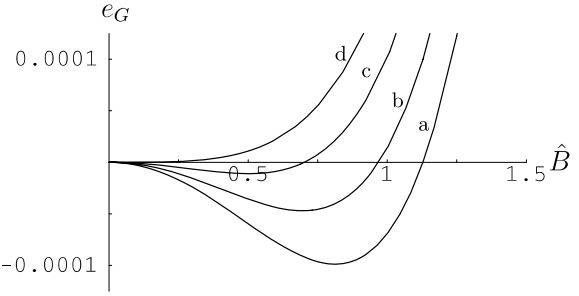

Fig. 27. Evolution of the BEC-regime normalized ground-state energy $e_G(\hat{B})$ Eq. (212), for parameters such that a continuous $SF_M \to N$ transition occurs. Here, $\gamma = 0.1$, $\hat{\delta} = -2$, $\hat{\mu} = -0.924$. For curves a, b, and c, $\hat{h} < \hat{h}_c$ with $\hat{h} = 1.0, 1.007$, and 1.014, respectively, and the minimum at $\hat{B} \neq 0$ represents the SF_M phase. For curve d, $\hat{h} = 1.020 > \hat{h}_c$ and the minimum is at $\hat{B} = 0$.

normal-state chemical potential Eq. (185), this $\hat{h}_c$ is equal to $\hat{h}_{c2}(\hat{\delta})$ that we have previously calculated Eq. (206b), plotted in the phase diagram (see Figs. 1 and 21). As discussed above, this transition corresponds to a point at which all of the molecules have dissociated into a fully polarized (single species) gas of atoms, with the molecular condensate n_m, characteristic of the SF_M state, vanishing. As such, experimentally (where it is ΔN rather than h that is controlled), the fully polarized normal state corresponds to a single point $\Delta N/N = 1$.

6.4.3. First-order SF_M–N transition: $\hat{\delta}_c < \hat{\delta} < \hat{\delta}_M$

In contrast to the above behavior, for $\hat{\delta} > \hat{\delta}_c$ at fixed density, the continuous transition at $\hat{V}_2 = 0$ [given by $\hat{h}_c$, Eq. (218)] is preempted by a first-order transition. This happens because $\hat{V}_4(\hat{h}, \hat{\delta})$ changes sign (with $e_G(\hat{B})$ still well-defined, stabilized at large $\hat{B}$ by the positive $\hat{V}_6$ term), becoming negative *before* $\hat{V}_2$ has a chance to vanish. We note that as long as $\hat{V}_2 > 0$ (and $\hat{V}_6 > 0$, valid for $\hat{V}_6 > 0$, valid for $\hat{h} \approx \hat{h}_m$ that we are considering here), independent of the sign of $\hat{V}_4$ there is a single $\hat{B} \neq 0$ minimum of Eq. (216) that characterizes the SF_M state. However, for $\hat{V}_4 > 0$ the SF_M state is given by $\hat{B}_+$ solution, while, for $\hat{V}_4 < 0$, it is the B_- solution that corresponds to the SF_M phase. The change in this behavior takes place when $\hat{V}_4 = 0$, corresponding to

$$\hat{h}_* \simeq 1.30\hat{\mu}, \tag{219}$$

[which, incidentally, is the $\mathcal{O}(\gamma^0)$ approximation to $\hat{h}_{c1}$ given in Eq. (209a)] and $\hat{B}_{SF,*} = \hat{B}_-(\hat{V}_4 = 0) = (\hat{V}_6/\hat{V}_2)^{1/4}$.

Once $\hat{V}_4 < 0$, as illustrated in Fig. 28, the shape of $e_G(\hat{B})$ changes qualitatively when $\hat{V}_2$ changes sign. With both $\hat{V}_2$ and $\hat{V}_4$ negative the normal-state extremum at $\hat{B} = 0$ turns into a *local minimum*. (Compare curves a and b in Fig. 28.) Concomitantly, both extrema in Eq. (216) become important, with the $\hat{B}_+$ solution giving the barrier (maximum) separating the SF_M $\hat{B}_-$ minimum from the normal-state minimum at $\hat{B} = 0$. At low $\hat{h} < \hat{h}_c$ (but larger than $\hat{h}_*$), the energy $e_G(\hat{B}_-)$ of the SF_M minimum is lower than that of the normal state (for which $e_G = 0$) and the SF_M remains a stable ground state. However, with increasing $\hat{h}$ the SF_M minimum rises and reaches the normal-state energy at the first-order condition

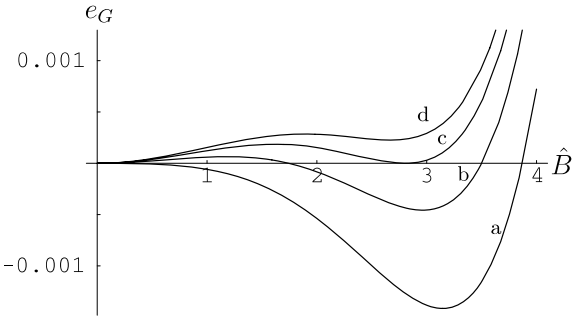

Fig. 28. Evolution of the BEC-regime normalized ground-state energy $e_G(\hat{B})$ Eq. (212), for parameters such that a first-order $SF_M \to N$ transition occurs. Here, $\gamma = 0.1$, $\hat{\delta} = -2$, $\hat{\mu} = -0.921$ and $\hat{h}$ takes four different values: (a) $\hat{h} = 1.317$, so that $\hat{V}_2 > 0$ and $\hat{V}_4 < 0$, (b) $\hat{h} = 1.322$, so that $\hat{V}_2 < 0$ and $\hat{V}_4 < 0$, (c) $\hat{h} = 1.325 = \hat{h}_c$, and (d) $\hat{h} = 1.326 > \hat{h}_c$.

$$0 = -\hat{V}_2\hat{B}_-^2 + \tfrac{1}{2}\hat{V}_4\hat{B}_-^4 + \tfrac{1}{3}\hat{V}_6\hat{B}_-^6, \tag{220}$$

giving

$$\hat{V}_4 = -\tfrac{4}{3}\hat{V}_6\hat{B}_-^2, \tag{221a}$$

or, equivalently (including arguments for clarity),

$$\hat{V}_2[\hat{\delta},\hat{h}_c,\hat{\mu}]\hat{V}_6[\hat{h}_c,\hat{\mu}] = -\frac{3}{16}\hat{V}_4^2[\hat{h}_c,\hat{\mu}], \tag{221b}$$

as the condition for the critical point $\hat{h}_c(\hat{\delta},\hat{\mu})$ of the first-order SF_M-N transition.

As is usual for first-order transitions and as discussed in Section 5 for the BCS regime, the state of the system for $\hat{h} > \hat{h}_c$ is determined by whether the system is kept at fixed chemical potential or at fixed average density (atom number). For the former case the system simply jumps from the SF_M to the normal (fully spin-polarized) state, and the density and magnetization are free to adjust discontinuously to this sudden change in state at $\hat{h}_c$.

On the other hand, for atom number fixed at N, a discontinuous change of state is not an option available to the system as this would require a change in N (and ΔN) that are fixed. As explained in Section 5.3, upon increasing $\hat{h}$, the system tunes its chemical potential to remain on the critical curve $\hat{h}_c(\hat{\delta},\hat{\mu})$ and instead phase separates into coexisting SF_M and normal states, in proportions so as to satisfy the imposed total number constraint.

We conclude this subsection by noting that the regime of phase separation (PS) at negative detuning consists of SF_M–N coexistence only for sufficiently low $\hat{\delta}$. At larger $\hat{\delta}$, the SF_M phase ceases to exist and the coexistence is between N and SF phases (as we find at low detunings in the BCS regime). To determine the boundary separating these possibilities, we note that, in the regime of phase separation, $\hat{h} = \hat{h}_c(\hat{\mu})$ with $\hat{h}_c$ approximately given by Eq. (221b). Implementing the constraint $4/3 = x\hat{n}_{SF} + (1-x)\hat{n}_N$ (where here SF can refer to the SF or SF_M states) allows us to study, numerically, the negative-detuning PS regime. The dashed line in Fig. 21 denotes where, in the PS regime, $\hat{h}_c = \hat{h}_m$ (indicating a continuous SF–SF_M transition inside the PS regime) and the dashed line in the fixed-polarization phase diagram Fig. 22 is thus obtained by converting this $\hat{h}$ boundary to polarization $\Delta N/N$.

6.5. Finite γ corrections to the SF_M–N phase-separation boundaries

Here, we use results of the previous section for the SF_M–N first-order transition (occurring for $\hat{\delta}_c < \hat{\delta} < \hat{\delta}_M$) to compute the phase-separation boundaries, correcting our previous $\mathcal{O}(\gamma^0)$ results. At fixed chemical potential difference (rather than polarization), the boundaries are $\hat{h}_{c1}(\hat{\delta})$ and $\hat{h}_{c2}(\hat{\delta})$, to zeroth order in γ given by Eqs. (209b) and (190b), respectively.

First focusing on $\hat{h}_{c1}(\hat{\delta})$, corrections to its zeroth order expression Eq. (209b) have two sources. One is the correction to the approximation of the chemical potential by $\hat{\mu} \approx \hat{\delta}/2$, only valid to $\mathcal{O}(\gamma^0)$. The other source of approximation is the location of the transition by $\hat{V}_4 = 0$, that is more accurately given by Eq. (221b).

To determine $\hat{\mu}(\hat{\delta},\hat{h})$ more accurately we turn to its defining equation, Eq. (197b), that can be written as

$$\hat{\delta} - 2\hat{\mu} = -\frac{\gamma\sqrt{|\hat{\mu}|}\pi}{2} - \gamma\sqrt{|\hat{\mu}|}\left[\sqrt{\hat{h}/|\hat{\mu}| - 1} - \tan^{-1}\sqrt{\hat{h}/|\hat{\mu}| - 1}\right]. \tag{222}$$

To first order in γ and near $\hat{h}_{c1}$ (of interest to us) Eq. (222) can be considerably simplified by replacing $\hat{h}$ by $\hat{h}_{c1}$, with the latter approximated by its zeroth order value in γ, Eq. (209a). This gives

$$\hat{\delta} - 2\hat{\mu} \approx -\frac{\gamma\sqrt{|\hat{\mu}|}\pi}{2} - 0.047\gamma\sqrt{|\hat{\mu}|}, \tag{223}$$

which, when solved for $\hat{\mu}$ gives

$$\hat{\mu} \approx \hat{\mu}^{(1)}(\hat{\delta}) \equiv -\frac{1}{64}\left(-\gamma'\pi + \sqrt{(\gamma'\pi)^2 + 32|\hat{\delta}|}\right)^2, \tag{224}$$

where $\gamma' \equiv \gamma[1 + 2(0.047)/\pi]$.

The second correction to $\hat{h}_{c1}$ comes from using the proper equation, Eq. (221a), (rather than $\hat{V}_4 = 0$) as the location of the first-order transition and the lower-field phase boundary $\hat{h}_{c1}(\delta)$. We write $\hat{h}_{c1} = \hat{h}_{c1}^{(0)} + \hat{h}_{c1}^{(1)}$, with $\hat{h}_{c1}^{(0)}$ the $\mathcal{O}(\gamma^0)$ expression given by Eq. (209a) and $\hat{h}_{c1}^{(1)}$ the correction of $\mathcal{O}(\gamma)$. Using Eqs. (193b) and (213a), as well as the $\mathcal{O}(\gamma^0)$ expression for $\hat{B}^2$ [i.e. Eq. (188)] along with Eq. (221a) leads to

$$F_4\left[\frac{\hat{h}_{c1}^{(0)} + \hat{h}_{c1}^{(1)}}{|\hat{\mu}|}\right] = -\frac{8\gamma}{3\pi|\hat{\mu}|^2}\left[1 - \frac{1}{2}(\hat{h}_{c1}^{(0)} - |\hat{\mu}|)^{\frac{3}{2}}\right]F_6\left[\frac{\hat{h}_{c1}^{(0)}}{|\hat{\mu}|}\right], \tag{225}$$

where on the right side we neglected $\hat{h}_{c1}^{(1)}$, valid to order $\mathcal{O}(\gamma)$. Expanding the left-hand side in small $\hat{h}_{c1}^{(1)}$, and using the fact that $F_4[\hat{h}_{c1}^{(0)}/|\hat{\mu}|] = F_4[1.30] = 0$ (Eq. (209a) above), $F'_4[1.30] = -0.74$ and $F_6[1.30] = 0.134$, we find

$$\hat{h}_{c1}^{(1)} \approx \frac{0.154\gamma}{|\hat{\mu}|}[1 - 0.082|\hat{\mu}|^{3/2}], \tag{226}$$

yielding

$$\hat{h}_{c1} \approx 1.30|\hat{\mu}| + \frac{0.154\gamma}{|\hat{\mu}|}[1 - 0.082|\hat{\mu}|^{3/2}]. \tag{227}$$

Now using $\hat{\mu}(\hat{\delta})$ in Eq. (227) we finally obtain to $\mathcal{O}(\gamma)$

$$\hat{h}_{c1}(\hat{\delta}) \approx 1.30|\hat{\mu}^{(1)}(\hat{\delta})| + \frac{\gamma 0.308}{|\hat{\delta}|}[1 - 0.029|\hat{\delta}|^{3/2}], \tag{228}$$

that we plot in Fig. 29, as a function of detuning δ (on the BEC side of $\delta < 0$) and compare it to a numerical determination of $\hat{h}_{c1}$ directly from the full ground-state energy Eq. (107).

Also, as illustrated in Fig. 30, for $\hat{\delta} = -2$, the linear decrease of $\hat{h}_{c1}$ with increasing γ exhibited in Eq. (228) also compares well for small γ with the γ dependence of the numerical solution (points). We expect the resulting increase in the regime of phase separation to remain qualitatively correct beyond this narrow-resonance ($\gamma \ll 1$) limit.

The above result for $\hat{h}_{c1}(\hat{\delta})$ can be easily translated into a critical polarization $\Delta N_{c1}(\delta)$ that is relevant for fixed spin-species number difference (fixed polarization) by inserting $\hat{h}_{c1}$, $\hat{\mu}(\hat{\delta})$ and $\hat{B}^2$ inside $\hat{m}(\hat{h})$, Eq. (179), that gives for the lower-critical polarization

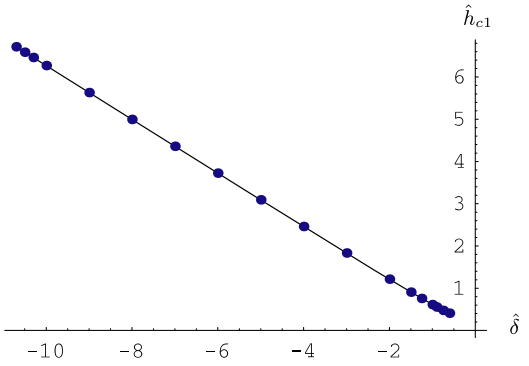

Fig. 29. Plot of $\hat{h}_{c1}(\hat{\delta}, \gamma = 0.1)$, the normalized lower chemical potential difference above which the system enters the regime of phase separation. The points are a numerical computation and the solid line is Eq. (228).

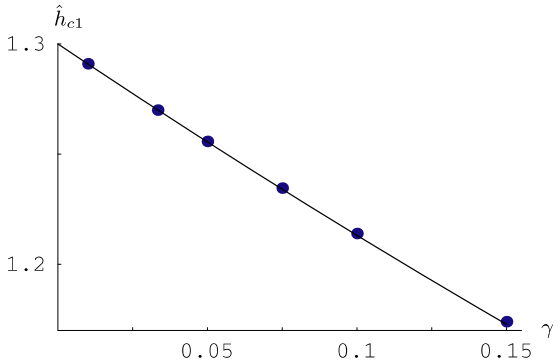

Fig. 30. Plot of $\hat{h}_{c1}(\hat{\delta}, \gamma)$ at one particular detuning ($\hat{\delta} = -2$) as a function of resonance width parameter γ.

$$\frac{\Delta N_{c1}}{N} = \frac{1}{2}\left(\sqrt{\hat{h}_{c1}^2 - \frac{2}{3}\gamma(1 - 0.029|\hat{\delta}|^{3/2})} - |\hat{\mu}^{(1)}|\right)^{\frac{3}{2}}, \tag{229}$$

above which the system phase separates into coexisting $\mathrm{SF_M}$ and N states.

We can also use Eq. (228) to compute the critical detuning $\hat{\delta}_M$ beyond which the $\mathrm{SF_M}$ phase ceases to exist and the PS is replaced by N–SF coexistence (as on the BCS side of the Feshbach resonance). It is determined by the point where $\hat{h}_m(\hat{\delta})$ and $\hat{h}_{c1}(\hat{\delta})$ intersect, i.e., $\hat{h}_m(\hat{\delta}_M) = \hat{h}_{c1}(\hat{\delta}_M)$, or equivalently $\Delta N_{c1}(\hat{\delta}_M) = 0$. Using the former condition, to $\mathcal{O}(\gamma)$ we find

$$1.69|\hat{\mu}|^2 + 0.40\gamma[1 - 0.082|\hat{\mu}|^{3/2}] = |\hat{\mu}|^2 + \frac{2}{3}\gamma, \tag{230}$$

that gives to leading order in γ

$$\hat{\mu}_M = -0.62\sqrt{\gamma}, \tag{231}$$

for the chemical potential at this intersection. Using the zeroth order relation $\hat{\mu} = \hat{\delta}/2$ gives, to leading order in γ,

$$\hat{\delta}_{\mathrm{M}} \approx -1.24\sqrt{\gamma}, \tag{232}$$

a result that compares favorably (see Fig. 21) with the numerical solution (solid point).

We turn next to the calculation of the upper-critical boundary, $\hat{h}_{c2}(\hat{\delta})$, of the phase-separation region. This is defined by where the normal-state chemical potential $\hat{\mu}_{\mathrm{N}}(\hat{h}, n) = 2^{2/3} - \hat{h}$ (Eq. (185)) intersects the first-order condition Eq. (221b). This yields the self-consistent set of equations

$$\hat{V}_2[\hat{\delta}, \hat{h}_{c2}, \hat{\mu}_{\mathrm{N}}] = -\frac{3}{16}\frac{\hat{V}_4[\hat{h}_{c2}, \hat{\mu}_{\mathrm{N}}]^2}{\hat{V}_6[\hat{h}_{c2}, \hat{\mu}_{\mathrm{N}}]}, \tag{233a}$$

$$\hat{\mu}_{\mathrm{N}} = 2^{2/3} - \hat{h}_{c2}, \tag{233b}$$

an expression that applies for $\delta > \delta_c$ (where the sixth-order expansion applies). Recall that, close to the first-order transition $\hat{h}_c$, $\hat{V}_4$ vanishes allowing a secondary minimum in e_{G} to form at $\hat{B} = 0$. This vanishing implies that the right side of Eq. (233a) is numerically small near $\hat{h}_c$ and may therefore be neglected (despite being formally of the same order in γ as the left side). This reduces Eq. (233a) to our previous approximate result Eq. (206b), derived assuming a second-order $\mathrm{SF_M}$–N transition at the point where $\hat{V}_2$ changes sign, and shows why Eq. (206b) accurately determines $\hat{h}_{c2}$ even in the first-order regime, as shown in Fig. 31.

In fact, Eq. (233a) shows that the true $\hat{h}_{c2}$ is slightly higher than that predicted by $\hat{V}_2 = 0$, since $\hat{V}_2 < 0$ in the N state and the right side is negative. This is as expected, as the first-order transition (that takes place for $\hat{\delta} > \hat{\delta}_c$) always precedes the spinodal point $\hat{V}_2 = 0$ at which the metastability of the normal state is lost.

6.6. Fixed chemical potential

Having determined the BEC-regime phase diagram for the physically-relevant case of fixed total atom density and population difference, for completeness in the present section

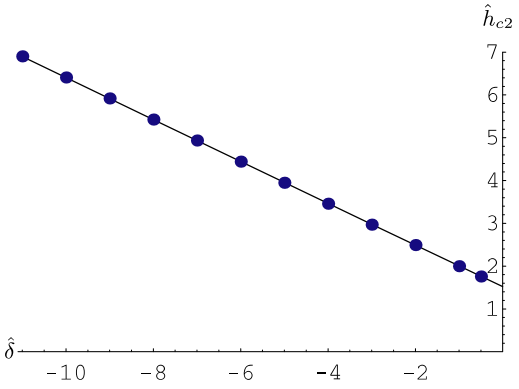

Fig. 31. Plot of $\hat{h}_{c2}(\hat{\delta})$, the normalized upper-critical chemical potential difference above which the system enters the normal (N) phase. The points are a numerical computation and the solid line is Eq. (206b).

we compute the phase diagram in the grand-canonical ensemble of fixed $\hat{\mu}$ and $\hat{h}$. Of course, in the grand-canonical ensemble there is no regime of phase separation. Thus, our main task is to find the critical curves for the first- and second-order phase transitions, focusing on the physically interesting regime of $\hat{\mu}$ near $\hat{\delta}/2$. This can be done by utilizing results derived in Sections 6.4.2 and 6.4.3. Starting in the singlet SF state at $\hat{h} = 0$, characterized by an effective bosonic chemical potential $\hat{\mu}_m = 2\hat{\mu} - \hat{\delta} + \mathcal{O}(\gamma)$, and lowering $\hat{\mu}$ from $> \hat{\delta}/2 + \mathcal{O}(\gamma)$ to $< \hat{\delta}/2 + \mathcal{O}(\gamma)$, the system undergoes a continuous transition from a molecular SF to a vacuum of molecules (and atoms, since $\hat{\mu} < 0$). More generally it is defined by the vanishing of the quadratic coefficient $\hat{V}_2[\hat{\delta}, \hat{h}, \hat{\mu}]$, giving

$$\hat{\mu}_c(\hat{\delta}, \hat{h} < \hat{h}_m) = -\frac{1}{64}\left(-\gamma\pi + \sqrt{(\gamma\pi)^2 + 32|\hat{\delta}|}\right)^2. \tag{234}$$

Since, for small $\hat{h} < \hat{h}_m$, the Landau coefficients $\hat{V}_\alpha$ are h-independent, the above result holds at $\hat{h} < \hat{h}_m$, leading to a strictly vertical SF-vacuum phase boundary (see Fig. 32).

Starting in this vacuum state ($\hat{\mu} < \hat{\mu}_c$), with increasing $\hat{h}$ the system undergoes a transition to the spin-polarized N state as $\hat{\mu}_\uparrow$ changes from negative to positive leading to a finite density of spin-up fermions (but still $\hat{B} = 0$, since $\hat{\mu} < \hat{\mu}_c$). We indicate this phase boundary in Fig. 32 by a (nearly) horizontal line.

Starting instead in the SF state at $\hat{\mu} > \hat{\mu}_c$ and increasing $\hat{h}$, a continuous SF-SF_M transition takes place as $\hat{m}$ becomes nonzero at $\hat{h}_m$. Using Eq. (204b) for $\hat{h}_m$ (approximately equal to $|\hat{\mu}|$ near the SF-to-Vacuum transition but strongly deviating from it at larger $\hat{\mu}$) along with Eq. (216), $\hat{B}_+^2$, for the normalized molecular density, yields the SF-to-SF_M boundary shown in Fig. 32.

As discussed in Section 6.4 there are two possibilities for exiting the resulting SF_M state into the N state. (i) If $\hat{V}_2$ changes sign (from positive to negative) *before* $\hat{V}_4$ becomes negative, the SF_M–N transition is second-order, and given by Eq. (218). (ii) If $\hat{V}_4$ becomes negative while $\hat{V}_2$ is still positive, then the SF_M–N transition is first-order. The tricritical

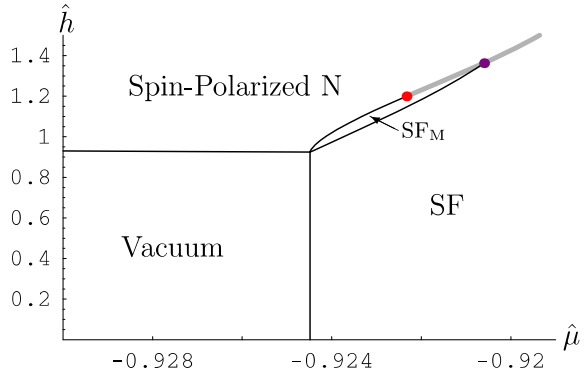

Fig. 32. Negative-detuning phase diagram in the grand-canonical ensemble at detuning $\hat{\delta} = -2$ and width $\gamma = 0.1$ showing superfluid (SF), magnetic superfluid (SF_M, thin region indicated by arrow), vacuum and normal spin-↑ phases. Black curves are continuous transitions and the gray curve is a first-order transition. The SF_M phase undergoes either a continuous [to the left of the red point at (−0.922,1.20)] or first-order [to the right of the red point] transition to the N phase. To the right of the purple point at (−0.9206,1.36), the SF_M phase ceases to exist and there is a direct first-order SF-to-N transition. (For interpretation of the references to color in this figure legend, the reader is referred to the web version of this paper.)

point [129] (whose existence was also recently confirmed and extended to finite temperature in Ref. [78]) $\hat{V}_4(\hat{h}_c, \hat{\mu}) = 0$ separating these two scenarios is indicated by a red solid point, with $\hat{V}_4 < 0$ (and transition first-order) and $\hat{V}_4 > 0$ (and transition second-order) to the right and left of this point, respectively. The gray curve indicates the first-order SF_M-to-N transition [computed using Eq. (221b)].

At larger $\hat{\mu}$, to the right on the figure, $\hat{h}_m$ intersects the first-order curve at the purple point at (−.9206,1.36). To the right of this point, the SF_M phase ceases to exist and there is a direct SF-to-N first-order transition. Note that, in this regime, our sixth-order approximation begins to be quantitatively invalid. However, this basic qualitative picture can be validated by directly (numerically) minimizing the full normalized ground-state energy Eq. (107).

6.7. Bogoliubov sound velocity in SF_M phase

In our earlier computation of $e_G(\hat{B})$, Eq. (192), among other quantities, we have obtained an effective four-boson coupling $\hat{V}_4(\hat{h}, \hat{\delta})$ that at zero molecular density is equivalent to the molecular T-matrix proportional to the molecular scattering amplitude. Thus, $\hat{V}_4(\hat{h}, \hat{\delta})$ is related to the molecular scattering length a_m, which is a measure of the effective molecular interaction induced by the Feshbach resonance coupling to atoms. We have found that, inside the SF_M phase, $\hat{V}_4(\hat{h}, \hat{\delta})$ is positive but decreases with increasing $\hat{h}$ and in fact nearly (to $\mathcal{O}(\gamma)$) vanishes at the boundary $\hat{h}_{c1}(\hat{\delta})$ to phase separation; see Eq. (209b) and the discussion in Section 6.3. Physically this represents a *repulsive* molecular Bose gas whose two-body repulsion nearly vanishes with increasing $\hat{h}$ at the transition to phase separation at $\hat{h}_{c1}(\hat{\delta})$.

A striking observable consequence of this is a concomitant suppression of the Bogoliubov sound velocity $u(\delta,\hat{h})$ with increasing $\hat{h}$ or population difference ΔN. The simplest way to obtain u is to use the standard result [117]

$$u^2 = \frac{1}{2m}\frac{\partial P}{\partial |B|^2}, \tag{235}$$

(recall the boson mass is $2m$), where P is the pressure.

Since the grand-canonical energy E_G is equal to $-PV$ with V the system volume, we have, plugging $\hat{B}^2 \simeq \hat{V}_2/\hat{V}_4$ into Eq. (212) (neglecting $\hat{V}_6$),

$$P = \frac{1}{2N(\epsilon_F)} B^4 \hat{V}_4, \tag{236}$$

where for clarity we have temporarily reverted to dimensionful quantities. Evaluating the derivative, and reverting back to the dimensionless boson density $\hat{B}^2 = B^2/c\epsilon_F^{3/2}$, we have

$$u^2 = \frac{\gamma^2 \pi \epsilon_F \hat{B}^2}{32m|\hat{\mu}|^{3/2}} F_4(\hat{h}/|\hat{\mu}|). \tag{237}$$

As we are primarily interested in fixed density, we insert the fixed-density expressions $\hat{\mu} \approx \hat{\delta}/2$ [valid to $\mathcal{O}(\gamma)$ on the BEC side of the resonance] and Eq. (188) for $\hat{B}^2$, yielding

$$u^2 \simeq u_0^2 \left[1 - \frac{1}{2}\left(\hat{h} - \frac{|\hat{\delta}|}{2}\right)^{3/2} \Theta\left(h - \frac{|\hat{\delta}|}{2}\right)\right] F_4\left(\frac{2\hat{h}}{|\hat{\delta}|}\right), \tag{238}$$

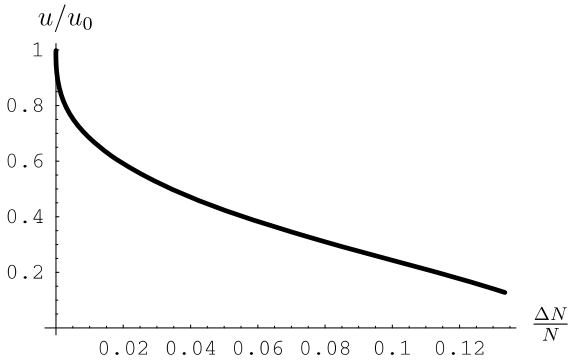

Fig. 33. Bogoliubov sound velocity u/u_0 as a function of polarization for the case $\hat{\delta} = -3$.

with u_0 the Bogoliubov sound velocity for $h = 0$ (i.e., in the SF phase)

$$u_0 = \frac{2^{3/4}\sqrt{\pi}\gamma}{8\sqrt{3}} \frac{v_F}{|\hat{\delta}|^{3/4}}. \tag{239}$$

Finally converting to fixed total density and population difference, we have

$$u \simeq u_0 \sqrt{1 - \frac{\Delta N}{N}} \sqrt{F_4 \left(1 + \frac{2^{5/3}}{|\hat{\delta}|} \left(\frac{\Delta N}{N}\right)^{2/3}\right)}, \tag{240}$$

for the sound velocity as a function of applied polarization. Note that there are two ways u can vanish with increasing ΔN, depending on whether the detuning is larger or smaller than δ_c, and, correspondingly, whether the transition is first or second order. For $\hat{\delta} > \hat{\delta}_c$, u (nearly; see Ref. [130]) vanishes at the first-order instability of the SF_M state to phase separation, when F_4 vanishes, as we have already discussed. For $\hat{\delta} < \hat{\delta}_c$, however, F_4 remains positive at the second-order SF_M to N transition. In this case, u vanishes at this second-order transition simply because the molecular density vanishes as $\Delta N \to N$.

In Fig. 33, we plot u/u_0 as a function of $\Delta N/N$ for the case $\hat{\delta} = -3$ and $\gamma = 0.1$, showing its suppression near the first-order transition at $\frac{\Delta N_{c1}}{N} \approx 0.133$, where it exhibits a jump discontinuity to zero (before $\hat{V}_4(\Delta N)$ actually vanishes [130]) upon entering the PS regime.

7. FFLO state of two-channel model

Until this point, we have focused on ground states of the two-channel Hamiltonian Eq. (61) assuming $\mathbf{Q} = 0$ pairing. However, it is well-known [86,87] that the BCS model (which our model corresponds to in the large positive detuning limit) under applied chemical potential difference possesses an alternative minimum, characterized by both periodic off-diagonal long-range pairing order and nonzero magnetization. Such states, which we generally refer to as FFLO states, break translational and rotational symmetries (and hence are examples of a supersolid [96–99]) and exhibit a compromise between the tendency to pair (due to attractive interactions) and the tendency to magnetize (due to the applied chemical potential difference h).

As we will show, deep in the BCS regime $\delta \gg 2\epsilon_F$, where the resonant two-channel model reduces to the BCS model, we reproduce well-known results in the literature

[86,87]. Our main contribution is the extension of these results on FFLO ground states to a resonant model at arbitrary detuning δ. We thereby predict the evolution of the FFLO state [i.e., we predict $Q(\delta,h)$ and the FFLO phase boundary] for δ outside the well-studied BCS regime. In terms of the phase diagram, our main prediction is that the FFLO state is unstable, i.e., squeezed out by the phase-separation regime and the normal state, for $\delta < \delta_* \simeq 2\epsilon_F$.

As we have already noted, we expect that FFLO-type ground states of Eq. (61) are adequately modeled [102] by assuming single-harmonic pairing, namely taking the pairing order to be $\Delta(\mathbf{r}) = \Delta_{\mathbf{Q}} e^{i\mathbf{Q}\cdot\mathbf{r}}$. With this assumption, it is straightforward (as we already have done in Section 4) to find the ground state energy $E_G(\Delta_{\mathbf{Q}},\mathbf{Q})$ as a function of wavevector $\mathbf{Q}$ and gap $\Delta_{\mathbf{Q}}$, and then to minimize $E_G(\Delta_{\mathbf{Q}},\mathbf{Q})$ over these parameters.

Our analysis is very similar to that of FF [86], though generalized to the present two-channel resonant Hamiltonian Eq. (61). Thus, our results differ from those of FF only away from the deep BCS limit. For $\delta \gg 2\epsilon_F$, however, our results map onto those of FF, finding that, instead of a phase transition from the SF to the N state at $h_c \simeq \Delta_{BCS}/\sqrt{2}$ (see Fig. 1), the FFLO state intervenes, so that there is a first-order SF to FFLO transition, followed by a second-order [105] FFLO to N transition at h_{FFLO}.

We now determine the region of the phase diagram in which the FFLO state has the lowest energy. The governing (variational) ground-state energy is given by Eq. (75) that we redisplay here for convenience:

$$\begin{aligned} E_G(\Delta_{\mathbf{Q}},\mathbf{Q}) = &\left(\frac{\epsilon_Q}{2} + \delta_0 - 2\mu\right)\frac{\Delta_{\mathbf{Q}}^2}{g^2} - \sum_k (E_k - \varepsilon_k) \\ &+ \sum_{\mathbf{k}} E_k(1 + \Theta(-E_{k\uparrow}) - \Theta(E_{k\downarrow}))) \\ &+ \sum_{\mathbf{k}} \left(\frac{\mathbf{k}\cdot\mathbf{Q}}{2m} + h\right)(1 - \Theta(-E_{k\uparrow}) - \Theta(E_{k\downarrow})). \end{aligned} \tag{241}$$

For the $\mathbf{Q} = 0$ case, we have already evaluated the first momentum sum appearing in Eq. (241). Examining Eqs. (74a) and (74b) reveals that, for this sum, having $\mathbf{Q} \neq 0$ simply shifts the chemical potential $\mu \to \tilde{\mu} \equiv \mu - Q^2/8m$. The remaining "excluded" sums in Eq. (241) (second and third lines) can also be evaluated [within the standard approximation of replacing $N(\epsilon) \to N(\epsilon_F)$, valid in the atomic degenerate limit of $\Delta/\mu \ll 1$] following FF; we do this in Appendix F. This yields

$$\begin{aligned} E_G \approx &-\frac{8}{15}N(\tilde{\mu})\tilde{\mu}^2 + \left(\frac{\epsilon_Q}{2} + \delta - 2\mu\right)\frac{\Delta_{\mathbf{Q}}^2}{g^2} + 2N(\tilde{\mu})\left(-\frac{\Delta_{\mathbf{Q}}^2}{4} + \frac{\Delta_{\mathbf{Q}}^2}{2}\ln\frac{\Delta_{\mathbf{Q}}}{8e^{-2}\tilde{\mu}}\right) \\ &+ \frac{N(\tilde{\mu})\Delta_{\mathbf{Q}}^2}{2\bar{Q}}\left[I(\bar{Q}+\bar{h}) - I(\bar{h}-\bar{Q}) + I(\bar{Q}-\bar{h})\right], \end{aligned} \tag{242}$$

where $I(x)$ is given by

$$I(x) \equiv \left[-\frac{1}{3}(x^2-1)^{3/2} - \sqrt{x^2-1} + x\cosh^{-1}x\right]\Theta(x-1), \tag{243}$$

and, using notation similar to that of FF, we have defined the rescaled wavevector $\bar{Q}$ and chemical potential difference $\bar{h}$:

$$\bar{Q} \equiv \frac{\tilde{k}_F Q}{2m\Delta_{\mathbf{Q}}}, \tag{244a}$$

$$\bar{h} \equiv \frac{h}{\Delta_{\mathbf{Q}}}, \tag{244b}$$

with $\tilde{k}_F = \sqrt{2m\tilde{\mu}}$ the Fermi wavevector associated with the shifted chemical potential. We note that E_G, Eq. (242), is consistent with FF, differing only in the ϵ_Q term that accounts for the molecular kinetic energy absent in the BCS-like model of FF.

From this point on, the determination of the phase diagram and the corresponding phases is conceptually simple, given by the minimization of $E_G(\Delta_{\mathbf{Q}},\mathbf{Q})$ with respect to $\mathbf{Q}$ and $\Delta_{\mathbf{Q}}$ (while satisfying the total number constraint). However, because the general structure of Eq. (242) is quite complicated, to do this generally is technically challenging and best done numerically. Nevertheless, analytical solutions are possible in a number of important limits.

We now briefly overview the structure of $E_G(\Delta_{\mathbf{Q}},\mathbf{Q})$, Eq. (242). At small Q, only the terms $\propto [I(\bar{Q}+\bar{h}) - I(\bar{h}-\bar{Q})]$ are nonzero; in the $Q \to 0$ limit these conspire so that Eq. (242) reduces to our previous result Eq. (118), from Section 5.2. At small h, the SF state studied in that section is still a stable minimum of Eq. (242) at $\Delta_{\mathbf{Q}} = \Delta_{BCS}$, $\mathbf{Q} = 0$, and remains so until the critical chemical potential difference h_c (that is remarkably close to the critical h studied in Section 5.2, approximated by $h_c \simeq \Delta_{BCS}/\sqrt{2}$). Already below h_c, $E_G(\Delta_{\mathbf{Q}},\mathbf{Q})$ exhibits a secondary *local* minimum at the FFLO-state $(\Delta_{\mathbf{Q}},\mathbf{Q})$ and, for $h > h_c$, there is a first-order transition into this magnetized finite-$\mathbf{Q}$ FFLO state that is nearly degenerate with the $\Delta_{\mathbf{Q}} = 0$ normal state. The FFLO state is only stable for a narrow window of h values (and sufficiently large detuning), undergoing a continuous transition to the N state at h_{FFLO}.

7.1. Second-order N–FFLO transition

Before studying the first-order SF–FFLO transition, it is convenient to first look at the simpler transition from the N state, that takes place upon lowering h from a large value. As was first shown by FF [86], this N–FFLO transition is in fact continuous in mean-field theory [105] of the standard Landau type.

This is possible because, for sufficiently large Q and small $\Delta_{\mathbf{Q}}$, the excluded-sum terms [i.e. the last line of Eq. (242)] convert the double minimum form of $E_G(\Delta_{\mathbf{Q}})$ (characteristic of the first-order transition that would take place at $Q = 0$) to a single, h,δ-dependent minimum that leads to a continuous N–FFLO transition.

The continuous nature of the N–FFLO transition allows us to accurately study its details by expanding $E_G(\Delta_{\mathbf{Q}},\mathbf{Q})$ in small $\Delta_{\mathbf{Q}}$. Since we expect the transition to take place at finite h (that we call h_{FFLO}) and finite $\mathbf{Q}$, its Landau expansion in small $\Delta_{\mathbf{Q}}$ is characterized by the large $\bar{Q}$, $\bar{h}$ limit as both are proportional to $1/\Delta_{\mathbf{Q}}$ according to Eqs. (244a), (244b). As we will verify a posteriori, the existence of the continuous N–FFLO transition furthermore requires, near h_{FFLO}, the system to be in the "doubly-depaired" (or "D") regime (in the notation of FF), characterized by $\bar{Q}+\bar{h} > 1$ and $\bar{Q}-\bar{h} > 1$, i.e., a regime in which excluded-sum contributions for both atom species (spin up and down) are nonzero. In this regime, the term $\propto I(\bar{h}-\bar{Q})$ vanishes and, to leading order, the other two excluded-sum terms give

$$I(\bar{Q}+\bar{h})+I(\bar{Q}-\bar{h}) \approx -\frac{2}{3}\bar{Q}^3 - 2\bar{Q}\bar{h}^2 - \bar{Q} + \bar{Q}\ln 4(\bar{Q}+\bar{h})(\bar{Q}-\bar{h}) + \bar{h}\ln\frac{\bar{Q}+\bar{h}}{\bar{Q}-\bar{h}} + \frac{1}{4}\left(\frac{\bar{Q}}{\bar{Q}^2-\bar{h}^2}\right), \tag{245}$$

where we utilized the expansion of $I(x)$ for large value of its argument:

$$I(x) \approx \Theta(x-1)\left[-\frac{x^3}{3} + \left(-\frac{1}{2}+\ln 2x\right)x + \frac{1}{8x}\right]. \tag{246}$$

As we will see, the above expansion Eq. (245) [to be used inside Eq. (242)] is sufficient to get a Landau expansion of $E_G(\Delta_{\mathbf{Q}},\mathbf{Q})$ up to fourth order in $\Delta_{\mathbf{Q}}$, required to capture the second-order N–FFLO transition. We furthermore expand the first term in Eq. (242) in small Q, finding

$$\frac{8}{15}N(\tilde{\mu})\tilde{\mu}^2 \approx \frac{8}{15}N(\mu)\mu^2 + \frac{1}{3}N(\mu)\bar{Q}^2\Delta_{\mathbf{Q}}^2. \tag{247}$$

It is easy to convince oneself that to lowest order necessary to capture this transition, in all other terms $\tilde{\mu}$ can be approximated by its unshifted ($Q=0$) value μ. Now, reverting to our dimensionless variables $\hat{\Delta}_{\mathbf{Q}}$, $\hat{\mu}$, and $\hat{h}$ [defined in Eqs. (105a), (105b), (105c), (105d), (105e)], defining a new dimensionless momentum

$$\hat{Q} \equiv \sqrt{\hat{\mu}}\frac{Q}{k_F}, \tag{248}$$

and combining Eqs. (247) and (245) inside E_G, Eq. (242), we obtain the sought-after quartic (in $\hat{\Delta}_{\mathbf{Q}}$) Landau expansion for the normalized ground-state energy e_G Eq. (105e):

$$e_G \approx -\frac{8}{15}\hat{\mu}^{5/2} + \frac{\gamma^{-1}\hat{Q}^2\hat{\Delta}_{\mathbf{Q}}^2}{2\hat{\mu}} + \sqrt{\hat{\mu}}\left[-\hat{\Delta}_{\mathbf{Q}}^2 - \hat{h}^2 + \frac{\hat{\Delta}_{\mathbf{Q}}^2}{2}\ln\frac{4(\hat{Q}+\hat{h})(\hat{Q}-\hat{h})}{\hat{\Delta}_{\mathrm{BCS}}^2} + \frac{\hat{h}\hat{\Delta}_{\mathbf{Q}}^2}{2\hat{Q}}\ln\frac{\hat{Q}+\hat{h}}{\hat{Q}-\hat{h}} + \frac{\hat{\Delta}_{\mathbf{Q}}^4}{8}\frac{1}{\hat{Q}^2-\hat{h}^2}\right], \tag{249}$$

where we used the zero-field ($\hat{h}=0$) BCS gap

$$\hat{\Delta}_{\mathrm{BCS}} = 8\mathrm{e}^{-2}\hat{\mu}\mathrm{e}^{-\gamma^{-1}(\hat{\delta}-2\hat{\mu})/\sqrt{\hat{\mu}}}, \tag{250}$$

to simplify the final expression. We note that in e_G, Eq. (249), an important cancellation of the nonanalytic $\hat{\Delta}_{\mathbf{Q}}^2\ln\hat{\Delta}_{\mathbf{Q}}$ terms has taken place. Namely, the $\hat{\Delta}_{\mathbf{Q}}^2\ln\hat{\Delta}_{\mathbf{Q}}$ term, characterizing the $\hat{h}=0$ BCS ground state energy (guaranteeing that a continuum, $\hat{h}=0$ degenerate Fermi gas with arbitrarily weak attractive interactions is always unstable to paired superfluidity) is exactly canceled by such a term arising from the finite-$\hat{h}$ excluded-sum contribution.

Minimizing E_G over $\hat{\Delta}_{\mathbf{Q}}$ (the gap equation), $\hat{Q}$ (which ensures that the total momentum vanishes in equilibrium [89]) and differentiating with respect to $\hat{\mu}$ [to obtain the number equation, Eq. (110b)] we obtain near the N–FFLO transition

$$\hat{\Delta}_{\mathbf{Q}}^2 \simeq 2\hat{h}^2(\lambda^2-1)\left[2-\frac{\gamma^{-1}\hat{h}^2}{\hat{\mu}^{3/2}}\lambda^2-\ln\frac{4\hat{h}^2(\lambda^2-1)}{\hat{\Delta}_{\mathrm{BCS}}^2}-\frac{1}{\lambda}\ln\frac{\lambda+1}{\lambda-1}\right], \tag{251a}$$

$$0 \simeq \frac{\gamma^{-1}\hat{h}^2}{\hat{\mu}^{3/2}}\lambda^2+1-\frac{1}{2\lambda}\ln\frac{\lambda+1}{\lambda-1}, \tag{251b}$$

$$\frac{4}{3} \simeq \frac{4}{3}\hat{\mu}^{3/2}+2\gamma^{-1}\hat{\Delta}_{\mathbf{Q}}^2+\frac{\hat{h}^2}{2\sqrt{\hat{\mu}}}, \tag{251c}$$

where we only kept terms to leading order in $\hat{\Delta}_{\mathbf{Q}}$ and γ and defined $\lambda = \hat{Q}/\hat{h}$. The simultaneous numerical solution to these equations yields $\hat{\Delta}_{\mathbf{Q}}$ and $\mathbf{Q}$ in the FFLO phase, as well as the critical chemical potential difference $\hat{h}_{\mathrm{FFLO}}$ above which $\hat{\Delta}_{\mathbf{Q}} \to 0$.

In Fig. 34 we plot, for $\gamma = 0.1$, $\hat{h}_{\mathrm{FFLO}}$ as a function of normalized detuning, along with $\hat{h}_{c1}$ and $\hat{h}_{c2}$. In Fig. 35, we plot the FFLO wavevector $Q(\hat{\delta}, \hat{h}_{\mathrm{FFLO}})$ at the transition [$Q(\hat{\delta}, \hat{h})$ is only weakly $\hat{h}$-dependent near the transition]. Indeed, the fact that Q is finite at the transition is consistent with our large $\bar{Q}, \bar{h}$ expansion above. To get an idea of the typical magnitude of pairing in the FFLO phase, in Fig. 36 we plot $\hat{\Delta}_Q(\hat{\delta}, \hat{h}_{c2})$, i.e., the strength of pairing at the FFLO-to-phase-separation phase boundary. To gain some intuition for these numerical results we examine analytically the solution to Eqs. (251a), (251b), (251c) in the large detuning ($\hat{\delta} \gg 1$) limit. In this regime, we can safely neglect the first term of Eq. (251b), as near the transition $\hat{h}^2 \approx \hat{h}_{\mathrm{FFLO}}^2 \ll \gamma$, with the latter inequality arising from simplest estimate of $\hat{h}_{\mathrm{FFLO}} \sim \hat{\Delta}_{\mathrm{BCS}}$. Our dropping of this first term in Eq. (251b) can be traced back to a neglect of the molecular dispersion, reducing our two-channel model to a single-channel one, equivalent to that studied by FF. With this simplification the momentum equation reduces to:

$$0 = 1-\frac{1}{2\lambda}\ln\frac{\lambda+1}{\lambda-1}, \tag{252}$$

that is solved by $\lambda \approx 1.200$. Using this inside Eq. (251a) (neglecting the term $\gamma^{-1}\hat{h}^2\lambda^2/\hat{\mu}^{3/2}$ in the latter) gives

$$\hat{\Delta}_{\mathbf{Q}}^2 \approx 2\hat{h}^2(\lambda^2-1)\ln\frac{\hat{\Delta}_{\mathrm{BCS}}^2}{4\hat{h}^2(\lambda^2-1)}. \tag{253}$$

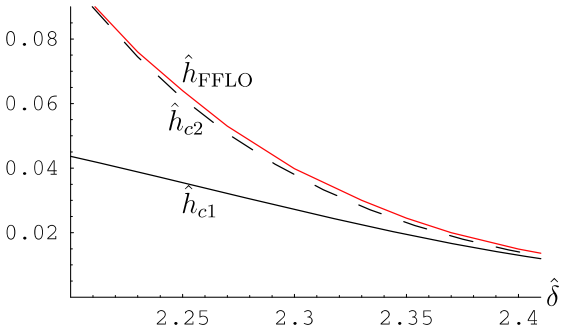

Fig. 34. Plot of the $\hat{h}_{\mathrm{FFLO}}$ phase boundary, along with $\hat{h}_{c2}$ and $\hat{h}_{c1}$, for $\gamma = 0.1$, as a function of normalized detuning $\hat{\delta}$. The FFLO phase is stable for $\hat{h}_{c2} < \hat{h} < \hat{h}_{\mathrm{FFLO}}$, as shown in the phase diagram Fig. 1.

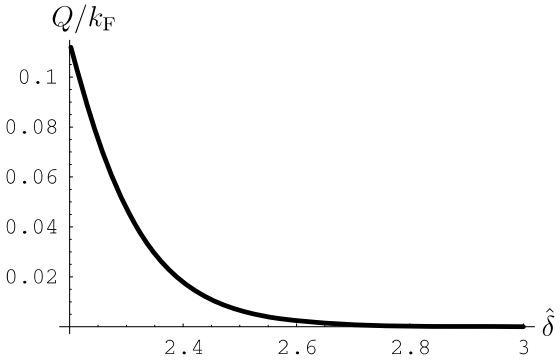

Fig. 35. Plot of wavevector $Q(\hat{\delta})$ of FF order, normalized to Fermi wavevector $k_F \equiv p_F/\hbar$ for $\gamma = 0.1$ as a function of Feshbach resonance detuning $\hat{\delta}$.

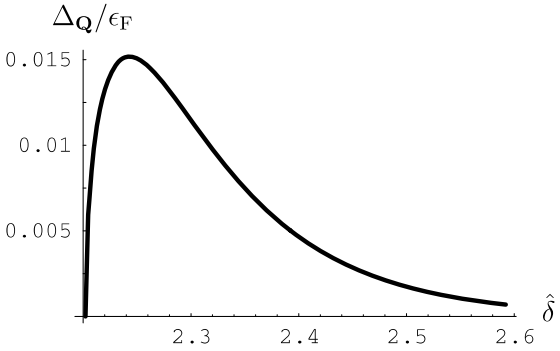

Fig. 36. Plot of maximum gap $\Delta_{\mathbf{Q}}(\delta,h_{c2})$ in FFLO phase as a function of Feshbach resonance detuning for the case $\gamma = 0.1$.

The vanishing of $\hat{\Delta}_{\mathbf{Q}}(\hat{h},\hat{\delta})$ then determines the critical point $\hat{h}_{\mathrm{FFLO}}$ for the N–FFLO continuous transition

$$\hat{h}_{\mathrm{FFLO}} \simeq \frac{\hat{\Delta}_{\mathrm{BCS}}}{2\sqrt{\lambda^2-1}} \simeq \eta\hat{\Delta}_{\mathrm{BCS}}, \tag{254a}$$

$$\simeq \eta\hat{\Delta}_{\mathrm{F}}[\gamma,\hat{\delta}]\exp\left[-\frac{\eta^2\hat{\delta}}{8\gamma}\hat{\Delta}_{\mathrm{F}}^2\right], \tag{254b}$$

with the constant of proportionality $\eta = 0.754$ in (expected) agreement with FF [86]. In the final line Eq. (254b), we used the number equation for $\hat{\mu}$ [Eq. (251c), which, as expected, precisely reduces to the N-state number equation at the transition where $\hat{\Delta}_{\mathbf{Q}} \to 0$; cf. Eq. (145)] to find $\hat{h}_{\mathrm{FFLO}}$ at fixed imposed density. Here, we remind the reader that $\hat{\Delta}_{\mathrm{F}}$ is defined in Eq. (141).

To this order of approximation (i.e., that of FF [86]) the $\hat{h}_{\mathrm{FFLO}}(\delta)$ (for the N–FFLO transition) and $\hat{h}_c(\delta) \approx \Delta_{\mathrm{BCS}}(\hat{\delta})/\sqrt{2}$ (for the FFLO–SF transition; see below) phase boundaries maintain a constant ratio as a function of $\hat{\delta}$. As we saw in Section 5.2, at fixed

number [determined by in addition imposing Eq. (251c)] the critical curve $\hat{h}_c(\hat{\delta},\hat{\mu})$ splits into upper-critical and lower critical boundaries $\hat{h}_{c2}(\hat{\delta},N)=\hat{h}_c(\hat{\delta},\hat{\mu}_{\rm FFLO}(\hat{\delta},N))$ and $\hat{h}_{c1}(\hat{\delta},N)=\hat{h}_c(\hat{\delta},\hat{\mu}_{\rm SF}(\hat{\delta},N))$, respectively, bounding the SF–FFLO coexistence region. For later reference we note that, because $\hat{\Delta}_{\mathbf{Q},\rm FFLO}\ll\hat{\Delta}_{\rm BCS}\ll\gamma$, the chemical potential $\hat{\mu}_{\rm FFLO}$ in the FFLO state is accurately given by its normal state value, $\hat{\mu}_{\rm N}$, the latter given by Eq. (251c), with $\hat{\Delta}_{\mathbf{Q}}\approx 0$, giving, at small $\hat{h}$, $\hat{\mu}_{\rm FFLO}\approx 1$. Just below the N–FFLO transition, the order parameter $\hat{\Delta}_{\mathbf{Q}}$ grows in the expected generic mean-field way [86]

$$\frac{\hat{\Delta}_{\mathbf{Q},\rm FFLO}}{\hat{\Delta}_{\rm BCS}}\simeq\sqrt{\frac{\hat{h}_{\rm FFLO}-\hat{h}}{\hat{h}_{\rm FFLO}}}\ \text{for}\ \hat{h}<\hat{h}_{\rm FFLO}, \tag{255}$$

with the characteristic $\hat{Q}$ reducing linearly with $\hat{h}$ according to $\hat{Q}\approx\lambda\hat{h}$.

We now go beyond the above FF approximation for $\hat{h}_{\rm FFLO}(\hat{\delta},\hat{\mu})$ by including the (so-far neglected) molecular dispersion in Eqs. (251a) and (251b). Combining these equations gives the order parameter

$$\hat{\Delta}_{\mathbf{Q}}^2\simeq 2\hat{h}^2(\lambda^2-1)\left[3-\frac{3}{2\lambda}\ln\frac{\lambda+1}{\lambda-1}-\ln\frac{4\hat{h}^2(\lambda^2-1)}{\hat{\Delta}_{\rm BCS}^2}\right], \tag{256}$$

that, when solved simultaneously with Eq. (251b), gives the more accurate, higher-order $\hat{h}_{\rm FFLO}(\hat{\delta},\hat{\mu})$ boundary. The latter is best determined numerically, as illustrated in Fig. 34. Its new important feature [beyond the lower order result in Eq. (254a)] is that $\hat{h}_{\rm FFLO}(\hat{\delta},\hat{\mu})$ is no longer proportional to $\hat{h}_c(\hat{\delta},\hat{\mu})$, crossing it [and therefore $\hat{h}_{c2}(\hat{\delta},N)$] at a detuning $\hat{\delta}_*$ (see Fig. 1), that is determined by the condition $\hat{h}_{\rm FFLO}(\hat{\delta}_*,\hat{\mu})=\hat{h}_c(\hat{\delta}_*,\hat{\mu})\simeq\hat{\Delta}_{\rm BCS}(\hat{\delta}_*,\hat{\mu})/\sqrt{2}$. Inserting this condition into Eq. (256) gives λ at this crossing, which we call λ_*:

$$0=3\left(1-\frac{1}{2\lambda_*}\ln\frac{\lambda_*+1}{\lambda_*-1}\right)-\ln\left[2(\lambda_*^2-1)\right]. \tag{257}$$

Solving Eq. (257) numerically gives $\lambda_*\approx 1.159$, only slightly lower than its FF value of $\lambda\approx 1.200$ in the asymptotic BCS regime. Inserting λ_* into Eq. (251b) yields the following implicit expression for δ_* at which $\hat{h}_{\rm FFLO}=\hat{h}_c$:

$$\frac{1}{2}\hat{\Delta}_{\rm BCS}[\delta_*,\hat{\mu}]^2=\frac{\hat{\mu}^{3/2}\gamma}{\lambda_*^2}\left[\frac{1}{2\lambda_*}\ln\frac{\lambda_*+1}{\lambda_*-1}-1\right], \tag{258a}$$

$$\simeq 0.094\hat{\mu}^{3/2}\gamma, \tag{258b}$$

with δ_* entering via $\hat{\Delta}_{\rm BCS}$, the BCS gap at $\hat{h}=0$. Using the explicit expression Eq. (120) in Eq. (258b) and approximating $\hat{\mu}_{\rm FFLO}\approx\hat{\mu}_{\rm N}\approx 1$, then gives

$$\hat{\delta}_*\approx 2-\frac{\gamma}{2}\ln 0.159\gamma, \tag{259}$$

where we emphasize that, for $\gamma<1$ (where the preceding expressions are valid), $\hat{\delta}_*$ is bounded by $2\epsilon_{\rm F}$ from below and is an increasing function of Feshbach resonance width γ, illustrated in Fig. 37.

Using the solution of Eqs. (251a) and (251b) for λ together with the definition of $\lambda=\hat{Q}/\hat{h}$ and Eq. (248), we can obtain the wavevector $Q(\delta,h)$ characterizing the FFLO

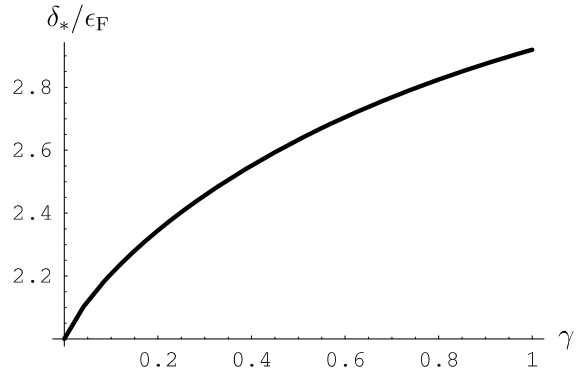

Fig. 37. Critical detuning δ_* beyond which the FFLO phase is stable at nonzero polarization, valid for narrow resonance (small γ).

state. Approximating $\hat{h}$ by its critical value $\hat{h}_{\rm FFLO}(\delta) \approx \eta\hat{\Delta}_{\rm BCS}$ and reintroducing Planck's constant, we find

$$Q \approx \frac{2\eta\lambda\Delta_{\rm BCS}}{\hbar v_{\rm F}}. \tag{260}$$

As we have mentioned, along the phase boundary $\hat{h}_{\rm FFLO}(\hat{\delta})$ a more precise numerical solution for $\hat{Q}(\hat{\delta})$ is given in Fig. 35.

We close this subsection by noting that the N–FFLO phase boundary $\hat{h}_{\rm FFLO}(\hat{\delta})$ can be easily converted into a critical polarization boundary $\Delta N_{\rm FFLO}(\hat{\delta})$ by using $\hat{h}_{\rm FFLO}(\hat{\delta})$ inside the expression for the normal-state spin imbalance $\Delta N(\hat{h})$, Eq. (116b). Doing this numerically gives $\Delta N_{\rm FFLO}(\hat{\delta})$, plotted along with ΔN_{c2} in the phase diagram Fig. 3, that for large detuning is given by

$$\frac{\Delta N_{\rm FFLO}}{N} \approx \frac{3\eta}{2}\hat{\Delta}_{\rm F}\exp\left[-\frac{\eta^2\hat{\delta}}{8\gamma}\hat{\Delta}_{\rm F}^2\right], \tag{261}$$

a result that we will estimate [along with Eq. (260)] in the context of recent experiments in Section 10.

7.2. First-order FFLO-SF transition and associated phase separation

The FFLO state arises as a result of a delicate balance between the normal state (selected by atom species imbalance) and the singlet-paired superfluid state (preferred by the attractive pairing interaction). It is characterized by an order parameter that is significantly smaller than that of a singlet BCS superfluid and by a finite magnetization $m = \Delta N/V$

$$m(h) = \int \frac{{\rm d}^3k}{(2\pi)^3}[\Theta(-E_{\mathbf{k}\uparrow}) - \Theta(-E_{\mathbf{k}\downarrow})], \tag{262}$$

that is quite close to that of the normal state

$$m_{\rm N} \simeq 2c\sqrt{\mu}h. \tag{263}$$

Hence, in many of its properties the FFLO state is quantitatively quite close to the normal state. This is illustrated in Fig. 38 by the proximity of the FFLO energy minimum to the normal state, $\hat{\Delta}_{\mathbf{Q}} = 0$.

As can be seen from the evolution of e_{G} with decreasing $\hat{h}$ below $\hat{h}_{\mathrm{FFLO}}(\hat{\delta}, \hat{\mu})$ (see Fig. 38b), a secondary local BCS minimum arises at finite $\hat{\Delta}_{\mathbf{Q}=0} = \hat{\Delta}_{\mathrm{BCS}}$. Upon further decreasing $\hat{h}$, this BCS singlet SF minimum becomes degenerate (Fig. 38a) with the FFLO

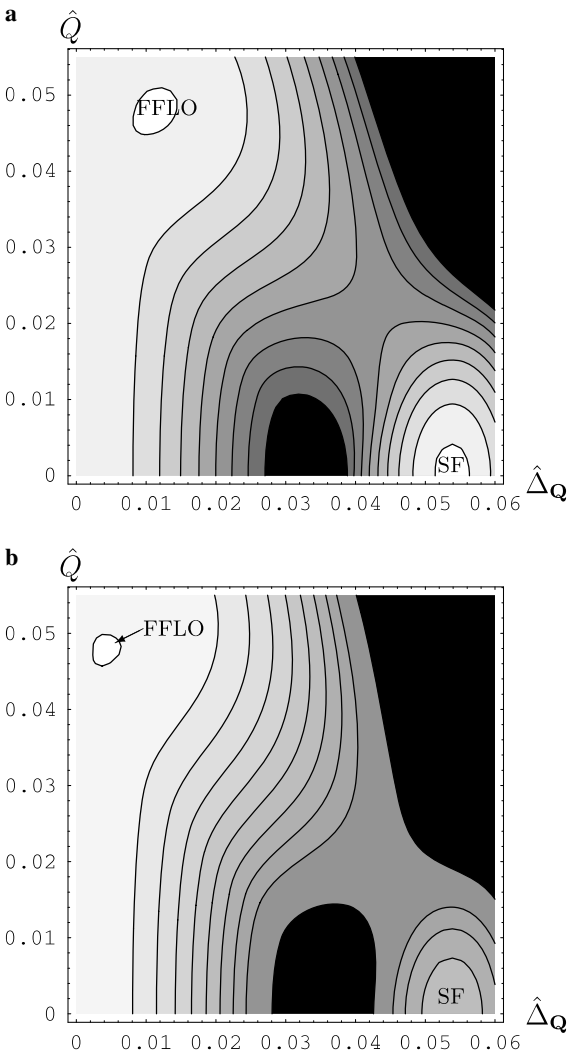

Fig. 38. Contour plots of the ground-state energy E_{G} (darker regions denote higher E_{G}) as a function of the normalized gap $\hat{\Delta}_{\mathbf{Q}}$ and the normalized wavevector $\hat{Q}$. For (a), $\hat{h} > \hat{h}_c$ so that a first-order transition from SF to FFLO has just occurred. For (b), $\hat{h} < \hat{h}_{\mathrm{FFLO}}$, so the FFLO minimum is approaching the $\hat{\Delta}_{\mathbf{Q}} = 0$ (N state) axis continuously and the local SF-state minimum has moved to higher energy. Note that the N phase occurs for *any* $\hat{Q}$ at $\hat{\Delta}_{\mathbf{Q}} = 0$.

one, and the resonant Fermi gas undergoes a first-order FFLO–SF transition by "jumping" from the FFLO minimum to this BCS one.

From the quantitative similarity of the normal and FFLO states' energetics, it is not surprising that we find this FFLO-SF transition at

$$\hat{h}_c(\hat{\delta},\hat{\mu}) \simeq \frac{2\eta}{2\eta^2+1}\hat{\Delta}_{\rm BCS} \simeq 0.706\hat{\Delta}_{\rm BCS}, \tag{264}$$

obtained using the approximate formula Eq. (255) for the order parameter near $\hat{h}_{\rm FFLO}$. This is extremely close to the N–SF first-order transition at $\hat{h}_c(\hat{\delta},\hat{\mu}) \approx \hat{\Delta}_{\rm BCS}/\sqrt{2} \approx .707\hat{\Delta}_{\rm BCS}$, studied in Section 5, where we ignored the existence of the FFLO state, validating our approximation of $\hat{h}_c(\hat{\delta},\hat{\mu})$ by $\hat{\Delta}_{\rm BCS}/\sqrt{2}$ elsewhere in this section. Consistently, $\hat{h}_c(\hat{\delta},\hat{\mu})$ is also only slightly lower than $\hat{h}_{\rm FFLO}(\hat{\delta},\hat{\mu})$ ensuring that the FFLO state is quantitatively indeed quite close to the normal state, occupying only a narrow sliver between $\hat{h}_{\rm FFLO}(\hat{\delta},\hat{\mu})$ and $\hat{h}_c(\hat{\delta},\hat{\mu})$ and limited to $\hat{\delta} > \hat{\delta}_* \approx 2$ on the phase diagram.

The analysis of the FFLO–SF first-order transition parallels our analysis in Section 5.2 for the N–SF transition (where the FFLO state was neglected). Because of the abovementioned similarity of the N and FFLO states all the results derived in Section 5.2 remain quantitatively accurate for the true FFLO-SF transition. To recap, for fixed chemical potentials and decreasing $\hat{h}$, the system simply jumps at $\hat{h}_c(\hat{\delta})$ from the FFLO minimum to the BCS SF minimum, exhibiting density and magnetization discontinuities given by Eqs. (135) and (263), respectively. The two superconducting order parameters $\hat{\Delta}_{\mathbf{Q}}$ and $\hat{\Delta}_0$ characterizing the FFLO and BCS SF states, respectively, also experience jump discontinuities with decreasing $\hat{h}$ at $\hat{h}_c(\hat{\delta},\hat{\mu})$, with $\hat{\Delta}_{\mathbf{Q}}$ jumping to 0 and $\hat{\Delta}_0$ jumping to the finite BCS value $\hat{\delta}_{\rm BCS}$. Correspondingly, Q jumps to zero as $\hat{h}$ reduced below $\hat{h}_c(\delta)$.

In contrast, (as also discussed in detail in Section 5.3) at fixed atom density n (or number N), neither the SF nor the FFLO (nor N) states can satisfy the number equation while remaining a global minimum of $e_{\rm G}$. Consequently, below $h_{c2}(\delta,{\rm N}) = h_c(\delta,\mu_{\rm FFLO}(N) \approx \mu_N)$ the gas phase separates into coexisting singlet-BCS SF and (at large detuning) FFLO state, in proportions $x(\delta,h)$ and $1-x(\delta,h)$ that are well-approximated using Eq. (177). This coexistence region is bounded from below by a lower-critical Zeeman field $h_{c1}(\delta,N) = h_c(\delta,\mu_{SF}(N))$, below which the system transitions into a single-component singlet SF.

We conclude this subsection by noting that, because of the existence of the $\hat{\delta}_*$ detuning point on the $\hat{h}_{\rm FFLO}(\hat{\delta})$ boundary, the phase separation (PS) regime between $\hat{h}_{c2}(\hat{\delta})$ and $\hat{h}_{c1}(\hat{\delta})$ is somewhat nontrivial. This arises from the fact that, for $\hat{\delta} \gg \hat{\delta}_*$ (deep in the BCS regime), it is the FFLO state to which the BCS SF is unstable above $\hat{h}_c(\hat{\delta},\hat{\mu})$. Thus, at large detunings, we expect the PS to consist of SF–FFLO coexistence. For $\hat{\delta} \ll \hat{\delta}_*$, on the other hand, we expect the regime of phase separation to consist of SF–N coexistence.

Our aim is to compute the boundary separating these two types of phase-separated mixture. We start by computing this boundary at fixed density and chemical potential difference, shown in Fig. 39, which can be done using a simple (approximate) argument. Consider a point $(\hat{\delta}_0,\hat{h}_0) = (\delta_0/\epsilon_{\rm F}, h_0/\epsilon_{\rm F})$ inside the region of phase separation. The uniform phases comprising the mixture at this point must have the *same* detuning δ_0 and chemical potential difference h_0 but different densities. Since both axes are normalized to $\epsilon_{\rm F} \propto n^{2/3}$, clearly such uniform phases lie on a ray emanating from the origin and intersecting $(\hat{\delta}_0,\hat{h}_0)$. This implies that the homogeneous states on either side of the regime of phase separation that intersect this ray will comprise the mixed state.

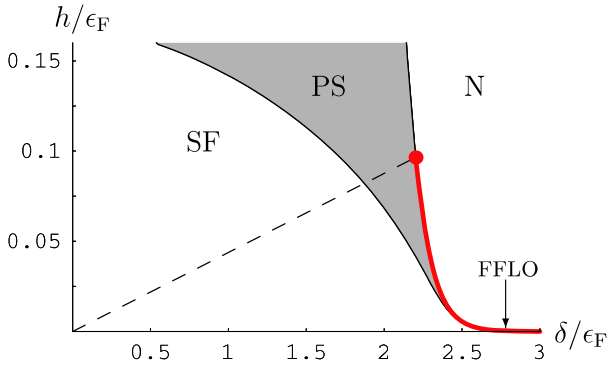

Fig. 39. Portion of the positive-detuning phase diagram for $\gamma = 0.1$ at fixed detuning δ and chemical potential difference h showing regions of normal phase (N), FFLO (along red curve), singlet superfluid (SF) and phase-separation (shaded, PS). The dashed line connects the critical point $(\delta_*, \hat{h}_{\rm FFLO}(\delta_*))$ with the origin. Below the dashed line in the shaded PS regime, the phase separation consists of coexisting SF and FFLO states, while above the dashed line it consists of coexisting SF and N states.

This procedure can be used to determine the composition of the mixed phase for any point in the regime of phase separation. In Fig. 39 we have drawn a dashed line connecting $(\hat{\delta}_*, \hat{h}_{\rm FFLO}(\delta_*)) \approx (2.202, .0965)$ with the origin. Clearly, for points inside the PS region that are above this dashed line the coexistence is between SF and N while for points below the dashed line it is between SF and FFLO.

Having found a simple approximate scheme [it is approximate because the location of $(\hat{\delta}_*, \hat{h}_{\rm FFLO})$ is not invariant with respect to changes of the density since γ is a function of ϵ_F] to determine the boundary between SF–N coexistence and SF–FFLO coexistence, we now obtain it in a different way, defining the boundary as the place where the N portion of the SF–N coexistence undergoes a second-order transition (with decreasing chemical potential difference) to the FFLO phase. The critical chemical potential difference $\hat{h}_{\rm FFLO}(\hat{\mu})$ at which this occurs satisfies Eqs. (251b) and (251a) with $\hat{\Delta} = 0$ for the latter:

$$0 = \frac{\gamma^{-1}\hat{h}_{\rm FFLO}(\hat{\mu})^2}{\hat{\mu}^{3/2}}\lambda^2 + 1 - \frac{1}{2\lambda}\ln\frac{\lambda+1}{\lambda-1}, \tag{265a}$$

$$0 = 2 - \frac{\gamma^{-1}\hat{h}_{\rm FFLO}(\hat{\mu})^2}{\hat{\mu}^{3/2}}\lambda^2 - \ln\frac{4\hat{h}_{\rm FFLO}(\hat{\mu})^2(\lambda^2-1)}{\hat{\Delta}_{\rm BCS}^2} - \frac{1}{\lambda}\ln\frac{\lambda+1}{\lambda-1}, \tag{265b}$$

where we include the chemical-potential argument in $\hat{h}_{\rm FFLO}(\hat{\mu})$ to emphasize that is distinct from $\hat{h}_{\rm FFLO}$ which we have already defined and which also satisfies the number equation; instead, here we must combine it with conditions appropriate to the mixed phase.

In fact, we have already studied the gap and number equations in the PS regime, assuming SF–N coexistence, in Section 5.6, where we expressed the total number constraint as an equation for the SF fraction x in Eq. (177); along with Eq. (178) for the normalized polarization and Eq. (163) (which provides the first-order condition relating μ and h in the mixed phase). For a particular $\Delta N/N$, such a procedure yields $\hat{h}(\hat{\mu})$ in the PS regime assuming SF–N coexistence; where this crosses $\hat{h}_{\rm FFLO}(\hat{\mu})$ given by Eqs. (265a) and (265b) leads to a phase boundary (plotted in Fig. 40) that marks the FFLO-N phase transition inside the PS regime.

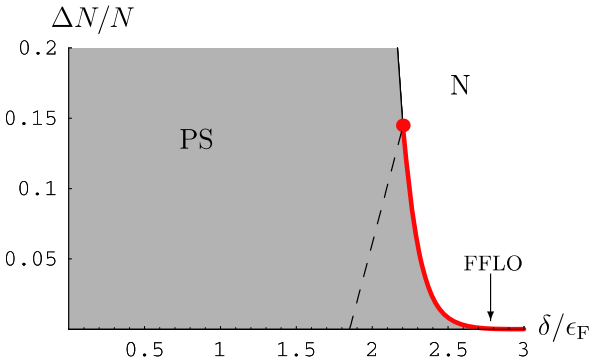

Fig. 40. Portion of the positive-detuning phase diagram for $\gamma = 0.1$ at fixed detuning δ and polarization ΔN showing regions of normal phase (N), FFLO (along red curve) and phase-separation (shaded, PS). Below the dashed line, the phase separation regime consists of coexisting SF and FFLO states, while above the dashed line it consists of coexisting SF and N states.

8. One-channel model

In the preceding sections, we have studied a resonantly-interacting Fermi gas across a Feshbach resonance as a function of detuning and chemical potential imbalance (or, equivalently, species asymmetry), summarized by the phase diagrams Figs. 1 and 3. We have limited our analysis to the two-channel model, Eq. (25), for reasons discussed in Section 3, namely, because it is characterized by a small parameter $\gamma \propto \sqrt{\Gamma_0/\epsilon_F}$ (with Γ_0 the Feshbach resonance width), that justifies, in the narrow resonance $\gamma \ll 1$ limit, a perturbative mean-field analysis across the resonance.

In contrast, the one-channel model (to which the two-channel model reduces in the broad-resonance $\gamma \gg 1$ limit) is characterized by a gas parameter $n^{1/3}|a_s|$ which diverges in the vicinity of the resonance where $k_F|a_s| \to \infty$. Hence, standard mean-field analysis (uncontrolled embellishments notwithstanding) is expected to become quantitatively unreliable across the resonance.

However, most present-day experiments on ^{40}K and ^{6}Li (e.g., the Feshbach resonance at 202 G in ^{40}K or at 830 G in ^{6}Li) are in the broad resonance limit (see Appendix A) and one is forced to analyze this analytically inaccessible limit. This is best done directly in a one-channel model. Although mean-field theory on the one-channel model is not expected to be accurate across a Feshbach resonance tuned to zero energy, it still may be a qualitatively correct interpolation between the deep BCS and BEC regimes where the gas parameter $n^{1/3}|a_s| \ll 1$. With this caveat in mind, in the present section we study, within mean-field theory, the single-channel model as a function of polarization and detuning (or, equivalently, s-wave scattering length a_s), with our results summarized by the phase diagrams Figs. 41 and 42 (which are in agreement with recent results [64,75,78]). Since the one- and two-channel models are so closely related (see Section 5), many of the calculations will be very similar to ones we have already presented in the context of the two-channel model.

We begin with the one-channel model Hamiltonian Eq. (51) in the grand-canonical ensemble (with system volume $V = 1$)

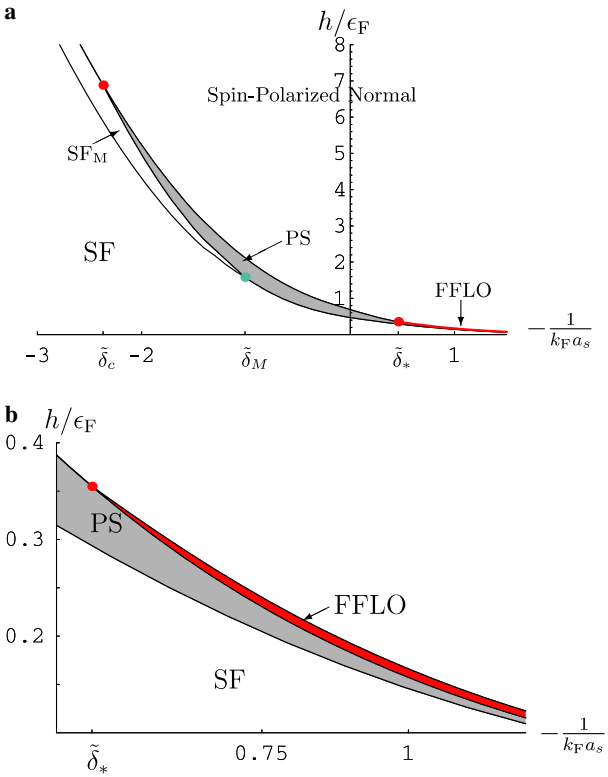

Fig. 41. Chemical potential difference, h, vs. coupling $\frac{1}{k_F a_s}$ phase diagram of the one-channel model showing regimes of FFLO, superfluid (SF), magnetized superfluid (SF_M), and phase separation (PS). Panel (a) is the global phase diagram and panel (b) is a zoom-in emphasizing the FFLO regime. The thick red dot at (−2.37,6.89) in the BEC regime is a tricritical point separating first and second order transitions. On the horizontal axes three critical detunings are labeled: $\tilde{\delta}_c \equiv -(k_F a_{sc})^{-1} = -2.37$, $\tilde{\delta}_M \equiv -(k_F a_{sM})^{-1} = -1.01$ and $\tilde{\delta}_* \equiv -(k_F a_{s*})^{-1} = 0.46$.

$$H = \sum_{\mathbf{k},\sigma} (\epsilon_k - \mu_\sigma) \hat{c}^\dagger_{\mathbf{k}\sigma} \hat{c}_{\mathbf{k}\sigma} + \lambda \sum_{\mathbf{kqp}} \hat{c}^\dagger_{\mathbf{k}\uparrow} \hat{c}^\dagger_{\mathbf{p}\downarrow} \hat{c}_{\mathbf{k}+\mathbf{q}\downarrow} \hat{c}_{\mathbf{p}-\mathbf{q}\uparrow}, \tag{266}$$

applying a standard mean-field analysis, by first assuming an expectation value

$$\lambda \langle \hat{c}_\downarrow(\mathbf{r}) \hat{c}_\uparrow(\mathbf{r}) \rangle = \Delta_{\mathbf{Q}} e^{i\mathbf{Q}\cdot\mathbf{r}}, \tag{267}$$

corresponding to pair condensation at a single wavevector $\mathbf{Q}$, with $\Delta_{\mathbf{Q}}$ and $\mathbf{Q}$ to be self-consistently determined. With this mean-field assumption, H, Eq. (266), reduces to the standard BCS mean-field form:

$$H = -\frac{|\Delta_{\mathbf{Q}}|^2}{\lambda} + \sum_k (\epsilon_k - \mu_\sigma) \hat{c}^\dagger_{\mathbf{k}\sigma} \hat{c}_{\mathbf{k}\sigma} + \sum_{\mathbf{k}} \left(\Delta^\dagger_{\mathbf{Q}} \hat{c}_{\mathbf{k}+\frac{\mathbf{Q}}{2}\downarrow} \hat{c}_{-\mathbf{k}+\frac{\mathbf{Q}}{2}\uparrow} + \hat{c}^\dagger_{-\mathbf{k}+\frac{\mathbf{Q}}{2}\uparrow} \hat{c}^\dagger_{\mathbf{k}+\frac{\mathbf{Q}}{2}\downarrow} \Delta_{\mathbf{Q}} \right). \tag{268}$$

With the identification of $\Delta_{\mathbf{Q}}$ with $gB_{\mathbf{Q}}$, its main distinctions from the two-channel model Eq. (62) are the lack of any dispersion in the $\Delta_{\mathbf{Q}}$ field [with $-\lambda^{-1}$ replacing $g^{-2}(\frac{1}{2}\epsilon_Q + \delta_0 - 2\mu)$] and the fact that the total atom-number constraint here involves only $N = \sum_{\mathbf{k},\sigma} \langle c^\dagger_{\mathbf{k}\sigma} c_{\mathbf{k}\sigma} \rangle$ rather than the analogous Eq. (77).

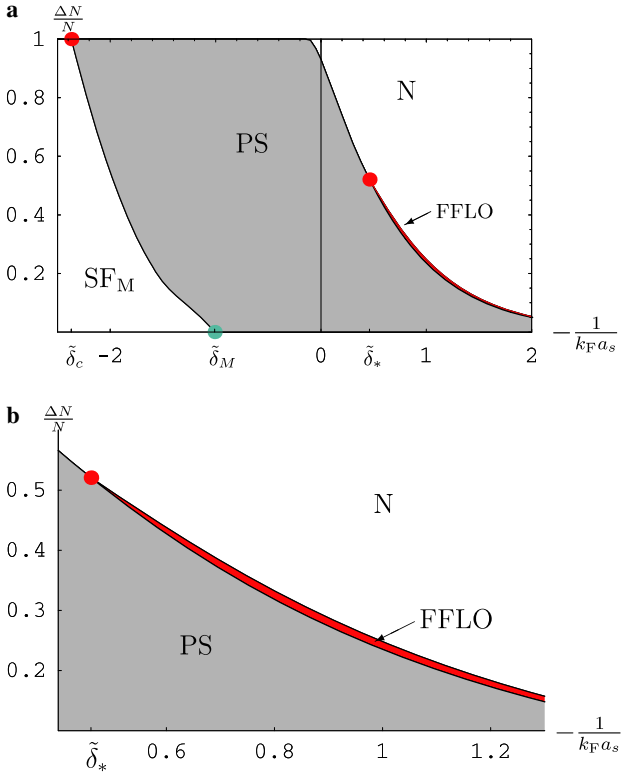

Fig. 42. Polarization $\Delta N/N$ vs. coupling $\frac{1}{k_F a_s}$ phase diagram of the one-channel model showing regimes of FFLO, superfluid (SF), magnetized superfluid (SF_M), and phase separation (PS). As in the preceding figure, panel (a) is the global phase diagram, panel (b) is a zoom-in emphasizing the FFLO regime, and on the horizontal axes the three critical detunings $\tilde{\delta}_c = -2.37$, $\tilde{\delta}_M = -1.01$, and $\tilde{\delta}_* = 0.46$ are labeled. Note that here (in contrast to a narrow Feshbach resonance $\gamma \ll 1$, Fig. 3) at unitarity, $(k_F a_s)^{-1} = 0$, the boundary between N and PS is at $\Delta N/N \simeq 0.93 < 1$, consistent with experiments [30].

As for the two-channel model, after this mean-field approximation (treating $\Delta_{\mathbf{Q}}$ as a c-number), everything else can be in principle computed exactly because the model is quadratic in fermion operators and can easily be diagonalized. Equivalently, the theory can be formulated via a coherent-state path integral, where $\Delta_{\mathbf{Q}}$ appears as a Hubbard–Stratonovich field used to decouple the quartic interaction [131] in H, Eq. (266). In this approach, the mean-field approximation corresponds to a saddle-point treatment of the field $\Delta_{\mathbf{Q}}$.

All $T = 0$ properties (on which we focus) follow directly from the corresponding ground state energy $E_G(\Delta_{\mathbf{Q}})$, with $\Delta_{\mathbf{Q}}$ appearing as a variational parameter. As in the two-channel case, we shall find that for much of the phase diagram the ground-state is characterized by $\mathbf{Q} = 0$. Anticipating this, we first focus on this $\mathbf{Q} = 0$ subspace, returning to the more general $\mathbf{Q} \neq 0$ case in Section 8.5 [where we display the full $\mathbf{Q}$-dependent ground-state energy as Eq. (334)]. With this simplification, we find the ground-state energy (taking $\Delta_{\mathbf{Q}=0} \equiv \Delta$ real):

$$E_G = -\frac{\Delta^2}{\lambda} + \sum_k (\xi_k - E_k) - \int_0^h m(h')\mathrm{d}h', \tag{269}$$

with $\xi_k \equiv \epsilon_k - \mu$ and where the magnetization

$$m(h) = \frac{2c}{3}\left[(\mu+\sqrt{h^2-\Delta^2})^{3/2}\Theta(\mu+\sqrt{h^2-\Delta^2}) - (\mu-\sqrt{h-\Delta^2})^{3/2}\Theta(\mu-\sqrt{h^2-\Delta^2})\right]. \tag{270}$$

The short-scale (ultraviolet cutoff Λ) dependence in the first momentum sum of Eq. (269), as usual, can be eliminated by re-expressing E_G in terms of the s-wave scattering length using the relation Eq. (52) between a_s and λ. This gives (converting sums to integrals)

$$E_G = -\frac{m}{4\pi a_s}\Delta^2 + \int \frac{d^3k}{(2\pi)^3}\left(\xi_k - E_k + \frac{\Delta^2}{2\epsilon_k}\right) - \int_0^h m(h')\mathrm{d}h', \tag{271}$$

which is almost identical to our two-channel ground-state energy [c.f. Eq. (102)]. We now proceed to study E_G, Eq. (271), in a variety of relevant regimes, finding the phase diagram at nonzero chemical potential difference h or population difference ΔN. We follow the standard practice of expressing all physical quantities as a function of the dimensionless coupling $-\frac{1}{k_F a_s} \propto \delta$ that "measures" the system's distance from the zero-energy resonance. In terms of this coupling, in the one-channel model the BCS regime occurs for $-\frac{1}{k_F a_s} > 1$ (i.e., a_s small and negative), the BEC regime occurs for $-\frac{1}{k_F a_s} < -1$ (i.e., a_s small and positive), and the crossover between these regimes takes place for $k_F|a_s| \gg 1$ across the unitary point where $k_F|a_s| \to \infty$.

Armed with $E_G(\Delta,\mu,h)$, the determination of the phases and transitions is conceptually straightforward. We simply minimize E_G over Δ and supplement the resulting gap equation, which ensures that $\Delta = \lambda\langle\hat{c}_\downarrow(\mathbf{r})\hat{c}_\uparrow(\mathbf{r})\rangle$ is satisfied in the ground-state, with the number equation ensuring that the total atom density equals the imposed density $n = \frac{4}{3}c\epsilon_F^{3/2}$. The resulting equations

$$0 = \frac{\partial E_G}{\partial \Delta}, \tag{272a}$$

$$N = -\frac{\partial E_G}{\partial \mu}, \tag{272b}$$

are well-known in the standard BEC–BCS crossover at $h = 0$ and equal spin population. At finite imposed population imbalance ΔN (equivalent to magnetization $m = \Delta N/V$) Eqs. (272a), must be solved simultaneously with

$$\Delta N = -\frac{\partial E_G}{\partial h}, \tag{273}$$

ensuring the imposed ΔN. As we shall see, however, caution must be exercised in using these equations to map out the phase diagram, since, at $h \neq 0$, they exhibit solutions that are local maxima of $E_G(\Delta)$ and therefore do not correspond to a ground state of the system [121]. Failing to ensure that solutions to Eq. (272a) are indeed minima of Eq. (269) has led to a number of incorrect results in the literature (see, e.g., Ref. [47,67,123]).

8.1. One-channel model at $h = 0$

For completeness and point of reference we review the mean-field theory of the single-channel model at equal populations by studying E_G at $h = 0$. Using dimensionless variables $\hat{\Delta} \equiv \Delta/\epsilon_F$, $\hat{\mu} \equiv \mu/\epsilon_F$ and $e_G = E_G/c\epsilon_F^{5/2}$ as in the two-channel model,

$$e_{\rm G} = -\frac{\pi}{2k_{\rm F}a_s}\hat{\Delta}^2 + \int_0^\infty d\epsilon\sqrt{\epsilon}\left(\epsilon - \hat{\mu} - \sqrt{(\epsilon-\hat{\mu})^2+\hat{\Delta}^2} + \frac{\hat{\Delta}^2}{2\epsilon}\right). \tag{274}$$

The well-known BEC–BCS crossover behavior [19–22] follows from minimizing $e_{\rm G}$ at fixed total density. This corresponds to simultaneously solving the gap and number equations (in dimensionless form)

$$0 = \frac{\partial e_{\rm G}}{\partial\hat{\Delta}}, \tag{275}$$

$$\frac{4}{3} = -\frac{\partial e_{\rm G}}{\partial\hat{\mu}}, \tag{276}$$

with numerical solutions given in Fig. 43. We can find simple analytic approximations to these solutions by evaluating the integral in Eq. (274) in the asymptotic BCS and BEC limits. In the BCS regime ($1 < -\frac{1}{k_{\rm F}a_s}$), $\hat{\mu} > 0$ and $\hat{\Delta} \ll \hat{\mu}$, yielding for $e_{\rm G}$ [using results from Appendix C]

$$e_{\rm G} \simeq -\frac{\pi\hat{\Delta}^2}{2k_{\rm F}a_s} - \frac{8}{15}\hat{\mu}^{5/2} - \sqrt{\hat{\mu}}\hat{\Delta}^2\left(\frac{1}{2} + \ln\frac{8e^{-2}\hat{\mu}}{\hat{\Delta}}\right). \tag{277}$$

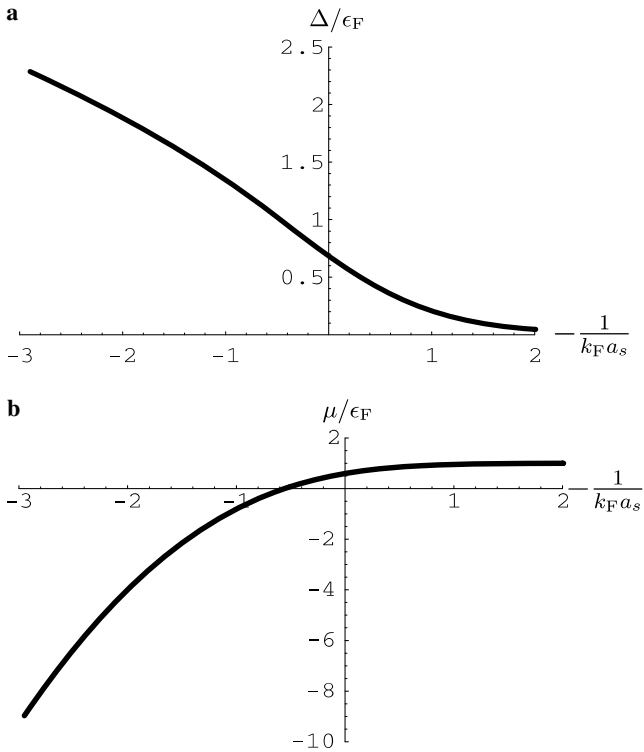

Fig. 43. Plots of (a) Δ and (b) μ as a function of coupling $-(k_{\rm F}a_s)^{-1}$, within mean-field theory for the single-channel model, each normalized to $\epsilon_{\rm F}$.

Using this approximation for e_G inside Eqs. (275) and (276) in turn gives the gap and number equations

$$\hat{\Delta} \simeq 8e^{-2}\hat{\mu}\exp\left[\frac{\pi}{2k_F a_s\sqrt{\hat{\mu}}}\right], \tag{278a}$$

$$\frac{4}{3} \simeq \frac{4}{3}\hat{\mu}^{3/2} + \frac{5}{4}\frac{\hat{\Delta}^2}{\sqrt{\hat{\mu}}} - \frac{\hat{\Delta}^2}{2\sqrt{\hat{\mu}}}\ln\frac{\hat{\Delta}}{8e^{-2}\hat{\mu}}, \tag{278b}$$

which, in the asymptotic BCS regime, are accurately solved by

$$\hat{\Delta} \approx \hat{\Delta}_F \equiv 8e^{-2}\exp\left[\frac{\pi}{2k_F a_s}\right], \tag{279}$$

$$\hat{\mu} \approx 1. \tag{280}$$

In the negative-detuning BEC regime of $-\frac{1}{k_F a_s} < -1$, in which $\hat{\mu} < 0$ and $|\hat{\mu}| \gg \hat{\Delta}$, we find e_G is approximated by

$$e_G \simeq -\frac{\pi\hat{\Delta}^2}{2k_F a_s} + \sqrt{|\hat{\mu}|}\frac{\hat{\Delta}^2}{2}\left(\pi + \frac{\pi}{32}\frac{\hat{\Delta}^2}{\hat{\mu}^2}\right), \tag{281}$$

that leads to the following approximate gap and number equations:

$$\frac{\pi}{2k_F a_s} - \frac{1}{2}\pi\sqrt{|\hat{\mu}|} \simeq \frac{\pi\hat{\Delta}^2}{32|\hat{\mu}|^{3/2}}, \tag{282a}$$

$$\frac{4}{3} \simeq \frac{\pi}{4\sqrt{|\hat{\mu}|}}\hat{\Delta}^2 - \frac{3\pi}{128|\hat{\mu}|^{5/2}}\hat{\Delta}^4. \tag{282b}$$

Accurate analytic approximations to these equations can be obtained by neglecting terms of higher order in $\hat{\Delta}$. Thus, we find

$$\hat{\mu} \approx -\frac{1}{(k_F a_s)^2}, \tag{283}$$

$$\hat{\Delta} \approx \sqrt{\frac{16}{3\pi k_F a_s}}, \tag{284}$$

where we see that the role of the gap and number equations is effectively reversed in the BEC regime, with the gap equation approximately determining $\hat{\mu}$ and the number equation approximately determining $\hat{\Delta}$. In the next few subsections we will extend the above by-now standard $h = 0$ analysis to finite h and finite imposed species imbalance ΔN.

8.2. BCS regime of one-channel model at $h \neq 0$

In the present section, we analyze the positive-detuning side of the resonance ($a_s < 0$) within the one-channel model at finite h. Our analysis will closely follow that of Section 5 for the two-channel model; with the results of that section in hand, we will be brief in deriving similar results for the one-channel model. In addition, as in Section 5, we will first neglect the possibility of the FFLO state in this section, returning to finite-$\mathbf{Q}$ ground states in Section 8.5. Evaluating the momentum and h integrals in Eq. (271), with approximations $\Delta \ll \mu$ and $h \ll \mu$ appropriate to the BCS regime, we obtain

$$E_G \approx -\frac{m}{4\pi a_s}\Delta^2 - \frac{8c}{15}\mu^{5/2} - c\sqrt{\mu}\Delta^2\left(\frac{1}{2} - \ln\frac{\Delta}{8e^{-2}\mu}\right) - c\sqrt{\mu}\left[h\sqrt{h^2-\Delta^2} - \Delta^2\cosh^{-1}(h/\Delta)\right]\Theta(h-\Delta). \tag{285}$$

We start in the grand-canonical ensemble at fixed μ and h. As we have already seen, the first line of Eq. (285) (E_G at $h = 0$) has a minimum at Δ_{BCS} given by

$$\Delta_{BCS} = 8e^{-2}\mu\exp\left[\frac{\pi\sqrt{\epsilon_F}}{2k_F a_s\sqrt{\mu}}\right]. \tag{286}$$

We recall that Δ_{BCS} and the corresponding ground state energy $E_G(\Delta_{BCS})$ remain h-independent at low h, consistent with a singlet magnetization-free BCS ground state. Physically, this is due to the fact that the $h = 0$ BCS state is gapped and h couples to a conserved quantity ΔN. Mathematically, because of the step function in Eq. (285), $E_G(\Delta_{BCS})$ can only become h-dependent for $h > \Delta_{BCS}$. However, before this can occur a first-order transition to the normal state $\Delta = 0$ takes place at

$$h_c(\mu) = \frac{\Delta_{BCS}}{\sqrt{2}} = 4\sqrt{2}e^{-2}\mu\exp\left[\frac{\pi\sqrt{\epsilon_F}}{2k_F a_s\sqrt{\mu}}\right], \tag{287}$$

determined by equating $E_{G,N} = E_G(\Delta = 0, h_c)$ and $E_{G,SF} = E_G(\Delta_{BCS}, h_c)$, that is clearly smaller than Δ_{BCS}. Hence, the BCS minimum remains stable and independent of h.

At fixed *density* n, the chemical potentials $\mu_{SF}(n)$ and $\mu_N(n)$ of the SF and N phases are bounded by the distinct atom-number constraint equations

$$n \approx \frac{4c}{3}\mu_{SF}^{3/2} + \frac{5}{4}\frac{c\Delta_{BCS}^2}{\sqrt{\mu_{SF}}} - \frac{c\Delta_{BCS}^2}{2\sqrt{\mu_{SF}}}\ln\frac{\Delta_{BCS}}{8e^{-2}\mu_{SF}}, \tag{288}$$

$$n \approx \frac{4c}{3}\mu_N^{3/2} + \frac{ch^2}{2\sqrt{\mu_N}}, \tag{289}$$

and therefore $\mu_{SF} \neq \mu_N$. As a result, the jump discontinuity at the first-order transition at h_c (for fixed μ) opens up into a coexistence region for fixed n, bounded by $h_{c1} = h_c(\mu_{SF})$ and $h_{c2} = h_c(\mu_N)$, respectively determined by the solutions of Eqs. (288) and (289) inside Eq. (287). As discussed at length in in Section 5.3, since neither the SF nor the N can satisfy the atom number constraint while minimizing E_G, for $h_{c1} < h < h_{c2}$ the system is forced to phase separate into a coexisting mixture of SF and N states.

It is straightforward to find h_{c1} and h_{c2} by numerically solving the sets of equations [i.e., Eqs. (288) and (287), and Eqs. (289) and (287)] that define them. At large $(k_F|a_s|)^{-1}$ in the BCS regime (large positive detuning), however, we can find accurate analytic approximations to these equations. To do this, we first write the corresponding sets of equations in dimensionless form ($\hat{h} \equiv h/\epsilon_F$, $\hat{\Delta} \equiv \Delta/\epsilon_F$, $\hat{\mu} \equiv \mu/\epsilon_F$) for $\hat{h}_{c1}$:

$$\frac{4}{3} \approx \frac{4}{3}\hat{\mu}_{SF}^{3/2} + \frac{5\hat{h}_{c1}^2}{2\sqrt{\hat{\mu}_{SF}}} - \frac{\hat{h}_{c1}^2}{\sqrt{\hat{\mu}_{SF}}}\ln\frac{\hat{h}_{c1}}{4\sqrt{2}e^{-2}\hat{\mu}_{SF}}, \tag{290a}$$

$$\hat{h}_{c1} = 4\sqrt{2}e^{-2}\hat{\mu}_{SF}\exp\left[\frac{\pi}{2k_F a_s\sqrt{\hat{\mu}_{SF}}}\right], \tag{290b}$$

and for $\hat{h}_{c2}$:

$$\frac{4}{3} \approx \frac{4}{3}\hat{\mu}_{\rm N}^{3/2} + \frac{\hat{h}_{c2}^2}{2\sqrt{\hat{\mu}_{\rm N}}}, \tag{291a}$$

$$\hat{h}_{c2} = 4\sqrt{2}e^{-2}\hat{\mu}_{\rm N}\exp\left[\frac{\pi}{2k_{\rm F}a_s\sqrt{\hat{\mu}_{\rm N}}}\right]. \tag{291b}$$

As in Section 5.2 where we studied the two-channel model, we solve these equations perturbatively about $\hat{\mu}_{\rm SF} \simeq 1$ and $\hat{\mu}_{\rm N} \simeq 1$, obviously a good approximation since $\hat{h}_{c1}$ and $\hat{h}_{c2}$ are exponentially small. Expressing $\hat{h}_{c1}$ and $\hat{h}_{c2}$ in terms of the gap Eq. (279) in that limit, we have:

$$\hat{h}_{c1} \approx \frac{\hat{\Delta}_{\rm F}}{\sqrt{2}}\exp\left[-\frac{\pi^2\hat{\Delta}_{\rm F}^2}{32(k_{\rm F}|a_s|)^2}\right], \tag{292a}$$

$$\hat{h}_{c2} \approx \frac{\hat{\Delta}_{\rm F}}{\sqrt{2}}\exp\left[-\frac{\pi^2\hat{\Delta}_{\rm F}^2}{32k_{\rm F}|a_s|}\right], \tag{292b}$$

with each expression only accurate to leading order in the argument of the exponential. Thus, we see that, in the asymptotic large $(k_{\rm F}|a_s|)^{-1}$ limit, $0 < \hat{h}_{c1} < \hat{h}_{c2}$, although in the deep BCS regime they become exponentially close to zero and to each other. We note that these expressions also agree exactly with the corresponding two-channel results Eqs. (144c) and (147b), using the relation Eq. (106) between the scattering length a_s and the detuning δ. However, as we shall see, such a simple correspondence only holds in the BCS regime and does not apply in the BEC regime. Physically, this correspondence occurs because the molecular dynamics that are accounted for in the two-channel model (but neglected in the one-channel model) are unimportant in the BCS regime.

To connect to experiments in which ΔN rather than h is imposed, $\hat{h}_{c1}$ and $\hat{h}_{c2}$ can be easily converted into critical polarizations using the general formula for the population difference:

$$\frac{\Delta N}{N} = \frac{1}{2}\left[(\hat{\mu} + \sqrt{\hat{h}^2 - \hat{\Delta}^2})^{3/2}\Theta(\hat{\mu} + \sqrt{\hat{h}^2 - \hat{\Delta}^2}) - (\hat{\mu} - \sqrt{\hat{h}^2 - \hat{\Delta}^2})^{3/2}\Theta(\hat{\mu} - \sqrt{\hat{h}^2 - \hat{\Delta}^2})\right] \times \Theta(\hat{h} - \hat{\Delta}). \tag{293}$$

Since $\hat{h}_{c1} < \hat{\Delta}_{\rm BCS}$, clearly Eq. (293) gives $\Delta N_{c1} = 0$. This is consistent with our earlier finding that the BCS SF ground state cannot tolerate any spin population difference in the BCS regime. Using $\hat{\Delta} = 0$ in the normal state we find

$$\frac{\Delta N_{c2}}{N} = \frac{1}{2}\left[(\hat{\mu}_{\rm N} + \hat{h}_{c2})^{3/2}\Theta(\hat{\mu}_{\rm N} + \hat{h}_{c2}) - (\hat{\mu}_{\rm N} - \hat{h}_{c2})^{3/2}\Theta(\hat{\mu}_{\rm N} - \hat{h}_{c2})\right], \tag{294}$$

$$\approx \frac{3}{2}\hat{h}_{c2}\sqrt{\hat{\mu}_{\rm N}}, \tag{295}$$

with the second expression applying for $\hat{h}_{c2} \ll \hat{\mu}_{\rm N}$ (which is always valid in the BCS regime of interest). Inserting Eq. (292b) into Eq. (295), and using $\hat{\mu}_{\rm N} \approx 1 - \frac{1}{8}\hat{\Delta}_{\rm F}^2$ [which follows from Eq. (291a) to leading order], we have

$$\frac{\Delta N_{c2}}{N} \approx \frac{3\hat{\Delta}_F}{2\sqrt{2}}\left(1-\frac{\pi\hat{\Delta}_F^2}{32k_F|a_s|}\right)\left(1-\frac{\hat{\Delta}_F^2}{8}\right), \tag{296}$$

$$\approx \frac{3\hat{\Delta}_F}{2\sqrt{2}}\exp\left[-\frac{\pi^2\hat{\Delta}_F^2}{32k_F|a_s|}\right], \tag{297}$$

where in the last line we used $(k_F|a_s|)^{-1} \gg 1$ and re-exponentiated, valid to leading order. Again, Eq. (297) agrees with the corresponding two-channel result Eq. (167b) using Eq. (106). And, as in the two-channel model, for sufficiently large $(k_F|a_s|)^{-1}$, there is a narrow regime of FFLO phase (neglected in this section) that intervenes between the regime of phase separation and the polarized N state. To remedy this, we must recompute the ground-state energy and number and gap equations including the possibility of a spatially-varying $\Delta(\mathbf{r})$. Before doing this (in Section 8.5), we first study the strong-coupling BEC regime at $a_s > 0$.

8.3. BEC regime of one-channel model

Here, we analyze E_G, Eq. (271), in the BEC regime of $a_s > 0$, still focusing on the case of $\mathbf{Q} = 0$, which, as we saw in Section 7, is actually not a restriction as the ground state in the BEC regime is always at $\mathbf{Q} = 0$. We also anticipate that $\mu < 0$ in the BEC regime, remaining valid even for finite h. Physically, this well-known property of the BEC regime is due to the finite molecular binding energy E_b that fixes $\mu \approx -E_b/2$. For $\mu < 0$, the $\mathbf{Q} = 0$ ground-state energy for the single-channel model, Eq. (271), can be simplified considerably by expanding it to leading order in $\Delta/|\mu|$:

$$E_G = -\frac{4}{15}c(h-|\mu|)^{5/2}\Theta(h-|\mu|) - V_2\Delta^2 + \frac{1}{2}V_4\Delta^4, \tag{298}$$

where the "Landau" coefficients are given by

$$V_2 \equiv \frac{m}{4\pi a_s} - c\sqrt{|\mu|}F_2(h/|\mu|), \tag{299a}$$

$$V_4 \equiv \frac{c\pi}{32|\mu|^{3/2}}F_4(h/|\mu|), \tag{299b}$$

with $F_2(x)$ and $F_4(x)$ given by Eqs. (194) and (195), respectively. The gap and number equations then reduce to

$$V_2 = \Delta^2 V_4, \tag{300a}$$

$$n = -\partial E_G/\partial\mu, \tag{300b}$$

with n the total fermion density. We emphasize that, like in the two-channel model, the naive solution of Eq. (300a) is only a *minimum* of the ground-state energy for sufficiently small h; at larger h it is a local *maximum* and therefore does not correspond to a physical ground state.

To leading order in the small $\Delta/|\mu|$ limit, Eqs. (300a) reduce to

$$V_2 = 0, \tag{301}$$

$$n = \frac{c\pi}{4\sqrt{|\mu|}}\Delta^2 + \frac{2}{3}c(h-|\mu|)^{3/2}\Theta(h-|\mu|). \tag{302}$$

First focusing on the gap equation, Eq. (301), and ignoring the weak $h/|\mu|$ dependence in the second term of V_2 we find (using $F_2(0) = \pi/2$)

$$0 = \frac{m}{4\pi a_s} - \frac{1}{2} c\pi \sqrt{|\mu|}, \tag{303}$$

which gives for the chemical potential [22]

$$\mu = -\frac{1}{2ma_s^2} = -\frac{E_b}{2} = -\frac{\epsilon_F}{(k_F a_s)^2}, \tag{304}$$

minus one-half the molecular binding energy $E_b = 1/ma_s^2$, a well-known result for $h = 0$, that we see extends approximately to $h > 0$. With this result, Eq. (302) becomes

$$n = \frac{\sqrt{2}c\pi}{4\sqrt{E_b}} \Delta^2 + \frac{2}{3} c \left(h - \frac{E_b}{2}\right)^{3/2} \Theta\left(h - \frac{E_b}{2}\right). \tag{305}$$

Clearly, the first and second terms on the right side of this number equation represent fermions bound into molecules and free spin-up fermions, respectively, characteristic of the magnetic superfluid (SF_M) phase that we have discussed for the two-channel model in Section 6. This allows us to relate the molecular condensate wave function (order parameter) to Δ via [22]

$$\psi_m^2 \equiv \frac{c\pi}{4\sqrt{2E_b}} \Delta^2, \tag{306}$$

giving for the number equation

$$n = 2\psi_m^2 + \frac{2}{3} c \left(h - \frac{E_b}{2}\right)^{3/2} \Theta\left(h - \frac{E_b}{2}\right). \tag{307}$$

It is also useful to define an effective molecular chemical potential

$$\mu_m \equiv E_b + 2\mu, \tag{308}$$

in terms of which our approximate solution to the gap equation above [i.e. Eq. (301)] simply corresponds to $\mu_m \approx 0$, as expected for a $T = 0$ Bose condensate. Re-expressing E_G in terms of μ and ψ_m, we find

$$E_G \approx -\frac{4}{15} c \left(h - \frac{E_b}{2}\right)^{5/2} \Theta\left(h - \frac{E_b}{2}\right) - \tilde{V}_2 \psi_m^2 + \frac{1}{2} \tilde{V}_4 \psi_m^4, \tag{309}$$

with the quadratic and quartic coefficients

$$\tilde{V}_2 \equiv 2E_b \left[1 - \frac{2}{\pi}\left(1 - \frac{\mu_m}{2E_b}\right) F_2\left(\frac{2h}{E_b}\right)\right], \tag{310}$$

$$\tilde{V}_4 \equiv \frac{4\pi}{\sqrt{E_b} m^{3/2}} F_4\left(\frac{2h}{E_b}\right). \tag{311}$$

Using Eqs. (306) and (307), we can obtain an approximate expression for the pair field Δ as a function of h:

$$\Delta^2 = \frac{\sqrt{8E_b}}{c\pi}\left[n - \frac{2c}{3}\left(h - \frac{E_b}{2}\right)^{3/2}\Theta\left(h - \frac{E_b}{2}\right)\right], \tag{312a}$$

$$= \Delta_0^2\left[1 - \frac{1}{2}\left(\frac{h}{\epsilon_F} - \frac{E_b}{2\epsilon_F}\right)^{3/2}\Theta\left(h - \frac{E_b}{2}\right)\right], \tag{312b}$$

with Δ_0 the pair field at $h = 0$:

$$\Delta_0 = \sqrt{\frac{2n\sqrt{2E_b}}{c\pi}} = \sqrt{\frac{4n\pi}{m^2 a_s}} = \epsilon_F\sqrt{\frac{16}{3\pi k_F a_s}}, \tag{313}$$

where we used Eq. (104) for n. The preceding equations determine the phase diagram of the single-channel model Eq. (266) on the BEC side of the resonance. We determine the phase diagram at fixed N and h, fixed N and ΔN, and fixed μ and h in Sections 8.3.1, 8.3.2 and 8.3.3, respectively, with the latter a prerequisite to studying *inhomogeneous* polarized paired Fermi condensates in a harmonic trap within the local density approximation.

8.3.1. Phase diagram at fixed $\hat{h}$ and density n

The three critical chemical-potential differences describing the phase diagram at fixed density and chemical potential difference are: h_m, the SF–SF_M transition point, h_{c1}, defined by when the SF_M phase becomes unstable to phase separation and h_{c2}, defined as the h above which the purely fermionic polarized N state is stable. By examining Eq. (270), we see that

$$h_m = \sqrt{\mu^2 + \Delta^2}, \tag{314}$$

with μ and Δ given by their values in the SF phase, i.e., Eqs. (304) and (313), respectively. As we found for the two-channel model in Section 6.3, h_{c1} is most easily (approximately) determined by finding the point where $\tilde{V}_4$ vanishes (so that molecules are no longer repulsive), signaling the first-order instability. Examining Eq. (311) and recalling $F_4(1.30) = 0$, we see that this occurs at $2h_{c1}/E_b = 1.30$. Finally, h_{c2} is defined as that h at which the molecular density vanishes according to Eq. (307) and the system consists of a fully-polarized Fermi gas. Taken together, these three critical h's are then given by:

$$h_m \simeq \sqrt{\frac{E_b^2}{4} + \frac{2n\sqrt{2E_b}}{c\pi}}, \tag{315a}$$

$$\simeq \epsilon_F\sqrt{\frac{1}{(k_F a_s)^4} + \frac{16}{3\pi k_F a_s}}, \tag{315b}$$

$$h_{c1} \simeq 0.65E_b = 1.30\frac{\epsilon_F}{(k_F a_s)^2}, \tag{315c}$$

$$h_{c2} \simeq \frac{1}{2}E_b + \left(\frac{3n}{2c}\right)^{2/3} = \epsilon_F\left(2^{2/3} + \frac{1}{(k_F a_s)^2}\right), \tag{315d}$$

where we have expressed them in terms of the molecular binding energy $E_b = 2\epsilon_F/(k_F a_s)^2$. Note that, as can be seen from the way it is displayed in the phase diagram Fig. 44, h_m is

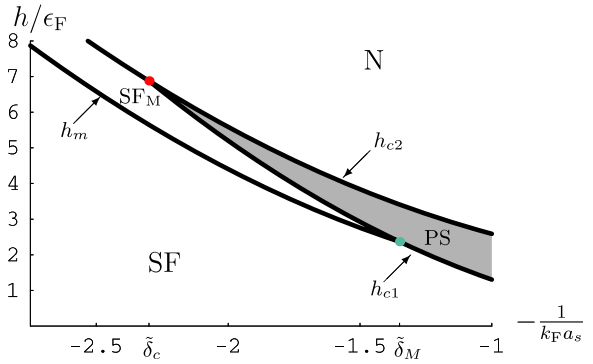

Fig. 44. Plot of *approximate* critical curves h_m [Eq. (315b)], h_{c1} [Eq. (315c)] and h_{c2} [Eq. (315d)] which separate regions of magnetized molecular superfluid (SF_M), a fully-polarized normal Fermi gas (N), and a singlet molecular superfluid (SF). The critical detunings $\tilde{\delta}_c \equiv -(k_F a_{sc})^{-1}$ and $\tilde{\delta}_M \equiv -(k_F a_{sM})^{-1}$ denote a tricritical point and the beginning of the SF_M phase, respectively. This approximate phase digram agrees well with the numerically-determined mean-field phase diagram for the single-channel model Fig. 41.

only defined for sufficiently large $(k_F a_s)^{-1}$ (to the left in the figure), and ceases to be defined when it crosses the lower critical h_{c1} boundary at the critical scattering length a_{sM} satisfying $(k_F a_{sM})^{-1} \approx 1.35$. Similarly, h_{c1} is only defined for small $(k_F a_s)^{-1}$, until it crosses h_{c2} at a_{sc} given by $(k_F a_{sc})^{-1} \approx 2.30$; this is a tricritical point. These two critical points are analogous to the critical detunings δ_M and δ_c in the two-channel model.

8.3.2. Phase diagram at fixed population difference

In the present subsection, we convert these critical h's to corresponding critical population differences (or magnetizations). To do this, we simply use $\Delta N(h)$, Eq. (179). Of course, since h_m is defined by the h at which the population difference ΔN increases from zero in a continuous fashion, $\Delta N_m = 0$. Moreover, everywhere on the BEC side $\Delta N_{c2}/N = 1$, as can be seen by plugging Eq. (315d) into Eq. (179); thus, a normal Fermi gas with anything less than complete polarization is unstable to pairing or phase separation in the deep BEC regime. We are therefore left with the computation of ΔN_{c1}, the population difference at which the polarized one-channel model (in the SF_M state) is unstable to phase separation. Eq. (179) yields for ΔN_{c1} [using Eq. (109); recall Eqs. (105a), (105b), (105c), (105d), (105e)]:

$$\frac{\Delta N_{c1}}{N} = \frac{1}{2}\left(\sqrt{\hat{h}_{c1}^2 - \hat{\Delta}^2} - |\hat{\mu}|\right)^{3/2} \Theta\left(\sqrt{\hat{h}_{c1}^2 - \hat{\Delta}^2} - |\hat{\mu}|\right), \tag{316}$$

where $\hat{\mu}$ is given by Eq. (304) and $\hat{\Delta}$ is given by its value at the transition, obtained by plugging h_{c1} into Eq. (312b):

$$\hat{\Delta}^2 \simeq \frac{16}{3\pi k_F a_s}\left[1 - \frac{1}{2}\left(\frac{1.30}{(k_F a_s)^2} - \frac{1}{(k_F a_s)^2}\right)^{3/2}\right], \tag{317}$$

which, along with Eqs. (316) and (315c) yields

$$\frac{\Delta N_{c1}}{N} \simeq \frac{1}{2}\left(\sqrt{\frac{(1.30)^2}{(k_F a_s)^4} - \hat{\Delta}^2} - \frac{1}{(k_F a_s)^2}\right)^{3/2}, \tag{318}$$

plotted in Fig. 45. This analytic approximation agrees well with the exact numerically-determined mean-field phase diagram for the single-channel model Fig. 42.

8.3.3. Phase diagram at fixed chemical potential

We conclude this subsection by computing the phase diagram in the grand-canonical ensemble at fixed μ and h that will be important for the extension of this bulk analysis to that of a trap in Section 9. Our analysis here will mirror that of the BEC regime of the two-channel model in the grand-canonical ensemble presented in Section 6.6.

To determine the phase diagram at fixed μ and h, it is most convenient to use the ground-state energy function Eq. (309) as a starting point. We first consider the case of $h = 0$ in the SF phase. Since E_G has the form of a conventional "ϕ^4" theory [129], with quadratic and quartic terms in the molecular field ψ_m, the vanishing of the quadratic coefficient signals a second-order SF-to-Vacuum transition in a well-studied universality class [132,133]. At $h = 0$ the point where this occurs is given by $\tilde{V}_{2,c} = \mu_{m,c} = 0$. For small $h < h_m$, the same qualitative behavior, of a SF-to-Vacuum transition at $\mu_{m,c} = 0$, persists and leads to the vertical phase boundary in Fig. 46. With increasing h, the vacuum phase undergoes a continuous transition to the spin-polarized N phase when $\mu_\uparrow$ becomes positive, yielding the phase boundary $h = (E_b - \mu_m)/2$.

Similarly, with increasing h the SF phase acquires a nonzero magnetization, entering the SF_M state, when $m(h)$ becomes nonzero at h_m satisfying Eq. (314). Using $\mu = \frac{1}{2}(\mu_m - E_b)$ and the sixth-order approximation for Δ^2 [i.e., the analogue within the one-channel model of our result Eq. (216) for the two-channel model] with Eq. (314) yields the SF–SF_M phase boundary depicted in Fig. 46.

As we saw for the two-channel model, for h sufficiently close to $|\hat{\mu}|$ (so that $\tilde{V}_4 > 0$) there is a continuous SF_M–N transition at $\tilde{V}_2 = 0$, yielding the following extension of $\mu_{m,c}$ at higher h:

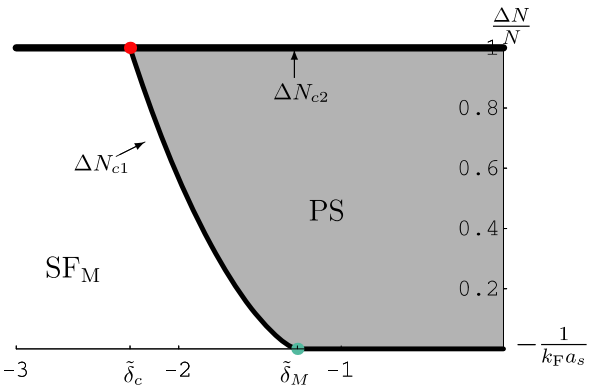

Fig. 45. Approximate (analytic) polarization-scattering length phase diagram on BEC side, for the single-channel model, illustrating the critical polarization boundaries ΔN_{c1} and $\Delta N_{c2} = N$, with critical detuning values $\tilde{\delta}_c$ and $\tilde{\delta}_M$ defined as in the Fig. 44. This approximate phase digram agrees well with the numerically-determined mean-field phase diagram for the single-channel model Fig. 42.

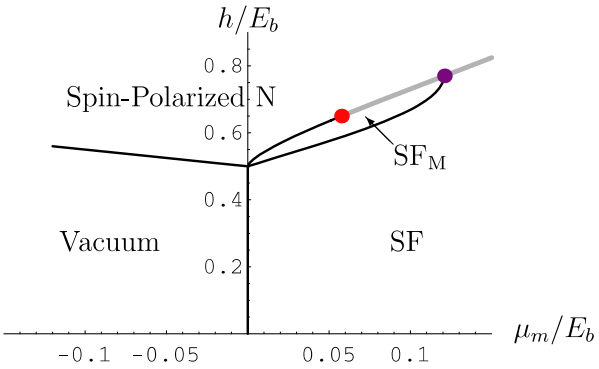

Fig. 46. Phase diagram in the grand-canonical ensemble for the single-channel model Eq. (266) as a function of molecular chemical potential μ_m and atomic chemical potential difference h, showing superfluid (SF), magnetic superfluid (SF_M), vacuum and fully-polarized N phases. Black lines denote continuous $T = 0$ transitions, while the gray curve denotes a first-order SF_M–N transition. The red dot at (0.058,0.65) is a tricritical point separating first-order and second-order SF_M–N transitions. Beyond the purple dot at (0.121,0.77), the SF_M phase ceases to exist.

$$\mu_{m,c} = E_b\left(2 - \frac{\pi}{F_2(2h/E_b)}\right), \tag{319}$$

a formula that applies to the left of the tricritical point at (0.058, 0.65) (where $\tilde{V}_4$ vanishes). Beyond this tricritical point, the fourth order expansion of the ground-state energy breaks down and we must incorporate the sixth-order term as we did in Section 6.4 for the two-channel model. Of course, the close analogy between the one and two-channel models means the sixth-order term is essentially the same. Inclusion of this term (which we shall derive in Section 9.2 below) yields a first-order SF_M–N transition at h_c (satisfying the analogue of Eq. (221b) for the one-channel model) at

$$\mu_{m,c} \simeq E_b\left(2 - \frac{\pi}{F_2(2h/E_b)}\left[1 - \frac{\pi^3}{256}\frac{(F_4(2h/E_b))^2}{F_6(2h/E_b)}\right]\right), \tag{320}$$

valid beyond the tricritical point

$$\mu_{m,c} > \mu_{m,tric.} \simeq 0.058E_b, \tag{321}$$

and plotted as a gray curve in Fig. 46.

As seen in the figure, at higher μ_m, the first-order curve Eq. (320) intersects the SF-SF_M transition curve h_m. Although our small-Δ expansion of E_G becomes quantitatively invalid in this regime, the existence of such an intersection at $\mu_m \approx 0.121E_b$ (the purple point in Fig. 46) is correct, as can be verified by an exact numerical minimization of the full ground-state energy. Beyond this point, the SF_M state ceases to exist, and there is a direct first-order SF–N transition.

8.4. Molecular scattering length and zeroth sound velocity

In the present subsection, we compute the molecular scattering length a_s and the corresponding zeroth sound velocity within the single-channel model. To do this, we need to

first calculate the molecular dispersion induced by atom-molecule resonant interactions. This requires a computation of the leading-order contribution to the energy due to spatial variations in Δ or ψ_m, which comes from computing the momentum-dependent part of the self energy (diagram Fig. 47):

$$\Sigma(q,\Omega) = \int \frac{\mathrm{d}^3 p}{(2\pi)^3} T \sum_{\omega} \frac{1}{\mathrm{i}\omega - \xi_{p\uparrow}} \frac{1}{\mathrm{i}\omega - \mathrm{i}\Omega + \xi_{\mathbf{q}-\mathbf{p}\downarrow}}, \tag{322}$$

with the ω being fermionic Matsubara frequencies and $\xi_{p\sigma} \equiv \epsilon_p - \mu_\sigma$. As usual, we shall take $T \to 0$; furthermore, we only require $\Sigma(q,0)$ to leading (quadratic) order in q. As in the gap equation, the short-scale (UV cutoff) dependence of $\Sigma(q,0)$ can be absorbed into the experimentally-measured scattering length a_s. Direct evaluation of Eq. (322) then yields (to quadratic order in q)

$$-\frac{1}{\lambda} + \Sigma(q,0) = -\frac{m}{4\pi a_s} + c\sqrt{\mu} F_2(h/|\mu|) + q^2 \frac{c}{32m|\mu|^{1/2}} F_q(h/|\mu|), \tag{323}$$

where

$$F_q(x) \equiv 1 - \left[\frac{2}{\pi}\tan^{-1}\sqrt{x-1} - \frac{4}{3\pi}\sqrt{x-1}\left(\frac{1}{x^2} + \frac{1}{2x}\right)\right]\Theta(x-1), \tag{324}$$

and we recall that $F_2(x)$ is given by Eq. (194). Clearly, the first two terms of Eq. (323) simply represent the previously-computed coefficient $-V_2$ in Eq. (298). The q-dependent part is new, and represents the energetic cost of spatial variations of Δ, or, more physically, the molecular kinetic energy. Thus, the generalization of E_{G}, Eq. (298), (restoring the system volume V) to the case of a spatially-varying Δ is simply given by (neglecting an overall Δ-independent constant term):

$$E_{\mathrm{G}} \approx \int \mathrm{d}^3 r \left[\frac{c F_q(h/|\mu|)}{32m|\mu|^{1/2}} |\nabla\Delta|^2 - V_2|\Delta|^2 + \frac{1}{2}V_4|\Delta|^4\right], \tag{325}$$

that in terms of ψ_m reduces to the standard Ginzburg–Landau form [using the relation of Δ to ψ_m, Eq. (306)]

$$E_{\mathrm{G}} \approx \int \mathrm{d}^3 r \left[\frac{|\nabla\psi_m|^2}{2m_b} - \tilde{V}_2|\psi_m|^2 + \frac{1}{2}\tilde{V}_4|\psi_m|^2\right]. \tag{326}$$

The molecular mass m_b is defined by

$$\frac{1}{m_b} = \frac{F_q(2h/E_b)}{2m}, \tag{327}$$

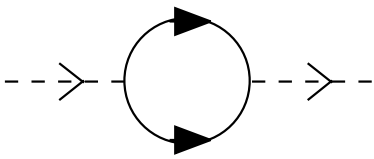

Fig. 47. Feynman diagram corresponding to the molecular self energy, in which the solid lines are atomic (fermion) propagators and the dashed lines are molecular propagators.

and therefore is not simply $2m$ but is enhanced through the function $F_q(2h/E_b)$. Note that, unlike the function $F_4(x)$ that vanishes indicating the instability of the $\mathrm{SF_M}$ phase, $F_q(x)$ is positive in the regime of interest $x > 1$.

This expression for m_b, together with $\tilde{V}_4$, allows us to deduce the molecular scattering length a_m

$$\tilde{V}_4 = \frac{8\pi a_s F_4(2h/E_b)}{F_q(2h/E_b) m_b}, \tag{328}$$

$$\equiv \frac{4\pi a_m}{m_b}, \tag{329}$$

where in the second line we used the well-known relation [127] between the quartic coefficient and the molecular scattering length a_m to identify

$$a_m(h) = 2a_s \frac{F_4(2h/E_b)}{F_q(2h/E_b)}, \tag{330}$$

that decreases with increasing h as we found in the two-channel model. We note here that, because Eq. (330) is computed only within the Born approximation (equivalent to our one-loop mean-field theory), it is certainly not quantitatively accurate. This is consistent with our caveat, made at the start of this section, about the uncontrolled accuracy of the mean-field approximation on the one-channel model. The level of this quantitative inaccuracy can be assessed by noting that our result for $a_m(h)$ reduces to [22] $a_m(h=0) = 2a_s$ that is known to be off the exact value in the dilute BEC limit of $a_m(h=0) = 0.6a_s$ found by Petrov et al. [134] (see also Refs. [135,28]), with the difference arising from strong molecular fluctuations about the mean-field theory solution [28]. Finding the generalization of the formula $a_m = 0.6a_s$ to finite chemical-potential difference [which would give the exact form of Eq. (330)] remains a challenging open problem.

Using Eq. (330), it is straightforward to find the sound velocity u inside the SF and $\mathrm{SF_M}$ phases using the standard expression [127]

$$u^2 = \frac{4\pi n_m a_m}{m_b^2}. \tag{331}$$

Following the analysis of Section 6.7 and using Eq. (330), we find

$$u^2 \simeq \frac{\pi n a_s}{m^2}\left[1 - \frac{1}{2}\left(\frac{h}{\epsilon_F} - \frac{E_b}{2\epsilon_F}\right)^{3/2}\Theta(2h - E_b)\right] F_q\left(\frac{2h}{E_b}\right) F_4\left(\frac{2h}{E_b}\right), \tag{332}$$

at fixed chemical potential difference h, or, at fixed polarization,

$$u^2 \simeq \frac{\pi n a_s}{m^2}\left(1 - \frac{\Delta N}{N}\right) F_q\left[(k_F a_s)^2\left(\frac{2\Delta N}{N}\right)^{2/3} + 1\right] \times F_4\left[(k_F a_s)^2\left(\frac{2\Delta N}{N}\right)^{2/3} + 1\right]. \tag{333}$$

With increasing ΔN, there are two ways $u(\Delta N)$ can vanish according to Eq. (333): For moderate detunings, $(k_F a_s)^{-1}$ close to unity, it vanishes when the effective molecular interaction proportional to the function F_4 vanishes at ΔN_{c1} approximately given by Eq. (318), signaling the first-order transition to the regime of phase separation. In contrast, for large negative detunings, deep in the BEC regime $\frac{1}{k_F a_s} > \frac{1}{k_F a_{sc}}$, the velocity $u(\Delta N)$ vanishes due to

the vanishing molecular density $n_m \propto (1 - \Delta N/N)$, before F_4 does. In this regime the vanishing of u simply signals the second-order transition to the normal state.

This concludes our description of the single-channel model Eq. (266) at finite chemical potential difference h in the BEC regime. Next, we study the FFLO regime of the single-channel model, confined to the positive-detuning BCS regime.

8.5. FFLO state in the one-channel model

In the present subsection, we analyze the FFLO ground state for the single-channel model Eq. (266). As in the preceding subsections, we shall be brief in our analysis as details closely resemble those for the two-channel model discussed in Section 7. For simplicity [102], we take the single-$\mathbf{Q}$ FF pairing ansatz for the ground state of the form $\Delta(\mathbf{r}) = \Delta_{\mathbf{Q}} e^{i\mathbf{Q}\cdot\mathbf{r}}$. Following our previous analysis, the ground state energy for this ansatz is [as before, exchanging the coupling λ for the s-wave scattering length a_s using Eq. (52)]:

$$E_G = -\frac{m}{4\pi a_s}\Delta_{\mathbf{Q}}^2 + \sum_k \left(\varepsilon_k - E_k + \frac{\Delta_{\mathbf{Q}}^2}{2\epsilon_k}\right) + \sum_{\mathbf{k}} [E_{\mathbf{k}\uparrow}\Theta(-E_{\mathbf{k}\uparrow}) + E_{\mathbf{k}\downarrow}\Theta(-E_{\mathbf{k}\downarrow})], \tag{334}$$

where we recall that E_k is given by Eq. (74b), ε_k is given by Eq. (74a), and $E_{\mathbf{k}\sigma}$ is given by Eqs. (74c) and (74d).

As in the two-channel case, the FFLO state in the single-channel model is described (in the grand-canonical ensemble) by the gap ($\partial E_G/\partial \Delta_{\mathbf{Q}} = 0$) and momentum equations ($\partial E_G/\partial Q = 0$), that, using Eq. (334), give

$$0 = -\frac{m}{2\pi a_s} - \sum_k \left(\frac{1}{E_k} - \frac{1}{\epsilon_k}\right) + \sum_k \frac{1}{E_k}(1 + \Theta(-E_{\mathbf{k}\uparrow}) - \Theta(E_{\mathbf{k}\downarrow})), \tag{335a}$$

$$0 = \frac{Q}{2}\sum_k \left[1 + \frac{\varepsilon_k}{E_k}(\Theta(-E_{\mathbf{k}\uparrow}) - \Theta(E_{\mathbf{k}\downarrow}))\right] - \frac{1}{Q}\sum_k \mathbf{k}\cdot\mathbf{Q}(\Theta(-E_{\mathbf{k}\uparrow}) + \Theta(E_{\mathbf{k}\downarrow})). \tag{335b}$$

We remark that the right side of Eq. (335b) can also be obtained by computing the expectation value of the momentum operator with respect to our variational ground-state wavefunction [89].

We now proceed to evaluate the momentum sums in Eqs. (335a), (335b), focusing on the small-$\Delta_{\mathbf{Q}}$ limit. Starting with the gap equation, the first sum in Eq. (335a) is

$$\sum_k \left(\frac{1}{E_k} - \frac{1}{\epsilon_k}\right) \simeq 2N(\tilde{\mu}) \ln \frac{8e^{-2}\tilde{\mu}}{\Delta_{\mathbf{Q}}}, \tag{336}$$

while the second, excluded, sum can be evaluated following the procedure of Appendix F. We find, assuming from the outset that we are in the doubly-depaired FFLO state occuring near the second-order FFLO-N transition at h_{FFLO} [86]:

$$\sum_k \frac{1}{E_k}(1 + \Theta(-E_{\mathbf{k}\uparrow}) - \Theta(E_{\mathbf{k}\downarrow})) \simeq \frac{N(\tilde{\mu})}{\bar{Q}}\left[G(\bar{Q} + \bar{h}) + G(\bar{Q} - \bar{h})\right], \tag{337}$$

where $\bar{Q} \propto 1/\Delta_{\mathbf{Q}}$ is given by Eq. (244a) and

$$G(x) \equiv (x\cosh^{-1}x - \sqrt{x^2 - 1})\Theta(x - 1). \tag{338}$$

With this result, the gap equation Eq. (335a) becomes

$$0 = -\frac{m}{2\pi a_s} - 2N(\tilde{\mu})\ln\frac{8e^{-2}\tilde{\mu}}{\Delta_{\mathbf{Q}}} + \frac{N(\tilde{\mu})}{\bar{Q}}\left[G(\bar{Q}+\bar{h}) + G(\bar{Q}-\bar{h})\right]. \tag{339}$$

Near the second-order transition at $\hat{h}_{\mathrm{FFLO}}$, we can expand the right side of Eq. (339) in small $\Delta_{\mathbf{Q}}$, using Eqs. (336) and (337). To leading order, we find

$$0 = -\frac{m}{2\pi a_s} - 2N(\tilde{\mu})\ln\frac{8e^{-2}\tilde{\mu}}{\Delta_{\mathbf{Q}}} + N(\tilde{\mu})\left(\ln 4(\bar{Q}^2-\bar{h}^2) + \frac{\bar{h}}{\bar{Q}}\ln\frac{\bar{Q}+\bar{h}}{\bar{Q}-\bar{h}} - 2 + \frac{1}{2}\frac{1}{\bar{Q}^2-\bar{h}^2}\right). \tag{340}$$

Expressing Eq. (340) in terms of the $h=0$ gap Δ_{BCS} in the single-channel model using

$$\frac{-m}{4\pi a_s} = N(\mu)\ln\frac{8e^{-2}\mu}{\Delta_{\mathrm{BCS}}}, \tag{341}$$

using $\tilde{\mu} \equiv \mu - Q^2/8m$, and switching to our dimensionless variables Eqs. (105a), (105b), (105c), (105d), (105e) and (248) we have, to leading order in $\hat{\Delta}_{\mathbf{Q}}$ and the dimensionless momentum $\hat{Q}$,

$$\hat{\Delta}_{\mathbf{Q}}^2 \simeq 2(\hat{Q}^2-\hat{h}^2)\left[2 - \ln\frac{4(\hat{Q}^2-\hat{h}^2)}{\hat{\Delta}_{\mathrm{BCS}}^2} - \frac{\hat{h}}{\hat{Q}}\ln\frac{\hat{Q}+\hat{h}}{\hat{Q}-\hat{h}} - \frac{\hat{Q}^2}{8\hat{\mu}^2}\ln\frac{8\hat{\mu}}{\hat{\Delta}_{\mathrm{BCS}}}\right], \tag{342}$$

which describes the magnitude of the pairing order parameter $\Delta_{\mathbf{Q}}$ in the FFLO regime near $\hat{h}_{\mathrm{FFLO}}$.

Turning to the momentum equation, we split the first line of Eq. (335b) into two sums:

$$\sum_k\left[1 + \frac{\varepsilon_k}{E_k}(\Theta(-E_{\mathbf{k}\uparrow}) - \Theta(E_{\mathbf{k}\downarrow}))\right] = \sum_k\left(1 - \frac{\varepsilon_k}{|\varepsilon_k|}\right) + \sum_k\left(\frac{\varepsilon_k}{|\varepsilon_k|} + \frac{\varepsilon_k}{E_k}(\Theta(-E_{\mathbf{k}\uparrow}) - \Theta(E_{\mathbf{k}\downarrow}))\right). \tag{343}$$

The first sum can be easily evaluated exactly:

$$\sum_k\left(1 - \frac{\varepsilon_k}{|\varepsilon_k|}\right) = \frac{4}{3}N(\tilde{\mu})\tilde{\mu}. \tag{344}$$

For the second sum in Eq. (343), we make a standard approximation, replacing the density of states by its value at the Fermi surface, valid for a degenerate Fermi gas (appropriate in the BCS limit). This gives:

$$\sum_k\left[1 + \frac{\varepsilon_k}{E_k}(\Theta(-E_{\mathbf{k}\uparrow}) - \Theta(E_{\mathbf{k}\downarrow}))\right] \simeq \frac{4}{3}N(\tilde{\mu})\tilde{\mu} + N(\tilde{\mu})(\sqrt{\tilde{\mu}^2+\Delta_{\mathbf{Q}}^2} - \tilde{\mu}), \simeq \frac{4}{3}c\tilde{\mu}^{3/2} + \frac{c\Delta_{\mathbf{Q}}^2}{2\sqrt{\tilde{\mu}}}, \tag{345}$$

with the last line applying for $\Delta_{\mathbf{Q}} \ll \tilde{\mu}$. The second momentum sum of Eq. (335b) can also be evaluated within this degenerate Fermi gas approximation, yielding

$$\frac{1}{Q}\sum_k \mathbf{k}\cdot\mathbf{Q}(\Theta(-E_{\mathbf{k}\uparrow})+\Theta(E_{\mathbf{k}\downarrow})) \simeq \frac{\Delta_{\mathbf{Q}}\tilde{k}_{\mathrm{F}}N(\tilde{\mu})}{6\bar{Q}^2} \times\left[2[(\bar{Q}+\bar{h})^2-1]^{3/2}-3\bar{h}\gamma(\bar{Q}+\bar{h})+2[(\bar{Q}-\bar{h})^2-1]^{3/2}+3\bar{h}\gamma(\bar{Q}-\bar{h})\right], \tag{346}$$

where $\gamma(x)\equiv(x\sqrt{x^2-1}-\cosh^{-1}x)\Theta(x-1)$. Combining these terms yields for the number equation Eq. (335b) (approximating $\tilde{k}_{\mathrm{F}}\approx k_{\mathrm{F}}$)

$$0\simeq\frac{4}{3}\frac{m\Delta_{\mathbf{Q}}\bar{Q}\mu}{k_{\mathrm{F}}}+\frac{m\Delta_{\mathbf{Q}}^3\bar{Q}}{2k_{\mathrm{F}}\mu} -\frac{\Delta_{\mathbf{Q}}k_{\mathrm{F}}}{6\bar{Q}^2}\left[2[(\bar{Q}+\bar{h})^2-1]^{3/2}-3\bar{h}\gamma(\bar{Q}+\bar{h})+2[(\bar{Q}-\bar{h})^2-1]^{3/2}+3\bar{h}\gamma(\bar{Q}-\bar{h})\right], \tag{347}$$

which, near $\hat{h}_{\mathrm{FFLO}}$ (and switching to our standard dimensionless variables), yields

$$0\simeq 1-\frac{\hat{h}}{2\hat{Q}}\ln\frac{\hat{Q}+\hat{h}}{\hat{Q}-\hat{h}}+\frac{\hat{Q}^2}{4\hat{\mu}^2}. \tag{348}$$

Our subsequent analysis of Eqs. (342) and (348) mirrors that of the two-channel gap and momentum equations [Eqs. (251a) and (251b), respectively] from Section 7. We are primarily interested in the width of the FFLO regime in the phase diagram as a function of $(k_{\mathrm{F}}|a_s|)^{-1}$, which at fixed $\hat{h}$ is bounded above by the second-order FFLO–N transition at $\hat{h}_{\mathrm{FFLO}}$ and below by the first-order SF–FFLO transition. We express the gap and momentum equations in terms of the parameter λ, defined by $\hat{Q}=\lambda\hat{h}$

$$\hat{\Delta}_{\mathbf{Q}}^2\simeq 2\hat{h}^2(\lambda^2-1)\left[2-\ln\frac{4\hat{h}^2(\lambda^2-1)}{\hat{\Delta}_{\mathrm{BCS}}^2}-\frac{1}{\lambda}\ln\frac{\lambda+1}{\lambda-1}-\frac{\lambda^2\hat{h}^2}{8\hat{\mu}^2}\ln\frac{8\hat{\mu}}{\hat{\Delta}_{\mathrm{BCS}}}\right], \tag{349}$$

$$0\simeq 1-\frac{1}{2\lambda}\ln\frac{\lambda+1}{\lambda-1}+\frac{\lambda^2\hat{h}^2}{4\hat{\mu}^2}. \tag{350}$$

As we saw in Section 7, in the asymptotic BCS regime $(k_{\mathrm{F}}|a_s|)^{-1}\gg 1$, upon dropping the exponentially small last term $\propto\hat{h}^2$, Eq. (350) is solved by $\lambda\approx 1.200$. [86] Inserting this λ value into Eq. (349) and neglecting the subdominant last term of Eq. (349), and setting $\hat{\Delta}_{\mathbf{Q}}=0$, we find [86]

$$\hat{h}_{\mathrm{FFLO}}(\hat{\mu})\simeq\eta\hat{\Delta}_{\mathrm{BCS}}, \tag{351}$$

with $\eta=0.754$, as for the deep-BCS two-channel model. This result applies for small $k_{\mathrm{F}}|a_s|$ in the BCS regime at fixed chemical potential. Combining this with the number equation (which fixes $\hat{\mu}$ at $\hat{\mu}\approx 1-\frac{\hat{h}_{\mathrm{FFLO}}^2}{4}\approx 1-\frac{\eta^2\hat{\Delta}_{\mathrm{F}}^2}{4}$) yields for $\hat{h}_{\mathrm{FFLO}}$ and ΔN_{FFLO}:

$$\hat{h}_{\mathrm{FFLO}}\simeq\eta\hat{\Delta}_{\mathrm{F}}\exp\left[-\frac{\pi\eta^2\hat{\Delta}_{\mathrm{F}}^2}{16k_{\mathrm{F}}|a_s|}\right], \tag{352a}$$

$$\frac{\Delta N_{\mathrm{FFLO}}}{N}\simeq\frac{3}{2}\sqrt{\hat{\mu}}\hat{h}_{\mathrm{FFLO}}, \simeq\frac{3\eta}{2}\hat{\Delta}_{\mathrm{F}}\exp\left[-\frac{\pi\eta^2\hat{\Delta}_{\mathrm{F}}^2}{16k_{\mathrm{F}}|a_s|}\right]. \tag{352b}$$

However, as we showed in the two-channel case, close to the resonance $\hat{h}_{\rm FFLO}$ approaches $\hat{h}_c \approx \hat{\Delta}_{\rm BCS}/\sqrt{2}$, with reduced $(k_{\rm F}|a_s|)^{-1}$, crossing it at a critical coupling strength $k_{\rm F}a_{s*}$ that we now determine. To do this, we first re-express the last term in square brackets in Eq. (349) in terms of a_s using Eq. (341), after setting $\hat{\Delta}_{\mathbf{Q}} = 0$:

$$0 \simeq 2 - \ln\frac{4(\lambda^2-1)}{\hat{\Delta}^2_{\rm BCS}} - \frac{1}{\lambda}\ln\frac{\lambda+1}{\lambda-1} - \frac{\hat{h}^2_{\rm FFLO}\lambda^2}{4\hat{\mu}^2} + \frac{\pi\lambda^2\hat{h}^2_{\rm FFLO}}{16\hat{\mu}^2 k_{\rm F}a_s\sqrt{\hat{\mu}}}. \tag{353}$$

Numerically solving Eqs. (353) and (350) for $\hat{h}_{\rm FFLO}(k_{\rm F}a_s)$, we find that $\hat{h}_{\rm FFLO}$ crosses $\hat{h}_c$ at

$$\frac{1}{k_{\rm F}|a_{s*}|} \approx 0.46, \tag{354}$$

defining the abovementioned critical coupling strength beyond which the FFLO state ceases to be stable within our mean field theory (as plotted in the phase diagram Fig. 41). Although the location of this crossing is not guaranteed to be accurate (due to the absence of a small parameter to justify mean field theory near unitarity), we do expect the existence of the crossing to survive beyond mean-field theory.

9. Polarized superfluidity in a trap: Local density approximation

The primary experimental application of our results on polarized paired superfluidity is that of trapped degenerate atomic gases. It is thus crucial to extend our results to take into account the effect of the potential $V_{\mathcal{T}}(\mathbf{r})$, that in a typical experiment is well-approximated by a harmonic-oscillator potential. While a full analysis of the effect of the trap is beyond the scope of this manuscript, in the present section we study this problem within the well-known local density approximation (LDA). We note that several recent studies (e.g., Refs. [52–55,58,59,68]) have also addressed polarized superfluidity in a trap.

For simplicity, and because of its more direct current experimental relevance, in this section we focus on the single-channel model Eq. (266). The generalization of this model to a trap is straightforward:

$$H = \sum_{\sigma=\uparrow,\downarrow}\int \mathrm{d}^3 r\left(\frac{|\nabla\hat{c}_\sigma(\mathbf{r})|^2}{2m} + (V_T(\mathbf{r}) - \mu_\sigma)|\hat{c}_\sigma(\mathbf{r})|^2\right) + \lambda\int \mathrm{d}^3 r\hat{c}^\dagger_\uparrow\hat{c}^\dagger_\downarrow\hat{c}_\downarrow\hat{c}_\uparrow, \tag{355}$$

where $\hat{c}_\sigma(\mathbf{r})$ is a fermionic field operator with Fourier transform $\hat{c}_{\mathbf{k}\sigma}$. Henceforth, to be concrete, we shall focus on an isotropic harmonic trap $V_T(\mathbf{r}) = V_T(r) = \frac{1}{2}m\Omega_T^2 r^2$, although this simplification can easily be relaxed. Within LDA (valid for a sufficiently smooth trap potential $V_{\mathcal{T}}(r)$, see our discussion in the introduction, Section 1.2), locally the system is taken to be well approximated as *uniform*, but with a local chemical potential given by

$$\mu(r) \equiv \mu - \tfrac{1}{2}m\Omega_T^2 r^2, \tag{356}$$

where the constant μ is the true chemical potential (a Lagrange multiplier) still enforcing the total atom number N. The spatially-varying spin-up and spin-down local chemical potentials are then [cf. Eq. (54a)]:

$$\mu_\uparrow(r) = \mu(r) + h, \tag{357}$$

$$\mu_\downarrow(r) = \mu(r) - h, \tag{358}$$

with the chemical potential difference h *uniform*. Thus, within LDA we approximate the system's energy density by that of a uniform system with spatial dependence (via the trap) entering only through $\mu(r)$. The ground state energy is then simply a volume integral of this energy density. Below we compute the resulting ground-state energy and analyze spatial profiles that emerge from it throughout the phase diagram. Within LDA, the phase behavior as a function of chemical potential, μ, translates into a spatial cloud profile through $\mu(r)$, with critical phase boundaries μ_c corresponding to critical radii defined by $\mu_c = \mu(r_c,h)$. [136] As we first predicted [36], this leads to a shell-like cloud structure that has subsequently been observed experimentally [30,31,35] and reproduced theoretically by a number of works [53,55,59,58].

Below we study these shell structures in much more detail using LDA. We note, however, that throughout our discussion, sharp (discontinuous) features (like the shell structure) that are arise are an artifact of LDA (precisely where it is invalid) and are expected to be smoothed on microscopic (Fermi wave-) length scales by the kinetic energy (or, surface tension [73]).

9.1. BCS regime

As we have seen, for a bulk system in the BCS regime ($a_s < 0$) there are three possible homogeneous phases: (1) the singlet superfluid phase (SF), which is paired and has zero local magnetization (2) the normal phase (N), and (3) the FFLO phase, which exhibits both pairing and local magnetization, but is only stable for a narrow window of chemical potential difference $\Delta_{\rm BCS}/\sqrt{2} < h < 0.754\Delta_{\rm BCS}$. The narrowness of the window of FFLO phase translates, within LDA, to a thin shell $r_c < r < r_c + \delta r$ of FFLO phase in a trap. Although the formalism that we shall now present can be easily generalized to find this shell, we believe that the LDA approximation (which relies on slow variations of physical quantities) is not quantitatively trustworthy for such a thin region, especially considering that the FFLO state itself varies over a large length scale $Q^{-1} \approx (k_{\rm F\uparrow} - k_{\rm F\downarrow})^{-1}$. This is not to say that the FFLO state is not observable in a trap, but merely that theoretical study of the FFLO state in a trap will require a more sophisticated technique than LDA [53]. Thus, in the following analysis we shall generally neglect the FFLO phase, briefly returning to it at the end of this section to estimate the expected width δr of the FFLO phase in a trap within LDA.

Taking advantage of our bulk results at fixed μ and h, in the SF state, the mean-field LDA ground-state energy is given by

$$E_{\rm G,SF} = \int d^3r \left[-\frac{8c}{15}\mu(r)^{5/2} - \frac{m}{4\pi a_s}\Delta(r)^2 + N(\mu(r)) \left(-\frac{1}{2}\Delta(r)^2 + \Delta(r)^2 \ln \frac{\Delta(r)}{8e^{-2}\mu(r)} \right) \right], \tag{359}$$

while in the N state it is given by

$$E_{\rm G,N} = -\frac{4c}{15} \int d^3r \left[(\mu(r)+h)^{\frac{5}{2}} + (\mu(r)-h)^{\frac{5}{2}} \right], \tag{360}$$

$$\approx \int d^3r \left[-\frac{8c}{15}\mu(r)^{5/2} - c\sqrt{\mu(r)}h^2 \right], \tag{361}$$

with the second line applying for $h \ll \mu(r)$ and we recall the dimensionful parameter c is defined in Eq. (100). The pairing field $\Delta(r)$ that locally minimizes Eq. (359) within LDA is then simply given by

$$\Delta(r) \equiv 8e^{-2}\mu(r)\exp\left[\frac{m}{4\pi a_s N(\mu(r))}\right]. \tag{362}$$

Plugging this into Eq. (359) yields

$$E_{\mathrm{G,SF}} = \int d^3r\left[-\frac{8c}{15}\mu(r)^{5/2} - \frac{1}{2}c\sqrt{\mu(r)}\Delta(r)^2\right], \tag{363}$$

so that, by comparing $E_{\mathrm{G,SF}}$, Eq. (363), with $E_{\mathrm{G,N}}$, Eq. (361), we find the critical chemical potential difference

$$\begin{aligned} h_c(r) &= \frac{\Delta(r)}{\sqrt{2}}, \\ &= 4\sqrt{2}e^{-2}\mu(r)\exp\left[\frac{m}{4\pi a_s N(\mu(r))}\right], \end{aligned} \tag{364}$$

at which the SF and N states *locally* have the same energy. Thus, within LDA, at fixed h any regions of the system that satisfy $h < h_c(r)$ are in the SF state while those that satisfy $h > h_c(r)$ will be in the N state. Since $\mu(r)$ in Eq. (356) decreases with increasing r it is clear that, within LDA, the higher-density superfluid regions will be confined to the center of the trap (where μ and thus h_c is largest), with the lower-density polarized N state expelled to the outside, as illustrated in Fig. 5. The resulting shell structure with radius $r_c(h)$ of the SF-N interface is implicitly given by

$$h = 4\sqrt{2}e^{-2}\mu(r_c)\exp\left[\frac{m}{4\pi a_s N(\mu(r_c))}\right], \tag{365}$$

a striking signature of the regime of phase separation in a trap.

To describe the shell structure of the regime of phase separation for positive detuning at fixed atom number N_σ, we exchange μ and h for the total atom number $N = N_\uparrow + N_\downarrow$ and normalized population difference $\frac{\Delta N}{N} = \frac{N_\uparrow - N_\downarrow}{N_\uparrow + N_\downarrow}$. To do this we first note that the local *total* atom density in the SF and N phases is given, respectively, by [cf. Eqs. (159) and (161)]

$$n_{\mathrm{SF}} \simeq \frac{4c}{3}\mu(r)^{\frac{3}{2}} + \frac{5c\Delta(r)^2}{4\sqrt{\mu(r)}} - \frac{c\Delta(r)^2}{2\sqrt{\mu(r)}}\ln\frac{\Delta(r)}{8e^{-2}\mu(r)}, \tag{366a}$$

$$n_{\mathrm{N}} = n_{\mathrm{N}\uparrow}(r) + n_{\mathrm{N}\downarrow}(r), \tag{366b}$$

$$\simeq \frac{4c}{3}\mu(r)^{\frac{3}{2}} + \frac{ch^2}{2\sqrt{\mu(r)}}, \tag{366c}$$

where the local density of spin-σ atoms in the N state is $n_{\mathrm{N}\sigma}(r) \equiv \frac{2c}{3}\mu_\sigma(r)^{3/2}$. Eqs. (366a), (366b), (366c) can also be easily obtained by functionally differentiating Eqs. (359) and (361) with respect to $\mu(r)$. To determine the chemical potential μ in the BCS regime, we note that the above expressions are each well-approximated by their first terms (which are identical). This underscores the weakness of pairing Δ and of the corresponding depairing field h_c in the BCS regime, with only a small fraction of states near the Fermi

surface paired, slightly modifying μ. We first consider the singlet BCS SF at $h = 0$. Since it is unmagnetized, $N_\uparrow = N_\downarrow$ and the total atom number is given by

$$N = \frac{4c}{3}\int d^3r(\mu - \frac{1}{2}m\Omega_T^2 r^2)^{3/2}, \tag{367}$$

where the integration is restricted to $r < R_0$, with the Thomas–Fermi (TF) radius

$$R_0 \equiv \sqrt{\frac{2\mu}{m\Omega_T^2}}, \tag{368}$$

defined by where $\mu(r)$ vanishes and approximately delineating the edge of the system [136]. We shall see below that, at $h \neq 0$, the spin-up and spin-down clouds actually have different Thomas–Fermi radii $R_\uparrow \neq R_\downarrow$. Evaluating the integral, we find

$$N = \frac{\pi^2 c}{6}\mu^{3/2}R_0^3 = \frac{\pi^2 c}{6}\mu^3\left(\frac{2}{m\Omega_T^2}\right)^{3/2}, \tag{369}$$

that gives $\mu = (3N)^{1/3}\hbar\Omega_T$ (a result that is valid beyond LDA [137]), with Eqs. (368) and (369) valid approximations for a cloud at small polarization.

Next, we turn to the mixed state where $\mu > \mu_c(r,h) > 0$, and, as a result, the abovementioned SF–N shell structure develops. Thus, for $r < r_c$ the system consists of a SF core and for $r_c < r < R$ the system consists of a polarized N Fermi gas. Thus, since $n_\uparrow = n_\downarrow$ in the SF sphere, the total $N_\uparrow - N_\downarrow$ is determined by the difference of the total number of spin-up and spin-down atoms in the normal shell outside r_c, which we label by $N_{N\uparrow}$ and $N_{N\downarrow}$. The corresponding atom numbers in these normal shells are given by:

$$N_{N\sigma} = \frac{2c}{3}\int_{r_c<r<R_\sigma} \mathrm{d}^3r\left(\mu_\sigma - \frac{1}{2}m\Omega_T^2 r^2\right)^{3/2}, \tag{370}$$

that lead to distinct Thomas–Fermi radii for spin $\uparrow$ and $\downarrow$:

$$R_\sigma = \sqrt{\frac{2\mu_\sigma}{m\Omega_T^2}}, \tag{371}$$

with the majority (taken as spin-$\uparrow$, for $h > 0$) population occupying the larger volume. Evaluating the integral in Eq. (370), we find

$$N_{N\sigma} = \frac{\pi^2 c}{12}\mu_\sigma^{3/2}R_\sigma^3[1 - f(r_c/R_\sigma)], \tag{372a}$$

with

$$f(x) \equiv \frac{2}{3\pi}\left[3\sin^{-1}x - x\sqrt{1-x^2}(8x^4 - 14x^2 + 3)\right]. \tag{372b}$$

Eq. (372a) counts the number of spin-σ atoms in a spherical shell of inner radius r_c and outer radius R_σ. For $0 < x < 1$, $f(x)$ is a monotonically increasing function of x with $f(0) = 0$ and $f(1) = 1$ (so that a shell of vanishing width naturally contains no atoms). Subtracting $N_{N\downarrow}$ from $N_{N\uparrow}$, we have for the polarization

$$\Delta N = N_{N\uparrow} - N_{N\downarrow}, \tag{373}$$

$$= \frac{\pi^2 c}{12}\left(\frac{2}{m\Omega_T^2}\right)^{3/2}\left(\mu_\uparrow^3\left[1 - f\left(\frac{r_c}{R_\uparrow}\right)\right] - \mu_\downarrow^3\left[1 - f\left(\frac{r_c}{R_\downarrow}\right)\right]\right). \tag{374}$$

Expanding Eq. (374) to leading order in h/μ (valid since $h_c(r) \ll \mu$ in the BCS regime), we have [using $R_{\uparrow,\downarrow} \simeq R_0(1 \pm h/2\mu)$, from Eqs. (368) and (371)]:

$$\Delta N \simeq \frac{\pi^2 c}{12}\left(\frac{2}{m\Omega_T^2}\right)^{3/2} h\mu^2(6[1 - f(x_c)] + x_c f'(x_c)), \tag{375}$$

with $f'(x)$ the derivative of $f(x)$ and where we have defined $x_c \equiv r_c/R_0$. Using Eq. (369) for N, (valid for $h \ll \mu$) we obtain

$$\frac{\Delta N}{N} \simeq \frac{h}{2\mu}(6[1 - f(x_c)] + x_c f'(x_c)). \tag{376}$$

Using Eq. (365) for x_c to eliminate h/μ, and defining k_F via $\mu = k_F^2/2m$ (an approximation corresponding to $\mu \approx \epsilon_F$, valid in the BCS regime), we thus have our final expression for x_c in the BCS regime:

$$\frac{\Delta N}{N} \simeq 2\sqrt{2}e^{-2}(1 - x_c^2)\exp\left[\frac{\pi}{2k_F a_s\sqrt{1 - x_c^2}}\right] \times (6[1 - f(x_c)] + x_c f'(x_c)). \tag{377}$$

For $\Delta N = 0$, Eq. (377) is solved by $x_c = 1$, i.e., the entire system is in the SF phase. With increasing difference ΔN in the number of spin-up and spin-down atoms, however, a thin shell of spin-polarized normal Fermi liquid forms on the outside of the cloud, corresponding to $x_c = r_c/R_0$ decreasing from unity. Although Eq. (377) cannot be solved analytically for x_c, the radius of the inner SF sphere, it is straightforward to determine it numerically, as shown in Fig. 48 for coupling strengths $k_F|a_s| = 2$, $k_F|a_s| = 1.5$ and $k_F|a_s| = 1$ (the latter falling outside the range of quantitative validity of the BCS approximation, but expected to be qualitatively correct). As illustrated in Fig. 48, $r_c(\Delta N)$ vanishes at a critical population difference ΔN_c beyond which the cloud is completely in the N phase, exhibiting Pauli

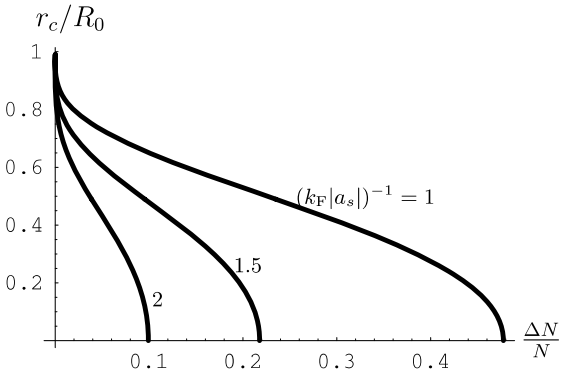

Fig. 48. Radius r_c (normalized to the TF radius R_0) of the SF cloud core as a function of imposed normalized population difference on the positive detuning BCS side of the resonance for coupling strengths (by which they are labeled) $(k_F|a_s|)^{-1} = 2$, $(k_F|a_s|)^{-1} = 1.5$, and $(k_F|a_s|)^{-1} = 1$.

paramagnetism and no pairing even at zero temperature. This critical population difference increases with increasing coupling strength, indicating the increased strength of Cooper-pairing as the Feshbach resonance is approached from positive detuning.

When the system is in the mixed phase, $0 < x_c < 1$, the local magnetization $m(r) = n_\uparrow(r) - n_\downarrow(r)$ will exhibit an interesting radius dependence that we now compute. We find for $m(r)$

$$m(r) = \frac{2c}{3}\mu^{3/2}\left[\left(1 - \frac{r^2}{R_0^2} + \frac{h}{\mu}\right)^{3/2} - \left(1 - \frac{r^2}{R_0^2} - \frac{h}{\mu}\right)^{3/2}\right]\Theta(r - r_c), \tag{378}$$

with the heaviside step function enforcing that $m(r)$ vanishes in the SF state, where $n_\uparrow(r) = n_\downarrow(r)$. For $r > r_c$, in the normal shell, $m(r) = n_N\uparrow(r) - n_N\downarrow(r)$ is nonzero and given in terms of $x = r/R_0$ and a population-difference scale (restoring $\hbar$ for clarity here)

$$m_0 \equiv \frac{2c}{3}\mu^{3/2} = \frac{2}{3}\frac{m^{3/2}\mu^{3/2}}{\sqrt{2}\pi^2\hbar^3}, \tag{379}$$

by

$$m(r) = m_0\left[\left(1 - x^2 + \frac{h}{\mu}\right)^{3/2} - \left(1 - x - \frac{h}{\mu}\right)^{3/2}\right]\Theta(x - x_c). \tag{380}$$

To plot $m(r)$ for a particular coupling and population difference, we combine Eq. (380) with Eq. (377) for $r_c(\Delta N)$ and Eq. (365) for h at that particular population difference and coupling. In Fig. 5, we do this for coupling $(k_F|a_s|)^{-1} = 1.5$ and two different values of the relative population difference: $\frac{\Delta N}{N} = 0.15$ (dashed) and $\frac{\Delta N}{N} = 0.20$ (solid). We note that, since the spin-$\uparrow$ TF radius $R_\uparrow$ is slightly larger than R_0, $m(r)$ is nonzero even slightly beyond unity in the figure.

In Fig. 49, we also plot the experimentally-accessible [30,31] individual spin-up and spin-down densities $n_\uparrow(r)$ and $n_\downarrow(r)$. As expected, for $r < r_c$, in the SF phase, $n_\uparrow(r) = n_\downarrow(r) = n_{SF}(r)/2$, with n_{SF} given by Eq. (366a). To obtain this plot, we need $n_\uparrow(r)$ and $n_\downarrow(r)$ at a particular μ.

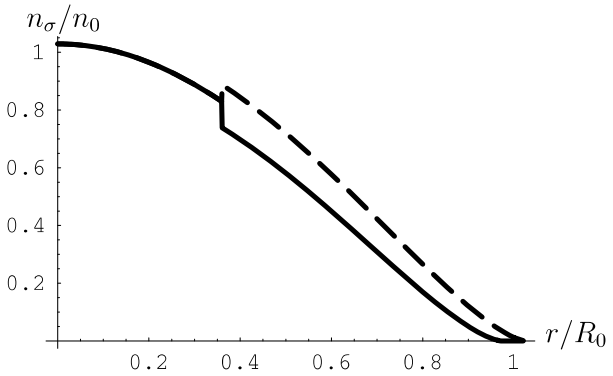

Fig. 49. Local fermion densities $n_\uparrow(r)$ and $n_\downarrow(r)$ (dashed and solid, respectively, normalized to $n_0 \equiv \frac{4}{3}c\mu^{3/2}$) as a function of radius (normalized to the $\Delta N = 0$ TF radius R_0) in the regime of phase separation in a harmonic trap for coupling $(k_F|a_s|)^{-1} = 1.5$ and $\frac{N_\uparrow - N_\downarrow}{N_\uparrow + N_\downarrow} = 0.15$.

Although in the above analytical calculation of μ we have neglected the subdominant Δ-dependent terms, in plotting $n_\uparrow(r)$ and $n_\downarrow(r)$ in Fig. 49 we have included them.

In the normal state, $n_\uparrow(r)$ and $n_\downarrow(r)$ are simply given by the two terms in Eq. (378):

$$n_{N\uparrow}(r) = \frac{2c}{3}\mu^{3/2}\left(1+\frac{h}{\mu}-x^2\right)^{3/2}\Theta\left(1+\frac{h}{\mu}-x^2\right), \tag{381}$$

$$n_{N\downarrow}(r) = \frac{2c}{3}\mu^{3/2}\left(1-\frac{h}{\mu}-x^2\right)^{3/2}\Theta\left(1-\frac{h}{\mu}-x^2\right). \tag{382}$$

Then, to obtain $n_\sigma(r)$ for a particular $(k_F a_s)^{-1}$ and population difference ΔN, we first determine x_c through Eq. (377) and then plot $n_\sigma(r) = \frac{1}{2}n_{SF}(r)\Theta(r_c - r) + n_{N\sigma}(r)\Theta(r - r_c)$. In Fig. 49 we plot the resulting $n_\uparrow(r)$ and $n_\downarrow(r)$ as a function of r for $(k_F a_s)^{-1} = 1.5$ and $\frac{\Delta N}{N} = 0.15$ (i.e. the same parameters as the dashed curve of Fig. 5), for which the SF–N boundary is at $x_c = 0.36$, i.e., at $r_c = 0.36R_0$,

Before proceeding to the LDA in the negative-detuning BEC regime, we compute the width δr of the FFLO phase in a trap. As we have noted above, because the FFLO phase intervenes between the SF and N phases, for a homogeneous system at fixed μ and h, strictly speaking LDA predicts a thin spherical shell of FFLO between the SF and N. To estimate the width of this shell, first imagine imposing a particular h so that the system is polarized. Now, r_c defined by $h \approx \Delta(r_c)/\sqrt{2}$ Eq. (365) denotes the critical radius at which the system jumps from the SF phase to the FFLO phase with increasing radius. Similarly, using Eq. (351), we see that at radius $r_c + \delta r$ defined by $h = h_{FFLO} = \eta\Delta(r_c + \delta r)$ the FFLO phase disappears continuously into the N phase. To find δr, we simply expand each of these equations to leading order in small δr and equate them, which [using Eq. (368)] yields (at $k_F|a_s| \gg 1$)

$$\frac{\delta r}{R_0} \simeq \left(1-\frac{1}{\sqrt{2}\eta}\right)\frac{2k_F|a_s|R_0}{\pi r_c}\left(1-\frac{r_c}{R_0}\right)^{3/2}. \tag{383}$$

The first factor $(1-\frac{1}{\sqrt{2}\eta}) \simeq 0.062$ in Eq. (383) is numerically small by virtue of the thinness of the FFLO region of the phase diagram, i.e., η being close to $1/\sqrt{2}$. The apparent divergence at $r_c \to 0$ is an artifact of approximating $(r_c + \delta r)^2 \simeq r_c^2 + 2\delta r r_c$, valid for $\delta r \ll r_c$, that can be easily fixed. Clearly, $\delta r \ll R_0$ simply because $k_F|a_s| \ll 1$ in the BCS regime. However, even for $k_F|a_s| = 1$, reading a typical value of $r_c/R_0 \simeq 0.5$ for $\Delta N/N = 0.2$ from Fig. 48 yields $\delta r/R_0 \approx 0.05$.

9.2. BEC regime

We now turn to the BEC regime in which $a_s > 0$. As we have already discussed in the preceding subsection, within LDA the phase structure in a trap follows from the phase diagram at fixed μ and h, with the local phase at position r determined by the local chemical potential $\mu(r)$ satisfying Eq. (356). However, an important distinction is that, as we found for the homogeneous case in Section 8.3, the chemical potential μ at the center of the trap is already negative in the BEC regime and therefore $|\mu(r)|$ does not vanish as in the BCS case.

We start by recalling the BEC-regime phase diagram in the grand-canonical ensemble Fig. 46, which we re-plot here (Fig. 50) as a function of h and the fermion chemical potential μ (zoomed-in to emphasize the SF_M phase). The black solid lines represent continuous

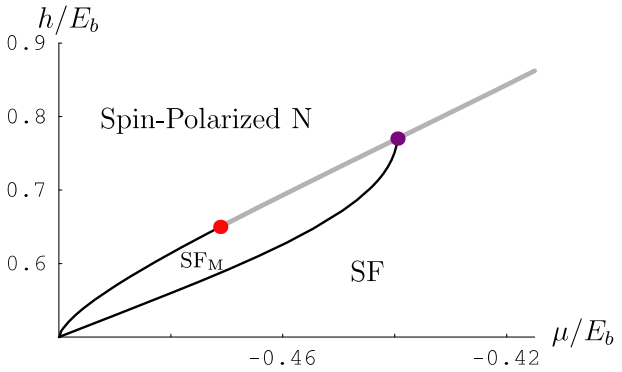

Fig. 50. Mean-field phase diagram (equivalent to Fig. 46) for the single-channel model Eq. (266) as a function of atomic chemical potential μ and atomic chemical potential difference h, each normalized to the molecular binding energy E_b, showing superfluid (SF), magnetic superfluid (SF_M), and fully-polarized normal (N) phases. Thin black lines denote continuous $T = 0$ transitions, while the gray thick curve denotes a first-order SF_M–N or SF–N transition. The red dot at $(-0.47,0.65)$ is a tricritical point separating first-order and second-order SF_M–N transitions while the purple dot at $(-0.44,0.77)$ shows the chemical potential above which the SF_M phase ceases to exist.

phase transitions between the SF_M and N phases (upper line), and between the SF and SF_M phases (lower line). The gray solid line denotes a first-order SF_M to N (or, to the right, a first-order SF to N) transition. Within LDA, a trapped fermion gas with particle number N and population difference ΔN is characterized by a certain chemical potential and chemical potential difference (μ,h) at the center of the trap that can be interpreted as a coordinate in Fig. 50. With increasing radius, $\mu(r)$ changes according to Eq. (356), tracing out a left-ward moving horizontal line segment $(\mu(r),h)$ on Fig. 50. Thus, if a polarized Fermi gas is in the SF phase at the center of the trap, with increasing radius it will generally go through the sequence of phases $SF \to SF_M \to N$, with the $SF_M \to N$ transition continuous for $h < 0.65E_b$ and first order for $h > 0.65E_b$ (the latter indicating jumps in the local density as we have seen in the preceding subsection).

The LDA ground-state energy, which determines μ and h as a function of N, ΔN and the scattering length a_s, is obtained by spatially integrating the local energy density $E_G[\Delta(r),\mu(r)]$ over the cloud's volume. We approximate the full uniform-case energy density Eq. (271) by expanding to sixth order in small Δ/E_b (with E_b the binding energy $E_b = \hbar^2/ma_s^2$). Defining dimensionless quantities $\bar{\Delta}(r) = \Delta(r)/E_b$, $\bar{\mu}(r) = \mu(r)/E_b$ and $\bar{h} = h/E_b$ (the latter not to be confused with the same symbol used in Sections 7 and 8.5) we find

$$\frac{E_G}{cE_b^{5/2}} = \int d^3r \left(-\frac{4}{15} c(h - |\mu(r)|)^{5/2} \Theta(h - |\mu(r)|) - \bar{V}_2(\bar{h},\bar{\mu}(r))\bar{\Delta}(r)^2 + \frac{1}{2}\bar{V}_4(\bar{h},\bar{\mu}(r))\bar{\Delta}(r)^4 + \frac{1}{3}\bar{V}_6(\bar{h},\bar{\mu}(r))\bar{\Delta}(r)^6 \right), \tag{384}$$

with the coefficients

$$\bar{V}_2(\bar{h},\bar{\mu}) = \frac{\pi}{2\sqrt{2}} - \sqrt{|\bar{\mu}|}F_2(\bar{h}/|\bar{\mu}|), \tag{385}$$

$$\bar{V}_4(\bar{h},\bar{\mu}) = \frac{\pi}{32|\bar{\mu}|^{3/2}}F_4(\bar{h}/|\bar{\mu}|), \tag{386}$$

$$\bar{V}_6(\bar{h},\bar{\mu}) = \frac{3}{32|\bar{\mu}|^{7/2}}F_6(\bar{h}/|\bar{\mu}|), \tag{387}$$

where $F_6(x)$ is given by Eq. (213b).

The local pairing field $\bar{\Delta}(r)$ is given by the gap equation [cf. Eq. (215)]

$$0 = -\bar{V}_2(\bar{h},\bar{\mu}(r))\bar{\Delta}(r) + \bar{V}_4(\bar{h},\bar{\mu}(r))\bar{\Delta}^3(r) + \bar{V}_6(\bar{h},\bar{\mu}(r))\bar{\Delta}^5(r), \tag{388}$$

which has the trivial (normal-state) solution $\bar{\Delta} = 0$, as well as the nontrivial solution (suppressing the arguments of the $\bar{V}_\alpha$ for simplicity)

$$\bar{\Delta}^2_\pm(r) = \frac{\bar{V}_4}{2\bar{V}_6}\left[-1 \pm \sqrt{1 + 4\bar{V}_2\bar{V}_6/\hat{V}_4^2}\right]. \tag{389}$$

As discussed in Section 6.4, the correct physical solution (locally corresponding to the SF or SF_M state) is given by the + of Eq. (389) for $\bar{V}_4 > 0$ and the − of Eq. (389) for $\bar{V}_4 < 0$.

Next, we determine equations for the local number density and magnetization. For the former, we find (keeping only leading-order terms) $n(r) = cE_b^{3/2}\bar{n}[\bar{h},\bar{\mu}(r)]$, with

$$\bar{n}[\bar{h},\bar{\mu}(r)] \simeq \frac{2}{3}(\bar{h} - |\bar{\mu}(r)|)^{3/2} + \frac{\bar{\Delta}(r)^2}{2\sqrt{|\bar{\mu}(r)|}}\left(\frac{\pi}{2} - \tan^{-1}\sqrt{\bar{h}/|\bar{\mu}(r)| - 1}\,\Theta(\bar{h} - |\bar{\mu}(r)|)\right), \tag{390}$$

the dimensionless density. Crucially, the spatial dependence of $\bar{n}[\bar{\mu}(r)]$ arises only via $\bar{\mu}(r)$. Similarly, the local magnetization $m(r) = cE_b^{3/2}\bar{m}[\bar{h},\bar{\mu}(r)]$ with

$$\bar{m}[\bar{h},\bar{\mu}(r)] = \frac{2}{3}\left(\sqrt{\bar{h}^2 - \bar{\Delta}(r)^2} - |\bar{\mu}(r)|\right)^{3/2}. \tag{391}$$

In terms of $n(r)$ and $m(r)$, the total particle number N and population difference ΔN are given by

$$N = \int \mathrm{d}^3 r n(r), \tag{392}$$

$$\Delta N = \int \mathrm{d}^3 r m(r), \tag{393}$$

constraints that determine $\bar{\mu}$ and $\bar{h}$ at a particular N and ΔN.

9.2.1. h = 0 case

We start by restricting attention to $\bar{h} = 0$, appropriate for $\Delta N = 0$. For this case, $\bar{\Delta}^2$, Eq. (389), vanishes continuously as $\bar{V}_2 \to 0$, which in a homogeneous system corresponds to a second-order SF-to-Vacuum transition, as discussed in Section 8.3.3. In the present LDA context, it corresponds to the vanishing of the molecular density at the boundary of the system. Thus, we can define the Thomas–Fermi radius R_{TF0}, where $\hat{V}_2$ vanishes, via this condition:

$$\bar{V}_2[0, \bar{\mu}(R_{\mathrm{TF0}})] = 0, \tag{394}$$

or,

$$\bar{\mu}(R_{\mathrm{TF0}}) = \bar{\mu}_0 - \frac{m\Omega_T^2}{2E_b} R_{\mathrm{TF0}}^2 = -\frac{1}{2}. \tag{395}$$

Solving Eq. (395) for R_{TF0} yields, [using Eq. (356)]

$$R_{\mathrm{TF0}} = \sqrt{\frac{E_b(2\bar{\mu}_0 + 1)}{m\Omega_T^2}}, \tag{396}$$

with the zero subscript on $\bar{\mu}_0$ and R_{TF0} indicating that they are for $h = 0$. We proceed to normalize the cloud radius r to R_{TF0}, defining $x = r/R_{\mathrm{TF0}}$, in terms of which the normalized chemical potential is

$$\bar{\mu}_0(x) = \bar{\mu}_0 - x^2\left(\bar{\mu}_0 + \frac{1}{2}\right). \tag{397}$$

With this definition, Eq. (392) becomes

$$N = N_0(2\bar{\mu}_0 + 1)^{3/2} \int \mathrm{d}x\, x^2 \bar{n}[\bar{h}, \bar{\mu}_0(x)], \tag{398}$$

with

$$N_0 = \frac{4\pi c E_b^3}{m^{3/2}\Omega_T^3}, \tag{399}$$

a characteristic particle number scale. One can easily estimate the parameter N_0 from typical experiments. For the case of ^{40}K, given typical values from the Jin group [13,1], we take scattering length $a_s = 750a_0$, (a_0 the Bohr radius) trap frequency $\Omega_{\mathrm{T}} = 2\pi \times 400\ \mathrm{s}^{-1}$. With these parameters, $N_0 \simeq 2 \times 10^8$ and we must adjust $\bar{\mu}_0$ to attain a realistic particle number. Numerically solving Eq. (398) to find the normalized chemical potential yields $\bar{\mu}_0 = -0.465$ for $N = 10^5$. Since the effective molecular chemical potential $\mu_m = E_b + 2\mu$ Eq. (308), which in dimensionless units is $\bar{\mu}_m = 2\bar{\mu} + 1$, we see that the deviation of $\bar{\mu}_0$ from -0.5 directly measures the effective molecular chemical potential. Consistently, we see from Eq. (397) that, at the boundary of the system ($x = 1$), $\bar{\mu}_0(x) = -\frac{1}{2}$ indicating a vanishing of the effective molecular chemical potential. In Fig. 51, we plot the effective normalized molecular density $\bar{n}_m = \pi\bar{\Delta}^2/8\sqrt{|\bar{\mu}|}$ as a function of radius for this case, showing the standard Thomas–Fermi profile for a molecular Bose condensate.

9.2.2. $h \neq 0$ case

At $h \neq 0$, the system becomes locally magnetized, with the total population difference given by Eq. (393). We now study our system at nonzero population difference by simultaneously solving this along with the number equation. In dimensionless form these are

$$N = N_0(2\bar{\mu}_0 + 1)^{3/2} \int \mathrm{d}x\, x^2 \bar{n}[h, \bar{\mu}(x)], \tag{400}$$

$$\Delta N = N_0(2\bar{\mu}_0 + 1)^{3/2} \int \mathrm{d}x\, x^2 \bar{m}[h, \bar{\mu}(x)], \tag{401}$$

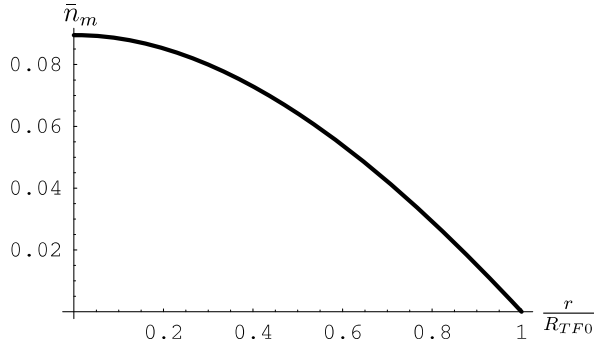

Fig. 51. Normalized molecular density $\bar{n}_m = n_m/cE_b^{3/2}$ as a function of radius for an unpolarized trapped fermion cloud, with parameters given in the text.

where we note that the dependence of Eq. (401) on $\bar{\mu}_0$ arises because we are still measuring the radial coordinate in units of the unpolarized system, i.e., we continue to use $x = r/R_{\mathrm{TF0}}$. To maintain constant N, the chemical potential $\bar{\mu}$ deviates slightly from $\bar{\mu}_0$ and the general formula for $\bar{\mu}(x)$ as a function of the normalized radius is

$$\bar{\mu}(x) = \bar{\mu} - x^2\left(\bar{\mu}_0 + \frac{1}{2}\right). \tag{402}$$

Using Eq. (402) along with Eqs. (400) and (401), it is straightforward to numerically study the cloud shape with increasing ΔN, using the same parameters as before.

As shown in Fig. 6 in Section 2.2, the typical sequence of phases with increasing radius that we find within LDA is $\mathrm{SF} \to \mathrm{SF_M} \to \mathrm{N}$. As in the positive-detuning BCS regime, this is due to the spin-polarized normal fermions having been expelled to the outer shell of the system. In this context, the $\mathrm{SF_M}$ phase that is unique to negative detuning represents a thin shell in which the singlet molecular bosons and outer normal-phase fermions "bleed" into each other. In Fig. 52 we plot the normalized molecular density $\bar{n}_m(r)$ and normalized magnetization $\bar{m}(r)$ as a function of radius for $\frac{\Delta N}{N} = 0.26$ (Fig. 52a) and $\frac{\Delta N}{N} = 0.73$ (Fig. 52b). Fig. 6a is for the same parameters but $\frac{\Delta N}{N} = 0.39$.

The three radii labeled on the horizontal axes of Figs. 52a and b, indicated in the cartoon picture Fig. 6b of the superfluid shell structure, are: R_{f1}, the radius below which $\bar{m}(r) = 0$, R_{TF}, the radius below which $\bar{n}_m(r) \neq 0$ and the system is superfluid and R_{f2}, the radius above which $\bar{m}(r) = 0$. Thus, for $r < R_{\mathrm{TF}}$ and $r < R_{f1}$, the system is in the SF phase, consisting of singlet molecular pairs while for $R_{f1} < r < R_{\mathrm{TF}}$ the system is in the $\mathrm{SF_M}$ phase with coexisting molecular pairs and single-species fermions. For $R_{\mathrm{TF}} < r < R_{f2}$ the system consists purely of single-species fermions.

With increasing $\frac{\Delta N}{N}$, R_{TF} and R_{f1} decrease and R_{f2} rapidly increases as the system is converted from a molecular superfluid to a single-species fermion gas. This behavior, seen in comparing Fig. 52a and b, is shown in detail in Fig. 53, in which we plot all three radii as a function of $\frac{\Delta N}{N}$. We note in particular that, for very large $\frac{\Delta N}{N}$, $R_{f1} \to 0$ with $R_{\mathrm{TF}} \neq 0$. Thus, in this regime, LDA predicts the sequence of phases with increasing radius to be $\mathrm{SF_M} \to \mathrm{N}$.

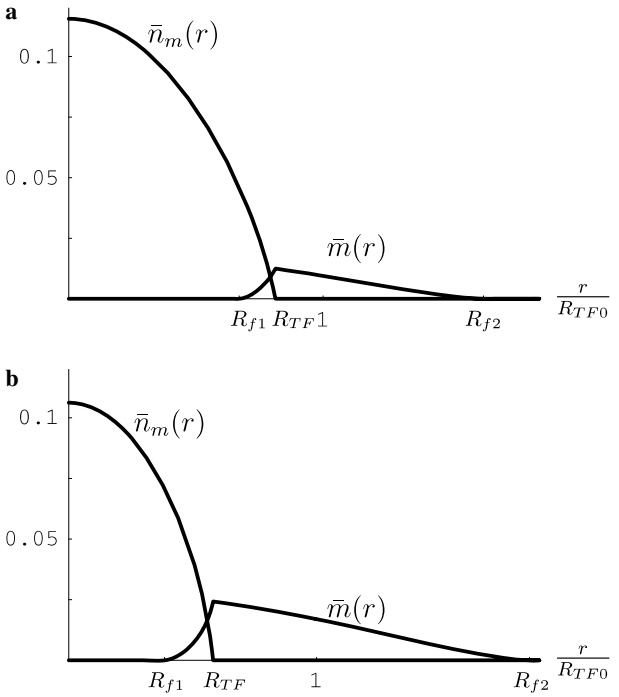

Fig. 52. Normalized molecular density $\bar{n}_m = n_m/cE_b^{3/2}$ and normalized magnetization $\bar{m} = m/cE_b^{3/2}$ as a function of radius for a polarized trapped fermion cloud, with (a) $\Delta N/N = 0.26$ and (b) $\Delta N/N = 0.73$ and other parameters given in the text.

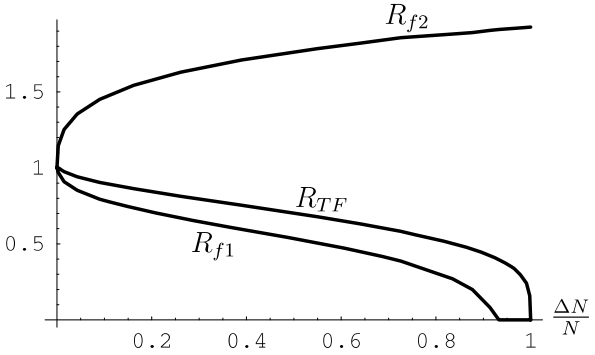

Fig. 53. Plots of the three radii R_{f2} (outer boundary of N phase), R_{TF} (outer boundary of $\mathrm{SF_M}$ phase) and R_{f1} (outer boundary of SF phase) characterizing the polarized cloud in the BEC regime within LDA.

10. Discussion and conclusions

10.1. Summary

In this lengthy manuscript, we have studied the rich zero-temperature phase behavior of a two-species (pseudo-spin up and down) Fermi gas interacting via a tunable Feshbach

resonance and constructed its phase diagram as a function of Feshbach resonance detuning δ and pseudo-spin population imbalance ΔN (and chemical potential difference h). Our main results relied on a well-controlled mean-field analysis of the two-channel model of fermions interacting via a Feshbach resonance that is quantitatively accurate in the narrow resonance limit. In addition, we have complemented this with a study of the one-channel model, appropriate for the wide resonance limit, for which the mean-field approximation that we use is not quantitatively justified near unitarity, but is expected to be qualitatively correct, finding an expected qualitative agreement between the two models.

As described in the main text, for h below a critical value that is exponentially small in the BCS regime of $\delta \gg 2\epsilon_F$, the fully-gapped singlet superfluid (SF) is stable and undergoes the (by now) standard BCS-BEC crossover with reduced δ. On the positive-detuning BCS side of the resonance, for h larger than $h_{c1}(\delta)$ the fixed atom-number constraint forces the system to enter a regime of phase separation (PS) consisting of coexisting singlet SF and partially magnetized FFLO states for $h_{c1} < h < h_{c2}$. At h_{c2}, for $\delta \gg 2\epsilon_F$, the system enters the periodically-paired FFLO phase, before undergoing a continuous [105] transtion to the normal Fermi gas (N) phase at h_{FFLO}. At lower detuning values $\delta \approx 2\epsilon_F$, the FFLO phase becomes unstable and the thin window of FFLO phase between h_{c2} and h_{FFLO} is "squeezed out." In this crossover regime, upon increasing h, the SF undergoes a direct first-order transition to the N phase, with SF–N coexistence for $h_{c1} < h < h_{c2}$ for fixed atom number.

On the negative-detuning BEC side of the resonance, for $h > h_m(\delta)$ the fully-gapped molecular SF undergoes a continuous transition to a homogeneous magnetized superfluid ground state (SF_M) composed of molecules and a single-species Fermi gas, with the latter responsible for the gapless atomic excitations and finite polarization characterizing the SF_M state. Upon further increase of the chemical potential difference, h, for $\delta > \delta_c$ the SF_M undergoes a first-order transition to a fully-polarized N phase, with, for fixed particle number, a phase-separated regime consisting of SF_M and N polarized states. In contrast, for $\delta < \delta_c$ there is a continuous SF_M-N transition. We give a detailed description of these $T = 0$ phases and phase boundaries characterizing the phase diagram, with many of our predictions already verified in recent experiments [30,31,35].

10.2. Relation to other work

Our study of polarized resonantly-interacting Fermi gases builds on a large body of work dating back to the seminal contributions of Clogston [84], Sarma [85], Fulde and Ferrell [86], and Larkin and Ovchinnikov [87]. These were followed by many studies of FFLO and related exotic paired superfluid states that, in additional to off-diagonal long-range order, also break spatial symmetries. These studies range from solid state electronic systems [95] to nuclear matter (quark-gluon plasma) [92,94,103], but until very recently were generally confined to the weakly-interacting BCS regime.

This theoretical effort has recently seen a resurgence of activity, stimulated by the discovery of tunable resonantly-paired superfluidity in degenerate atomic Fermi gases [1–6]. However, perhaps the first theoretical work to study atomic gases with unequal spin populations in the BCS regime, by Combescot [37], preceded these experiments. Also preceding such experiments was the proposal by Liu and Wilczek [38] of the breached pair state, that is closely related to the FFLO and SF_M phases. Other notable theoretical work on spin-polarized Fermi gases in the BCS regime includes that by Mizushima et al. [41],

who studied signatures of FFLO phases in cold fermion experiments but did not determine the conditions necessary (i.e., the phase boundaries) for the observation of such states and that by Bedaque, et al. [39], who emphasized the first-order nature of the SF–N transition and the concomitant regime of phase separation (missed in an important work by Gubankova et al. [138], see Ref. [139] for a discussion).

Later, in a predominantly numerical work Carlson and Reddy [42] extended the study of polarized paired superfluids across the resonance to include the BEC regime, still not including a trap. One important prediction in Ref. [42] is numerical evidence for a uniform magnetized paired superfluid around the unitary point, corresponding to a finite critical value of polarization (species imbalance) to produce phase separation. The unitary point under applied polarization was also studied by Cohen [43], who derived general conditions for phase separation in this regime.

These early microscopic studies and ideas that followed were compiled into a general phenomenological phase diagram by Son and Stephanov [48]. The first microscopic *analytical* study of the problem across the BCS-BEC crossover was done by Pao et al. [47] within the single-channel model via mean-field theory. On the BCS side their study of a uniform Fermi gas (that ignored the interesting FFLO state), was consistent with earlier BCS-regime studies [85,39]. However, their extension to the BEC regime was done incorrectly, leading to a qualitatively wrong phase boundary below which the magnetized superfluid SF_M is unstable. [121] The correct zero-temperature mean-field phase diagram for the single-channel model (consistent with our earlier work on the two-channel model [36]) was published by Gu et al. [64], by Chien et al. [75], and by Parish et al [78], although these authors also neglected the possibility of an FFLO state.

Our work [36] presented the first analytical prediction of a complete (full range of detuning) phase diagram for a resonantly-interacting Fermi gas within the more general two-channel model. Our work also included a detailed study of the FFLO state (extending the original work of Fulde and Ferrell and Larkin and Ovchinnikov to a resonant tunable interaction) as well as a prediction regarding the experimental consequences of the trap. With regard to the former our main contribution was a prediction of the phase boundaries ($h_{\rm FFLO}(\delta)$ and $h_{c2}(\delta)$) for the FFLO state, showing their crossing at $\delta_* \approx 2\epsilon_F$ that leads to the elimination of the FFLO state for $\delta < \delta_*$. With regard to the trap that we studied within LDA, as summarized in the inset of Fig. 1 and last section of our earlier publication [36], with many additional details presented here, our main prediction is that, in a trap, phase separation leads to the recently observed [30,31,35] shell-like cloud profile, with interfacial boundaries whose detailed dependence on detuning and population imbalance we predict.

Our original study also clearly identified the source of the error of Pao et al. in computing phase boundaries in the BEC regime. We unambiguously showed that much of the BEC regime that they claimed to be a uniform stable magnetized superfluid (SF_M in our notation), was in fact a phase separated regime, consisting of coexisting SF_M and fully polarized normal Fermi gas. We have explicitly identified the error in Ref. [47] by reproducing their (in our view erroneous) results. The error stems from the fact that some solutions to the gap equation correspond to saddle points or maxima of the variational ground state energy $E_G(\Delta_{\mathbf{Q}})$. Pao et al. only used the positivity of *local* magnetic susceptibilities and the superfluid stiffness to check stability of the identified solutions. Since this stability criterion is not stringent enough, being necessary but not sufficient, certain solutions of the gap equation identified as stable in Ref. [47] are in fact maxima of $E_G(\Delta_{\mathbf{Q}})$ and therefore in

fact unstable [122]. In the presence of a first-order transition a careful study of $E_G(\Delta_Q)$ (best done in the grand-canonical ensemble [139], with number constraints only imposed a posteriori) is necessary in order to ensure that extrema solutions to the gap equation indeed correspond to stable phases that *minimize* E_G.

Following the subsequent experimental observations by Zwierlein et al. [30] and by Partridge et al. [31], qualitatively consistent with our original predictions (e.g., the shell-like phase structure of the atomic cloud as a signature of phase separation in a trap, the expulsion of magnetization to the outer shell, the general location of phase boundaries and their qualitative detuning and population imbalance dependence), there has been an explosion of theoretical activity. Many of our $T = 0$ predictions have been carefully verified and extended in important ways by many works that followed (see, however, Refs. [47,67,121]). These include nontrivial extensions to a finite temperature [75,78], uncontrolled but elaborate extensions to a broad resonance treated within the one-channel model (beyond our original mean-field approximation), as well as more detailed studies of the effects of the trap [52–55,58,59,73,68], and extensions of the FFLO [50] and other related exotic states [49,51,60]. A notable work by De Silva and Mueller [58] demonstrated that consistency with experiments [31] requires a breakdown of LDA in an anisotropic trap; clearly LDA must also obviously break down at an interface between coexisting phases. This was followed by a detailed treatment of the trap beyond LDA [73], an issue that was also addressed in Refs. [68,32].

The experimental observation [31] (that, however, has not been seen in the MIT experiment [30,35], see also Refs. [32,33]) of the existence of a uniform magnetized superfluid at the unitary point (where $1/k_F a \to 0$) and a corresponding critical polarization ($\Delta N_c/N \approx 0.09$) necessary to drive it to phase separate has generated considerable theoretical interest. With the exception of the theory by Ho and Zhai [62], that attempts to account for this feature via a phenomenological model of Bogoliubov quasi-particle pairing, to our knowledge no model has been able to capture this putative experimental feature; some support for it however exists in the original Monte-Carlo work by Carlson and Reddy [42]. From our perspective, this seemingly qualitative feature reduces to a *quantitative* question of the location of the critical detuning δ_M point in Fig. 3 (or, equivalently, the a_{sM} point in Fig. 42) Our work shows unambiguously that for a *narrow* resonance ($\gamma \ll 1$) at $T = 0$, δ_M most definitely falls in the BEC regime (negative detuning), thereby excluding the uniform magnetized SF_M state from the unitary point. Our mean-field theory predicts the critical scattering length for the broad-resonance one-channel model to be close to $k_F a_{sM} \simeq 1$, again excluding the SF_M state from unitarity. For reasons discussed in the Introduction, Section 1, however, mean-field theory for a broad resonance (relevant to present-day experiments) is not quantitatively valid for a broad resonance. Thus, it is quite possible that for finite T [140] and a broad resonance δ_M indeed shifts to a positive detuning, with the experimental findings of ΔN_c [31] then naturally interpreted as the observation of the SF_M phase at the unitary point.

10.3. Experimental predictions

Most of our predictions were made both for a narrow resonance within a two-channel model and for a broad resonance within a one-channel model. As discussed in the Introduction, the former has an important advantage that it is quantitatively accurate with the width of the resonance as the small expansion parameter. However, unfortunately,

experiments are deep in the broad-resonance regime, where the two-channel model *exactly* [28] reduces to a one-channel model, that in the interesting crossover regime cannot be treated analytically in a quantitatively trustworthy way. We do, however, expect it to give qualitatively correct predictions. And, as mentioned earlier, indeed we find that recent experimental findings are qualitatively consistent with our wide-resonance predictions done within the one channel model.

However, as we discussed above, our perturbative mean-field analysis, in either the narrow or broad resonance limit, does not find a uniform magnetized superfluid near the unitary point and a corresponding finite critical population imbalance ΔN_c.

Another feature that is seen in experiments [30] is that at unitarity the upper-critical boundary where coexistence ends and the normal state takes over is given by $\Delta N_{c2}/N \approx 0.7 < 1$. That is, the transition from phase separation is to a normal state that is only 70% polarized. This seemingly qualitative feature is actually a quantitative question. In contrast to experiments, as we show in the main text (see Fig. 3) our quantitatively accurate narrow resonance two-channel model analysis (that can answer such a question) at the resonance position unambiguously predicts the transition directly to a fully-polarized normal state, i.e., $\Delta N_{c2}/N \approx 1$ at unitarity. However, the less quantitatively trustworthy broad-resonance limit gives a prediction of $\Delta N_{c2}/N \simeq 0.93 < 1$, more consistent with experiments. Pick your poison.

We expect that many of our general predictions will continue being fundamental to the understanding of specific experiments. Our predictions that can be already directly tested (some have already been qualitatively tested [30,31]) are for the atomic cloud phase composition and spatial density and magnetization profiles. Most of these have already been discussed in Section 9, summarized by Figs. 5, 6, 49–53, where we give details of the phase separation-driven cloud shell structure, dependences of radii on detuning and population imbalance, and detailed spatial gas profiles that can be imaged by cloud expansion.

In principle, the FFLO state (that was the original impetus for our study) should exhibit particularly striking experimental signatures, associated with its simultaneous ODLRO and spontaneous breaking of translational and orientational symmetry, encoded in $\Delta_{\mathbf{Q}}$. For a homogeneous cloud, the typical population imbalance required to enter the FFLO state is given by Eq. (261), which in dimensionful units is approximately (recall $\eta \simeq 0.754$)

$$\frac{\Delta N_{\mathrm{FFLO}}}{N} \approx \frac{3\eta \Delta_{\mathrm{BCS}}}{2\epsilon_{\mathrm{F}}}, \tag{403}$$

which we can easily estimate using typical values of Δ_{BCS} and ϵ_{F} from experiments. For example, the last data point of Fig. 2 of Ref. [6] has Fermi temperature $T_{\mathrm{F}} = 1.2\ \mu\mathrm{K}$ and gap $\Delta_{\mathrm{BCS}}/h \approx 1$ KHz (here h is Planck's constant). Converting the former to frequency units yields the Fermi energy $\epsilon_{\mathrm{F}} \approx 25$ KHz and $\Delta_{\mathrm{BCS}}/\epsilon_{\mathrm{F}} \approx .04$, which, when inserted into Eq. (403), yields $\Delta N_{\mathrm{FFLO}}/N \approx .05$, a rather small polarization that will grow closer to the resonance.

Upon expansion (after projection onto a molecular condensate [1]), a *trapped* cloud in the FFLO (supersolid [96–99]) phase should exhibit peaks

$$n(\mathbf{r}, t) \propto \mathcal{F}\left(\mathbf{r} - \frac{\hbar t \mathbf{Q}}{m}\right), \tag{404}$$

in the density profile $n(\mathbf{r},t)$ at time t set by the FFLO wavevector $\mathbf{Q}$, reminiscent of a Bose superfluid state trapped in a periodic optical potential [109], but contrasting from it by the *spontaneous* (since translational symmetry is broken spontaneously) nature of the peaks.

The width of the peaks (given by the function $\mathcal{F}(\mathbf{r})$ that is a Gaussian for a Gaussian trapped cloud, see Appendix G) is set by the inverse spatial extent of the FFLO state. Using the same typical numbers as above from the experiments of Ref. [6], the typical wavevector Q [given by Eq. (260)] can be estimated to be $Q^{-1} \approx 5\mu$m.

The formula Eq. (404) assumes the simplest FFLO-type superfluid $B(\mathbf{r}) \propto e^{i\mathbf{Q}\cdot\mathbf{r}}$. However, as we have discussed, in reality the true ground state in the FFLO regime of the phase diagram will likely be a more complicated (but nearly degenerate) state containing more Fourier modes [87,94,93,90] $\mathbf{Q}_n$, yielding a more complicated density profile of the expanded gas given by the more general formula Eq. (G.9) in Appendix G.

Also, the spontaneous anisotropy of the FFLO state should manifest itself in the atom shot noise distribution [110–112], with peaked $\mathbf{k}, -\mathbf{k}$ correlations that are anisotropic around the Fermi surface with the axis of symmetry spontaneously selected by the $\mathbf{Q}$'s characterizing the FFLO ground state.

However, there might be serious impediments for such a direct detection of the FFLO state in trapped atomic gases. As we showed this phase is confined to a narrow sliver of the phase diagram on the BCS side of the resonance. Within LDA, this narrow range of δh in chemical potential difference translates into a thin FFLO shell at r_c of width [using Eq. (383)]

$$\delta r \sim 0.04 k_F |a_s| \frac{R_0^2}{r_c}\left(1 - \frac{r_c^2}{R_0^2}\right), \tag{405}$$

(applying for r_c not too small) with the cloud radius R_0. Now the (above-mentioned) width of the spontaneous Bragg peaks will be limited from below by this finite shell width as $\delta Q = 2\pi/\delta r$. This places a requirement that $Q \gg 2\pi/\delta r$ in order to be able to resolve the peaks. This is consistent with the condition of applicability of LDA. On the other hand in Section 7 we found the optimum Q characterizing FFLO state is given by $Q \propto \Delta_{BCS}/\hbar v_F$ [Eq. (260)] Hence it is clear that, generally, $Q\delta r \ll 1$.

The identification of phases and the corresponding quantum and thermal phase transitions should also be possible through thermodynamics by measuring, for example, the heat capacity. Although we have not done detailed quantitative studies of this, general arguments [141] predict that the SF_M and FFLO states at low T should be characterized by a heat capacity that is linear in T due to gapless atomic excitations around the majority particle Fermi surface of the SF_M state. This dependence should distinguish the SF_M and FFLO states from a fully gapped BCS–BEC singlet SF state. On the other hand the finite molecular BEC peak and ODLRO, along with their dependence on detuning and polarization, should distinguish the SF_M and FFLO states from the normal Fermi gas (N) state. Direct observation of gapless atomic excitations via Bragg spectroscopy [142] should also be possible. Phase transitions should also be readily identifiable via standard thermodynamic anomalies, such as divergences of susceptibilities across a transition, in addition to effects observable in the density and magnetization profiles.

We hope that our work on this exciting subject of polarized resonant superfluids will stimulate further careful and detailed experimental studies to test our predictions.

Acknowledgments

We gratefully acknowledge useful discussions with S. Choi, J. Gaebler, V. Gurarie, D. Jin, A. Lamacraft, J. Levinsen, E. Mueller, K. Rajagopal, C. Regal, J. Stewart,

M. Veillette as well as support from NSF DMR-0321848 and the Packard Foundation. DES also acknowledges the Aspen Center for Physics where part of this work was carried out.

Appendix A. Scattering amplitude

For completeness, in this Appendix we review the properties of the s-wave scattering amplitude following Refs. [114,26]. The s-wave scattering amplitude is related to the phase shift $\delta_s(k)$ (not to be confused with the bare and renormalized Feshbach resonance detunings δ_0 and δ, respectively) by

$$f_0(k) = \frac{1}{2ik}\left(e^{2i\delta_s} - 1\right). \tag{A.1}$$

Clearly, the unitarity requirement $|2\ ikf_0 + 1| = 1$ is automatically satisfied, which implies that f_0 may be written as

$$f_0 = \frac{1}{g_0(k) - ik}, \tag{A.2}$$

with $g_0(k)$ a real function of k^2. At low energies, expanding the denominator to leading order in k^2 yields

$$f_0(k) = \frac{1}{-a_s^{-1} + r_0k^2/2 - ik}, \tag{A.3}$$

with a_s the s-wave scattering length and r_0 the effective range, that for our resonant two-channel model is actually negative.

The simplest way to compute the scattering amplitude (in vacuum, $\mu = 0$) for the two-channel model Eq. (25) is to note that it is proportional to the molecular propagator $G_b(E) = \langle \hat{b}(E)\hat{b}^\dagger(E)\rangle$,

$$G_b(E) = \frac{1}{E - \delta_0 - \Sigma(0,E)}, \tag{A.4}$$

with $\Sigma(q,E)$ the molecular self energy (diagram in Fig. 47; see Ref. [26]):

$$\Sigma(q,E) = g^2 \int \frac{d^3p}{(2\pi)^3} T\sum_\omega \frac{1}{i\omega - \epsilon_p}\frac{1}{i\omega - i\Omega + \epsilon_{\mathbf{q}-\mathbf{p}}}\bigg|_{i\Omega\to E+i0^+}. \tag{A.5}$$

Taking the $q = 0$ and low-E limit, we obtain

$$\Sigma(0,E) \approx -i\frac{g^2m^{3/2}}{4\pi}\sqrt{E} - g^2\int \frac{d^3p}{(2\pi)^3}\frac{m}{p^2}, \tag{A.6}$$

which, when used in Eq. (A.4), gives $G_b(E)$ in the low-energy limit. Defining the physical (renormalized) detuning $\delta = \delta_0 - g^2\int \frac{d^3p}{(2\pi)^3}\frac{m}{p^2}$ to absorb the short (molecular) scale dependence in the scattering amplitude, we have

$$f_0(E) = -\frac{\sqrt{\Gamma_0/m}}{E - \delta + i\sqrt{\Gamma_0}\sqrt{E}}, \tag{A.7}$$

$$f_0(k) = -\frac{\sqrt{\Gamma_0/m}}{k^2/m - \delta + i\sqrt{\Gamma_0}k/\sqrt{m}}, \tag{A.8}$$

with

$$\Gamma_0 \equiv \frac{g^4 m^3}{16\pi^2}, \tag{A.9}$$

a measure of the width of the resonance and where an overall factor [that is the constant of proportionality between $G_b(E)$ and $f_0(E)$] is fixed using the unitarity condition Eq. (A.2). In obtaining Eq. (A.8), we replaced $E \to k^2/2m_r$, with $m_r = m/2$ the reduced mass. Comparing Eq. (A.8) to Eq. (A.3), we identify

$$a_s^{-1} = -\frac{\delta\sqrt{m}}{\sqrt{\Gamma_0}}, \tag{A.10}$$

$$r_0 = -\frac{2}{\sqrt{m}\sqrt{\Gamma_0}}, \tag{A.11}$$

in terms of the detuning δ and the width Γ_0.

A.1. Experimental determination of parameters

The detuning parameter δ is related to the difference in rest energy between the closed channel and the open channel [10,143]. For a Feshbach resonance tuned to low energy δ by a magnetic field, we expect $\delta \propto (B - B_0)$ near the position of the resonance, where B_0 is the field at which the resonance is at zero energy. Determining the precise constant of proportionality requires a detailed atomic physics analysis that is beyond the scope of this manuscript. However, we can approximate δ by the Zeeman energy difference between the closed and open two-atom states. The latter are approximately dominated by electronic triplet (open channel) and singlet (closed channel) states, giving

$$\delta \approx 2\mu_B(B - B_0), \tag{A.12}$$

with μ_B the Bohr magneton. With this approximation, we can extract parameters of our model, the most important being the width of the resonance, from current experiments. Using Eq. (A.12) inside Eq. (A.10), we get

$$a_s^{-1} = -\frac{2\mu_B\sqrt{m}}{\sqrt{\Gamma_0}}(B - B_0), \tag{A.13}$$

which should be compared with the form [10]

$$a_s = a_{bg}\left(1 - \frac{B_w}{B - B_0}\right), \tag{A.14}$$

observed near a resonance [13,17], with B_w defined to have the same sign as a_{bg}. For $B \to B_0$, Eq. (A.14) can be written as

$$a_s^{-1} \simeq -\frac{B - B_0}{a_{bg}B_w}, \tag{A.15}$$

and comparison to Eq. (A.13) gives

$$\sqrt{\Gamma_0} = \frac{2\sqrt{m}\mu_B a_{bg} B_w}{\hbar}, \tag{A.16a}$$

$$r_0 = -\frac{\hbar^2}{m\mu_B a_{bg} B_w}, \tag{A.16b}$$

where we have reinserted the correct factors of $\hbar$ so that Γ_0 has units of energy and r_0 has units of length. Experiments at JILA on ^{40}K have studied a resonance with [13] $a_{bg} = 92$Å and $B_w = 9.76$ G. Using $m = 6.64 \times 10^{-26}$ kg gives $r_0 \approx 10$ Å and $\sqrt{\Gamma_0} = 4.06 \times 10^{-13}\sqrt{\text{J}}$. Comparing the width Γ_0 to the Fermi energy ϵ_F yields the parameter $\gamma \propto \sqrt{\Gamma_0/\epsilon_F}$ Eq. (37) characterizing the two-channel model. We find, for a typical $\epsilon_F = 3 \times 10^{-33} J$ (see Ref. [111]), $\gamma \approx 6600$ and $1/k_F|r_0| \approx 2600$. Clearly, this Feshbach resonance is quite broad.

For the 830 G ^{6}Li resonance studied in Ref. [17], we have $|a_{bg}| = 744$ Å and $|B_w| = 300$ G, that together with $m = 9.96 \times 10^{-27}$ kg, gives $\sqrt{\Gamma_0} = 3.93 \times 10^{-11}\sqrt{J}$ and $|r_0| = 0.5$Å. A typical value for the Fermi energy may be taken from Zwierlein et al [2], who quote $k_F^{-1} \simeq 2000 a_0$, with $a_0 = 0.529$ Å the Bohr radius. This yields $k_F = 9.4 \times 10^6 m^{-1}$, $\epsilon_F = \hbar^2 k_F^2/2m = 4.9 \times 10^{-29}$J, $\gamma \simeq 5000$ and $1/k_F|r_0| \approx 1982$, also a very broad resonance.

Finally, we consider the narrow ^{6}Li resonance near 543 G studied, e.g., in Ref. [15]. Although to our knowledge fermionic superfluidity has not been observed near this resonance, in the near future it is quite likely. Estimating $|a_{bg}| = 100 a_0$ and $|B_w| \approx 0.1G$ yields (using $T_F \approx 1.4$ μK from Ref. [15]) $\gamma \simeq 18$ and $1/k_F|r_0| \approx 7.3$.

A.2. Bound states and resonances of the scattering amplitude

The poles of the scattering amplitude determine the positions of bound-states and resonances [114]. Since r_0 is negative [114,26,29], we write f_0 as

$$f_0(k) = \frac{1}{-a_s^{-1} - |r_0|k^2/2 - \mathrm{i}k}, \tag{A.17}$$

with the poles given by the quadratic equation:

$$k_p = \frac{\mathrm{i} \pm \mathrm{i}\sqrt{1 + 2|r_0|/a_s}}{-|r_0|}. \tag{A.18}$$

The only subtlety is that these solutions do not always correspond to physical bound states or resonances. Purely imaginary poles are physical bound states only if $\mathrm{Im}k_p > 0$, such that the corresponding wavefunction decays at large radius. Complex poles correspond to a resonance only if the real part of the energy $\mathrm{Re}\,E > 0$ *and* $\mathrm{Im}\,E < 0$.

For the BEC regime $a_s > 0$, we can identify the correct pole as the $-$ of Eq. (A.18),

$$k_p = \frac{\mathrm{i} - \mathrm{i}\sqrt{1 + 2|r_0|/a_s}}{-|r_0|}, \tag{A.19}$$

since it is the one that in the $r_0 \to 0$ limit yields the correct pole at $k_p = \mathrm{i}a_s^{-1}$. This pole is at $k_p = \mathrm{i}\kappa$ with κ a real and *positive* (as required) wavevector (since $\sqrt{1 + 2|r_0|/a_s} > 1$) and thus corresponds to a bound state [114,144] at energy $E_p = -\kappa^2/2m_r = -\kappa^2/m$, with $m_r = m/2$ the reduced mass. Eq. (A.19) then yields

$$E_p = -\frac{2}{mr_0^2}\left[1+\frac{|r_0|}{a_s}-\sqrt{1+\frac{2|r_0|}{a_s}}\right], \tag{A.20}$$

$$= -\frac{\Gamma_0}{2}\left[1+\frac{2|\delta|}{\Gamma_0}-\sqrt{1+\frac{4|\delta|}{\Gamma_0}}\right], \tag{A.21}$$

where in the final equality we used Eqs. (A.10) and (A.11). For $|r_0| \ll a_s$ or $|\delta| \ll \Gamma_0$, $\kappa \approx 1/a_s$, a regime that is referred to as "universal." The bound-state energy is $E_p \approx -\frac{1}{ma_s^2} = -\frac{\delta^2}{\Gamma_0}$. In the opposite limit of $|r_0| \gg a_s$ or $|\delta| \gg \Gamma_0$, $\kappa \approx \sqrt{\frac{2}{a_s|r_0|}}$, corresponding to the bound-state energy $E \approx -(|r_0|a_s m)^{-1} = \delta$. Thus, in this regime the bound state simply follows the detuning.

On the BCS side $a_s < 0$, for $2|r_0| < |a_s|$ both the + and − of Eq. (A.18) apparently give solutions of the form $k_p = i\kappa$ for κ real. But since, for both, κ is negative, they do not correspond to a physical bound state since the corresponding wavefunction is an exponentially growing solution of the radial Schrödinger equation [114,144]. On the other hand, for $2|r_0| > |a_s|$, the pole k_p is complex. Choosing the correct sign of the square root, we have the physical pole at

$$k_p = \frac{1}{|r_0|}\sqrt{\frac{2|r_0|}{|a_s|}-1}-\frac{\mathrm{i}}{|r_0|}. \tag{A.22}$$

This pole corresponds to a physical resonance (by definition) only when the real part of the energy of the pole is *positive* while the imaginary part is negative. The resonance energy is

$$E = \frac{k_p^2}{m} = \frac{2}{mr_0^2}\left(\frac{|r_0|}{|a_s|}-1-\mathrm{i}\sqrt{2|r_0|/|a_s|-1}\right), \tag{A.23}$$

which can be written in terms of the real part of the pole location E_r and width Γ as

$$E = E_r - i\Gamma, \tag{A.24}$$

$$E_r \equiv \frac{2}{mr_0^2}\left(\frac{|r_0|}{|a_s|}-1\right) = \delta - \frac{1}{2}\Gamma_0, \tag{A.25}$$

$$\Gamma \equiv \frac{2}{mr_0^2}\sqrt{2|r_0|/|a_s|-1} = \frac{\Gamma_0}{2}\sqrt{\frac{4\delta}{\Gamma_0}-1}, \tag{A.26}$$

where again we used Eqs. (A.10) and (A.11). Thus, there is a true resonance for $1/|a_s| > 1/|r_0|$ (or, $\delta > \Gamma_0/2$), with a width $\Gamma > \Gamma_0/2$. We note that $E_r \to 0$ as $\delta \to \Gamma_0/2$, but $\Gamma(\delta)$ remains finite at this point with $\Gamma(\delta = \Gamma_0/2) = \Gamma_0/2$.

The positive-energy resonance in the two-channel model can also be seen in the s-wave partial cross section $\sigma_0 = \frac{4\pi}{k^2}\sin^2\delta_s$. Using Eqs. (A.1) and (A.2), the phase shift δ_s satisfies

$$\mathrm{e}^{2\mathrm{i}\delta_s} = \frac{g_0 + \mathrm{i}k}{g_0 - \mathrm{i}k}, \tag{A.27}$$

$$g_0 = -a_s^{-1} + r_0 k^2/2, \tag{A.28}$$

so that σ_0 is given by

$$\sigma_0 = \frac{4\pi}{g_0^2 + k^2}. \tag{A.29}$$

Using Eq. (A.28) and $E = k^2/m$, we find for $a_s < 0$ after straightforward algebra:

$$\sigma_0 = \frac{16\pi}{r_0^2 m^2} \frac{1}{(E - E_r)^2 + \Gamma^2}, \tag{A.30}$$

the Lorentzian structure expected for a resonance.

Appendix B. Ground-state energy of two-channel model

In this Appendix, we give details of the derivation of the mean-field ground-state energy for the two-channel model, Eq. (76), presented in Section 4. There, we expressed the effective fermion action in terms of the fermion Green function $G(\mathbf{k},\omega)$, defined in Eqs. (72) and (71). Now, we must simply compute the expectation values of H_K and H_F, defined in Eqs. (64a) and (64b).

B.1. Computation of $\langle H_K \rangle$

We start by noting that Eq. (54a) implies that H_K can be written in the form [this also follows from Eq. (61)]

$$\langle H_K \rangle = \sum_{\mathbf{k},\sigma} \xi_k \langle \hat{c}^\dagger_{\mathbf{k}\sigma} \hat{c}_{\mathbf{k}\sigma} \rangle - h\Delta N, \tag{B.1}$$

with ΔN the population difference:

$$\Delta N = \sum_{\mathbf{k}} \left(\langle \hat{c}^\dagger_{\mathbf{k}\uparrow} \hat{c}_{\mathbf{k}\uparrow} \rangle - \langle \hat{c}^\dagger_{\mathbf{k}\downarrow} \hat{c}_{\mathbf{k}\downarrow} \rangle \right). \tag{B.2}$$

We now compute the two terms of Eq. (B.1) in turn. The first is given by

$$\begin{aligned} \sum_{\mathbf{k},\sigma} \xi_k \langle \hat{c}^\dagger_{\mathbf{k}\sigma} \hat{c}_{\mathbf{k}\sigma} \rangle = & \sum_{\mathbf{k}} \xi_{-\mathbf{k}+\frac{\mathbf{Q}}{2}} T \sum_{\omega_n} \frac{i\omega_n + \xi_{\mathbf{k}+\frac{\mathbf{Q}}{2}\downarrow}}{(i\omega_n - \xi_{\mathbf{k}-\frac{\mathbf{Q}}{2}\uparrow})(i\omega_n + \xi_{\mathbf{k}+\frac{\mathbf{Q}}{2}\downarrow}) - |\Delta_{\mathbf{Q}}|^2} \\ & + \sum_{\mathbf{k}} \xi_{\mathbf{k}+\frac{\mathbf{Q}}{2}} T \sum_{\omega_n} \frac{i\omega_n + \xi_{\mathbf{k}-\frac{\mathbf{Q}}{2}\uparrow}}{(i\omega_n + \xi_{\mathbf{k}-\frac{\mathbf{Q}}{2}\uparrow})(i\omega_n - \xi_{\mathbf{k}+\frac{\mathbf{Q}}{2}\downarrow}) - |\Delta_{\mathbf{Q}}|^2}, \end{aligned} \tag{B.3}$$

where we have defined $\xi_{k\sigma} \equiv \epsilon_k - \mu_\sigma$. The first frequency sum in Eq. (B.3) is easily evaluated after factorizing the denominator:

$$T \sum_{\omega_n} \frac{i\omega_n + \xi_{\mathbf{k}+\frac{\mathbf{Q}}{2}\downarrow}}{(i\omega_n - \xi_{\mathbf{k}-\frac{\mathbf{Q}}{2}\uparrow})(i\omega_n + \xi_{\mathbf{k}+\frac{\mathbf{Q}}{2}\downarrow}) - |\Delta_{\mathbf{Q}}|^2} = T \sum_{\omega_n} \frac{i\omega_n + \xi_{\mathbf{k}+\mathbf{Q}/2\downarrow}}{(i\omega_n - E_{\mathbf{k}\uparrow})(i\omega_n + E_{\mathbf{k}\downarrow})}, \tag{B.4}$$

$$= \frac{1}{2E_{\mathbf{k}}} \left[(E_{\mathbf{k}\downarrow} + \xi_{\mathbf{k}+\frac{\mathbf{Q}}{2}\downarrow}) n_F(E_{\mathbf{k}\downarrow}) + (E_{\mathbf{k}\uparrow} - \xi_{\mathbf{k}+\frac{\mathbf{Q}}{2}\downarrow}) n_F(E_{\mathbf{k}\uparrow}) \right], \tag{B.5}$$

with $n_F(x)$ the Fermi function and where we used Eqs. (74a), (74b), (74c), (74d). Taking the $T \to 0$ limit, in which $n_F(x) \to \Theta(-x)$, we have

$$T\sum_{\omega_n}\frac{i\omega_n+\xi_{\mathbf{k}+\frac{\mathbf{Q}}{2}\downarrow}}{(i\omega_n-\xi_{\mathbf{k}-\frac{\mathbf{Q}}{2}\uparrow})(i\omega_n+\xi_{\mathbf{k}+\frac{\mathbf{Q}}{2}\downarrow})-|\Delta_{\mathbf{Q}}|^2}$$
$$=\frac{1}{2}[\Theta(-E_{\mathbf{k}\uparrow})+\Theta(E_{\mathbf{k}\downarrow})]+\frac{\varepsilon_k}{2E_k}[\Theta(-E_{\mathbf{k}\uparrow})-\Theta(E_{\mathbf{k}\downarrow})]. \tag{B.6}$$

A similar result for the second frequency sum in Eq. (B.3) may be obtained by taking $\mathbf{Q}\to-\mathbf{Q}$ and $h\to-h$ in Eq. (B.6) (since this operation interchanges $\xi_{\mathbf{k}+\frac{\mathbf{Q}}{2}\downarrow}$ and $\xi_{\mathbf{k}-\frac{\mathbf{Q}}{2}\uparrow}$):

$$T\sum_{\omega_n}\frac{i\omega_n+\xi_{\mathbf{k}-\frac{\mathbf{Q}}{2}\uparrow}}{(i\omega_n+\xi_{\mathbf{k}-\frac{\mathbf{Q}}{2}\uparrow})(i\omega_n-\xi_{\mathbf{k}+\frac{\mathbf{Q}}{2}\downarrow})-|\Delta_{\mathbf{Q}}|^2}$$
$$=\frac{1}{2}[\Theta(-E_{\mathbf{k}\downarrow})+\Theta(E_{\mathbf{k}\uparrow})]+\frac{\varepsilon_k}{2E_k}[\Theta(-E_{\mathbf{k}\downarrow})-\Theta(E_{\mathbf{k}\uparrow})], \tag{B.7}$$
$$=1-\frac{1}{2}[\Theta(-E_{\mathbf{k}\uparrow})+\Theta(E_{\mathbf{k}\downarrow})]+\frac{\varepsilon_k}{2E_k}[\Theta(-E_{\mathbf{k}\uparrow})-\Theta(E_{\mathbf{k}\downarrow})], \tag{B.8}$$

where in the last line we used $\Theta(x)=1-\Theta(-x)$. Inserting these sums into Eq. (B.3), we have after a straightforward rearrangement:

$$\sum_{\mathbf{k},\sigma}\xi_k\langle\hat{c}^\dagger_{\mathbf{k}\sigma}\hat{c}_{\mathbf{k}\sigma}\rangle=\sum_{\mathbf{k}}\varepsilon_k+\sum_{\mathbf{k}}\frac{\varepsilon_k^2}{E_k}[\Theta(-E_{\mathbf{k}\uparrow})-\Theta(E_{\mathbf{k}\downarrow})]$$
$$-\sum_{\mathbf{k}}\frac{\mathbf{k}\cdot\mathbf{Q}}{2m}[\Theta(-E_{\mathbf{k}\uparrow})+\Theta(E_{\mathbf{k}\downarrow})]. \tag{B.9}$$

Following the same procedure as above, ΔN is given by

$$\Delta N=\sum_{\mathbf{k}}T\sum_{\omega_n}\left[\frac{i\omega_n+\xi_{k+\frac{\mathbf{Q}}{2}\downarrow}}{(i\omega_n-\xi_{\mathbf{k}-\frac{\mathbf{Q}}{2}\uparrow})(i\omega_n+\xi_{\mathbf{k}+\frac{\mathbf{Q}}{2}\downarrow})-|\Delta_{\mathbf{Q}}|^2}-\frac{i\omega_n+\xi_{\mathbf{k}-\frac{\mathbf{Q}}{2}\uparrow}}{(i\omega_n+\xi_{\mathbf{k}-\frac{\mathbf{Q}}{2}\uparrow})(i\omega_n-\xi_{\mathbf{k}+\frac{\mathbf{Q}}{2}\downarrow})-|\Delta_{\mathbf{Q}}|^2}\right], \tag{B.10}$$
$$=\sum_{\mathbf{k}}(-1+\Theta(-E_{\mathbf{k}\uparrow})+\Theta(E_{\mathbf{k}\downarrow})), \tag{B.11}$$

which can be combined with Eq. (B.9) to yield (using $\sum_{\mathbf{k}}\mathbf{k}\cdot\mathbf{Q}=0$)

$$\langle H_K\rangle=\sum_{\mathbf{k}}\varepsilon_k+\sum_{\mathbf{k}}\frac{\varepsilon_k^2}{E_k}[\Theta(-E_{\mathbf{k}\uparrow})-\Theta(E_{\mathbf{k}\downarrow})]$$
$$+\sum_{\mathbf{k}}\left(\frac{\mathbf{k}\cdot\mathbf{Q}}{2m}+h\right)[1-\Theta(-E_{\mathbf{k}\uparrow})-\Theta(E_{\mathbf{k}\downarrow})], \tag{B.12}$$

used in the main text.

B.2. Computation of $\langle H_F\rangle$

The computation of $\langle H_{\mathrm{F}}\rangle$ follows straightforwardly along the lines of the calculation of $\langle H_K\rangle$ presented above. The two terms comprising $\langle H_{\mathrm{F}}\rangle$ are identical, and yield

$$\langle H_F\rangle=\sum_{\mathbf{k}}T\sum_{\omega_n}\frac{2|\Delta_{\mathbf{Q}}|^2}{(i\omega_n-\xi_{\mathbf{k}-\frac{\mathbf{Q}}{2}\uparrow})(i\omega_n+\xi_{\mathbf{k}+\frac{\mathbf{Q}}{2}\downarrow})-|\Delta_{\mathbf{Q}}|^2},$$
$$=\sum_k\frac{|\Delta_{\mathbf{Q}}|^2}{E_k}[\Theta(-E_{\mathbf{k}\uparrow})-\Theta(E_{\mathbf{k}\downarrow})], \tag{B.13}$$

the result used in the main text.

B.3. Ground state energy at $\Delta_{\mathbf{Q}} = 0$

One simple check on our expression for E_G, Eq. (75), is the limit $\Delta_{\mathbf{Q}} \to 0$, required to reproduce (at arbitrary $\mathbf{Q}$) the ground-state energy for a normal Fermi gas under a finite chemical potential difference h, a quantity that we also use in the main text. Taking this limit, we have

$$E_G = \sum_{\mathbf{k}} (\varepsilon_k - |\varepsilon_k|) + \sum_k |\varepsilon_k| (1 + \Theta(-E_{\mathbf{k}\uparrow}) - \Theta(E_{\mathbf{k}\downarrow})) + \sum_{\mathbf{k}} \left(\frac{\mathbf{k}\cdot\mathbf{Q}}{2m} + h \right) (1 - \Theta(-E_{\mathbf{k}\uparrow}) - \Theta(E_{\mathbf{k}\downarrow})), \tag{B.14}$$

where now, at $\Delta_{\mathbf{Q}} = 0$, $\Theta(-E_{\mathbf{k}\uparrow})$ and $\Theta(E_{\mathbf{k}\downarrow})$ are given by

$$\Theta(-E_{\mathbf{k}\uparrow}) = \Theta\left[\frac{\mathbf{k}\cdot\mathbf{Q}}{2m} + h - |\varepsilon_k| \right], \tag{B.15}$$

$$= \Theta(h - \xi_{\mathbf{k}-\frac{\mathbf{Q}}{2}}) \Theta(\varepsilon_k) + \Theta(\xi_{\mathbf{k}+\frac{\mathbf{Q}}{2}} + h) \Theta(-\varepsilon_k),$$

$$\Theta(E_{\mathbf{k}\downarrow}) = \Theta\left[\frac{\mathbf{k}\cdot\mathbf{Q}}{2m} + h + |\varepsilon_k| \right], \tag{B.16}$$

$$= \Theta(\xi_{\mathbf{k}+\frac{\mathbf{Q}}{2}} + h) \Theta(\varepsilon_k) + \Theta(h - \xi_{\mathbf{k}-\frac{\mathbf{Q}}{2}}) \Theta(-\varepsilon_k).$$

The second lines of Eqs. (B.15) and (B.16) can each be verified by considering the first lines for $\varepsilon_k > 0$ and $\varepsilon_k < 0$. With these expressions in hand, Eq. (B.14) may be considerably simplified. Inserting them into Eq. (B.14), and combining all the momentum sums, we have

$$E_G = \sum_{\mathbf{k}} \left[\varepsilon_k \left(1 + \Theta(h - \xi_{\mathbf{k}-\frac{\mathbf{Q}}{2}}) - \Theta(\xi_{\mathbf{k}+\frac{\mathbf{Q}}{2}} + h) \right) + \left(\frac{\mathbf{k}\cdot\mathbf{Q}}{2m} + h \right) \left(1 - \left(\Theta(h - \xi_{\mathbf{k}-\frac{\mathbf{Q}}{2}}) - \Theta(\xi_{\mathbf{k}+\frac{\mathbf{Q}}{2}} + h) \right) \right) \right]. \tag{B.17}$$

Next, using the identity $\Theta(x) = 1 - \Theta(-x)$, Eq. (B.17) further simplifies to

$$E_G = \sum_{\mathbf{k}} \left(\varepsilon_k - \frac{\mathbf{k}\cdot\mathbf{Q}}{2m} - h \right) \Theta(h - \xi_{\mathbf{k}-\frac{\mathbf{Q}}{2}}) + \sum_{\mathbf{k}} \left(\varepsilon_k + \frac{\mathbf{k}\cdot\mathbf{Q}}{2m} + h \right) \Theta(-h - \xi_{\mathbf{k}+\frac{\mathbf{Q}}{2}}), \tag{B.18}$$

where we note that, since the sums over $\mathbf{k}$ are restricted to small $\mathbf{k}$ by the step functions, the sums are each convergent at large $\mathbf{k}$. Therefore, it is valid to shift $\mathbf{k} \to \mathbf{k} + \mathbf{Q}/2$ and $\mathbf{k} \to \mathbf{k} - \mathbf{Q}/2$ in the first and second terms, respectively, which yields

$$E_G = \sum_{\mathbf{k}} [(\xi_k - h) \Theta(h - \xi_k) + (\xi_k + h) \Theta(-h - \xi_k)], \tag{B.19}$$

the correct result for the ground-state energy of a normal Fermi gas under an applied chemical potential difference.

Appendix C. BEC–BCS crossover at $h = 0$

In this Appendix, we review the BEC–BCS crossover [19–27] exhibited by H, Eq. (61), at zero chemical potential difference $h = 0$. This will set the stage for our subsequent

treatment at finite h of interest to us and will also serve to establish notation. The mean-field ground-state energy E_G associated with H is Eq. (76). After taking $h = 0$ in the Eq. (76), to be completely general one must then minimize over $\mathbf{Q}$ and $B_{\mathbf{Q}}$. However, in the absence of any chemical potential difference it is clear that E_G is minimized by $\mathbf{Q} = 0$ as there is no energetic gain (only cost) of FFLO-type states. Thus, at the outset we set $\mathbf{Q} = 0$ along with $h = 0$ in Eq. (76), obtaining (writing Δ_0 as Δ for notational simplicity):

$$E_G = (\delta - 2\mu)\frac{\Delta^2}{g^2} + \sum_k \left(\xi_k - E_k + \frac{\Delta^2}{2\epsilon_k}\right), \tag{C.1}$$

where we have defined

$$\xi_k \equiv \epsilon_k - \mu = \frac{k^2}{2m} - \mu, \tag{C.2}$$

and used Eq. (27) for the renormalized detuning δ. We first compute E_G in the normal state $\Delta = 0$:

$$E_G(\Delta = 0) = \sum_k (\xi_k - |\xi_k|), \tag{C.3a}$$

$$= -\frac{8}{15} c\mu^{5/2}\Theta(\mu), \tag{C.3b}$$

where we converted the sum to an integral and used the three-dimensional density of states $N(E) = c\sqrt{E}$ with

$$c \equiv \frac{m^{3/2}}{\sqrt{2}\pi^2}. \tag{C.4}$$

Combining this with Eq. (C.1) then gives:

$$E_G = (\delta - 2\mu)\frac{\Delta^2}{g^2} - \frac{8}{15} c\mu^{5/2}\Theta(\mu) + I(\mu, \Delta), \tag{C.5}$$

where

$$I(\mu, \Delta) \equiv \int \frac{\mathrm{d}^3 k}{(2\pi)^3}\left(|\xi_k| - E_k + \frac{\Delta^2}{2\epsilon_k}\right), \tag{C.6}$$

where we have converted the momentum sum to an integral.

The standard BEC–BCS crossover follows from finding the minimum of E_G which satisfies the gap equation

$$0 = \frac{\partial E_G}{\partial \Delta}, \tag{C.7a}$$

while satisfying the number constraint

$$N = -\frac{\partial E_G}{\partial \mu}, \tag{C.7b}$$

which we evaluate numerically in Fig. C.1.

For a narrow Feshbach resonance ($\gamma \ll 1$), we can find accurate analytic approximations to E_G in Eq. (C.5) in all relevant regimes. The first step is finding an appropriate approximation to Eq. (C.6), which has drastically different properties depending on

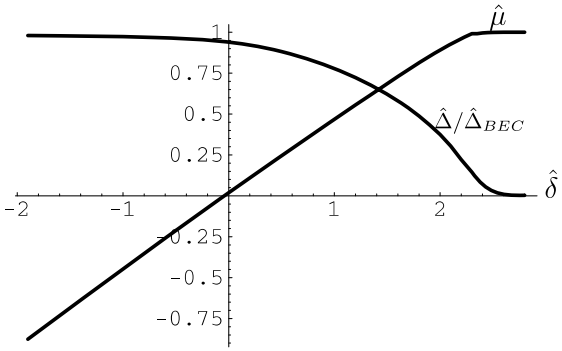

Fig. C.1. Plot of $\hat{\Delta}/\hat{\Delta}_{\rm BEC}$ (i.e., the gap normalized to its asymptotic value $\hat{\Delta}_{\rm BEC} = \sqrt{2\gamma/3}$) in the BEC regime and $\hat{\mu}$, as a function of normalized detuning $\hat{\Delta} = \delta/\epsilon_{\rm F}$ for $\gamma = 0.1$.

whether $\mu > 0$ (so that the low-energy states are near the Fermi surface) or $\mu < 0$ (so that there is no Fermi surface and excitations are gapped with energy bounded from below by $|\mu|$). We proceed by first evaluating the derivative $\frac{\partial I}{\partial \Delta}$ and then integrating the expression with constant of integration $I(\mu,0) = 0$.

$$\frac{\partial I}{\partial \Delta} = -\Delta \int \frac{d^3k}{(2\pi)^3}\left(\frac{1}{E_k} - \frac{1}{\epsilon_k}\right), \tag{C.8a}$$

$$= -c\Delta \int_0^\infty \sqrt{\epsilon} d\epsilon \left(\frac{1}{\sqrt{(\epsilon-\mu)^2+\Delta^2}} - \frac{1}{\epsilon}\right), \tag{C.8b}$$

$$\simeq -2N(\mu)\Delta \ln\frac{8e^{-2}\mu}{\Delta}, \quad \mu > 0; \quad \mu \gg \Delta, \tag{C.8c}$$

$$\simeq N(\mu)\Delta\left[\pi + \frac{\pi}{16}\left(\frac{\Delta}{\mu}\right)^2\right], \quad \mu < 0; \quad |\mu| \gg \Delta, \tag{C.8d}$$

Eq. (C.8d) may be obtained by Taylor expanding the integrand in $\Delta \ll |\mu|$ and integrating term by term, with details of the derivation of Eq. (C.8c) appearing in Ref. [29]. Integrating with respect to Δ, we thus have

$$I \simeq \begin{cases} -N(\mu)\left(\frac{\Delta^2}{2} + \Delta^2 \ln\frac{8e^{-2}\mu}{\Delta}\right) & \mu > 0; \mu \gg \Delta, \\ N(\mu)\frac{\Delta^2}{2}\left[\pi + \frac{\pi}{32}\left(\frac{\Delta}{\mu}\right)^2\right] & \mu < 0; |\mu| \gg \Delta, \end{cases} \tag{C.9a}$$

Having computed $E_{\rm G}(\mu,\Delta)$ in the regimes of interest, the phase diagram is easily deduced by finding Δ that minimizes $E_{\rm G}(\mu,\Delta)$, subject to the total atom number constraint Eq. (C.7b).

C.1. BCS regime

The BCS regime is defined by $\delta \gg 2\epsilon_{\rm F}$, where $\Delta \ll \mu$ and $\mu \simeq \epsilon_{\rm F} > 0$, with pairing taking place in a thin shell around the well-formed Fermi surface. In this regime, $E_{\rm G}$ is given by

$$E_{\rm G} \simeq -c\frac{\sqrt{\mu}}{2}\Delta^2 + \frac{\Delta^2}{g^2}(\delta - 2\mu) + c\sqrt{\mu}\Delta^2 \ln\frac{\Delta}{8e^{-2}\mu} - \frac{8}{15}c\mu^{5/2}. \tag{C.10}$$

It is convenient to work with the dimensionless variables defined in Eqs. (105a), (105b), (105c), (105d), (105e). The normalized ground-state energy $e_{\rm G}$ in the BCS regime is then given by

$$e_{\rm G} \equiv \frac{E_{\rm G}}{c\epsilon_{\rm F}^{5/2}} \simeq -\frac{\sqrt{\hat{\mu}}}{2}\hat{\Delta}^2 + \hat{\Delta}^2(\hat{\delta} - 2\hat{\mu})\gamma^{-1} + \sqrt{\hat{\mu}}\hat{\Delta}^2 \ln\frac{\hat{\Delta}}{8e^{-2}\hat{\mu}} - \frac{8}{15}\hat{\mu}^{5/2}, \tag{C.11}$$

where, γ, defined in Eq. (37), is a dimensionless measure of the Feshbach resonance width Γ_0 to the Fermi energy. With this, (C.7a) and (C.7b) become

$$0 = \frac{\partial e_{\rm G}}{\partial\hat{\Delta}}, \tag{C.12a}$$

$$\simeq 2\hat{\Delta}(\hat{\delta} - 2\hat{\mu})\gamma^{-1} + 2\sqrt{\hat{\mu}}\hat{\Delta}\ln\frac{\hat{\Delta}}{8e^{-2}\hat{\mu}}, \tag{C.12b}$$

$$\frac{4}{3} = -\frac{\partial e_{\rm G}}{\partial\hat{\mu}}, \tag{C.12c}$$

$$\simeq \frac{5}{4}\frac{\hat{\Delta}^2}{\sqrt{\hat{\mu}}} + \frac{4}{3}\hat{\mu}^{3/2} + 2\hat{\Delta}^2\gamma^{-1} - \frac{\hat{\Delta}^2}{2\sqrt{\hat{\mu}}}\ln\frac{\hat{\Delta}}{8e^{-2}\hat{\mu}}, \tag{C.12d}$$

that admits the normal state ($\hat{\Delta} = 0$, $\hat{\mu} = 1$) and the BCS SF state

$$\hat{\Delta} \simeq \hat{\Delta}_{\rm BCS}(\hat{\mu}) \equiv 8e^{-2}\hat{\mu}e^{-\gamma^{-1}(\hat{\delta}-2\hat{\mu})/\sqrt{\hat{\mu}}}, \tag{C.13a}$$

$$\frac{4}{3} \simeq \frac{4}{3}\hat{\mu}^{3/2} + 2\hat{\Delta}^2\gamma^{-1}. \tag{C.13b}$$

where in the second line we approximately neglected the first term on the right side of Eq. (C.12d), valid since $\hat{\Delta}_{\rm BCS} \ll 1$ (and $\gamma \ll 1$). It is easy to show that the BCS solution is always a minimum of $E_{\rm G}$.

The meaning of the two terms on the right side of Eq. (C.13b) is clear once we recall its form in terms of dimensionful quantities:

$$n \simeq \frac{4}{3}c\mu^{3/2} + 2|b|^2, \tag{C.14}$$

i.e., the first term simply represents the total unpaired atom density, reduced below n since $\mu < \epsilon_{\rm F}$, while the second term represents the density of atoms bound into molecules, i.e., twice the molecular density $|b|^2$. Qualitatively, we see that at large $\hat{\delta}$, $\hat{\Delta} \ll 1$, implying from the number equation that $\hat{\mu} < 1$.

C.2. BEC regime

We next consider the BEC regime defined by $\delta < 0$. As we shall see, in this regime $\mu < 0$ and $|\mu| \gg \Delta$, so that Eq. (C.9a), $I(\mu,\Delta)$, applies. This yields, for the normalized ground-state energy,

$$e_{\mathrm{G}} \simeq (\hat{\delta} - 2\hat{\mu})\hat{\Delta}^2\gamma^{-1} + \sqrt{|\hat{\mu}|}\frac{\hat{\Delta}^2}{2}\left[\pi + \frac{\pi}{32}\left(\frac{\hat{\Delta}}{\hat{\mu}}\right)^2\right], \tag{C.15}$$

and, for the gap and number equations (dividing by an overall factor of $\hat{\Delta}$ in the former)

$$0 \simeq 2\gamma^{-1}(\hat{\delta} - 2\hat{\mu}) + \sqrt{|\hat{\mu}|}\left[\pi + \frac{\pi}{16}\left(\frac{\hat{\Delta}}{\hat{\mu}}\right)^2\right], \tag{C.16a}$$

$$\frac{4}{3} \simeq 2\gamma^{-1}\hat{\Delta}^2 + \frac{\hat{\Delta}^2\pi}{4\sqrt{|\hat{\mu}|}}. \tag{C.16b}$$

As noted in Ref. [22], in the BEC regime the roles of the two equations are reversed, with $\hat{\mu}$ approximately determined by the gap equation and $\hat{\Delta}$ approximately determined by the number equation. Thus, $\hat{\mu}$ is well-approximated by neglecting the term proportional to $\hat{\Delta}^2$ in Eq. (C.16a), giving

$$\hat{\mu} \approx \frac{\hat{\delta}}{2}\left[\sqrt{1 + \frac{\gamma^2\pi^2}{32|\hat{\delta}|}} - \frac{\gamma\pi}{\sqrt{32|\hat{\delta}|}}\right]^2. \tag{C.17}$$

At large negative detuning, $|\hat{\delta}| \gg 1$, where it is valid in the BEC regime, Eq. (C.17) reduces to $\mu \approx \hat{\delta}/2$, with the chemical potential tracking the detuning.

Inserting Eq. (C.17) into Eq. (C.16b) yields

$$\hat{\Delta}^2 = \frac{2\gamma}{3}\left[1 - \frac{\gamma\pi}{\sqrt{(\gamma\pi)^2 + 32|\hat{\delta}|}}\right]. \tag{C.18}$$

Using $\hat{\Delta} = \Delta/\epsilon_{\mathrm{F}}$ and the relation $\Delta^2 = g^2 n_m$ between Δ and the molecular density, we have

$$n_m = \frac{3}{4}\gamma^{-1}\hat{\Delta}^2 n, \tag{C.19}$$

$$\simeq \frac{n}{2}\left[1 - \frac{\gamma\pi}{\sqrt{(\gamma\pi)^2 + 32|\hat{\delta}|}}\right], \tag{C.20}$$

which, as expected (given the fermions are nearly absent for $\mu < 0$) simply yields $n_m \approx n/2$ in the asymptotic (large $|\hat{\delta}|$) BEC regime.

Appendix D. Derivation of Eq. (102)

In the present appendix, we provide the steps leading from Eq. (97) to Eq. (102). To this end we need to evaluate

$$S(h) = S_1(h) + S_2(h), \tag{D.1}$$

$$S_1(h) \equiv E_k \sum_k \Theta(h - E_k), \tag{D.2}$$

$$S_2(h) \equiv -h \sum_k \Theta(h - E_k). \tag{D.3}$$

We shall derive Eq. (102) by showing that $\partial S/\partial h = -m(h)$, with $m(h)$ given by Eq. (99b). Since $S(0) = 0$ (recall $E_k > 0$), this is sufficient. First, using $\Theta'(x) = \delta(x)$ with $\delta(x)$ the Dirac delta function, we have

$$\frac{\partial S_1}{\partial h} = \sum_k E_k \delta(h - E_k) = h \sum_k \delta(h - E_k), \tag{D.4}$$

$$\frac{\partial S_2}{\partial h} = -\sum_k \Theta(h - E_k) - h \sum_k \delta(h - E_k). \tag{D.5}$$

Adding these, we obtain

$$\frac{\partial S}{\partial h} = -\sum_k \Theta(h - E_k) = -Vm(h), \tag{D.6}$$

which provides the connection between Eqs. (97) and (102).

Appendix E. Derivation of leading-order contribution to T-matrix

The leading-order contribution to the T-matrix is given by the Feynman diagram in Fig. 25 (corresponding to molecular scattering), with external momenta and frequencies set equal to zero. We find it easiest to compute this diagram by starting at finite temperature T before taking the $T \to 0$ limit. Standard analysis gives

$$T_m = g^4 T \sum_\omega \int \frac{\mathrm{d}^3 p}{(2\pi)^3} \frac{1}{(\mathrm{i}\omega - \xi_{p\uparrow})^2} \frac{1}{(-\mathrm{i}\omega - \xi_{p\downarrow})^2}, \tag{E.1}$$

with $\xi_{p\sigma} = \epsilon_p - \mu_\sigma$ as in the main text. The fermionic Matsubara frequency sum can be straightforwardly evaluated using standard techniques: [145]

$$S(A,B) \equiv T \sum_\omega \frac{1}{(\mathrm{i}\omega - A)^2} \frac{1}{(\mathrm{i}\omega - B)^2}, \tag{E.2}$$

$$= \frac{d}{dA} \frac{d}{dB} T \sum_\omega \frac{1}{\mathrm{i}\omega - A} \frac{1}{\mathrm{i}\omega - B}, \tag{E.3}$$

$$= \frac{d}{dA} \frac{d}{dB} \frac{n_\mathrm{F}(A) - n_\mathrm{F}(B)}{A - B}. \tag{E.4}$$

Taking the $T \to 0$ limit, in which $n_F(x) \to \Theta(-x)$ and evaluating the derivatives, we have

$$S(A,B) = \frac{-2}{(A-B)^3} [\Theta(-A) - \Theta(-B)] - \frac{\delta(A)}{B^2} - \frac{\delta(B)}{A^2}. \tag{E.5}$$

Using Eq. (E.5) for $S(A,B)$, with $A = \xi_{p\uparrow}$ and $B = -\xi_{p\downarrow}$, the molecular T-matrix is (using the density of states $N(\epsilon) = c\sqrt{\epsilon}$) given by:

$$T_m = -\frac{cg^4}{4}\int_0^\infty d\epsilon\sqrt{\epsilon}\frac{1}{(\epsilon-\mu)^3}\left[\Theta(-\epsilon+\mu_\uparrow)-\Theta(\epsilon-\mu_\downarrow)\right] - cg^4\int_0^\infty d\epsilon\sqrt{\epsilon}\left[\frac{\delta(\epsilon-\mu_\uparrow)}{(\epsilon-\mu_\downarrow)^2}+\frac{\delta(\epsilon-\mu_\downarrow)}{(\epsilon-\mu_\uparrow)^2}\right]. \tag{E.6}$$

Since we are in the BEC regime, $\mu<0$. Taking (without loss of generality) $h>0$, we have $\mu_\downarrow<0$ always and the second step function in the first line of Eq. (E.6) is always unity. Moreover, for the same reason, the second delta function in the second line is always zero. However, $\mu_\uparrow$ does change signs with increasing h, so that the first delta function in the second line can contribute. Evaluating the remaining integrals in Eq. (E.6) then yields

$$T_m = \frac{cg^4\pi}{32|\mu|^{3/2}}F_4(h/|\mu|), \tag{E.7}$$

with $F_4(x)$ defined in Eq. (195), the result used in the main text.

Appendix F. Computation of excluded sums

In this Appendix, we provide details for the computation of the "excluded sums" appearing in the ground-state energy Eq. (241) [86]. The first such sum is

$$S_1 \equiv \sum_k E_k(1+\Theta(-E_{\mathbf{k}\uparrow})-\Theta(E_{\mathbf{k}\downarrow})). \tag{F.1}$$

Using Eqs. (74c) and (74d) for $E_{\mathbf{k}\sigma}$, we see the first step function gives unity for (with θ the angle between k and Q, and in this section dropping the subscript $\mathbf{Q}$ on $\Delta_{\mathbf{Q}}$ for simplicity)

$$\frac{kQ\cos\theta}{2m}+h>\sqrt{\varepsilon_k^2+\Delta^2}, \tag{F.2}$$

while the second gives unity for

$$\frac{kQ\cos\theta}{2m}+h>-\sqrt{\varepsilon_k^2+\Delta^2}, \tag{F.3}$$

and each vanishes otherwise. Clearly, if Eq. (F.2) is satisfied, then so is Eq. (F.3). Thus, out of four possibilities only two nonzero contributions to Eq. (F.1) occur, when either both inequalities are satisfied or when both are violated.

The conditions Eqs. (F.2) and (F.3) restrict the momentum sum in Eq. (F.1) to the immediate vicinity of the Fermi surface. Thus, we shall replace $k\to\tilde{k}_{\mathrm{F}}$ on the left side of Eqs. (F.2) and (F.3), where $\tilde{k}_{\mathrm{F}}$ is the Fermi wavevector associated with the adjusted chemical potential $\tilde{\mu}\equiv\mu-Q^2/8m$, i.e., $\tilde{k}_{\mathrm{F}}^2/2m=\tilde{\mu}$. Following Ref. [86], we now determine where these conditions intersect the Fermi surface where $\varepsilon_k\to 0$. In this limit, Eqs. (F.2) and (F.3) can be written as

$$\cos\theta>\cos\theta_{\min}\equiv\frac{1-\bar{h}}{\bar{Q}}, \tag{F.4}$$

$$\cos\theta>\cos\theta_{\max}\equiv-\frac{1+\bar{h}}{\bar{Q}}, \tag{F.5}$$

where (as in the main text) we defined the rescaled momenta $\bar{Q} \equiv \frac{\tilde{k}_F Q}{2m\Delta}$ and the rescaled chemical potential difference $\bar{h} \equiv \frac{h}{\Delta}$.

Now, S_1 can be straightforwardly computed (converting sums to integrals via $\sum_k \to \frac{N(\tilde{\mu})}{2} \int d\varepsilon \int d\cos\theta$)

$$S_1 = \Delta N(\tilde{\mu}) \int_{\cos\theta_{\min}}^{1} d\cos\theta \int_0^{\varepsilon_+} d\varepsilon \sqrt{1 + \frac{\varepsilon^2}{\Delta^2}} + \Delta N(\tilde{\mu}) \int_{-1}^{\cos\theta_{\max}} d\cos\theta \int_0^{\varepsilon_+} d\varepsilon \sqrt{1 + \frac{\varepsilon^2}{\Delta^2}}, \tag{F.6}$$

where

$$\varepsilon_+ \equiv \Delta \sqrt{(\bar{Q}\cos\theta + \bar{h})^2 - 1}, \tag{F.7}$$

is the maximum energy at a particular θ where the contribution to S_1 is finite. The two lines of Eq. (F.6) correspond to the cases when both Eqs. (F.2) and (F.3) are satisfied, or both violated, respectively.

Clearly, if $\cos\theta_{\max} < -1$ or $\cos\theta_{\min} > 1$ (as defined by Eqs. (F.4) and (F.5)) then these integrals simply vanish. These limits are manifested in the final expression by step (Θ) functions in the final result. Furthermore, we have implicitly assumed in Eqs. (F.4) and (F.5) that $\frac{1-\bar{h}}{\bar{Q}} < 1$, and $-\frac{1+\bar{h}}{\bar{Q}} > -1$. If either assumption is not valid, then the corresponding integration range over $\cos\theta$ in Eq. (F.6) becomes $\int_{-1}^{1} d\cos\theta$. Taking this into account, the integrals in Eq. (F.6) yield for S_1:

$$S_1 = \frac{N(\tilde{\mu})\Delta^2}{2\bar{Q}} \left[H(\bar{Q} + \bar{h}) + H(\bar{Q} - \bar{h}) - H(\bar{h} - \bar{Q})\right], \tag{F.8}$$

$$H(x) \equiv \left[\frac{1}{3}(x^2 - 1)^{3/2} + x\cosh^{-1}x - \sqrt{x^2 - 1}\right]\Theta(x - 1).$$

Following the same procedure for S_2, the final line of Eq. (241), gives

$$S_2 \equiv \sum_k \left(\frac{\mathbf{k}\cdot\mathbf{Q}}{2m} + h\right)(1 - \Theta(-E_{\mathbf{k}\uparrow}) - \Theta(E_{\mathbf{k}\downarrow})), \tag{F.9}$$

$$= -\frac{N(\tilde{\mu})\Delta^2}{3\bar{Q}} \left[J(\bar{Q} + \bar{h}) + J(\bar{Q} - \bar{h}) - J(\bar{h} - \bar{Q})\right], \tag{F.10}$$

with

$$J(x) \equiv (x^2 - 1)^{3/2}\Theta(x - 1), \tag{F.11}$$

which is the result used in the main text.

Appendix G. Free expansion

In this Appendix, for completeness we review the free expansion dynamics of a trapped Bose gas, recalling how it yields information about the initial boson momentum distribution [146–149]. This is of interest here as free expansion is a direct probe able to distinguish and identify the phases discussed in this paper. Its application to the FFLO state requires

an additional first step of sweeping the resonance in the usual manner [1] to project the FFLO state onto a finite momentum molecular condensate.

We take the initial state of the Bose system to be a condensate characterized by a single-particle wavefunction $B_0(\mathbf{r})$. After time t of free expansion, $B_0(\mathbf{r})$ evolves into $b(\mathbf{r},t)$ given by

$$b(\mathbf{r},t) = \int \frac{\mathrm{d}^3k}{(2\pi)^3}\tilde{B}_0(\mathbf{k})\mathrm{e}^{\mathrm{i}\mathbf{k}\cdot\mathbf{r}}\mathrm{e}^{-\mathrm{i}\hbar tk^2/2m}, \tag{G.1}$$

$$\tilde{B}_0(\mathbf{k}) = \int \mathrm{d}^3rB_0(\mathbf{r})\mathrm{e}^{-\mathrm{i}\mathbf{k}\cdot\mathbf{r}}, \tag{G.2}$$

governed by the free-particle Schrödinger equation. The corresponding spatial boson density distribution at time t is

$$n(\mathbf{r},t) = \langle\hat{b}^\dagger(\mathbf{r},t)\hat{b}(\mathbf{r},t)\rangle \simeq b^*(\mathbf{r},t)b(\mathbf{r},t). \tag{G.3}$$

Inserting Eq. (G.1) into Eq. (G.3), using Eq. (G.2), and shifting $\mathbf{k}\to\mathbf{k}+m\mathbf{r}/\hbar t$, we have

$$n(\mathbf{r},t) \simeq \int \mathrm{d}^3r_1\mathrm{d}^3r_2f(\mathbf{r}_1,\mathbf{r}_2)\mathrm{e}^{\mathrm{i}\frac{m}{\hbar t}\mathbf{r}\cdot(\mathbf{r}_1-\mathbf{r}_2)}B_0^*(\mathbf{r}_1)B_0(\mathbf{r}_2), \tag{G.4}$$

$$f(\mathbf{r}_1,\mathbf{r}_2) \equiv \int \frac{\mathrm{d}^3k}{(2\pi)^3}\frac{\mathrm{d}^3k'}{(2\pi)^3}\mathrm{e}^{\mathrm{i}(\mathbf{k}\cdot\mathbf{r}_1-\mathbf{k}'\cdot\mathbf{r}_2)}\mathrm{e}^{\mathrm{i}\frac{\hbar t}{2m}(k^2-k'^2)}, \tag{G.5}$$

The function $f(\mathbf{r}_1,\mathbf{r}_2)$ can be evaluated by changing variables to $\mathbf{k},\mathbf{k}' = \mathbf{p}\pm\mathbf{q}/2$, giving

$$\begin{aligned} f(\mathbf{r}_1,\mathbf{r}_2) &= \int \frac{\mathrm{d}^3p}{(2\pi)^3}\frac{\mathrm{d}^3q}{(2\pi)^3}\mathrm{e}^{\mathrm{i}\mathbf{p}\cdot(\mathbf{r}_1-\mathbf{r}_2)}\mathrm{e}^{\mathrm{i}\mathbf{q}\cdot(\mathbf{r}_1+\mathbf{r}_2)/2}\mathrm{e}^{\mathrm{i}(\hbar t/m)\mathbf{p}\cdot\mathbf{q}}, \\ &= \left(\frac{m}{2\pi\hbar t}\right)^3\mathrm{e}^{\mathrm{i}m(\mathbf{r}_1+\mathbf{r}_2)(\mathbf{r}_1-\mathbf{r}_2)/2\hbar t}, \end{aligned} \tag{G.6}$$

Inserting Eq. (G.6) into Eq. (G.4), we find

$$n(\mathbf{r},t) \simeq \left(\frac{m}{2\pi\hbar t}\right)^3\int \mathrm{d}^3r_1\mathrm{d}^3r_2\mathrm{e}^{\mathrm{i}\frac{m}{\hbar t}(\mathbf{r}_1-\mathbf{r}_2)\cdot(\mathbf{r}+\frac{1}{2}[\mathbf{r}_1+\mathbf{r}_2])}\times B_0^*(\mathbf{r}_1)B_0(\mathbf{r}_2). \tag{G.7}$$

Noting that the initial cloud is small compared to the expanded one, we may neglect $\mathbf{r}_1$ and $\mathbf{r}_2$ compared to $\mathbf{r}$ in the exponential in the first line of Eq. (G.7) since $\mathbf{r}$ is measured in the expanded cloud while $\mathbf{r}_1$ and $\mathbf{r}_2$ are confined to the initial cloud. This reduces $n(\mathbf{r},t)$ to

$$n(\mathbf{r},t) \simeq \left(\frac{m}{2\pi\hbar t}\right)^3\tilde{B}_0^*\left(\frac{m}{\hbar t}\mathbf{r}\right)\tilde{B}_0\left(\frac{m}{\hbar t}\mathbf{r}\right), \tag{G.8}$$

$$\simeq \left(\frac{m}{2\pi\hbar t}\right)^3 n_{\mathbf{k}=\frac{m}{\hbar t}\mathbf{r}}, \tag{G.9}$$

where $n_{\mathbf{k}}$ is the momentum distribution function. Thus, as advertised, the density profile $n(\mathbf{r},t)$ in the expanded cloud probes the *initial* momentum distribution. For the simplest trapped FFLO-type state $B_0(\mathbf{r}) = B_{\mathbf{Q}}(\mathbf{r})\mathrm{e}^{\mathrm{i}\mathbf{Q}\cdot\mathbf{r}}$, Eq. (G.9), with $B_{\mathbf{Q}}(\mathbf{r})$ the shape of the amplitude envelope determined by the trap. Taking it (for concreteness and simplicity) to be a Gaussian $B_{\mathbf{Q}}(\mathbf{r}) \propto \mathrm{e}^{-r^2/2R_0^2}$ and using Eq. (G.9) we find

$$n(\mathbf{r},t) \propto \exp\left[-\left(\mathbf{r}-\frac{\hbar t}{m}\mathbf{Q}\right)^2\Big/\left(\frac{\hbar t}{m}R_0^{-1}\right)^2\right], \tag{G.10}$$

i.e., a Gaussian peaked at $\mathbf{r} = \frac{\hbar \mathbf{Q}}{m}$ thus probing the FFLO wavevector $\mathbf{Q}$. Requiring the peak location be much larger than the Gaussian width $\hbar t/mR_0$ thus implies that $QR_0 \gg 1$ is necessary to observe the FFLO state in this manner.

References

[1] C.A. Regal, M. Greiner, D.S. Jin, Phys. Rev. Lett. 92 (2004) 040403.
[2] M.W. Zwierlein, C.A. Stan, C.H. Schunck, S.M.F. Raupach, A.J. Kerman, W. Ketterle, Phys. Rev. Lett. 92 (2004) 120403.
[3] J. Kinast, S.L. Hemmer, M.E. Gehm, A. Turlapov, J.E. Thomas, Phys. Rev. Lett. 92 (2004) 150402.
[4] M. Bartenstein, A. Altmeyer, S. Riedl, S. Jochim, C. Chin, J.H. Denschlag, R. Grimm, Phys. Rev. Lett. 92 (2004) 203201.
[5] T. Bourdel, L. Khaykovich, J. Cubizolles, J. Zhang, F. Chevy, M. Teichmann, L. Tarruell, S.J.J.M.F. Kokkelmans, C. Salomon, Phys. Rev. Lett. 93 (2004) 050401.
[6] C. Chin, M. Bartenstein, A. Altmeyer, S. Riedl, S. Jochim, J.H. Denschlag, R. Grimm, Science 305 (2004) 1128.
[7] M. Greiner, C.A. Regal, D.S. Jin, Phys. Rev. Lett. 94 (2005) 070403.
[8] G.B. Partridge, K.E. Strecker, R.I. Kamar, M.W. Jack, R.G. Hulet, Phys. Rev. Lett. 95 (2005) 020404.
[9] M.W. Zwierlein, J.R. Abo-Shaeer, A. Schirotzek, C.H. Schunck, W. Ketterle, Nature 435 (2005) 1047.
[10] E. Timmermans, P. Tommasini, M. Hussein, A. Kerman, Phys. Rep. 315 (1999) 199.
[11] K. Dieckmann, C.A. Stan, S. Gupta, Z. Hadzibabic, C.H. Schunck, W. Ketterle, Phys. Rev. Lett. 89 (2002) 203201.
[12] K.M. O'Hara, S.L. Hemmer, M.E. Gehm, S.R. Granade, J.E. Thomas, Science 298 (2002) 2179.
[13] C.A. Regal, D.S. Jin, Phys. Rev. Lett. 90 (2003) 230404.
[14] T. Bourdel, J. Cubizolles, L. Khaykovich, K.M.F. Magālhaes, S.J.J.M.F. Kokkelmans, G.V. Shlyapnikov, C. Salomon, Phys. Rev. Lett 91 (2003) 020402.
[15] K.E. Strecker, G.B. Partridge, R.G. Hulet, Phys. Rev. Lett. 91 (2003) 080406.
[16] R.A. Duine, H.T.C. Stoof, Phys. Rep. 396 (2004) 115.
[17] M. Bartenstein, A. Altmeyer, S. Riedl, R. Geursen, S. Jochim, C. Chin, J.H. Denschlag, R. Grimm, A. Simoni, E. Tiesinga, C.J. Williams, P.S. Julienne, Phys. Rev. Lett. 94 (2005) 103201.
[18] T. Köhler, K. Góral, P.S. Julienne, cond-mat/0601420.
[19] D.M. Eagles, Phys. Rev. 186 (1969) 456.
[20] A.J. Leggett, in: A. Pekalski, R. Przystawa (Eds.), Modern Trends in the Theory of Condensed Matter, Springer-Verlag, Berlin, 1980.
[21] P. Nozières, S. Schmitt-Rink, J. Low Temp. Phys. 59 (1985) 195.
[22] C.A.R. Sá de Melo, M. Randeria, J.R. Engelbrecht, Phys. Rev. Lett. 71 (1993) 3202.
[23] E. Timmermans, K. Furuya, P.W. Milonni, A.K. Kerman, Phys. Lett. A 285 (2001) 228.
[24] M. Holland, S.J.J.M.F. Kokkelmans, M.L. Chiofalo, R. Walser, Phys. Rev. Lett. 87 (2001) 120406.
[25] Y. Ohashi, A. Griffin, Phys. Rev. Lett. 89 (2002) 130402, Phys. Rev. A 67 (2003) 033603.
[26] A.V. Andreev, V. Gurarie, L. Radzihovsky, Phys. Rev. Lett. 93 (2004) 130402.
[27] J. Stajic, J.N. Milstein, Q. Chen, M.L. Chiofalo, M.J. Holland, K. Levin, Phys. Rev. A 69 (2004) 063610.
[28] J. Levinsen, V. Gurarie, Phys. Rev. A 73 (2006) 053607.
[29] V. Gurarie, L. Radzihovsky, cond-mat/0611022.
[30] M.W. Zwierlein, A. Schirotzek, C.H. Schunck, W. Ketterle, Science 311 (2006) 492.
[31] G.B. Partridge, W. Li, R.I. Kamar, Y. Liao, R.G. Hulet, Science 311 (2006) 503.
[32] M.W. Zwierlein, W. Ketterle, cond-mat/0603489.
[33] G.B. Partridge, W. Li, R.I. Kamar, Y. Liao, R.G. Hulet, cond-mat/0605581.
[34] M.W. Zwierlein, C.H. Schunck, A. Schirotzek, W. Ketterle, cond-mat/0605258.
[35] Y. Shin, M.W. Zwierlein, C.H. Schunck, A. Schirotzek, W. Ketterle, Phys. Rev. Lett. 97 (2006) 030401.
[36] D.E. Sheehy, L. Radzihovsky, Phys. Rev. Lett. 96 (2006) 060401.
[37] R. Combescot, Europhys. Lett. 55 (2001) 150.
[38] W.V. Liu, F. Wilczek, Phys. Rev. Lett. 90 (2003) 047002.
[39] P.F. Bedaque, H. Caldas, G. Rupak, Phys. Rev. Lett. 91 (2003) 247002.
[40] H. Caldas, Phys. Rev. A 69 (2004) 063602.
[41] T. Mizushima, K. Machida, M. Ichioka, Phys. Rev. Lett. 94 (2005) 060404.

[42] J. Carlson, S. Reddy, Phys. Rev. Lett. 95 (2005) 060401.
[43] T.D. Cohen, Phys. Rev. Lett. 95 (2005) 120403.
[44] P. Castorina, M. Grasso, M. Oertel, M. Urban, D. Zappalà, Phys. Rev. A 72 (2005) 025601.
[45] A. Sedrakian, J. Mur-Petit, A. Polls, H. Müther, Phys. Rev. A 72 (2005) 013613.
[46] K. Yang, Phys. Rev. Lett. 95 (2005) 218903.
[47] C.-H. Pao, S.-T. Wu, S.-K. Yip, Phys. Rev. B 73 (2006) 132506.
[48] D.T. Son, M.A. Stephanov, Phys. Rev. A 74 (2006) 013614.
[49] K. Yang, cond-mat/0508484.
[50] J. Dukelsky, G. Ortiz, S.M.A. Rombouts, K. van Houcke, Phys. Rev. Lett. 96 (2006) 180404.
[51] K. Yang, S. Sachdev, Phys. Rev. Lett. 96 (2006) 187001.
[52] P. Pieri, G.C. Strinati, Phys. Rev. Lett. 96 (2006) 150404.
[53] J. Kinnunen, L.M. Jensen, P. Törmä, Phys. Rev. Lett. 96 (2006) 110403.
[54] W. Yi, L.-M. Duan, Phys. Rev. A 73 (2006) 031604.
[55] F. Chevy, Phys. Rev. Lett. 96 (2006) 130401.
[56] L. He, M. Jin, P. Zhuang, Phys. Rev. B 73 (2006) 214527.
[57] H. Caldas, cond-mat/0601148.
[58] T.N. De Silva, E.J. Mueller, Phys. Rev. A 73 (2006) 051602.
[59] M. Haque, H.T.C. Stoof, Phys. Rev. A 74 (2006) 011602.
[60] S. Sachdev, K. Yang, Phys. Rev. B 73 (2006) 174504.
[61] A. Bulgac, M.M. Forbes, A. Schwenk, Phys. Rev. Lett. 97 (2006) 020402.
[62] T.-L. Ho, H. Zhai, cond-mat/0602568.
[63] X.-J. Liu, H. Hu, Europhys. Lett. 75 (2006) 364.
[64] Z.-C. Gu, G. Warner, F. Zhou, cond-mat/0603091.
[65] K. Yang, cond-mat/0603190.
[66] H. Hu, X.-J. Liu, Phys. Rev. A 73 (2006) 051603.
[67] M. Iskin, C.A.R. Sá de Melo, cond-mat/0604184; see Ref. [123].
[68] A. Imambekov, C.J. Bolech, M. Lukin, E. Demler, cond-mat/0604423.
[69] L.M. Jensen, J. Kinnunen, P. Törmä, cond-mat/0604424.
[70] M. Mannarelli, G. Nardulli, M. Ruggieri, cond-mat/0604579.
[71] W. Yi, L.-M. Duan, Phys. Rev. A 74 (2006) 013610.
[72] C.-H. Pao, S.-K. Yip, J. Phys. Cond. Mat. 18 (2006) 5567.
[73] T.N. De Silva, E.J. Mueller, cond-mat/0604638.
[74] H. Caldas, cond-mat/0605005.
[75] C.-C. Chien, Q. Chen, Y. He, K. Levin, cond-mat/0605039.
[76] T. Koponen, J. Kinnunen, J.-P. Martikainen, L.M. Jensen, P. Törmä, cond-mat/0605169.
[77] A. Sedrakian, H. Muther, A. Polls, cond-mat/0605085.
[78] M.M. Parish, F.M. Marchetti, A. Lamacraft, B.D. Simons, cond-mat/0605744.
[79] F. Chevy, cond-mat/0605751.
[80] A. Recati, I. Carusotto, C. Lobo, S. Stringari, cond-mat/0605754.
[81] L. He, M. Jin, P. Zhuang, cond-mat/0606322.
[82] K.B. Gubbels, M.W.J. Romans, H.T.C. Stoof, cond-mat/0606330.
[83] J.-P. Martikainen, Phys. Rev. A 74 (2006) 013602.
[84] A.M. Clogston, Phys. Rev. Lett. 9 (1962) 266.
[85] G. Sarma, J. Phys. Chem. Solids 24 (1963) 1029.
[86] P. Fulde, R.A. Ferrell, Phys. Rev. 135 (1964) A550.
[87] A.I. Larkin, Yu.N. Ovchinnikov, Zh. Eksp. Teor. Fiz. 47 (1964) 1136, [Sov. Phys. JETP 20, 762 (1965)].
[88] L.G. Aslamazov, Zh. Eksp. Teor. Fiz. 55 (1968) 1477, Sov. Phys. JETP 28 (1969) 773.
[89] S. Takada, T. Izuyama, Prog. Theor. Phys. 41 (1969) 635.
[90] S. Matsuo, S. Higashitani, Y. Nagato, K. Nagai, J. Phys. Soc. Jpn. 67 (1998) 280.
[91] D.F. Agterberg, K. Yang, J. Phys. Cond. Mat. 13 (2001) 9259.
[92] M. Alford, J.A. Bowers, K. Rajagopal, Phys. Rev. D 63 (2001) 074016.
[93] R. Combescot, C. Mora, Europhys. Lett. 68 (2004) 79.
[94] J.A. Bowers, K. Rajagopal, Phys. Rev. D 66 (2002) 065002.
[95] H.A. Radovan, N.A. Fortune, T.P. Murphy, S.T. Hannahs, E.C. Palm, S.W. Tozer, D. Hall, Nature 425 (2003) 51;
A. Bianchi, R. Movshovich, C. Capan, P.G. Pagliuso, J.L. Sarrao, Phys. Rev. Lett. 91 (2003) 187004.

[96] A.F. Andreev, I.M. Lifshitz, Zh. Eksp. Teor. Fiz. 56 (1969) 2057, [Sov. Phys. JETP 29, 1107 (1969)].
[97] G.V. Chester, Phys. Rev. A 2 (1970) 256.
[98] A.J. Leggett, Phys. Rev. Lett. 25 (1970) 1543.
[99] E. Kim, M.H.W. Chan, Nature 427 (2004) 225, Science 305 (2004) 1941.

[100] To show this, first calculate the thermodynamic critical field by equating the energy-density penalty $H^2/8\pi$ for expelling a magnetic field with the condensation-energy density gain for pairing $N(\epsilon_F)\Delta^2/2$. They are equal at the thermodynamic critical field H_c:

$$H_c = \sqrt{4\pi N(\epsilon_F)}\Delta.$$

We define H_c^Z as the critical Zeeman field at which superconductivity would be destroyed by the purely Zeeman effect. Under an applied field a normal Fermi gas acquires a magnetization $M = \chi_P H$ due to the Zeeman effect, with the Pauli susceptibility $\chi_P = 2N(\epsilon_F)\mu_B^2$ (see, e.g., Ref. [117]). At H_c^Z, the energy gained by magnetizing is equal to the BCS condensation energy:

$$\frac{\chi_P (H_c^Z)^2}{2} = \frac{N(\epsilon_F)\Delta^2}{2},$$

or $H_c^Z = \Delta\sqrt{N(\epsilon_F)/\chi_P} = \Delta/\sqrt{2}\mu_B$, a field known as the Clogston upper limit [84] for the critical field of a superconductor. The ratio H_c/H_c^Z therefore satisfies

$$\frac{H_c^2}{(H_c^Z)^2} = \left(\frac{\sqrt{3}}{\pi^2}\right)^{\frac{2}{3}} \frac{e^2 n^{1/3}}{mc^2},$$

with n the electron density. Since the ratio on the right side is the Coulomb energy divided by the electron rest energy, clearly it is $\ll 1$. Hence, in conventional superconductors, superconductivity is destroyed by orbital effects long before the Zeeman effect comes into play. Models that yield the FFLO state essentially assume the opposite.

[101] The situation in type-II superconductors is even less hopeful as there at the lower critical field $H_{c1} < H_c$, the vortex lattice appears, further obscuring effects of the Zeeman field.

[102] One may ask whether more complicated FFLO-type pairing states, containing more Fourier components, are more stable. The simplest such generalization, referred to as the Larkin-Ovchinnikov (LO) state [87], takes the form $\Delta(r) = \Delta_Q \cos Q \cdot r$. Using a finite temperature Ginzburg–Landau analysis, LO in fact showed that the LO order parameter has slightly lower energy than the single plane wave ansatz, which we refer to as the Fulde–Ferrell (FF) state [86]. In fact, subsequent work [94] has found that states containing even more Q vectors are slightly more favorable. Fortunately, such more complicated FFLO-type states are generally found [93,90] to be only marginally more stable than the FF state we consider here (see, however, Ref. [94,103]). This implies that although the true ground state is very likely more complicated, possessing a richer real-space structure, the region of the phase diagram where we find the FFLO state should be quantitatively accurate. Of course, the difficulty of finding the true FFLO-type ground state (unsolved even in the simpler case of an infinite homogeneous three dimensional system), is further complicated in the setting of atomic physics experiments that are typically conducted a harmonic trap. [41,53].

[103] In Ref. [94] Bowers and Rajagopal (BR) studied a large class of generalized FFLO states, finding that states having more Fourier components Q (forming a FCC crystal structure) are much lower in energy than the single plane-wave state studied here. Based on this instability BR argued that such generalized crystalline superfluid FFLO states may be stable over a far larger range of Zeeman fields than the single-Q FFLO state considered here. Although intriguing, we do not find these arguments persuasive enough to overturn the predictions of our detailed controlled calculation, that is consistent with a general wisdom on this issue. Firstly, Ref. [94] is based on a Landau [Taylor expansion $E(\Delta_Q)$ in Δ_Q] expansion at $T = 0$ for a strongly first-order transition. As a result there is no small parameter that controls or validates predictions that follow from this uncontrolled Taylor expansion. Consistent with this concern, BR find the energy of these states to be unbounded from below. Furthermore, as discussed above [102], these results of BR directly contradict other work [87,93,90] on this issue that find such more complicated FFLO states to be only marginally more stable.

[104] Since γ is inversely proportional to $\sqrt{\epsilon_F}$, i.e., the proper measure of the width of the resonance is in its relation to the Fermi energy, it is quite conceivable that even presently studied Feshbach resonances can be made to be narrow in this dimensionless sense, by considerably increasing the size of the atomic cloud.

[105] The FFLO → N transition is only continuous within mean-field theory, and can be argued to be generically driven first order by fluctuations. [106–108].
[106] L.D. Landau, Phys. Z. Sowejetunion 11 (1937) 26, reprinted in Collected papers of L.D. Landau, D. ter Haar, ed. (Permagon, New York, 1965).
[107] S.A. Brazovskii, Zh. Eksp. Teor. Fiz. 68 (1975) 42, [Sov. Phys. JETP 41, 85 (1975)].
[108] S. Alexander, J. McTague, Phys. Rev. Lett. 41 (1978) 702.
[109] M. Greiner, O. Mandel, T. Esslinger, T.W. Hänsch, I. Bloch, Nature 415 (2002) 39.
[110] E. Altman, E. Demler, M.D. Lukin, Phys. Rev. A 70 (2004) 013603.
[111] M. Greiner, C.A. Regal, J.T. Stewart, D.S. Jin, Phys. Rev. Lett. 94 (2005) 110401.
[112] A. Lamacraft, Phys. Rev. A 73 (2006) 011602.
[113] Y.B. Rumer, JETP 10 (1960) 409.
[114] L.D. Landau, E.M. Lifshitz, Quantum Mechanics: Non-relativistic Theory, Permagon, New York, 1977.
[115] For small $|\delta| < \Gamma_0$ the negative energy pole $E_p = -\delta^2/\Gamma_0$ corresponds to a bound state only for $\delta < 0$. For $\delta > 0$ this pole is a so-called virtual bound state [114], corresponding to $\mathrm{Im}(k) < 0$ and therefore an exponentially growing rather than a decaying eigenstate and therefore is not a physical bound state.
[116] V. Gurarie, L. Radzihovsky, A.V. Andreev, Phys. Rev. Lett. 94 (2005) 230403.
[117] J.W. Negele, H. Orland, Quantum Many-particle Systems, Addison Wesley, 1988.
[118] J.R. Schrieffer, Theory of Superconductivity, Perseus, 1999.
[119] P.-G. de Gennes, Superconductivity of Metals and Alloys, Benjamin, New York, 1966.
[120] M. Tinkham, Introduction to Superconductivity, McGraw-Hill, 1996.
[121] Recently, a number of papers [47,67] have appeared in the literature with a mean-field phase diagram for resonantly interacting fermions that disagrees qualitatively with our mean-field phase diagram reported in Ref. [36] (particularly in the negative-detuning BEC regime). These Refs. [47,67] also disagree with other recent work [64,75,78] on the one and two-channel models that are in agreement with our results. [36] We believe the origin of this discrepancy is that the authors of Refs. [47,67] erroneously study solutions of the gap equation that are maxima or saddle points (rather than minima) and which do not correspond to any physical ground state of the system; this thereby leads to incorrect results (see also Ref. [122]). The authors of Ref. [45] (and references therein) erroneously report a polarization-dependent gap of the BCS state [Eq.(1) of Ref. [45]] that is actually the polarization dependence of the unstable Sarma solution [a local maximum of $E_G(\Delta)$],

$$\frac{\Delta_{\mathrm{Sarma}}}{\Delta_{\mathrm{BCS}}} = \sqrt{1 - \frac{4}{3}\frac{\Delta N}{N}\frac{\epsilon_F}{\Delta_{\mathrm{BCS}}}},$$

obtained by combining Eqs. (117), (122) and (109) (approximating $\hat{\mu} \simeq 1$ for simplicity). Such problems stem from the existence of first-order transitions at finite h (where E_G exhibits maxima and saddle points), but do not arise at $h = 0$.
[122] D.E. Sheehy and L. Radzihovsky, preprint cond-mat/0608172.
[123] Subsequent to the initial appearence of the preprint of this manuscript, as well as our Comment (Ref. [122]) on Ref. [47], the authors of Ref. [67] altered their previously incorrect phase diagram (appearing in versions 1,2,3 of cond-mat/0604184). The published version now appears to be in agreement with our work, at least in the equal-mass case considered here.
[124] Note that here we used a more general expression for $e_{G,SF}$ than is necessary for the computation of $\hat{\Delta}_{BCS}$. This is necessary for the computation of $\hat{h}_{c1}$ and $\hat{h}_{c2}$ in Section 5.3.
[125] Since we are studying a homogeneous "box" trap, fixed N corresponds to fixed uniform density. We will generalize this to a fixed N in the experimentally-relevant case of a harmonic trap in Section 9.
[126] L. Viverit, C.J. Pethick, H. Smith, Phys. Rev. A 61 (2000) 053605.
[127] A.L. Fetter, J.D. Walecka, Quantum Theory of Many-particle Systems, McGraw Hill, New York, 1971.
[128] While our calculation of $a_m(h)$ is confined to the Born approximation, we expect the qualitative finding of a vanishing of $a_m(h)$ at a critical h to remain in a full calculation. [28].
[129] P. Chaikin, T.C. Lubensky, Principles of Condensed Matter Physics, Cambridge University Press, Cambridge, 1995.
[130] In actuality, the first-order transition slightly precedes the vanishing of the scattering length (and concomitant vanishing of the sound velocity). This follows from the fact that, prior to the first-order transition, the SF_M state is in a locally stable minimum of $E_G(B)$ with a finite Bogoliubov sound velocity.
[131] H. Kleinert, Fortschr. Phys. 26 (1978) 565.

[132] D.I. Uzunov, Phys. Lett. 87A (1981) 11.
[133] S. Sachdev, Quantum Phase Transitions, Cambridge University Press, Cambridge, 1999.
[134] D.S. Petrov, C. Salomon, G.V. Shlyapnikov, Phys. Rev. Lett. 93 (2004) 090404.
[135] I.V. Brodsky, M.Yu. Kagan, A.V. Klaptsov, R. Combescot, X. Leyronas, cond-mat/0507240.
[136] Clearly, LDA breaks down at the edge of the cloud as well as near r_c, corresponding to the first-order transition where LDA unphysically predicts an infinitely sharp jump discontinuity in the spatial profile, that will be cut off by the kinetic energy.
[137] D.A. Butts, D.S. Rokhsar, Phys. Rev. A 55 (1997) 4346.
[138] E. Gubankova, W.V. Liu, F. Wilczek, Phys. Rev. Lett. 91 (2003) 032001.
[139] M.M. Forbes, E. Gubankova, W.V. Liu, F. Wilczek, Phys. Rev. Lett. 94 (2005) 017001.
[140] At finite T it is easy to see that the SF_M is no longer a phase distinct from the SF since they both have a finite magnetization and have the same symmetry.
[141] A.A. Abrikosov, L.P. Gorkov, I.E. Dzyaloshinskii, Methods of Quantum Field Theory in Statistical Physics, Dover, 1975.
[142] J. Steinhauer, N. Katz, R. Ozeri, N. Davidson, C. Tozzo, F. Dalfovo, Phys. Rev. Lett. 90 (2003) 060404; S. Richard, F. Gerbier, J.H. Thywissen, M. Hugbart, P. Bouyer, A. Aspect, Phys. Rev. Lett. 91 (2003) 010405.
[143] S.J.J.M.F. Kokkelmans, M.J. Holland, Phys. Rev. Lett. 89 (2002) 180401.
[144] G. Baym, Lecture Notes in Quantum Mechanics, Addison-Wesley, 1969.
[145] G.D. Mahan, Many Particle Physics, Plenum, New York, 1990.
[146] M.H. Anderson, J.R. Ensher, M.R. Matthews, C.E. Wieman, E.A. Cornell, Science 269 (1995) 198.
[147] K.B. Davis, M.-O. Mewes, M.R. Andrews, N.J. van Druten, D.S. Durfee, D.M. Kurn, W. Ketterle, Phys. Rev. Lett. 75 (1995) 3969.
[148] M. Holland, J. Cooper, Phys. Rev. A 53 (1996) 1954.
[149] N. Read, N.R. Cooper, Phys. Rev. A 68 (2003) 035601.